Simulation of Additive Manufacturing Process Physics and Properties in Powder Bed Electron-Beam Melting of Ti-6Al-4V

Mark Hedreen

A thesis
submitted in partial fulfillment of the
requirements for the degree of
Master of Science in Mechanical Engineering

University of Washington
2020

Committee:
Ramulu Mamidala
John Kramlich
Junlan Wang

Program Authorized to Offer Degree:
Mechanical Engineering

University of Washington

Abstract

Simulation of Additive Manufacturing Process Physics and Properties in Powder Bed Electron-Beam Melting of Ti-6Al-4V

Mark Hedreen

Chair of the Supervisory Committee:
Ramulu Mamidala
Department of Mechanical Engineering

Electron-Beam Melting (EBM) is a novel additive manufacturing process that is capable of producing production-quality parts. However, part quality and microstructure are still highly variable. In order to improve the ability to develop better process parameters, experimental and numerical methods were preliminarily developed to better understand the process physics and phenomena. The state of the art in EBM process and process simulation is discussed and areas in need of further development are identified. An infrared camera is calibrated and used to attempt to measure temperatures in situ. A coupled computational fluid dynamics-thermal model is implemented in ANSYS Fluent in order to simulate the meltpool dynamics and heat transfer. This modeling approach allows for accurate resolution of process physics while avoiding excessive computational cost or time. Predicted and experimental melt pool topologies are compared for differing process and component conditions and with similar data. The effects of part geometry and process parameters on solidification rates and other microstructural characteristics are discussed and compared with experimental data. The experimental and numerical data from this work is compared with similar data from the literature and future improvements and developments are discussed.

Acknowledgments

I am very grateful to Professor Ramulu for giving me the opportunity to work on this project and for all of his guidance, mentorship, and help over the past year and a half. Since the start of this research project, I have learned an unbelievable amount about additive manufacturing, metallurgy, and process simulation and it has been a wonderful experience to be able to work in a group that is on the cutting edge in so many areas. I would also like to thank Professor Kramlich and Professor Wang for being on my thesis committee and for all of their advice and suggestions.

I would like to give a special thanks to The Boeing Company for their financial support of this work and many other additive manufacturing projects at the University of Washington.

This work would not have been possible without the hard work of Eric Bol and Curtis Doyle and I cannot thank them enough for helping me so much. They were invaluable in designing, running, and analyzing countless experiments and especially in just always being willing to talk about research and bounce ideas around. I would like to also thank everyone else from the Manufacturing Science and Technology Laboratory for their help, support, and friendship, including Dr. Rishi Pahuja, Dr. Nishita Anandan, Dr. Bryan Ferguson, Dr. Harinder Oberoi, Dr. Stefan Hovik, Abdullah Alajmi, Sai Krovvidi, Jeremy Ryatt, Melody Mojib, Garrett Kelley, Sayem Abdullah, and many others. I am also grateful to Professor Arola and the members of his research group for letting me participate in their discussions as well as lending me both their technical advice and equipment.

Lastly, but certainly not least, I would like to thank my friends and family, both in Seattle and everywhere else, for their love and support, I wouldn't have been able to do it without all of you!

Mark Hedreen
December 27, 2019

Contents

List of Figures

List of Tables

Symbols and Abbreviations

Unit and symbol conventions

Unless otherwise specified, the following unit system will always be used: meters, kilograms, seconds, Kelvin, volts, and amps.

Constants and variables that only appear once will not be included in these lists.

For material properties, the subscripts s, p, and l will be used to refer to the bulk solid, powder bed, and liquid states, respectively.

Vectors will be given using the arrow notation ($\vec{A}$) and matrices will be given in boldface ($\mathbf{A}$).

Physical Constants

σ_{SB}	Stefan-Boltzmann constant ($5.670 \times 10^{-8}\ W/m^2 * K^4$)
g	Gravitational acceleration ($9.81\ m^2/s$)
k_B	Boltzmann constant ($1.381 \times 10^{-23}\ J/K$)
N_A	Avogadro's number ($6.022 \times 10^{23}\ 1/mol$)
R	Gas constant ($8.314\ J/mol * K$)

Variables

α	Thermal diffusivity (m^2/s)
β	Liquid fraction
β_T	Coefficient of thermal expansion ($1/K$)
γ_i	Activity coefficient
γ_s	Surface tension (N/m)
$\Delta\overline{G}_i^{ex}$	Excess Gibbs energy (J/mol)
ϵ	Total emissivity
η	Dynamic viscosity ($Pa - s$)
Λ	Powder structure factor
λ	Wavelength (m)

ρ	Density (kg/m^3)
σ_b	Standard deviation of beam width (m)
$\boldsymbol{\tau}$	Shear stress (Pa)
$\boldsymbol{\tau}_{Ma}$	Marangoni stress (Pa)
ϕ	Porosity
ϕ'	Arbitrary scalar
ϕ_a	Evaporation coefficient
A	Mushy zone constant
Bo	Bond number
C	IR camera counts
c_p	Specific heat $(J/kg * K)$
D	Diffusivity (m^2/s)
d_b	Full width at half magnitude diameter (m)
d_g	Gas particle diameter (m)
G	Thermal gradient (K/m)
H	Specific enthalpy (J/kg)
h_{off}	Line hatching offset (m)
I_B	Beam current (A)
I_{xy}	Power distribution in the radial direction $(1/m^2)$
I_z	Power distribution in the vertical direction
Kn	Knudsen number
k	Thermal conductivity $(W/m * K)$
k_{eff}	Effective conductivity of powder bed
L_λ	Radiation intensity (W/m^2)
L_c	Characteristic meltpool length (m)
L_g	Characteristic powder bed length (m)
L_{fus}	Latent heat of fusion (J/kg)
$L_{j,k}^{(n)}$	Mixing energy for binary alloy $j-k$ (J/mol)
L_{vap}	Latent heat of vaporization (J/kg)
L_{vap}^0	Latent heat of vaporization at absolute zero (J/kg)
Ma	Marangoni number
m	Material flag
m_i	Molar mass (kg)
P	Pressure (Pa)
P^0	Vapor pressure of pure element (Pa)
P^s	Vapor pressure of element in an alloy (Pa)
Pe	Péclet number
p_0	Ambient pressure (Pa)
$\dot{q}$	Volumetric or surface heat flux $(W/m^3$ or $W/m^2)$
R	Solidification front velocity (m/s)
Re	Reynolds number
Re_γ	Surface tension Reynolds number
Re_c	Critical Reynolds number
r	In plane distance to center of beam (m)

$\vec{S}$	Sink term (N)
Sc	Schmidt number
T	Temperature (K)
T_a	Ambient temperature (K)
T_{dens}	Densification temperature (K)
T_{crit}	Critical temperature (K)
T_l	Liquidus temperature (K)
T_{ref}	Reference temperature (K)
T_s	Solidus temperature (K)
t	Time (s)
t_{int}	Integration time (s)
u	Velocity (m/s)
u_c	Characteristic velocity (m/s)
V_B	Beam voltage (V)
W	Radiative power (W)
W_i	Mass evaporation flux (kg/m^2)
w_i	Weight percent composition
X_i	Molar percent composition
x	Sintered neck radius ratio
Z	Atomic number
z	Depth below surface (m)
z_s	Electron beam penetration depth (m)

Abbreviations

AM	Additive manufacturing
BCC	Body centered cubic
BSE	Backscattered electrons
CA	Cellular Automata
CFD	Computational fluid dynamics
CWM	Computational welding mechanics
DED	Directed energy deposition
DSC	Differential scanning calorimetry
EBM	Electron beam melting
EBSD	Electron backscatter diffraction
FCC	Face centered cubic
FDM	Finite difference method
FEM	Finite element method
FO	Focus offset
FVM	Finite volume method
FWHM	Full width at half maximum
GA	Gas atomization
HAZ	Heat affected zone

HIP	Hot isostatic pressing
IR	Infrared
JMA	Johnson-Mehl-Avrami
KMC	Kinetic Monte Carlo
LBM	Lattice Boltzmann method
LFA	Laser flash analysis
LOF	Lack of fusion
ND	Neutral density
PA	Plasma atomization
PBF	Powder bed fusion
PDE	Partial differential equation
PF	Phase Field
PREP	Plasma rotating electrode process
PSD	Particle size distribution
SC	Simple cubic
SEM	Scanning electron microscope
SF	Speed function
SLM	Selective laser melting
SLS	Selective laser sintering
UDF	User-defined function
UDM	User-defined memory
UDS	User-defined scalar
WPM	Weld process modeling
XCT	X-ray computed tomography
XRD	X-ray diffraction

Chapter 1

Introduction

Additive manufacturing has already revolutionized many areas of industry and is continuing to grow at an exponential rate [1]. Previously reserved mainly for rapid prototyping and mockups, additive manufacturing (AM) is becoming a competitive alternative to traditional manufacturing processes for critical structural parts. This is due in no small part to the development of various AM techniques for metal components which allow for almost limitless geometrical freedom while achieving mechanical properties similar or even superior to wrought or cast processes [2]. Powder bed fusion (PBF) is one of the most popular and powerful metal AM methods, and has already achieved a major foothold.

Electron beam melting (EBM) is one of the two major PBF processes, along with selective laser melting (SLM). A brief overview of the process can be seen in Fig. 1.1a. First, a layer of metal powder is deposited onto the build plate and spread with a rake to ensure even coverage. Next, the beam is de-focused and quickly scanned across the surface to sinter the new powder layer to the rest of the build. Next, the focused beam is used to selectively melt the powder together in the desired shape of the component. Once that layer is complete, then the table is lowered and the process is repeated until the entire part has been built. Essentially, thousands of particles are welded together to make a solidified component that is embedded in a block of loosely attached sintered powder. The sintered powder is then removed and the solidified parts can be extracted. A comparison between beam modes during heating and melting is given in. Fig. 1.1b. One of the advantages of EBM is that the beam can be either used in a hatching style or can quickly alternate between different locations to allow for an effect similar to multiple beams melting at once.

Titanium alloys, in particular Ti-6Al-4V, are an ideal material for PBF applications. Ti-6Al-4V has many excellent properties that have made it widely popular in aerospace, biomedical, and other applications. Its high strength, excellent corrosion resistance, and low density make it an ideal choice for many components [4, 5]. However, Ti-6Al-4V is difficult to manufacture using conventional methods. Low thermal conductivity, a high degree of strain hardening, and significant reactivity to oxygen greatly increase the challenge and cost of production of Ti-6Al-4V using traditional processes [4]. A common metric used to characterize the economics of manufacturing processes is "buy-to-fly", which is the ratio of material purchased to the final component mass; ideally, this is as close to 1:1 as possible. Traditional Ti-6Al-4V processes in aerospace have a ratio of 12-25:1, while AM can be as low as 3-12:1 [4].

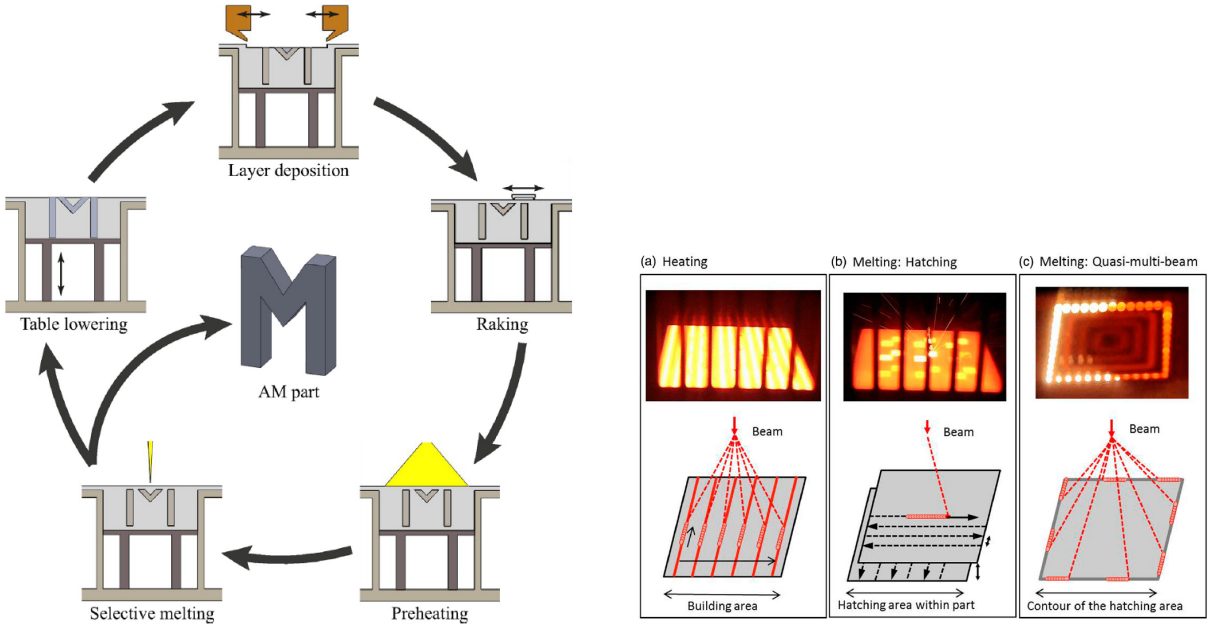

(a) Steps in the EBM process [3]

(b) Beam modes [2]

Figure 1.1: EBM Process overview

However, before metal AM can be fully integrated into the factory floor, a better understanding needs to be gained of the process physics and resulting component qualities. Qualification of AM processes, especially in fatigue and fracture critical applications, is currently poorly understand, not well standardized, and highly expensive [6]. AM processes introduce many anisotropies and complications into the final part, and research into these is still a very young field. Much experimental work has already been done at the Manufacturing Science and Technology Laboratory (MSTL) on the unique nature of PBF manufactured parts, but there has been little work done to close the loop by connecting observed mechanical properties with the physics at play during the PBF process [7]. Numerical simulation offers the ability to gain better understanding and control of the EBM process physics and to improve the properties of additively manufactured components.

Chapter 2

Background

2.1 EBM Manufacturing and Process

2.1.1 Overview of EBM Process and Parameters

A picture of the baseplate area is given in Fig. 2.1b. The electron beam column is mounted directly above the baseplate. The baseplate itself is mounted onto a vertical stage. First, a layer of powder is swept from the powder hopper across the baseplate using the rake. Next, it is preheated and then melted using the electron beam. The stage then drops one layer height (typically 50-70 μm) and the process is repeated. The whole process takes place under an atmosphere of approximately 0.1 Pa of He, which is essentially a vacuum. The baseplate is approximately 200x200 mm and the maximum vertical height that can be produces is approximately 350 mm. The minimum feature size depends very heavily on process parameters, but is on the order of 0.5-1 mm. After the build is finished, the solidified components are embedded in a block of loosely sintered powder. This block is broken down using the powder recovery system, which essentially abrasively blasts the block using Ti-6Al-4V powder as its feedstock. The sintered powder can then be reused, which allows for usage rates upwards of 90%, though not without some chemical change, which is discussed in Section 2.2.1.

The EBM process has many parameters that can be used to tune and control the manufacturing process. Determination of the optimal process parameters is a highly active area of research in both industry and academia. The process-property relationships in EBM are highly complex and a full investigation would be out of the scope of this work, but a brief discussion on relevant parameters and their importance will be given here.

One key processing technique that differentiates EBM from laser-based PBF is the ability to pre-heat the powder bed. This is done by defocusing the beam and rapidly scanning over the next layer until it has reached the build temperature, which is typically in the range of 900-1000 K, and has lightly sintered the powder [9, 10]. Sintering the powder greatly increases its thermal conductivity, which in conjunction with the elevated build temperature, significantly reduces the thermal gradients in the component [11]. This allows for significantly smaller support structures as well as lower residual stresses than in SLM. Lowering the thermal gradient also has the effect of reducing cooling rates, which generally results in less martensite and a more ductile microstructure [10, 12]. Another beneficial effect of sintering is the prevention of electrostatic scattering of powder,

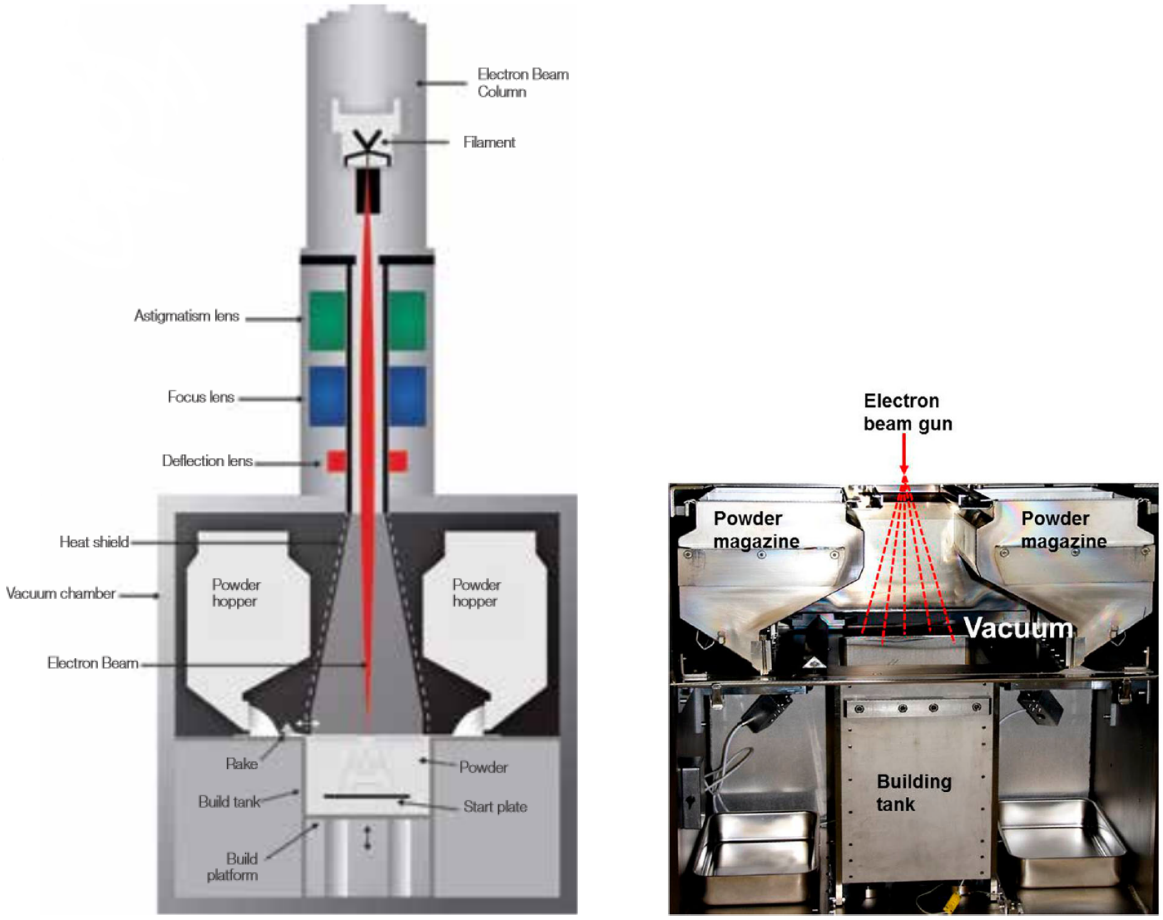

(a) Schematic of machine architecture [8]

(b) Picture of baseplate area [2]

Figure 2.1: Architecture and layout of Arcam EBM machine

which can reduce part quality or even cause build failure [11, 13]. Because the electron beam is fully electronically controlled, there are very few limitations on how the beam can be scanned. The scanning speed can be increased up to 8000 m/s, which allows for essentially instantaneous translation of the melting beam. The effects of scanning parameters on part quality have been very widely studied, but as yet there is not one parameter set that consistently achieves the best quality.

In their EBM control software, Arcam has an abstraction layer between the user inputs. For example, rather than directly increasing velocity, the speed function (SF) can be increased, which has the effect of increasing velocity, but the exact amount is not known. Furthermore, the machine automatically adjusts process parameters based on the part geometry and this level of process control is not accessible or modifiable by the machine operator [14]. The collection of process settings is referred to as a process theme. These process themes contain all the process parameters

and settings, including whether the process uses a continuous contour melting or spot melting.

Price et al. found that the scanning speed could be calculated based on SF and build height as [15]:

$$v_s = (-0.7343h + 28.554)SF \tag{2.1}$$

Where v_s is scanning speed in m/s and h is the current build height in mm.

It is convenient to define several normalized metrics of energy input. These allow for comparison across widely different process parameters or even to other AM or welding processes [16]. Line energy is defined as:

$$E_{line} = \frac{V_B I_B}{v_s} \tag{2.2}$$

Where V_B is beam voltage, I_B is beam current, and v_s is scanning speed. From there, the applied energy per unit area is [11]:

$$E_{area} = \left(\frac{E_{line}}{h_{off}}\right) n_{scan} \tag{2.3}$$

Where h_{off} is the line hatching offset and n_{scan} is the number of repetitions of the scanning parameter.

2.1.2 In situ Process Observation and Measurement

In situ process observation is a very active area of research in virtually all AM materials and processes. Lack of established measurement and monitoring techniques has repeatedly been identified as one of the major obstacles holding back qualification and adoption of metal AM in critical structural applications [6, 17–20]. Process observation research can broadly be divided into three objectives: model validation, defect detection, and active control [20]. While these objectives are by no means mutually exclusive, this review will focus on the first two. Furthermore, while much of the research on monitoring processes such as SLM, SLS, and DED is applicable to other EBM, this review will focus on EBM specific research. More detailed reviews can be found in Refs. [17–20].

There are a number of challenges specific to EBM that make in situ observation particularly difficult [18]. All EBM machines have a thermocouple mounted to the bottom of the baseplate and an optical camera mounted at the top of the vacuum chamber. However, these are of limited usage in measurement applications. The thermocouple only provides a single data point and the optical camera is too low resolution to be of use. The entire process is conducted in vacuum chamber at high temperatures, which is a challenging environment for electronics to survive. Attempting to mount a camera to a viewport in the chamber is complicated by the severe metallization of any exposed surface due to evaporated material and the necessity of leaded glass in order to block X-rays generated by the electron-beam [21, 22]. Unlike in laser-based systems, where it is possible to

use the same optical path as the laser for camera systems, the location of the electron gun column forces all cameras to be slightly offset and angled, which distorts image quality [21]. Furthermore, usage of an infrared (IR) camera, or pyrometer, is complicated by the challenge of detecting the boundaries between sintered powder and bulk material, which have major differences in emissivity [23]. In order to better understand the benefits and limitations of IR imaging, it is useful to review the underlying physics. The intensity of radiation given off by an ideal blackbody for a wavelength λ is given by Planck's law [24]:

$$L_\lambda = \frac{2hc^2}{\lambda^5} \frac{1}{\exp\left\{\frac{hc}{\lambda k_b T}\right\} - 1} \tag{2.4}$$

Where h is Planck's constant, c is the speed of light, and k_b is Boltzmann's constant. However, a blackbody is a mathematical abstraction and no real material matches it behavior exactly. The emissivity is defined as the ratio between the blackbody intensity and the intensity of a graybody, which is a body which has a lower intensity for a given temperature and wavelength [25]:

$$\epsilon_\lambda = \frac{L_\lambda^{GB}}{L_\lambda^{BB}} \tag{2.5}$$

Where ϵ_λ is the spectral emissivity for a given wavelength and L_λ^{GB} and L_λ^{BB} are the graybody and blackbody intensities, respectively. From this definition, the emissivity is in the range of $0 \leq \epsilon \leq 1$, with a value of 1 corresponding to a blackbody. By integrating Planck's law for a graybody over all wavelengths, the relationship between the emitted power W and temperature is found [25]:

$$P = \epsilon \sigma_{SB} A T^4 \tag{2.6}$$

Where σ_{SB} is the Stefan-Boltzmann constant. Note that this integration implicitly included an integration of ϵ_λ over all wavelengths. This is referred to as total emissivity. In reality, ϵ is a function of temperature, wavelength, angle, surface conditions, and other material and problem specific conditions. For the purposes of this work, unless otherwise stated emissivity will be assumed to be the total emissivity and to only be a function of temperature. This assumption is not rigourously accurate, but there was insufficient resources to measure the dependencies of all the possible conditions and a literature review was not able to find enough data either. A further discussion of the challenges of determining the emissivity of Ti-6Al-4V and a review of the values in the literature is given in Section 2.3.2. In addition to ϵ, it is also convenient to define the transmissivity τ and reflectivity ρ. Transmissivity defines how well the object is able to transmit radiation and reflectivity defines how well it can reflect absorption. These properties are defined by the following relationship [25]:

$$1 = \epsilon + \tau + \rho \tag{2.7}$$

Since all the materials studied in this work are fully opaque, they have a value of $\tau = 0$. Reflectivity and emissivity are then related by $1 = \epsilon + \rho$. The total power measured by the camera is then [25]:

$$W_{camera} = W_{object} + (1 - \epsilon_{object})W_{ambient} \tag{2.8}$$

$$W_c = \sigma_{SB} A \left(\epsilon_o T_o^4 + (1 - \epsilon_o)\epsilon_a T_a^4\right) \tag{2.9}$$

The first term represents the power emitted by the object itself and the second term represents the power emitted by the ambient environment that is then reflected off the object to reach the camera. This means that not only must the nature of the object being observed be understood, but the entire surroundings of the target must also be properly evaluated in order to read the correct temperature.

Despite these difficulties, many researchers have successfully implemented a top mounted IR camera to monitor and take measurements of builds. Schwerdtfeger et al. used a top mounted IR camera to detect and track defects in Ti-6Al-4V [26]. In order to prevent metallization of the viewing window, they used a metal shutter that closed during printing and opened between layers; a schematic of their setup is given in Fig. 2.2a. Their camera had a pixel resolution of approximately 830 μm, which is too large to detect many defects. The Wicker group at the University of Texas at El Paso used a similar camera and shutter system to develop methods for defect detection and automatic temperature control in Ti-6Al-4V [24, 27–34]. In order to accurately measure temperatures, they calibrated the IR camera against a blackbody with a thermocouple. They were able to detect defects down to 600 μm, but noted that the IR camera overpredicted defect size compared to CT analysis.

One of the major limitations of the shutter-type systems is that they cannot measure the temperatures during sintering and melting due to rapid metallization at high temperatures. Due to its low melting point, Al evaporates very heavily and deposits onto all surfaces in the vacuum chamber, including any windows. Experimental measurements of the metallization show that it is dominated by Al [36, 37]. A group from Oak Ridge National Lab developed an IR camera that used a scrolling tape film to continuously clean metallization from the window and used it to measure temperatures and detect defects down to approximately 100 μm in Ti-6Al-4V and IN718 [22, 23, 38–40]. In order to distinguish between sintered and bulk material, they developed an algorithm to track the temperature reached by each pixel that would then modify its emissivity if it reached the melting point. They used their algorithm to analyze solidification rates and gradients and were also able to correlate measured defects and fatigue strength for varying process conditions. An example image from their results is given in Fig. 2.3. Boone et al. developed a comparable system that was able to record the melting process with a resolution of 66-79 μm and at much higher framerates [41]. They implemented a similar tracking system to distinguish between sintered and solidified material and were able to achieve a temperature range of 950-1630 K.

In addition to top mounted IR cameras, some additional work has been done imaging through the frontal viewport; a picture of a typical setup is given in Fig. 2.2b. The Chou group from the University of Alabama and NASA measured temperatures by aiming a camera through the viewport on the front window of the machine [15, 35, 37, 42, 43]. Metallization of the viewing window is not preventable with this approach and in order to account for the effects an empirical

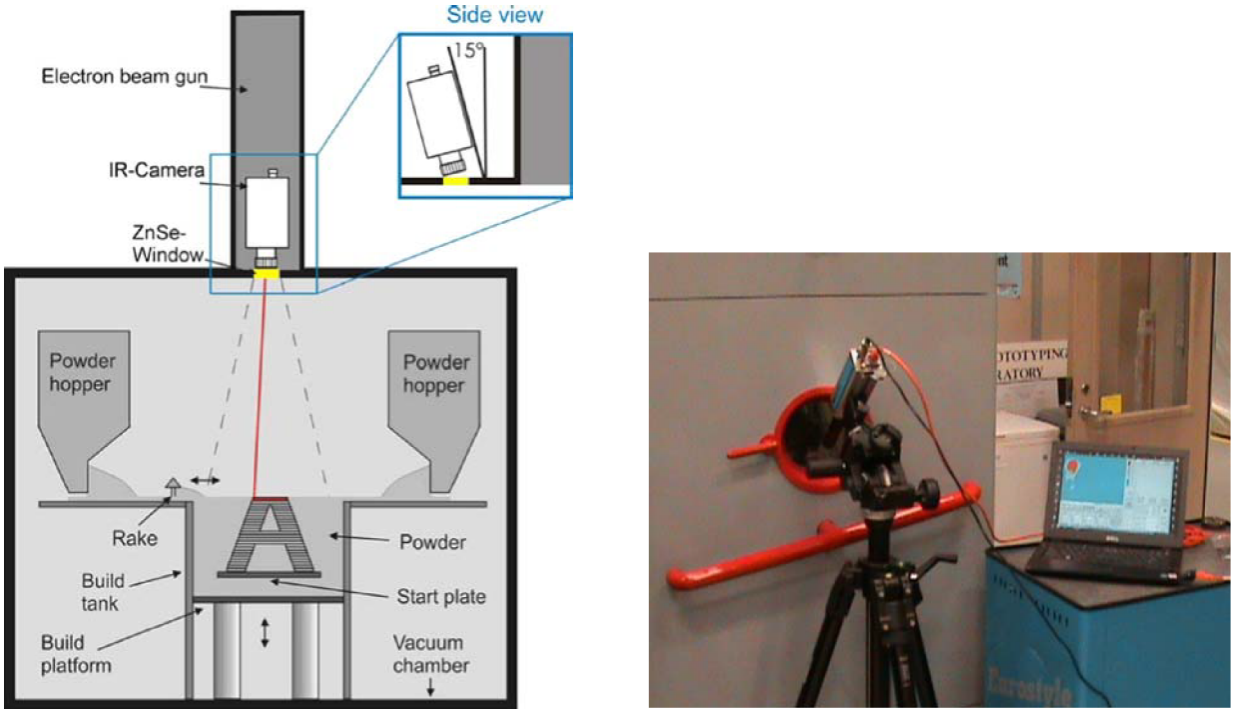

(a) Typical top-mounted camera schematic [26]

(b) Typical front looking camera setup [35]

Figure 2.2: Top-mounted vs. front looking IR camera setups

calibration was developed by comparing the transmission through pieces of glass that had been used for varying amounts of time. Another issue with this approach is that due to the heatshield location, the field of view is skewed and only of a small spatial area. However, despite these limitations, they were still able to measure temperatures from the build area.

In addition to IR imaging, there has also been some work using other imaging techniques. Scharowsky et al used a top mounted optical camera with a framerate of 4,000-6,000 fps to observe meltpool dynamics [21]. They used a laser to illuminate the meltpool and tracked the frequency of oscillations in order to observe the meltpool fluid dynamics. Wong et al. modified the heatshield design in order to measure backscattered electrons (BSE) and generate an optical-like image of parts [44–46]. Their equipment is still in the prototyping stage and cannot be operated during melting, but is able to generate very high resolution images of defects; a comparison between an optical image and a BSE generated image is given in Fig. 2.4. The Körner group has also developed a BSE detection system that they used to rapidly generate process maps based on detected porosity [47, 48]. Rather than having to print and then post-process samples, they were able to detect defects as they were printing, greatly improving the speed of process map generation. Arcam is also developing a BSE-based measurement system, but few details have been released and it is not yet available [8].

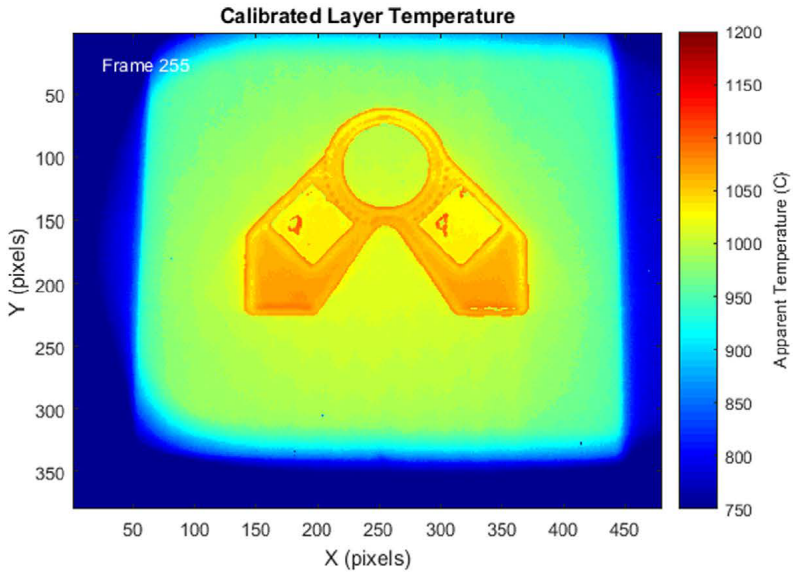

Figure 2.3: Measured temperatures during EBM of IN718 by Raplee et al [23]

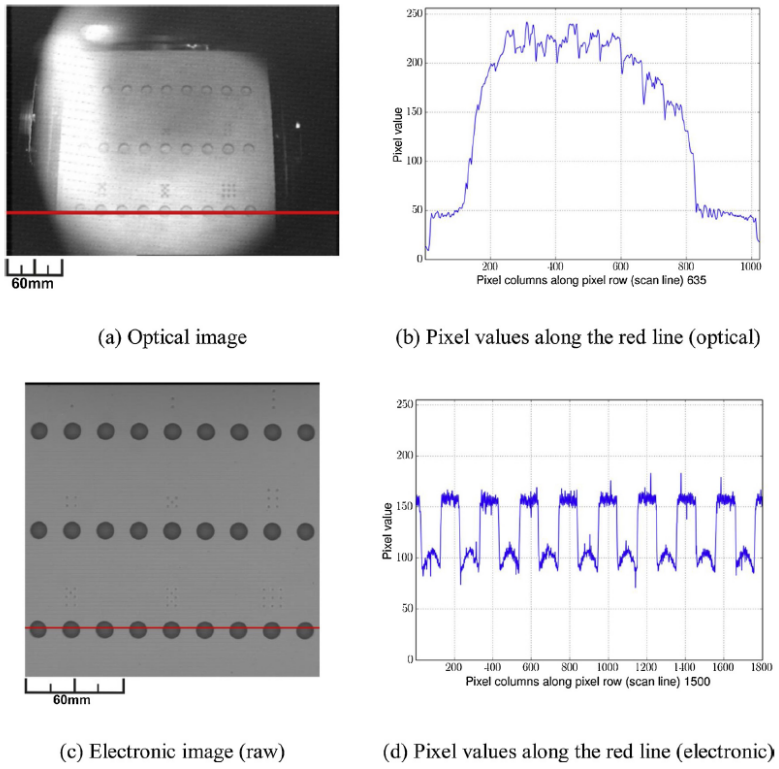

(a) Optical image

(b) Pixel values along the red line (optical)

(c) Electronic image (raw)

(d) Pixel values along the red line (electronic)

Figure 2.4: Comparison between optical image and BSE generated result from Wong et al. [44]

2.2 Properties of EBM Built Components

2.2.1 Microstructure of EBM Built Ti-6Al-4V

Ti-6Al-4V is an α-β alloy, with the transition occurring at approximately 1270 K. Al helps stabilize the α phase, while V stabilizes the β phase [49]. Unlike many conventional manufacturing processes, the microstructure of PBF parts is extremely heterogeneous. This is due to the wide variation in thermal history experienced at different areas of the build chamber, and is dependent on material choice, component geometry, and process parameters [10, 50]. The cooling rates and thermal gradients in EBM are significantly higher than many other manufacturing processes and typically on the order of 10^4-10^5 K/s and 10^8-10^9 K/m [2, 4, 51]. There is also a significant anisotropy between the build direction and the in-plane directions, caused by high thermal gradient between the heat source and the baseplate. This generally leads to tall, columnar microstructures in the build direction that extend across multiple layers [10].

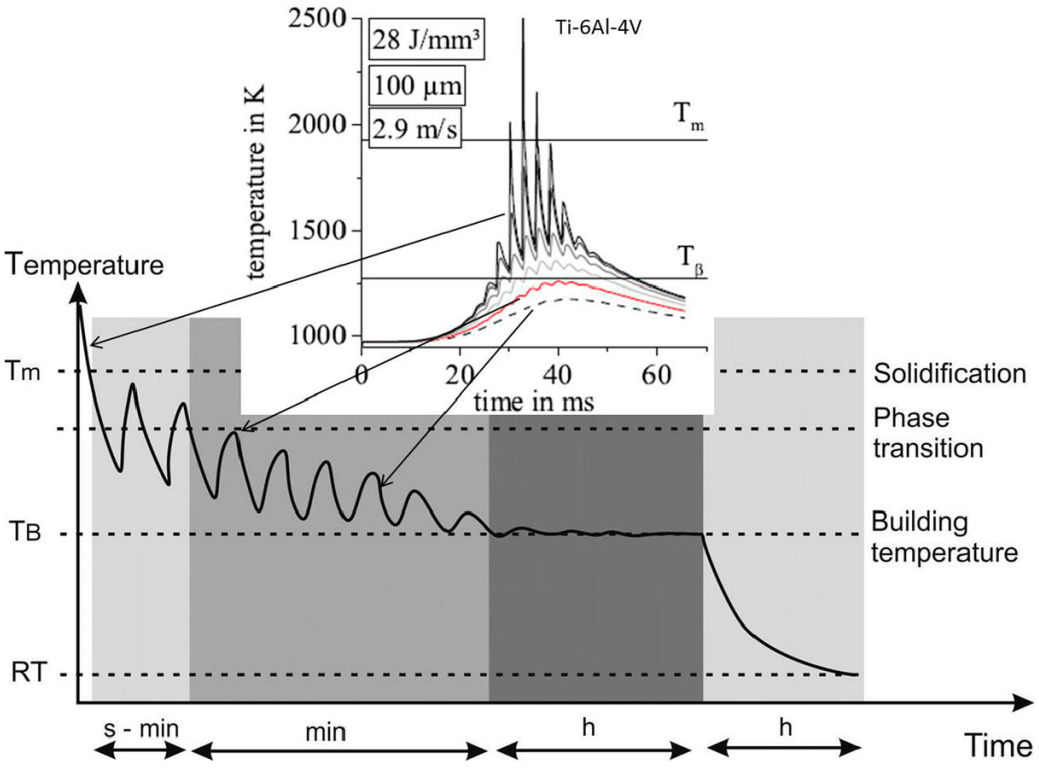

Figure 2.5: Thermal cycling about the α-β transition [2]

Grain formation from the meltpool is driven by three different regimes of thermal conditions [4, 10, 52–54]. After solidification, the β phase is formed, which transforms into martensitic α' due to the rapid cooling rate. α' is formed when the initial temperature is above the martensite start temperature, which is on the order of 850-1050 K, and the cooling rate is higher than 410 K/s [10]. Depending on the process parameters and component geometry, areas of solidified metal may be re-melted multiple times, repeating this process. This cycling behavior is depicted

in Fig. 2.5 [2]. As more layers are added on top of existing metal, the previously deposited layer undergoes significant thermal cycling between the build temperature and elevated but non-melting temperature, which causes the decomposition of the α' phase into the α-β phase. As more layers, and hence more thermal mass, are deposited above a given layer, the magnitude of thermal cycling decreases, resulting in a near iso-thermal holding at the build temperature. Quasi-static heat treatment above 973 K has been found to result in complete decomposition of α', which explains the small volume of martensite found in most EBM studies [10]. Lastly, there is a slow cooling to room temperature.

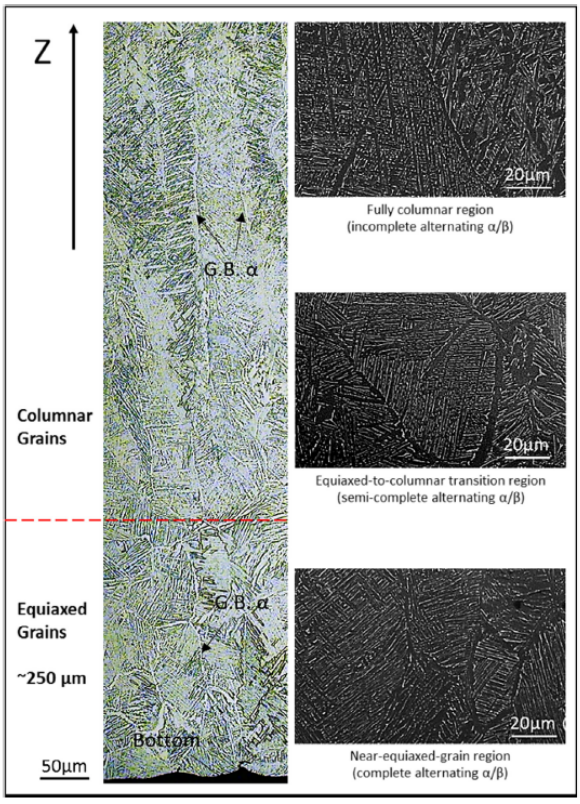

(a) Equiaxed-columnar transition on the lower section of parts [49]

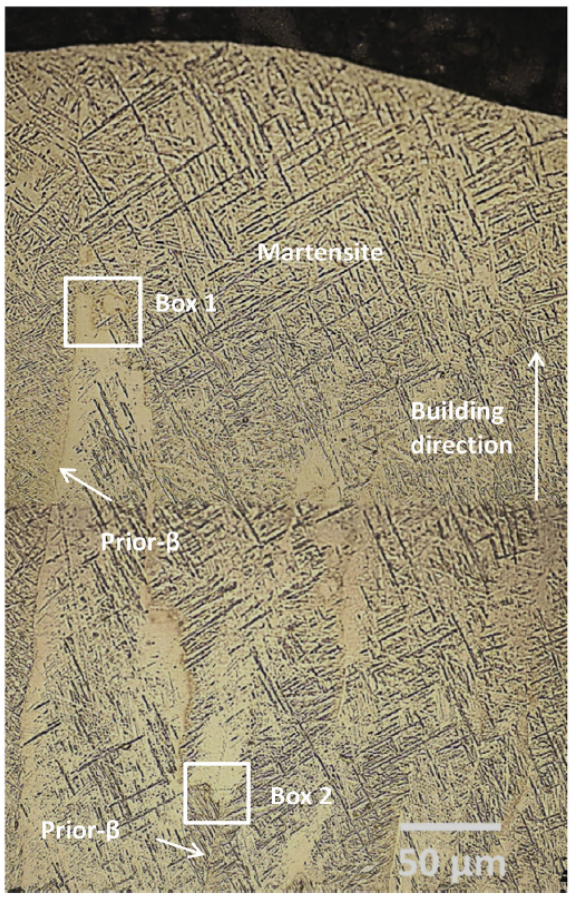

(b) The α-β to α' transition on the upper section of parts [55]

Figure 2.6: Spatial dependency of microstructure on the upper and lower ends of parts

Spatially, this also results in three major regions. The first is the bottom 250 μm of the part, which has an equiaxed β microstructure and is pictured in Fig. 2.6a [49]. This quickly transitions to an α-β columnar region, with a small mixed transition. The columnar regions extends all the way to the top of the part, which is pictured in Fig. 2.6b [55]. At approximately 500 μm below the top surface of the part, the microstructure transitions from a mixed α-β into α'. This martensite was formed due to rapid cooling, but unlike the rest of the part, did not go through the thermal cycling that is given in Fig. 2.5 and therefore did not decompose. This behavior also complicates

attempts to determine the microstructure based on IR observation, as it is impossible to capture the sub-surface thermal cycling; numerical methods are necessary to fully understand how the microstructure forms.

Another cause of microstructural change is the preferential evaporation of Al. Due to its low melting point, Al evaporates significantly more than Ti or V. However, Juechter et al. found that under normal process parameters, the compositional change was very small [56]. Only when the processing conditions were modified to increase the max temperature was a significant change in composition produced. While powder recycling is very common in EBM, it is not without some risks. Nandwana et al. found that oxygen contamination linearly increased over five builds, but was still within the ASTM limits [36]. Extrapolation of their results suggests that within 10-11 builds the oxygen levels would be above the maximum allowable.

2.2.2 Defects and Part Quality

Imperfections and variability are inherent in any manufacturing method, but those seen in AM differ significantly from conventional processes and deserve special attention. With proper choice of parameters, EBM can achieve densities of 99.9% of bulk material, but it is difficult to fully eliminate porosity [57]. Porosity falls into two main categories: gas pores and lack of fusion defects, which can be seen in Fig. 2.7. Gas pores occur due to pores being created inside the particles during the Gas Atomization (GA) process typically used to manufacture the powder [5, 57]. Alternative methods of powder creation such as Plasma Rotated Electrode Process (PREP) or Plasma Atomization (PA) have been shown to greatly reduce the occurrence of gas pores, but there was no significant effect on tensile strength in IN718 components made with GA or PREP powder [58]. Lack of fusion defects occur due to poor bonding between the layer currently being melted and previously solidified metal, often due to usage of sub-optimal process parameters, and are typically larger than gas pores [4, 51]. Lack of fusion defects also tend to have wider shapes in the plane of the build, with sharp corners that can act as stress concentrations and initiate failure [4]. Fractography of EBM Ti-6Al-4V specimens shows that fracture in many cases initiates at these defects [59, 60]. Furthermore, components with higher porosity tend to have worse mechanical properties, though it is difficult to draw a direct relation between measured porosity and resulting properties [57, 59, 61]. While hot isostatic pressing (HIP) can close some pores, this adds significant cost and does not work for all defects [51]. Keyhole melting, which occurs due to highly localized evaporation and is a common cause of defects in SLM and some welding processes, is not observed in EBM, most likely due to process controls implemented by Arcam on the beam power [61]. Surface roughness is also poor in EBM, with typical values on the order of $R_a = 25 - 35\mu m$ [62]. The surface roughness is also highly dependent on geometry, particularly thickness, and process parameters.

Residual stress is a significant issue in PBF due to the significant thermal gradients present during the melting and solidification of new layers. Fundamentally, the growth of residual stresses can be thought of as a two step process, which is depicted in Fig. 2.8. When a new powder layer is melted, a significant temperature gradient is created in the build direction, which causes recently deposited layers to expand. As the new layer solidifies and cools, it contracts, creating residual stresses [63, 64]. This mechanism is complicated by the fact that the heat source is only applied to a single point, meaning that there are significant thermal gradients in the plane of the

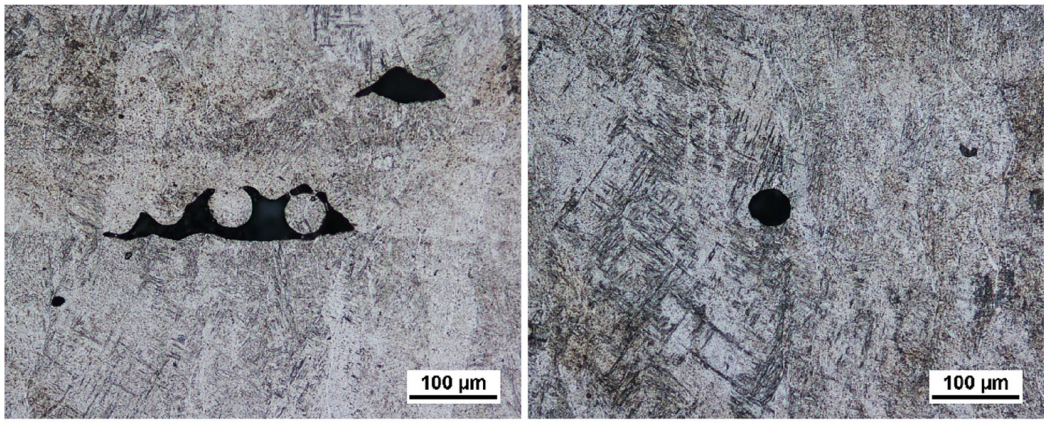

Figure 2.7: Porosity in EBM of Ti-6Al-4V; left: lack of fusion defects, right: gas pores [57]

build and non-uniform solidification and cooling. In practice, this means that residual stresses are highly dependent on material, part geometry, and process parameters [63]. Due to the usage of pre-heating in EBM, residual stresses are much lower than in SLM and can even be considered insignificant in many applications. Hrabe et al. measured negligible residual stresses in as-built, stress relieved, and HIPed EBM Ti-6Al-4V samples and found that the as-built and stress relieved samples had identical high cycle fatigue performance, which they attributed to in-situ stress relief due to the high build temperature [60]. Edwards et al. also measured residual stresses in Ti-6Al-4V and found results in good agreement with those of Hrabe et. al and also noted that the magnitude quickly diminished in surface depth and was significantly less than stresses in SLM of Ti-6Al-4V [65, 66]. Sochalski-Kolbus et al. compared residual stresses from SLM and EBM of IN718 and also found that residual stresses in EBM were significantly lower [67].

As a consequence of these quality issues, particularly LOF voids and surface roughness, the fatigue strength of EBM built Ti-6Al-4V is significantly lower than conventionally produced material, even though the tensile strength is often comparable or even superior [50, 68]. HIP and surface machining are able to improve the fatigue strength by closing internal voids and removing stress concentrations caused by the surface roughness, respectively. However, Chern et al. note that HIP or surface machining alone does not produce fatigue strength equivalent to conventional results and that it is only with the application of both processes that the equivalent fatigue strength is possible. These post-processing techniques add significant cost and time to the manufacturing process and ideally could be eliminated through a better understanding of process physics and optimized process parameters.

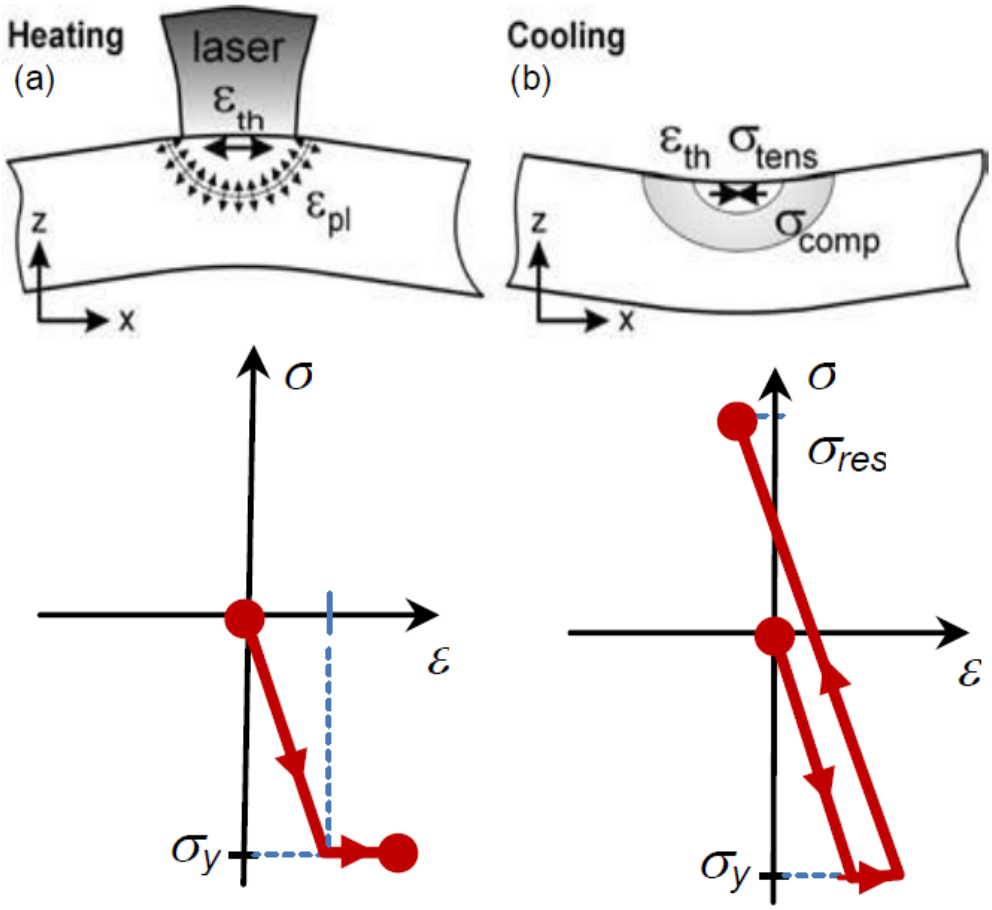

Figure 2.8: Residual stress development during PBF; a) Heating from melting of new layer causes thermal expansion of previous layers and b) Cooling from solidification causes contraction [64]

2.3 Analysis of Process Physics in EBM

2.3.1 Heat and Mass Transfer Mechanisms

The physics of AM are complex, involving highly non-linear heat and mass transfer effects. A brief list of effects is given in Fig. 2.9. Many different phenomena and effects play a role in determining the final part quality, drawing from a diverse range of engineering fields.

Transient heat transfer in a solid is given by:

$$\frac{\partial(\rho H)}{\partial t} = \nabla \cdot (k \nabla T) + \dot{q} \tag{2.10}$$

Where ρ is density, H is specific enthalpy, k is conductivity, T is temperature, and $\dot{q}$ is the volumetric heat source from the boundary conditions. Due to the effects of phase changes and large temperature variations, all material properties (ρ, k, etc.) are assumed to be functions

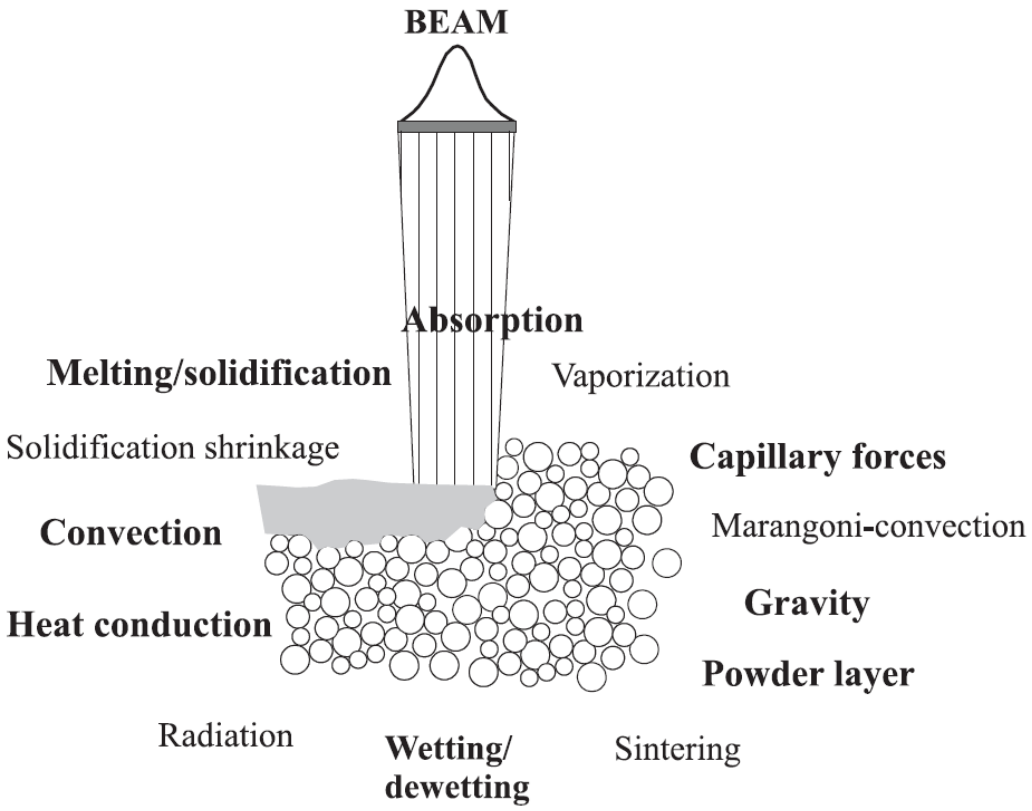

Figure 2.9: Thermal, fluid, and mechanical effects during the EBM process [69]

of space, time, and temperature unless otherwise stated. In order to account for melting and solidification, it is useful to define H as:

$$H = \int_{T_{ref}}^{T_s} c_p \, dT + \beta L_{fus} \tag{2.11}$$

Where c_p is the specific heat, L_{fus} is the latent heat of fusion, T_{ref} is a reference temperature, and β is the liquid fraction, defined as:

$$\beta = \begin{cases} 0 & T < T_s \\ \frac{T - T_l}{T_l - T_s} & T_s \leq T \leq T_l \\ 1 & T_l < T \end{cases} \tag{2.12}$$

Where T_l and T_s are the liquidus and solidus temperatures of the alloy, respectively. Unlike pure elements, which melt isothermally at a single temperature value, alloys have a partially melted or mushy region between the solidus and liqudus temperatures. In order to account for the effects of fluid flow on heat transfer, the fluid dynamics of the meltpool are resolved using the incompressible Navier-Stokes equations [70]:

$$\boldsymbol{\nabla} \cdot \vec{u} = 0 \tag{2.13}$$

$$\frac{\partial \vec{u}}{\partial t} + \boldsymbol{\nabla} \cdot (\vec{u} \otimes \vec{u}) = -\frac{1}{\rho}\boldsymbol{\nabla} P + \frac{1}{\rho}\boldsymbol{\nabla} \cdot \boldsymbol{\tau} + \vec{F} + \vec{S} \tag{2.14}$$

$$\frac{\partial E}{\partial t} + \boldsymbol{\nabla} \cdot (\vec{u} E) = -\boldsymbol{\nabla} \cdot \vec{u} + \frac{1}{\rho}\boldsymbol{\nabla} \cdot (\boldsymbol{\tau} \cdot \vec{u}) + \frac{1}{\rho}\boldsymbol{\nabla} \cdot (k \boldsymbol{\nabla} T) + \dot{q} + \vec{F} \cdot \vec{u} \tag{2.15}$$

Where $\vec{u}$ is the velocity, P is the pressure, $\boldsymbol{\tau}$ is the shear stress, $\vec{F}$ is the body forces, $\vec{S}$ is the solidification sink term, and E is the internal energy. In order to account for the effects of partially solidified areas on fluid flow, a sink term is added to the RHS of the momentum equation, Eq. (2.14). The effects of solidification are based on an analytical model derived by Voller and Prakash [71]. The mushy region is assumed to follow Darcy's law for fluid in a porous medium, which is given by [71]:

$$\vec{u} = -\frac{K}{\eta}\boldsymbol{\nabla} P \tag{2.16}$$

Where η is the dynamic viscosity and K is the permeability, which is assumed to be a function of β. From this, the Carmen-Koseny equation is derived [71]:

$$\boldsymbol{\nabla} P = -A\frac{(1-\beta)^2}{\beta^3}\vec{u} \tag{2.17}$$

Where A is the mushy zone constant. The source term in Eq. (2.14) follows as [71]:

$$\vec{S} = A\frac{(1-\beta)^2}{\beta^3 + \varepsilon}\vec{u} \tag{2.18}$$

Where ε is a small value, assumed to be 10^{-3}, to prevent division by zero. A has the effect of tuning the strength of solidification on melting; some analytical relationships have been proposed based on the dynamic viscosity and material microstructure, but it is typically assumed to be in the range of $10^3 - 10^6$ [71, 72]. This model allows for a smooth transition in fluid flow between solid and liquid areas. When $\beta = 0$, i.e. in a solid region, the sink term is equivalent to A/ε, which means that the damping force is equivalent to $10^6 - 10^8$ times the magnitude of the velocity and essentially forces the velocity to 0. On the other hand, when $\beta = 1$, the sink term is equal to 0, which shows that there is no effect in fully liquid regions. The shear stress term $\boldsymbol{\tau}$ in the momentum equation is given by [70]:

$$\boldsymbol{\tau} = \eta\left((\boldsymbol{\nabla} \cdot \vec{u} + \boldsymbol{\nabla} \cdot \vec{u}^T) - \frac{2}{3}\boldsymbol{\nabla} \cdot P\mathbf{I}\right) \tag{2.19}$$

Where $\mathbf{I}$ is the identity matrix. In this work, the dynamic viscosity η is assumed to be a function of temperature, but constant with regards to shear rate. The main cause of fluid flow in the meltpool

is Marangoni stress, which occurs due to the thermal gradient on the free surface of the meltpool causing variations in surface tension [73]. Temperature dependent surface tension is given by:

$$\gamma_s(T) = \gamma_s^{ref} + \frac{\partial \gamma_s}{\partial T}(T - T_{ref}) \tag{2.20}$$

Where γ_s is the surface tension and γ_s^{ref} is the surface tension at some reference temperature T_{ref}. The induced Marangoni stress is then given by:

$$\boldsymbol{\tau}_{Ma} = \frac{\partial \gamma_s}{\partial T}(\boldsymbol{\nabla} T)_{\partial\Omega} \tag{2.21}$$

Where $\boldsymbol{\tau}_{Ma}$ is the induced shear stress, γ_s is the surface tension, and $\partial\Omega$ is the free surface of the liquid. In many alloys commonly used for EBM, including Ti-6Al-4V and IN718, the derivative of γ_s is negative, which causes fluid to be driven away from the center of the meltpool [74, 75].

It is often useful to define several dimensionless numbers to characterize the mass and heat transfer regimes of the meltpool and allow comparisons across different domains [76, 77]. Particularly in additive manufacturing applications, where there are both a wide variety of processes, materials, and paramters to tune, dimensionless numbers allow the analysis to be approximated and simplified based on first principles.The input characteristic parameters and material parameters are given in Table 2.1 and a summary of the equations and their values is given in Table 2.2. Reynolds number characterizes the ratio of inertial forces to viscous forces and helps estimate the onset of turbulent flow [78]:

Table 2.1: Characteristic process physical properties in EBM of Ti-6Al-4V

Length, temperature, and velocity	
ΔT	1575 K [79]
L_c	$350\mu m$ [74]
u_c	0.76 m/s [80]
Ti-6Al-4V material properties at T_l	
ρ	$3920\,\mathrm{kg/m^3}$ [81]
β_T	$5.78 \times 10^{-5}\,\mathrm{K^{-1}}$ [81]
η	7×10^{-3}Pa-s [82]
α	$8.6 \times 10^{-6}\,\mathrm{m^2/s}$ [81]
$\partial\gamma_s/\partial T$	$-4.1 \times 10^{-4}\,\mathrm{N/(m\,K)}$ [83]

$$\mathrm{Re} = \frac{\rho u_c L_c}{\eta} \tag{2.22}$$

Where u_c is the characteristic velocity and L_c is the characteristic length. Generally, u_c is taken to be maximum velocity and L_c is half of the meltpool width. The characteristic velocity can be estimated by relating the surface tension force and the viscous force [84]:

$$\frac{\Delta\gamma_s}{L_c} = \frac{\eta u_c}{L_c} \tag{2.23}$$

$$u_c = \frac{\Delta\gamma_s}{\eta} \tag{2.24}$$

$$u_c = \frac{\partial\gamma_s}{\partial T}\frac{\Delta T}{\eta} \tag{2.25}$$

Where ΔT is taken to be the maximum temperature minus the liquidus temperature. Reynolds number is used to characterize a fluid flow as laminar or turbulent, depending on if the value is above or below a transition point known as the critical Reynolds number, Re_c. This value is problem-specific and qualitatively defined. Substituting Eq. (2.25) into Eq. (2.22) gives the surface tension Reynolds number [84]:

$$\mathrm{Re}_\gamma = \left|\frac{\partial\gamma_s}{\partial T}\right|\frac{\rho L_c \Delta T}{\eta^2} \tag{2.26}$$

The transition between laminar and turbulent flow in a meltpool is not well established and is an area of active research. Jamshidinia et al. and Kidess et al. both cite $\mathrm{Re} = 600$ as the transition point and Saldi cites that $\mathrm{Re}_\gamma \gg 100$ leads to turbulent surface behavior [80, 84, 85]. The calculated values are $\mathrm{Re} = 150$ and $\mathrm{Re}_\gamma = 1.8 \times 10^4$. This suggests that surface behavior in the meltpool may be more turbulent but the overall kinetics tend to be laminar. However, this is just a rough approximation, as ρ, η, and u_c are all highly variable across the meltpool. No significant studies could be found in the AM modeling literature on the effects of turbulence and even in the welding modeling literature, which is a much older field and shares many similarties with AM, there is no consensus [84, 85]. In a review and study on modeling of laser welding, Kidess et al. also note that almost all common turbulence models are developed for aerodynamic applications and may not be accurate for the fluid behavior seen in a meltpool [85]. Furthermore, they note that many empirical corrections to fluid and thermal properties to account for turbulent effects do not correctly emulate experimental behavior. They suggest that more complex models that are better able to handle the coupling between heat source, solidification behavior, and meltpool dynamics are necessary. Accordingly, the fluid flow will be assumed laminar in this analysis, as it is not clear that turbulence modeling provides any benefit for the increased computational cost. Péclet number characterizes the ratio of convective to conductive heat transfer in a fluid [78]:

$$\mathrm{Pe} = \frac{u_c L_c}{\alpha} \tag{2.27}$$

Where α is the thermal diffusivity, defined as $k/\rho c_p$. When $\mathrm{Pe} \gg 1$ convective heat transfer dominates and correspondingly as $\mathrm{Pe} \ll 1$ conduction dominates. The calculated value is $\mathrm{Pe} = 31$, which demonstrates that convective heat transfer is the dominant mechanism, rather than conductive. Analyses of meltpool physics that do not take into account convective effects are likely to be innacurate due to this. The Marangoni number characterizes the effects of surface tension [76]:

$$\mathrm{Ma} = -\frac{\partial \gamma_s}{\partial T}\frac{L_c \Delta T}{\eta \alpha} \tag{2.28}$$

This can be thought of as the ratio in which a gradient in temperature is dissipated by convection vs conduction [76]. The calculated value is $\mathrm{Ma} = 3.8 \times 10^3$, which shows that Marangoni stress and temperature gradients are what drive the meltpool physics. This is very similar to welding processes, where the value of the Marangoni number is also on the order of $10^2 - 10^5$ [84]. The dominance of surface tension is further shown by the Bond number, which characterizes the relative importance between buoyancy and surface tension in driving fluid flow [84]:

$$\mathrm{Bo} = \left|\frac{\partial \gamma_s}{\partial T}\right|^{-1} \rho g \beta_T L_c^2 \tag{2.29}$$

Where β_T is the coefficient of thermal expansion. The calculated value is on the order of $\mathrm{Bo} = 6.6 \times 10^{-4}$. This shows that surface tension effects dominate the meltpool behavior and that buoyancy can be neglected. This greatly simplifies the analysis by allowing the assumption of constant fluid density. The ratio of convective and diffusive transfer on the chemical composition of the meltpool is given by the Schmidt number [79]:

$$\mathrm{Sc} = \frac{\eta}{\rho D} \tag{2.30}$$

Where D is the diffusion coefficient. Ivanchenko et al. estimated the following value for diffusion of Al in liquid Ti-6Al-4V [86]:

$$D_{Al} = \left(10 \times 10^{-8}\,\mathrm{m}^2/\,\mathrm{sec}\right) \exp\left\{\frac{2.5 \times 10^5\,\mathrm{J/mol}}{R}\left(\frac{1}{T_{liq}} - \frac{1}{T}\right)\right\} \tag{2.31}$$

Where R is the gas constant. Schmidt number is plotted in Fig. 2.10. Only at very high temperatures does diffusion become relevant, whereas for most of the processing window it is inconsequential. Furthermore, due to Marangoni stress coupling surface temperature and fluid velocity, the areas of highest temperature will also have the highest rate of convective transfer. Experimental results also show that diffusion has a negligible contribution to compositional changes in Ti-6Al-4V [56, 79]. In order to characterize the behavior of the atmosphere of the machine, it is convenient to define the Knudsen number [79]:

$$\mathrm{Kn} = \frac{\lambda_{mfp}}{L_g} \tag{2.32}$$

Where λ_{mfp} is the mean free path of the gas and L_g is the characteristic length scale, which is taken to be the diameter of a particle of powder [87]. When the Knudsen number is less than 0.1, the atmosphere can be treated as a continuum and at values greater than 10 it is a free-molecular

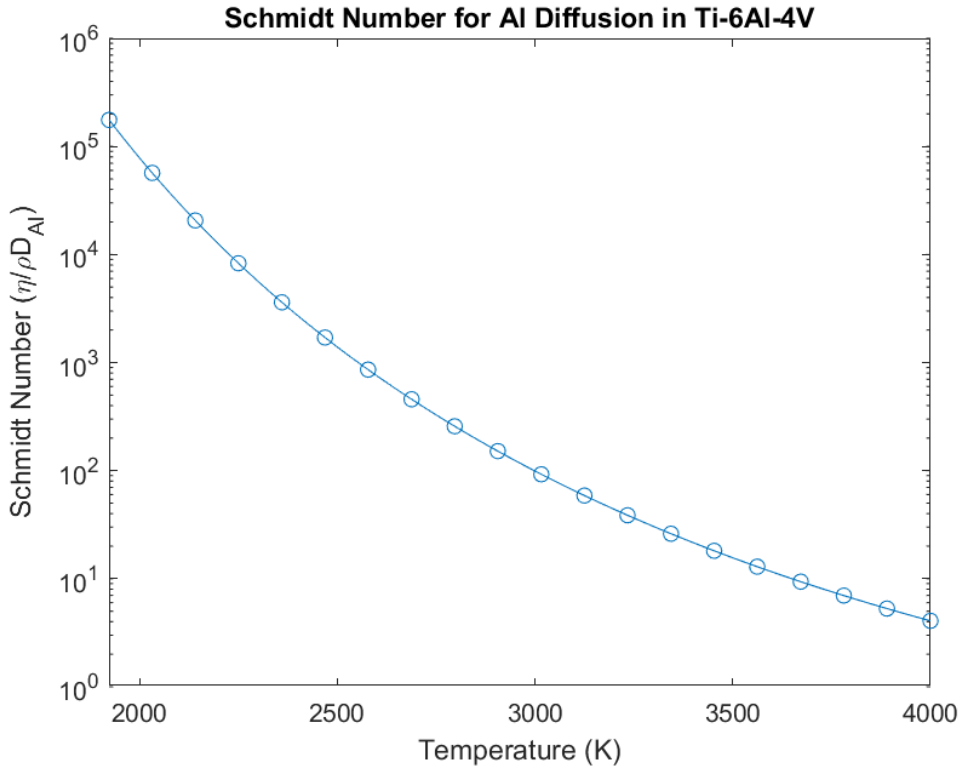

Figure 2.10: Schmidt number for transfer of Al in liquid Ti-6Al-4V

flow, with a transition region between 0.1-10 [79]. Assuming the atmosphere is an ideal gas, the mean free path can be calculated from kinetic gas theory as [78]:

$$\lambda_{mfp} = \frac{k_b T}{\sqrt{2}\pi d_g^2 p_0} \tag{2.33}$$

$$\text{Kn} = \frac{k_b T}{\sqrt{2}\pi d_g^2 p_0 L_g} \tag{2.34}$$

Where k_b is the Boltzmann constant, d_g is the diameter of a gas molecule, and p_0 is the atmospheric pressure. The typical processing conditions of an A2X machine are a temperature of 1000 K and a 0.01 Pa atmosphere of He, which has a diameter of 2.2×10^{-10}m. The calculated value is approximately Kn $= 10^4$, meaning that the atmosphere is negligible and the process can be assumed to take place in a vacuum. In comparison, changing to atmospheric pressure and keeping all other conditions the same – i.e. an atmosphere similar to SLM/SLS processes – results in a value of Kn $= 10^{-2}$. Based on this analysis, the atmosphere is well within the free molecular regime and convection is negligible, which means that the only two mechanisms of heat loss are radiation and evaporation. A full list of the dimensionless numbers and their values is given in Table 2.2. Through this simple analysis, it has been qualitatively shown that surface tension driven convection is the dominant mechanism of heat and mass transfer in the meltpool. Any

analysis of process physics in EBM must consider Marangoni stress in order to properly resolve the problem.

Table 2.2: Typical values of dimensionless numbers in EBM

Name	Equation	Calculated value
Re	$\frac{\rho u_c L_c}{\eta}$	150
Re_γ	$\left\lvert\frac{\partial\gamma_s}{\partial T}\right\rvert\frac{\rho L_c \Delta T}{\eta^2}$	1.8×10^4
Pe	$\frac{u_c L_c}{\alpha}$	31
Bo	$\left\lvert\frac{\partial\gamma_s}{\partial T}\right\rvert^{-1}\rho g \beta_T L_c^2$	6.6×10^{-4}
Ma	$-\frac{\partial\gamma_s}{\partial T}\frac{L_c \Delta T}{\eta\alpha}$	3.8×10^3
Sc	$\frac{\eta}{\rho D}$	$10^2 - 10^5$
Kn	$\frac{k_b T}{\sqrt{2}\pi d_g^2 p_0 L_g}$	10^4

The two main sources of heat loss during EBM are radiative heat transfer to the atmosphere and evaporation from the meltpool. Both of theses mechanisms are nonlinear in temperature and heavily dependent on the material condition. However, a number of analytical relationships are available to help characterize them. From Eq. (2.6), the total heat flux due to radiation can be expressed as:

$$\dot{q}_{rad} = -\sigma_{SB}\epsilon(T^4 - T_a^4) \tag{2.35}$$

The unit convention in this equation, and for all other mass and heat fluxes, is that a positive flux is adding heat (or mass) to the body and a negative flux is removing it. Rodriguez et al. measured the temperature of the heat shield during printing and found it was approximately 600 K [31]. A major challenge in properly applying this boundary condition is understanding the temperature dependency of ϵ as well as its value in a powder bed. Further discussion of ϵ is given in Section 2.3.2.

Evaporation is assumed to have a negligible effect on the mass, but the thermal loss is significant enough to be considered [73, 75]. Furthermore, recoil pressure will not be modeled. The heat flux formulation is based on the implementation given by Klassen for the Ti-Al system, with additional details and experimental validation on the Ti-Al-V system based on work by Ivanchenko, Semiatin, and Ivasishin [79, 86, 88]. Vapor pressure of a pure element i is given by the Clausius-Clapeyron equation, sometimes also referred to as the Dupreé-Rankine equation [86]:

$$P_i^0 = F_i * 10^{\left(-\frac{A_i}{T}+B_i\right)} * T^{C_i} \tag{2.36}$$

Where P_i^0 is the vapor pressure of a pure element i, F_i is a constant to convert the units into Pa, and A_i, B_i, and C_i are fitting parameters; the values used for Ti, Al, and V are given in Table 2.8b. The resulting vapor pressures are plotted in Fig. 2.11b. In order to take into account the effects of the multicomponent system, the partial vapor pressure of element i in the Ti-Al-V system is defined as [86]:

$$P_i^s = X_i \gamma_i P_i^0 \tag{2.37}$$

Where P_i^s is the vapor pressure of the element in the system, X_i is the molar fraction, and γ_i is the activity coefficient. Many works assume that $\gamma_i = 1$, which is known as Raoult's law, but this is a simplification and is often inaccurate at high temperatures [79]. The activity coefficient can be calculated based on the excess Gibbs free energy of the system [86]:

$$\gamma_i = \exp\left\{\frac{\Delta\overline{G}_i^{ex}}{RT}\right\} \tag{2.38}$$

Where $\Delta\overline{G}_i^{ex}$ is the excess Gibbs energy for a given alloying element. Calculation of $\Delta\overline{G}_i^{ex}$ in a ternary alloy is derived from the mixing energies in the binary alloy systems, which are based on data compiled by Ansara et al. [89]. The implementation here is based on the derivations given by Ivanchenko et al [86]. For brevity, only the expansion for Al is given, the expansions for Ti and V are similar and can be found in Appendix A.1:

$$\begin{aligned}\Delta\overline{G}_{Al}^{ex} = {} & X_{Ti}(1-X_{Al})\sum_{n=0}^{2}\left[L_{Al,Ti}^{(n)}(X_{Al}-X_{Ti})^n\right] + X_{Al}X_{Ti}(X_V+2X_{Ti})\left(L_{Al,Ti}^{(1)} + 2L_{Al,Ti}^{(2)}(X_{Al}-X_{Ti})\right) \\ & + (1-X_{Al})X_V\sum_{n=0}^{2}\left[L_{Al,V}^{(n)}(X_{Al}-X_V)^n\right] + X_{Al}X_V(X_{Ti}+2X_V)L_{Al,V}^{(1)} \\ & - X_{Ti}X_V\sum_{n=0}^{1}\left[L_{Ti,V}^{(n)}(X_{Ti}-X_V)^n\right] + X_{Ti}X_V(X_V-X_{Ti})L_{Ti,V}^{(1)}\end{aligned} \tag{2.39}$$

Where $L_{i,j}^{(n)}$ is the mixing energy constants for a given binary alloy, which are given in Table 2.8c. Even in a relatively simple ternary alloy, this calculation is cumbersome; for a more complex alloy such as IN718, it would not be pragmatic. The Gibbs energies are linear in temperature but non-linear with respect to composition. The resulting values of activity coefficient can be seen in Fig. 2.11a. While Ti and V follow Raoult's law well, Al diverges significantly, ranging from an activity coefficient of 0.2 at the liquidus temperature to 2.5 at 4000 K. As Al is the most prone to evaporation, this means that proper implementation of γ_i is key to accurately capturing its behavior. The evaporated mass flux can be given by the following, which is sometimes referred to as Langmuir's equation [79]:

$$W_i = -\phi_a P_i^s \sqrt{\frac{m_i}{2\pi RT}} \tag{2.40}$$

Where W_i is the mass flux of an element, ϕ_a is the evaporation coefficient, and M_i is the molar mass [79]. ϕ_a accounts for the thermodynamic effects of the phase and pressure change during

mass evaporation; a more detailed explanation is given by Klassen [79]. Due to the high Knudsen number of EBM, it can assumed to be a constant value of 0.82. The latent heat of vaporization is defined using the following relationship [79]:

$$L_{vap,i} = L^0_{vap,i}\sqrt{1 - \left(\frac{T}{T_{crit}}\right)^2} \tag{2.41}$$

Where $L^0_{vap,i}$ is the latent heat of vaporization at absolute zero and T_{crit} is the critical temperature; the values used in this analysis are given in Table 2.8b. The critical temperature is the temperature above which the liquid phase cannot exist due to its high energy instantly causing vaporization [90]. The temperatures seen in EBM are significantly below the critical temperatures of Ti, Al, and V and the temperature dependency of $L_{vap,i}$ is small. From this, the heat flux due to evaporation is [79]:

$$\dot{q}_{evap,i} = W_i L_{vap,i} \tag{2.42}$$

The combined heat losses from evaporation and radiation are plotted in Fig. 2.11c. The contribution of each mechanism normalized by the total heat flux is given in Fig. 2.11d. Due to both its low vapor pressure and low percent composition, V evaporation is negligible for all temperatures considered in this analysis, never contributing more than 1% of the total heat flux. Radiation is the dominant mechanism below 2200 K, but at higher temperatures Al evaporation quickly becomes the main mechanism. Radiation is proportional to T^4, while evaporation is approximately proportional to $10^{-1/T}$, which is why there is a major shift between the two sources as temperature increases.

To better understand the effects of the two mechanisms, it is useful to consider the meltpool as a point mass, with an assumed area equivalent to a circle of 700 μm in diameter, which is approximately the dimensions measured by Jamshidinia et al [74]. Assuming an input power of 660 W, under radiative heat loss alone and using an emissivity of 0.4, the point mass would have a steady state temperature of approximately 16500 K. Including evaporative heat loss, however, reduces the steady state temperature to 3600 K. Klassen found a similar numerical result, where the maximum temperature with evaporative heat loss was approximately 3560-3660 K and the maximum temperature without evaporative heat loss was found to never reach a steady value [79]. Modeling of evaporative heat loss is key to preventing extremely high temperatures from being produced, which are nonphysical, numerical artifacts and do not represent the physics of the system.

While EBM in itself is a relatively new technique, electron beams have been widely used for many other engineering and scientific applications and there is much analytical, experimental, and numerical work in the literature; a detailed review is given by Klassen [79]. Several models have been proposed to model the heat flux from the electron beam and their advantages and disadvantages will be discussed. Unlike lasers, where absorption of the beam is highly dependent on material state and properties, the electron beam heat flux is generally independent of material state [72]. The generic form of the heat source equation is typically [3]:

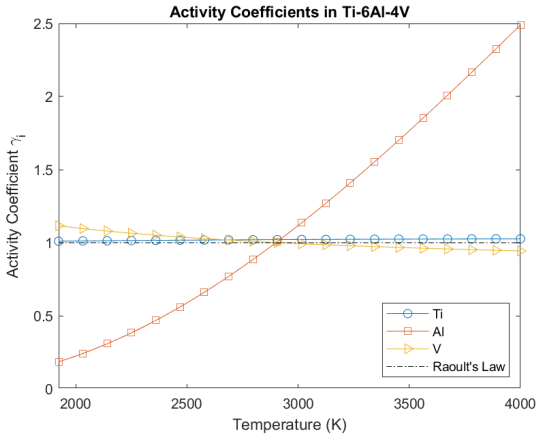

(a) Activity coefficient γ_i

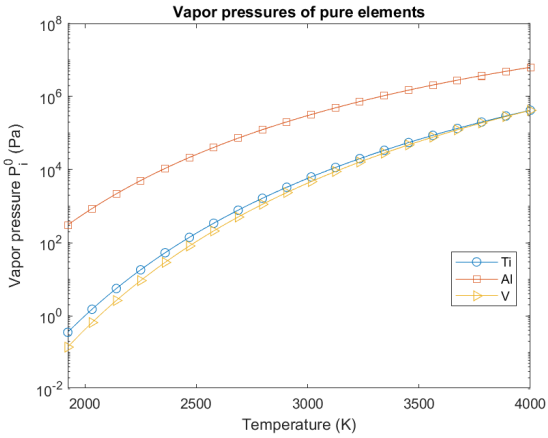

(b) Vapor pressures P_0^i of pure Ti, Al, and V

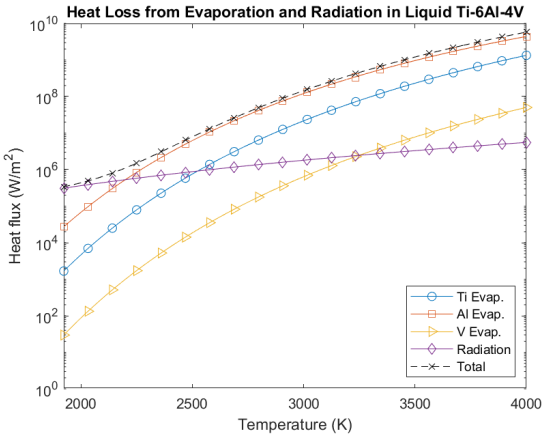

(c) Heat loss due to evaporation and radiation in the liquid phase

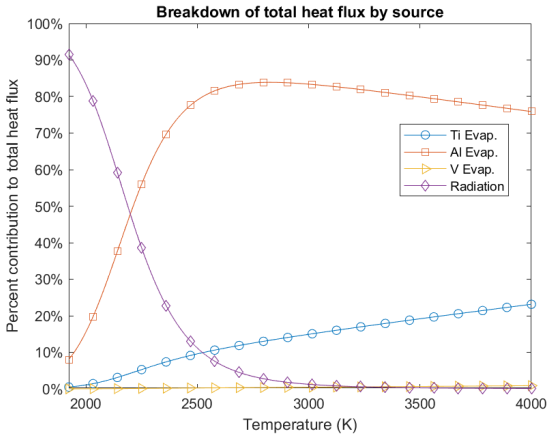

(d) Normalized heat loss from evaporation and radiation

Figure 2.11: Calculation of heat loss due to evaporation and radiation of liquid Ti-6Al-4V

$$\dot{q}_{EB} = I_B V_B I_{xy} I_z \tag{2.43}$$

Where I_{xy} is the in-plane distribution and I_z is the vertical distribution of energy. While I_B and V_B are process parameters, determining I_{xy} and I_z is more challenging and a variety of different models have been proposed for both. One key difference between laser and electron beam modeling is that electrons penetrate into the metal, while lasers are purely a surface heat source. A commonly used relationship for this penetration distance is [75]:

$$z_{s,square} = 2.1 \times 10^{-11} \frac{V_B^2}{\rho} \tag{2.44}$$

Where z_s is the penetration distance. The density is usually assumed to be constant in order to simplify the calculation. A more complex model is given by Klassen [79]:

$$z_{s,power} = \left(2.76 \times 10^{-2} \frac{\text{mol}}{\text{m}^2}\right) \frac{m_a N_a \left(\frac{V_B}{1\text{kV}}\right)^{5/3} \left(1 + 9.78 \times 10^{-4} \frac{V_B}{1\text{kV}}\right)^{5/3}}{Z^{8/9} \rho \left(1 + 1.957 \times 10^{-3} \frac{V_B}{1\text{kV}}\right)^{4/3}} \tag{2.45}$$

Where N_a is Avogadro's number and Z is atomic number. A comparison between the two models is shown in Table 2.3, based on material properties given in Table 2.8a. There is little difference between the square model and power law model; this is likely due to the relatively low beam voltage [79]. Several models also exist for the vertical distribution, which is a complex topic. The simplest is given by Shen and Chou, which is based on electron beam welding models [91]:

Table 2.3: Comparison between penetration depth models at $V_B = 60 \times 10^3$V

$z_s(\mu\text{m})$	Ti-6Al-4V
Square [75]	19.3
Power law [79]	18.8

$$I_{z,Shen} = \frac{2}{z_s}\left(1 - \frac{z}{z_s}\right) \tag{2.46}$$

While this equation is easy to implement, it lacks physical significance. A commonly used distribution is given by Zäh and Lutzmann [92]:

$$I_{z,Zah} = \frac{1}{z_s}\left(-3\left(\frac{z}{z_s}\right)^2 + 2\frac{z}{z_s} + 1\right) \tag{2.47}$$

It is based on experimental work, but specifics about its derivation are not given. A much more in-depth treatment of this problem is given by Klassen, which is based on analytical fundamentals with corrections to match experimental data [79]. The fraction of electron energy absorbed at a given z level is given by:

$$\varepsilon_A = (1 - \eta_{B,\infty}\epsilon_{B,\infty})\left(1 - \frac{\eta_T \epsilon_T}{C}\right) \tag{2.48}$$

Where $\eta_{B,\infty}$ represents the ratio of electrons backscattered at the surface, $\epsilon_{B,\infty}$ is the energy of backscattered electrons, η_T is the ratio of electrons that penetrate to a given distance, ϵ_T is the energy of electrons at a given penetration depth, and C is a correction term [79]. The full listing of these equations is not relevant to the analysis and can be found in Appendix A.2. From Eq. (2.48), the vertical distribution can be calculated by simply taking the derivative [79]:

$$I_{z,Klassen} = \frac{1}{z_s}\left(\frac{\partial \varepsilon_A}{\partial z}\right) \tag{2.49}$$

A comparison between these three penetration models is given in Fig. 2.12. Klassen's model is non-linear with respect to Z, so both Ti-6Al-4V and IN718 have been plotted. The simple polynomial proposed by Zäh and Lutzmann is broadly similar to the more complex implementation given by Klassen. Another difference is that Klassen's model includes in itself a backscattering calculation, though some authors have scaled Zäh and Lutzmann's model to take into account absorption efficiency [75]. The predicted backscattering for Ti-6Al-4V is 14%. Unless the meshing size is a small fraction of z_s, i.e. on the order of $1\mu m$, the difference is likely negligible. The radial distribution I_{xy} is typically given by a Gaussian equation [93]:

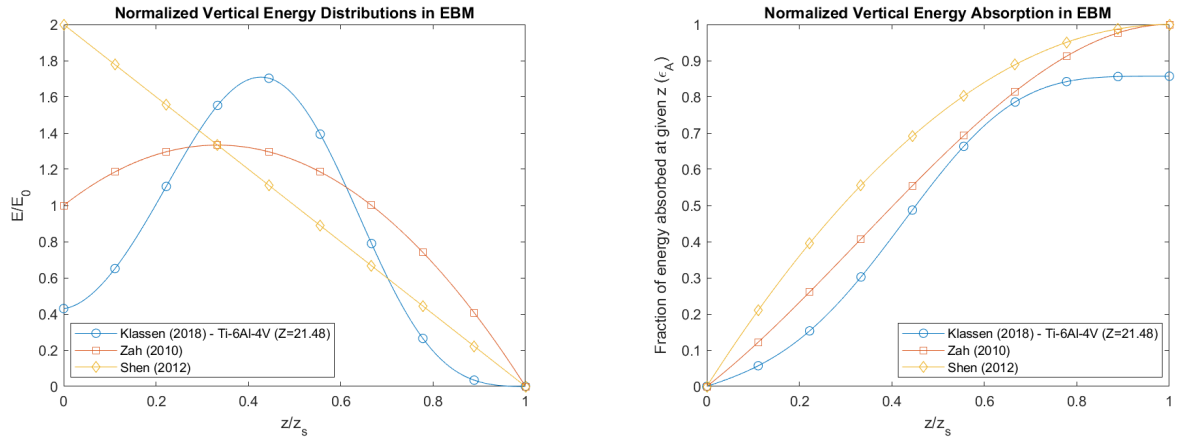

(a) Normalized energy absorption

(b) Fraction of energy absorbed at given depth (ε_A)

Figure 2.12: Comparison between different vertical energy distributions models [79, 91, 92]

$$I_{xy} = \frac{1}{2\pi\sigma_b^2} \exp\left\{-\frac{r^2}{2\sigma_b^2}\right\} \tag{2.50}$$

Where r is the planar distance from a given point to the center of the beam and σ_b is the standard deviation of beam width. The full width at half maximum (FWHM) diameter d_B can then be calculated as [93]:

$$d_b = 2\sigma_b\sqrt{2\ln 2} \tag{2.51}$$

The FWHM diameter corresponds to the radial distance at which the beam power has reached half of its maximum value. Determination of d_b is complicated by the fact that it is dependent on process parameters and machine architecture, as well as there not being a consistent standard of reporting FWHM or another measurement of diameter. In this work, a value of $d_b = 350\mu m$ will be assumed, which is in line with many values reported in the literature [2, 56]. This corresponds to a standard deviation of $\sigma_b = 149\mu m$. The FHWM diameter from several models in the literature and is given in Table 2.4. If the authors' model did not follow the format given in Eq. (2.50), then the equivalent FWHM diameter was calculated to match their model. A contour map of the

resulting volumetric heat flux is given in Fig. 2.13. The conditions for this figure are a 60 kV beam, Ti-6Al-4V substrate, 350 μm FWHM diameter, and a 1W beam power, i.e. unit power input.

Table 2.4: Selected literature values for FWHM diameter

Reference	d_b (μm)
Zäh and Lutzmann [92]	220
Cheng et al. [43]	650
Raghavan et al. [94]	200-800
Degenhardt [93]	290-330
Shen and Chou [91]	1180
Knapp et al. [75]	670
Klassen [79]	240
Lee et al. [95]	110

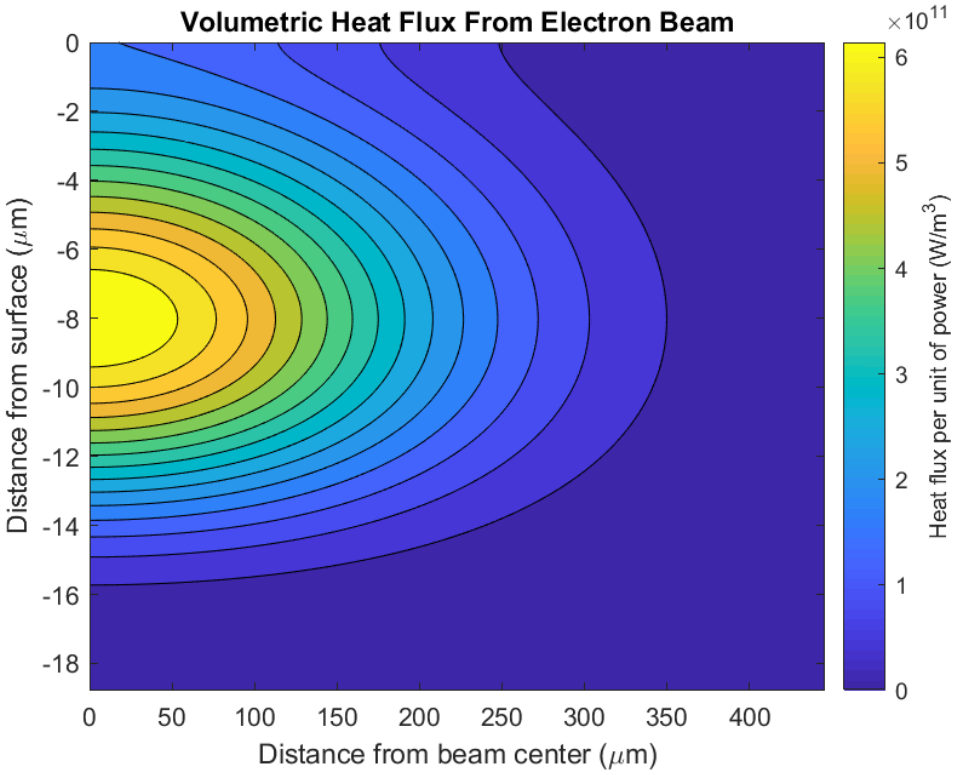

Figure 2.13: Unit volumetric heat flux per unit input power from 60 kV beam in Ti-6Al-4V.

2.3.2 Ti-6Al-4V Material Properties

Determination of the relevant thermal properties for usage in EBM analysis is challenging. There are four separate regimes that must be considered: sintered powder, bulk solid, liquid, and mushy or partially melted. While the differences in mechanical properties and microstructure between EBM and conventionally manufactured Ti-6Al-4V have been widely studied and reported in the literature, there have been very few studies on the differences in thermal behavior. Furthermore, modeling of the thermal properties of the powder bed is complicated by its stochastic nature. Setting aside the issues unique to additively manufactured parts, there are many issues inherent to measurement of high temperature thermal properties.

Three figures from the literature that illustrate these issues are given in Fig. 2.14. It is worth nothing that all three of these examples are using conventionally manufactured Ti-6Al-4V and standard testing methods. Fig. 2.14a, from Homporová et al, demonstrates large variations in measured enthalpy by differential scanning calorimetry (DSC) solely due to changed cooling rates[96]. As the material is reheated back to 1020 C, differing amounts of martensitic α' – $21 \pm 1\%$, $22 \pm 2\%$, and $30 \pm 5\%$, for water quenching, air cooling, and furnace cooling, respectively – lead to major differences in the energy profile. Fig.2.14b, from Kaschnitz et al, depicts a change in melting temperature depending on heating rate [97]. As heating rate increases, the alloy tends to melt at a single temperature, similar to a pure metal, rather than over a range between a solidus and liqiudus temperature; they attribute this shift to solute segregation due to non-equilibrium

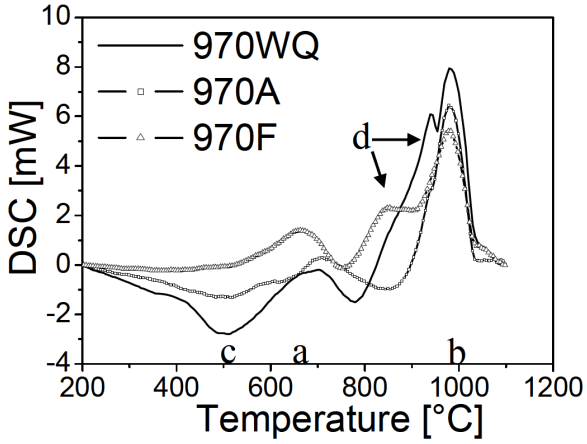

(a) Enthalpy for 3 different cooling rates after heating at 970 C: water quenched (WQ), air cooled (A), and furnace cooled (F). Endothermic peaks marked at a and b, with an exothermic peak at c [96]

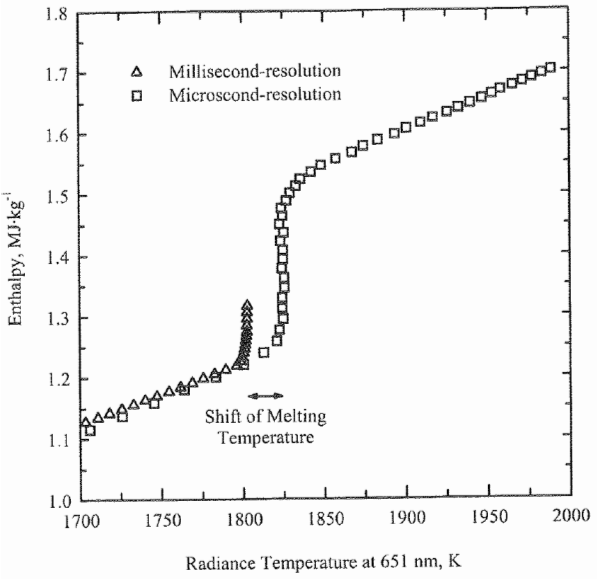

(b) Enthalpy during melting as measured by DSC at $10^7 K/s$ and $10^3 K/s$ [97]

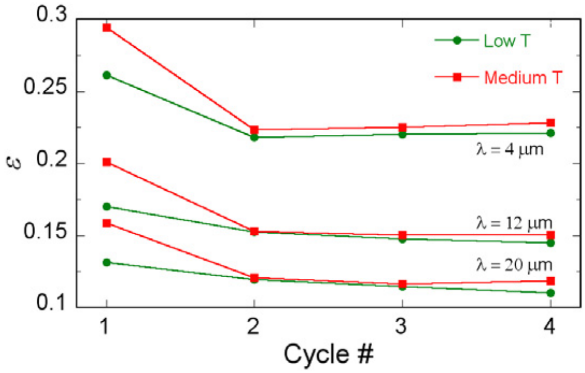

(c) Variations in emissivity after multiple heating cycles under an inert atmosphere due to annealing of surface stresses [98]

Figure 2.14: Challenge of controlling effects of material history and measurement method on thermal properties of Ti-6Al-4V

effects. Fig. 2.14c, from González-Fernández et al, demonstrates changes in emissivity of Ti-6Al-4V after multiple heating cycles under an inert atmosphere [98]. No variations in oxidation or surface roughness were observed and XRD and SEM analysis also did not detect any changes; the cause was annealing of residual surface stresses induced during the sample manufacturing process. All three of these examples stem from issues commonly seen in EBM – martensitic microstructure, high heating and cooling rates, and residual thermal stresses; this is by no means an exhaustive

list, but simply highlights the challenges in determining thermal properties to be used in analysis.

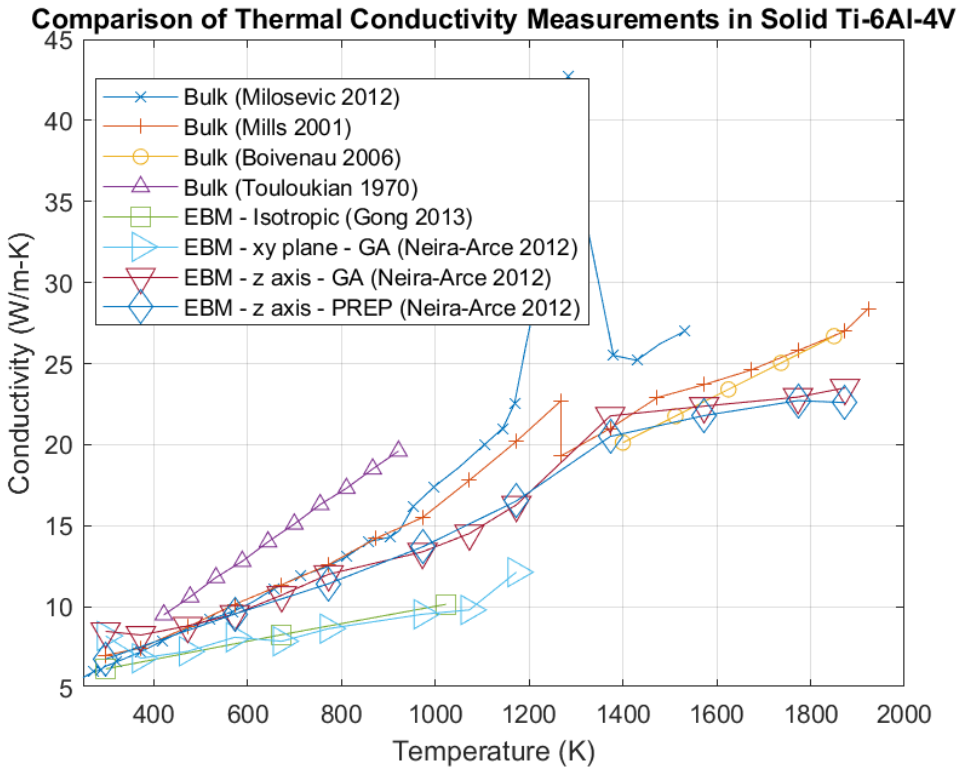

Figure 2.15: Comparison of measured thermal conductivity in bulk Ti-6Al-4V [81, 99–103]

Measured values of thermal conductivity for bulk Ti-6Al-4V from the literature are given in Fig. 2.15 [81, 99–103]. While the properties generally agree below 1100 K and above 1400 K, measurements in this region are widely scattered due to the effect of the $\alpha - \beta$ phase change. Milošević and Aleksić report an increase of almost $20 W/m - K$, whereas Neira-Arce did not measure any change at all and Mills notes only a slight change. Gong et al reported that they found conductivity to be isotropic, but their measured values are found to be very similar to the x-y plane measurements from Neira-Arce; in both cases, the in plane conductivity is roughly 75%-80% of the build direction values. Neira-Arce suggested that this variation is due to the columnar grains commonly seen in EBM, which lead to significant anisotropy in mechanical properties [50, 99].

Determination of the effective thermal conductivity of sintered powder in a vacuum is difficult and highly dependent on process variables. Many experiments and models in the literature are for conductivity of loose powder in an atmosphere, which is the condition most often seen in SLM/SLS and traditional heat transfer applications. Analytical and experimental work has shown that heat transfer in those scenarios is dominated by the atmosphere composition and pressure, with powder composition and density being of secondary importance [104, 105]. In contrast, the dominant mechanism in EBM conditions is heat transfer through the sintered necks between particles, with inter-particle radiation as a secondary effect [87]. Experimental data from Gong et al. and Smith

et al. is given in Fig. 2.16 [103, 106]. The data from Gong et al and Smith et al is in relatively good agreement for the build direction, which has an average conductivity of $5-10\%$ of the bulk material conductivity. Gong et al. also report much higher conductivity in the x-y plane, which agrees somewhat with numerical analysis of XCT data by Leung et al. though they measured a much smaller difference than Gong et al. [11]. However, given the discrepancy of the solid conductivity data reported by Gong et al., this issue may be due to the difficulties of measuring sintered powder properties. Neira-Arce attempted to measure sintered powder conductivity under vacuum, but was unable to get good measurements without a 1 atm Ar atmosphere, which means that the data is not applicable to EBM [99]. Two parameters are defined to aid in the analysis of sintered powder, effective conductivity k_{eff} and porosity ϕ:

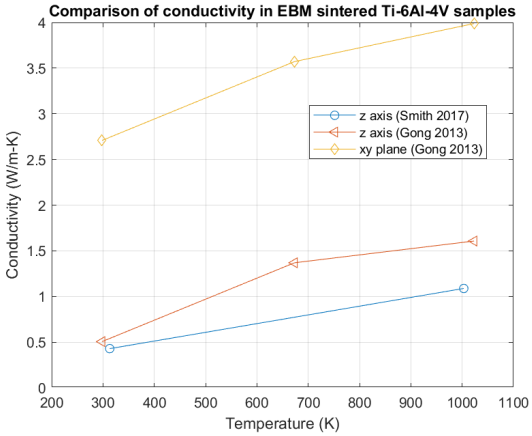

(a) Experimental measurements of sintered Ti-6Al-4V powder conductivity by Smith et al and Gong et al

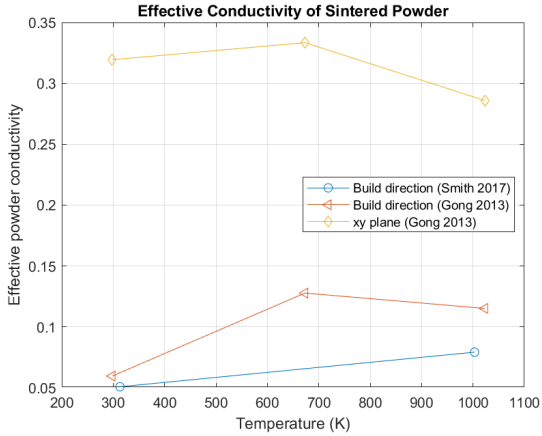

(b) Measured sintered powder conductivities normalized by bulk data from Neira-Arce

Figure 2.16: Comparison of measured thermal conductivity in sintered Ti-6Al-4V powder [99, 103, 106]

$$k_{eff} = \frac{k_{powder}}{k_{solid}} \tag{2.52}$$

$$\phi = \frac{\rho_{powder}}{\rho_{solid}} \tag{2.53}$$

These are the ratios of powder conductivity and density to bulk solid; a value of 1 would indicate that the powder is identical to the solid and a value of 0 would effectively be an empty void. Some papers in the literature use the opposite definition of porosity, i.e. 100% corresponds to a void and 0% corresponds to bulk material; for clarity, all expressions in this work have been rephrased to use a consistent definition. In Fig. 2.17a, the effects of modifications to the preheat sintering energy on the measured density are given, based on data from Leung et al. and Smith et al [11, 106]. It is worth noting that the two groups modified preheating energy in slightly different ways, so the data is not a direct comparison except at the default settings, but the comparison still illustrates the point. Increasing the preheating energy by over three times only increased porosity

from 52% to 56%. In comparison, the measured and numerically calculated conductivity is given in Fig. 2.17b. Again, this is not a direct comparison, as Smith et al. experimentally measured the conductivity and Leung et al. applied numerical analysis to XCT data [11, 106]. Tripling the preheating energy resulted in a significant increase in conductivity, yet density was unchanged. The key parameter is the influence of sintered neck size. The Gusarov-Tolochko model accounts for the heat transfer through sintered neck conduction and inter-particle radiation [87, 104]:

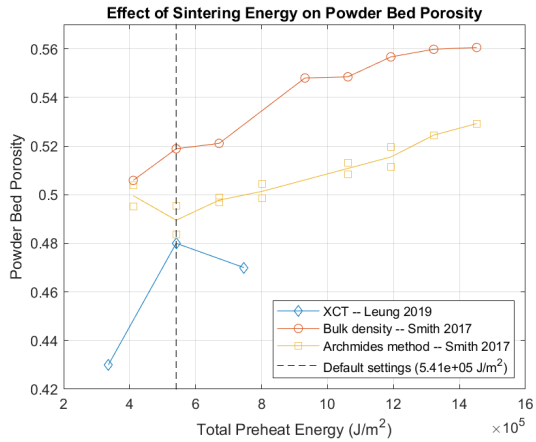

(a) Effects of sintering energy on measured density

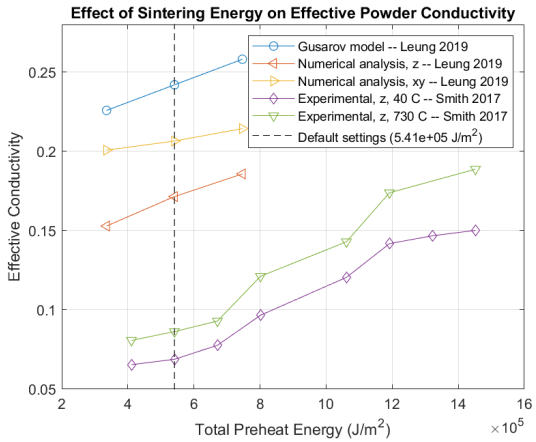

(b) Effects of sintering energy on measured and numerical conductivity

Figure 2.17: Effect of different sintering parameters on powder bed porosity and conductivity [11, 106]

$$k_p = k_{cond} + k_{rad} \tag{2.54}$$

$$k_{cond} = k_s \Lambda x \tag{2.55}$$

$$k_{rad} = \frac{16}{3} L_g \sigma_{SB} T^3 \tag{2.56}$$

In the conductive term, Λ is a geometrical factor depending on the packing density of the powder and x is the ratio of sintered neck radius to particle radius. Gusarov et al. derived values of Λ for four idealized packing structures, given in Table 2.5. In order to apply this model to porosities other than these four, Gusarov et al. suggest interpolation, though they note that this is not rigorously true as the same porosity can have multiple different packing structures [104]. In the radiative term, L_G is the mean free path between particles, which is assumed to be the same as the particle diameter of 60 μm [87]. In the EBM processing conditions, the radiative term is significantly less than the conductive term; at 1000 K, for example, the predicted radiative conductivity is 0.02 W/(m K). Therefore, radiative transfer will be ignored and conductive transfer will be assumed to be the only mechanism. Determination of x is the key difficulty in applying the Gusarov-Tolochko model. Gusarov et al. suggest a possible range of 0.1-0.3 and Gong et al. estimated neck sizes seen in SEM to be on the order of 1 - 10 μm, which assuming an average particle diameter of 60 μm results in a range of 0.02-0.20 [103, 104]. In Fig. 2.18a, the

effects of preheating energy on neck radius are given. The measurements from Smith et al. is calculated by applying the Gusarov-Tolochko model to measured conductivity and density, while the measurements from Leung et al. are based on analysis of XCT data [11, 106]. The two sets of data are not in good agreement, as the predicted neck size ratio is different by a factor of over 3x. It is unclear if this is due to differences in XCT analysis vs back-calculation or some other factor. However, given the ranges suggested by Gusarov et al. and neck size ratios measured by Gong et al, this indicates that the data from Smith et al. is likely more accurate. In Fig. 2.18b, comparisons of the various experimental, numerical, and analytical predictions. In the data from Smith et al., the default process settings are marked with a star; the effective conductivity is approximately 7%. In this analysis, this value will assumed to be the effective conductivity of powder going forward. Accurate determination of x and k_{eff} is still an open question, as there is significant disagreement with all available experimental data. Furthermore, x is heavily dependent on processing conditions. Another challenge is that in areas that are close to fully melted regions, but not fully melted themselves, x will likely increase because the temperature will rise to the sintering range of approximately $0.7T_{sol}$ [87]. Without a better understanding of the sintering kinetics present in this system, it is not feasible to include this level of prediction in a model.

Table 2.5: Effective thermal conductivity parameters for Gusarov-Tolochko model [87, 104]

Packing structure	Porosity	Λ
Diamond	0.340	0.433
Simple cubic (SC)	0.524	1
Body-centered cubic (BCC)	0.680	1.732
Face-centered cubic (FCC)	0.740	2.828

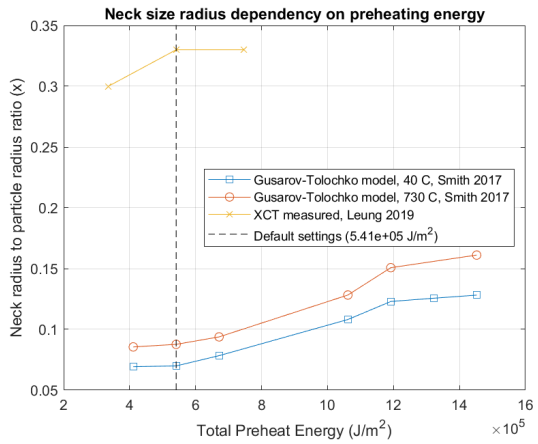

(a) Effects of sintering energy on calculated and measured neck size ratio x

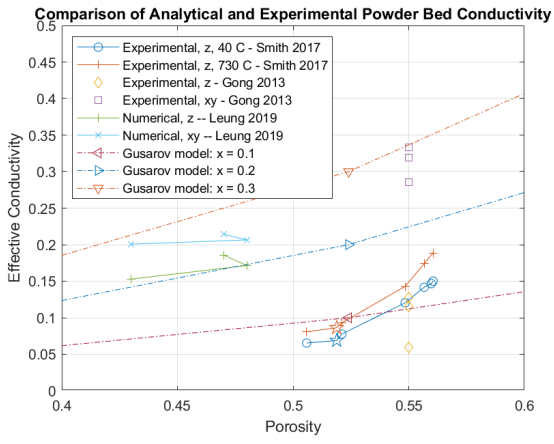

(b) Comparison of Gusarov-Tolochko model and experimental data

Figure 2.18: Neck size ratio effects on analytical and experimental conductivity [11, 103, 106]

Measured values of specific heat from the literature are given in Fig. 2.19 [81, 97, 99–101, 107, 108]. Similarly to what was seen in the thermal conductivity measurements, there is relatively good

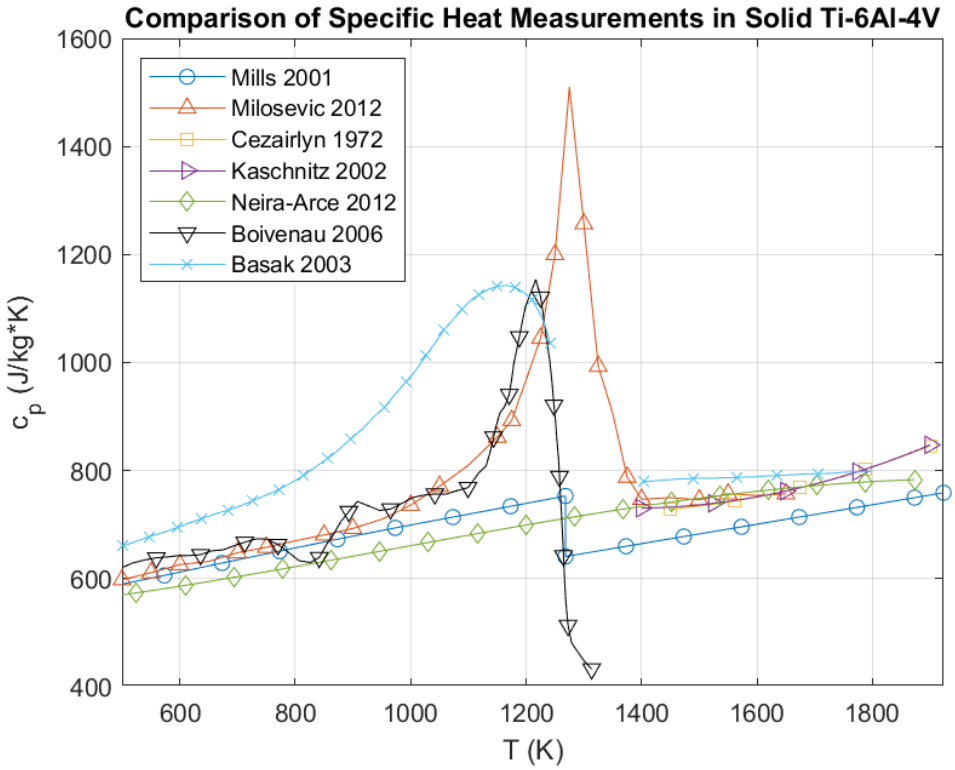

Figure 2.19: Comparison of measured specific heat in bulk Ti-6Al-4V [81, 97, 99–101, 107, 108]

agreement below 1000 K and above 1400 K and significant disparities near the $\alpha - \beta$ transition. Basak et al., Boivineau et al., and Milošević and Aleksić all report major peaks in specific heat, though the magnitude and location of the deviation is different in all three cases. The discrepancy is likely due to differences in heating rate. Specific heat taken at low heating rates near the $\alpha - \beta$ transition are heavily effected by the phase change effects. In Fig. 2.20, measured specific heats from bulk samples using DSC and laser flash analysis (LFA) by Neira-Arce are plotted for GA and PREP powder [99]. DSC is a relatively slow measurement technique and the effects of microstructural change were so great that a negative specific heat was measured, which is obviously non-physical. LFA is a relatively fast measurement technique and no effects of microstructural change were seen and the data is in good agreement with the literature, as seen in Fig. 2.19. Similar effects in bulk material have been reported by Kaschnitz et al. and Homporová et al [96, 97]. conventional bulk materials.

Specific heat of a powder is generally assumed to to be the same as of the bulk material. Measurements from Neira-Arce of the specific heat of new and recycled GA and PREP powder are given in Fig. 2.21a [99]. He was unable to use the LFA technique on powder samples, so all measurements for powder are taken using DSC, which means that the measurement rate is slow enough for microstructural effects to take place. All four measurements are in relatively good agreement up until the $\alpha - \beta$ transition, after which they diverge shaprly. The divergence is further illustrated by the difference in enthalpy between new and old samples, which is plotted in

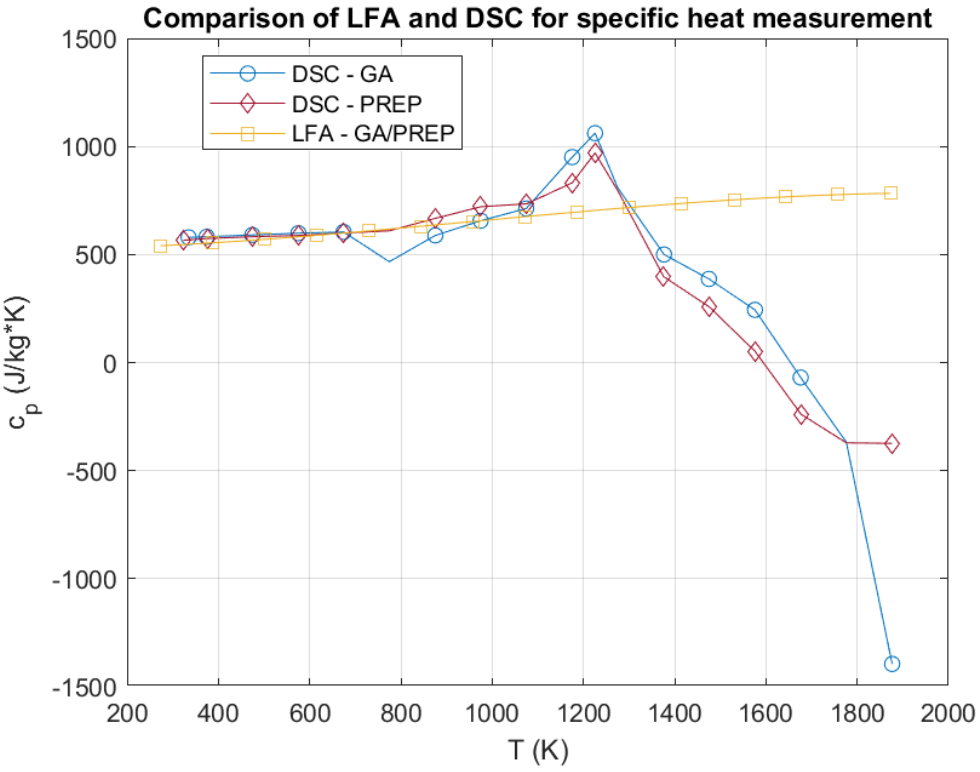

Figure 2.20: Comparison in measured specific heat between differential scanning calorimetry (DSC) and laser flash analysis (LFA) [99]

Fig. 2.21b and calculated following Eq. (2.11). The recycled powder samples have significantly lower enthalpy until the $\alpha - \beta$ transition and then the enthalpy suddenly peaks afterwards. Neira-Arce suggests that this is due to the combined effects of oxide contamination, which is commonly seen in recycled powders, and the same microstructural issues present in the bulk material DSC measurements [99].

Measured values of emissivity from the literature are given in Fig. 2.22 [38, 99, 100, 107, 109–111]. The data from Neira-Arce and Dinwiddie et al. is for EBM built components and all other references are using conventionally manufactured samples. The measurements seem to roughly fall into two groups, with one group being Neira-Arce, Milošević and Aleksić, and Cezairliyan et al., and the other Jones et al., Dinwiddie et al., and Shur and Peletskii, with Touloukian and Dewitt as an outlier between the two. All tests were conducted in vacuum, so oxidation is not an issue. One potential issue is surface roughness, as that has been reported to severely affect measured emissivity, but not all authors report the sample conditions so this cannot be determined [111].

Experimental measurements of powder bed emissivity from Neira-Arce and Dinwiddie et al. are given in Fig. 2.23a [38, 99]. A significant jump in emissivity was noted at approximately 1050 K by Neira-Arce, but he was unsure of the cause [99]. However, since this is at the very end of the temperature range for EBM, it does not directly affect the parameters. In order to predict the emissivity of a randomly packed powder bed, the Sih-Barlow model is very widely used [112]:

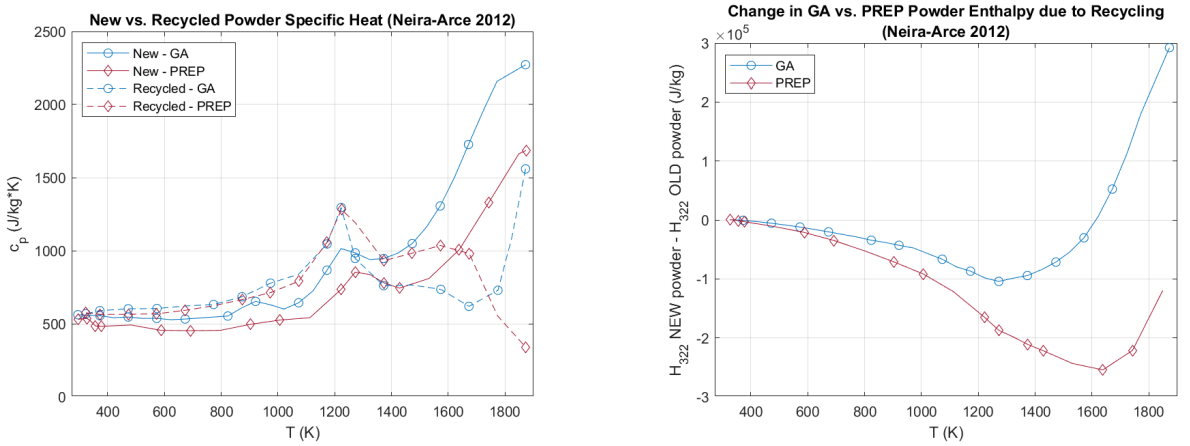

(a) Effects of recycling on measured powder specific heat

(b) Change in enthalpy between new and recycled powder

Figure 2.21: Effects of powder recycling on specific heat and enthalpy of powder [99]

$$\epsilon_p = A_H \epsilon_H + (1 - A_H)\epsilon_s \tag{2.57}$$

$$A_h = \frac{0.908(1-\phi)^2}{1.908(1-\phi)^2 - 2(1-\phi) + 1} \tag{2.58}$$

$$\epsilon_H = \frac{\epsilon_s \left(2 + 3.082 \left(\frac{\phi}{1-\phi}\right)^2\right)}{\epsilon_s \left(1 + 3.082 \left(\frac{\phi}{1-\phi}\right)^2\right) + 1} \tag{2.59}$$

Where ϵ_p is the powder bed emissivity and ϵ_s is the bulk emissivity. The original equations by Sih and Barlow were written with the opposite porosity convention, i.e. $\phi = 0$ corresponds to a fully dense material, and have been rewritten to follow the porosity convention of this work. A modified version is given by Galati et al. for a BCC packing of powders ($\phi = 0.68$) [113]:

$$\epsilon_p = \epsilon_s \left(0.47 + \frac{0.53}{0.25 - 0.75\epsilon_s}\right) \tag{2.60}$$

Comparisons between experimental data for Ti-6Al-4V and IN718 and the analytical models at various porosities is given in Fig. 2.23b. None of the experimental data corresponds particularly well with any of the models. The data from Neira-Arce is highly noisy and irregular. Both measurements from Dinwiddie et al. are in roughly the same ratio of bulk to powder emissivity, but in Ti-6Al-4V the emissivities changed together, while in IN718 the powder emissivity was essentially constant despite changes in the bulk emissivity. The powder bed porosity was not given by Dinwiddie et al., but it can be seen that none of the models at any porosity are close to predicting the measured values. Clearly, new models need to be developed to better understand emissivity in a powder bed. One potential issue is the formation of an oxide layer. Ideally, the

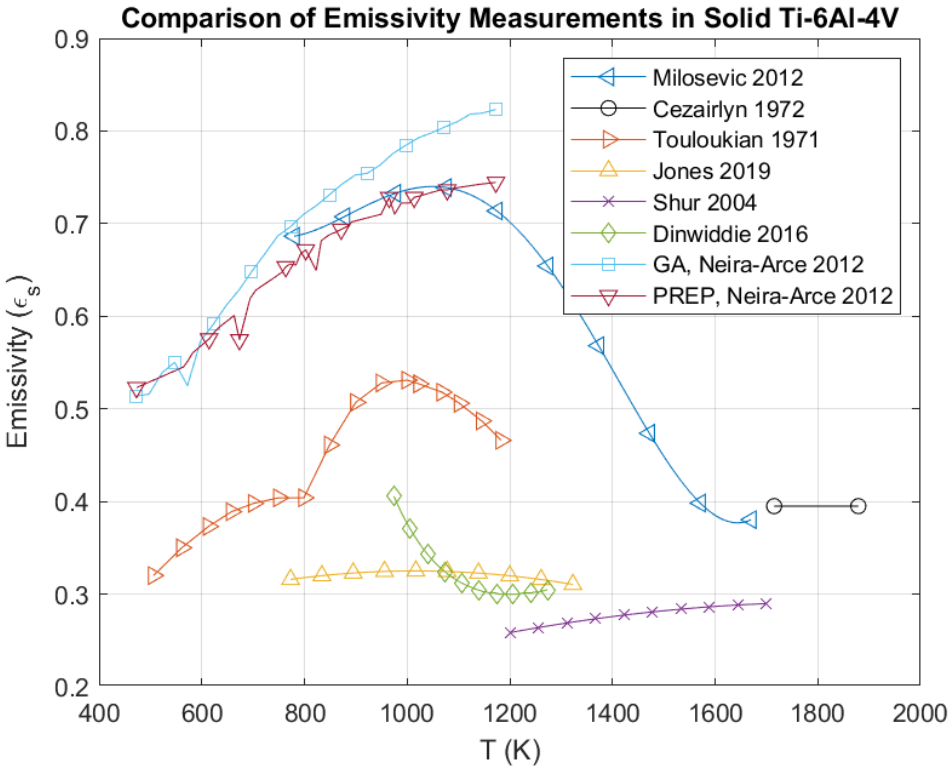

Figure 2.22: Comparison of measured emissivity in solid Ti-6Al-4V [38, 99, 100, 107, 109–111]

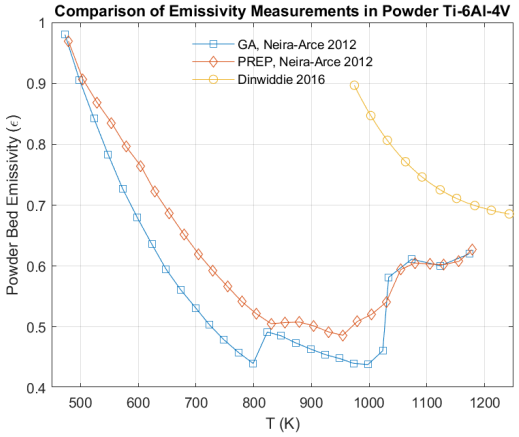

(a) Experimentally measured powder bed emissivities

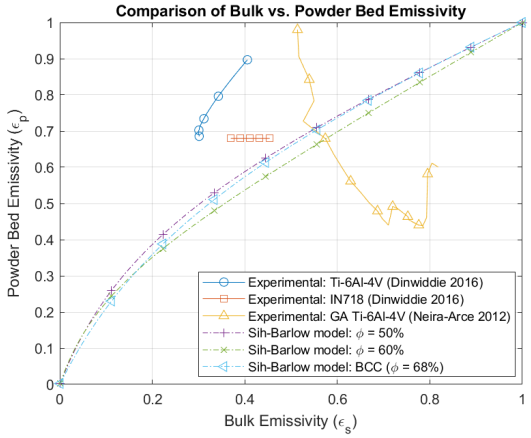

(b) Comparison between experimental and analytical predictions for powder bed emissivity

Figure 2.23: Experimental and analytical determinations of powder bed emissivity [38, 99, 112, 113]

emissivity would be measured directly after printing while still in the vacuum chamber, so that the sample is never exposed to any atmosphere, but this presents numerous experimental difficulties and to date has not been done. Rodriguez attempted this experimental approach but was only able to measure values up to 500 K, far below the region of interest [24].

Measurement of the thermal properties of liquid Ti-6Al-4V is extremely challenging for a variety of reasons. The high melting point and extreme reactivity make containing the liquid metal very difficult. Furthermore, measurement of properties like conductivity is complicated by the necessity to separate the effects of convection and conduction on the measured heat transfer. Furthermore, properties like surface tension and viscosity require either levitation of the sample using magnetic techniques or performing the experiment in a microgravity environment. Further discussions of experimental methods for liquid metals are given in Refs. [82, 83, 114]. In this analysis, undercooling will be ignored. Experimental measurement would be extremely challenging if not impossible and neglecting its effects simplifies the analysis at little cost in accuracy. The recommended approach for calculation of properties in the mushy region by Mills is to linearly interpolate the reported values at the liquidus and solidus temperatures and will be adopted in this work [81]. Mills also notes that ideally these properties would be given as a function of cooling rate, which corroborates the data from Kaschnitz et al. plotted in Fig. 2.14b, but this is often not possible due to a lack of experimental data [81, 97].

Table 2.6: Specific heat and thermal conductivity of liquid Ti-6Al-4V

Reference	c_p (J/kg-K)	k (W/m-K)
Mills [81]	831	34.6
Boivineau et al. [101]	1126	$28.53 + 1.83 \times 10^{-2}(T - T_l)$
Kaschnitz et al. [97]	931	–
Zhou and Wei [115]	713	–

Measured values for specific heat and conductivity in the liquid phase are given in Table 2.6. All authors found specific heat to be independent of temperature. There is significant scatter between the values. Kaschnitz et al. also comment on this scatter, but are unable to suggest any possible cause for this discrepancy [97]. The thermal conductivity measurements of Mills and Boivineau et al. also have wide variation. However, Mills notes that the theoretical conductivity should be approximately 27.5 (W/m-K) and that the experimental value of 34.6 (W/m-K) is questionable, which is much more in line with the values given by Boivineau et al. [81]. The emissivity of liquid Ti-6Al-4V was measured by Boivineau et al. to be [101]:

$$\epsilon = 0.405 - 1.05 \times 10^{-5}(T - T_{liq}) \tag{2.61}$$

This is in agreement with the values of 0.39 given by Cezairliyan et al. for solid Ti-6Al-4V at 1900 K and 0.33 by Ishikawa et al. for pure Ti at 1943 K [107, 117]. Measured values for the temperature dependence of surface tension are given in Table 2.7. Egry et al. were unable to account for the discrepancy between their results in normal gravity and in microgravity. One major challenge in modeling of steel welds is that the temperature dependency of surface tension is very heavily dependent on chemical composition, in particular oxygen concentration, which means that

Table 2.7: Temperature dependence of surface tension in liquid Ti-6Al-4V

Reference	$\frac{\partial \gamma_s}{\partial T}$ (N/m-K)
Zhou and Wei [115]	-3.13×10^{-4}
Wunderlich [116]	-4.71×10^{-4}
Egry et al., 1 g [83]	-3.6×10^{-4}
Egry et al., Microgravity [83]	-4.1×10^{-4}

minor changes in oxygen levels result in major differences in weld behavior due to reversing the sign of $\partial \gamma_s / \partial T$ [84]. However, Brillo et al. found that for pure Ti, the sign will always be negative, even at very high concentrations of oxygen, which suggests that the sensitivity of Ti-6Al-4V to oxygen impurities is likely less than many ferrous alloys [118]. On the other hand, Schneider et al. measured surface tension in liquid Ti-3.5Al-4.4V and found that the temperature dependency was -9×10^{-4} (N/m-K), over double the magnitude reported for Ti-6Al-4V [119]. Temperature dependent viscosity is modelled using the Arrhenius equation [114]:

$$\eta = \eta_0 \exp\left\{\frac{E_0}{RT}\right\} \tag{2.62}$$

Where η_0 is the reference viscosity and E_0 is the activation energy for viscous flow. While some analytical relationships have been suggested for these values, they are typically based on experimental data [114]. Experimental measurement is difficult due to the high temperatures involved and the inability to directly measure viscosity; more detailed discussions on commonly used methods are given in Refs. [82, 114]. Experimental data from Raush and Wunderlich is plotted in Fig. 2.24, along with numerical predictions from Mills [81, 82, 116]. In addition, experimental data for pure Ti from Ishikawa et al. and Paradis et al. is given for reference [120, 121]. Raush reports a much lower margin of error than Wunderlich, so his results will be used in the analysis. The large deviation between Ishikawa et al. and Paradis et al. for pure Ti is unexpected, especially given that both measurements were made using similar experimental methods.

For the purposes of evaporation and electron penetration analysis, Ti-6Al-4V is assumed to be a purely ternary alloy, with no impurities and at nominal composition. The idealized chemical composition of Ti-6Al-4V is given in Table 2.8a. Molar fraction of a component i in an alloy of n elements is given by [79]:

$$X_i = \frac{\frac{w_i}{m_i}}{\sum_{j=1}^{n} \frac{w_j}{m_j}} \tag{2.63}$$

Calculation of Z in an alloy of n elements is given by the following [79]:

$$Z = \frac{\sum_{i=1}^{n} \left[w_i \frac{Z_i^2}{m_i} \right]}{\sum_{i=1}^{n} \left[w_i \frac{Z_i}{m_i} \right]} \tag{2.64}$$

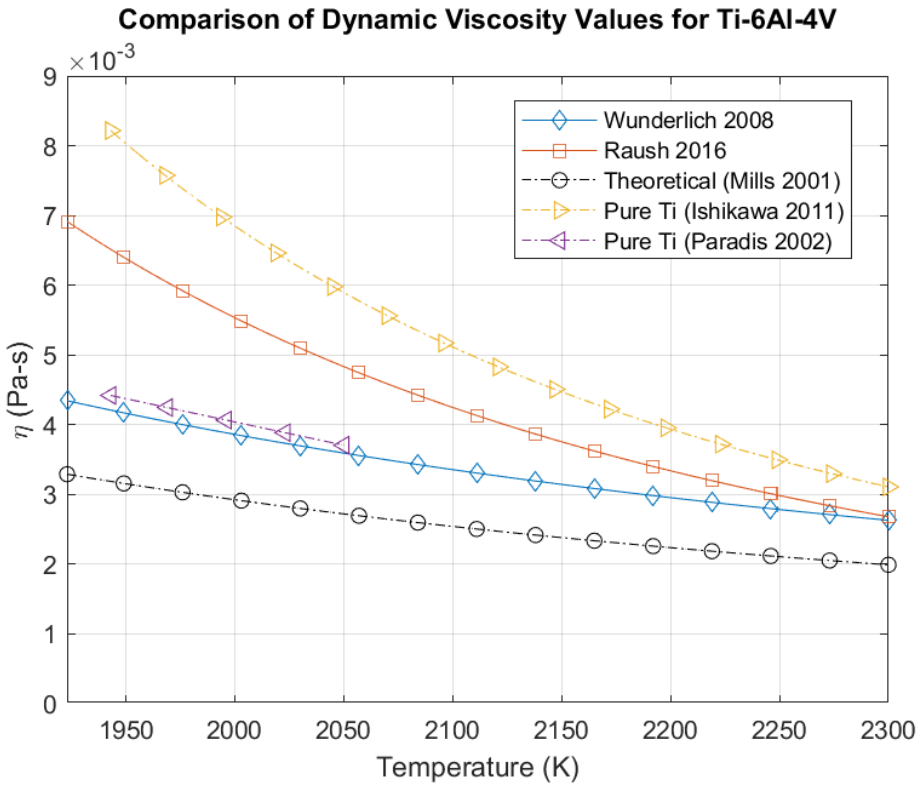

Figure 2.24: Comparison of experimental and numerical data for Ti-6Al-4V viscosity [81, 82, 116, 120, 121]

Material properties used to calculate the vapor pressure and temperature dependency of the latent heat of vaporization are given in Table 2.8b. The mixing energies, which are used to calculate the adjusted vapor pressures for the Ti-6Al-4V system, are given in Table 2.8c.

Table 2.8: Compositional and evaporative properties of Ti-6Al-4V

(a) Idealized chemical composition of Ti-6Al-4V [122]

	Weight comp. (w_i)	Molar comp. (X_i)	Atomic number (Z_i)	Molar mass (m_i, kg)
Ti	0.9	0.862	22	47.88×10^{-3}
Al	0.06	0.102	13	26.98×10^{-3}
V	0.04	0.036	23	50.94×10^{-3}
Ti-6Al-4V	–	–	21.48	46.7×10^{-3}

(b) Critical temperature, latent heat of vaporization, and Clausius-Clapeyron constants [79, 86, 90, 123]

	T_{crit} (K)	L^0_{vap} (J/kg)	A_i	B_i	C_i	F_i
Ti	11790	9.76×10^6	22946	10.581	-0.373	133.3
Al	6700	11.6×10^6	16379	9.979	-0.336	133.3
V	12500	9.23×10^6	24378	10.762	-0.325	133.3

(c) Mixing energies for Ti-Al, Ti-V, and Al-V systems [89]

Binary system (j, k)	$L^{(0)}_{j,k}$ (J/mol)	$L^{(1)}_{j,k}$ (J/mol)	$L^{(2)}_{j,k}$ (J/mol)
Ti-Al	$-108250 + 38T$	$-6000 + 5T$	15000
Ti-V	1400	4100	–
Al-V	$-50725 + 9T$	$-15000 + 8T$	–

2.4 EBM Process Simulation

Numerical process simulation offers the ability to gain a deeper understanding of the physics and analyze the phenomena that occurs in EBM. Much of the modeling work is descended from the field of computational welding mechanics (CWM) and weld process modeling (WPM). There are many numerical similarities between the simulation techniques for welding and PBF, particularly in the necessity to resolve the meltpool dynamics and the relationships between fluid behavior and final part quality [124, 125]. However, there are two key differences between PBF and welding that substantially increase the modeling complexity. In welding, the parent material is almost always a well-characterized bulk material that is highly regular and can easily be tested. In PBF, on the other hand, the substrate is either a powder bed, which is inherently stochastic and behaves very differently from fully dense solid, or recently solidified bulk material, which has a very inhomogenous, HAZ-like microstructure [50]. The other significant difference is that a welded structure typically has a small number of welds, while a PBF component essentially consists of tens of thousands of individual welds, greatly increasing the size and complexity of the analysis [125]. Work from the field of casting modeling has also been applied to PBF, especially in the area of microstructural prediction during solidification processes [126].

Many different modeling techniques have been developed for EBM, some based on previous work from other fields and others created from the ground up for AM. These models can broadly be divided into four categories, listed in increasing order of accuracy and computational cost: analytical thermal, numerical thermal, coupled thermal-fluid dynamics, and discrete particle models. Each of these models has their own advantages and disadvantages and no single model is able to answer every question of interest. By far the most significant challenge in PBF process modeling

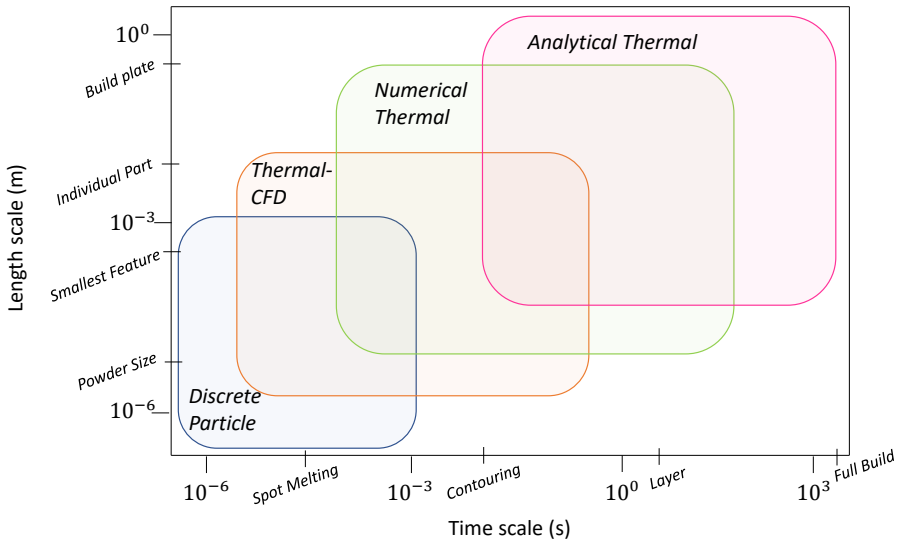

Figure 2.25: Characteristic length and time scales of the EBM process and various modeling techniques

is the wide range of length and time scales [127]. The four model categories and characteristic length and time scales for various aspects of EBM are compared in Fig. 2.25. This is by no means a quantitative comparison, but provides some qualitative information about what can and cannot be captured with each family of models. A brief review of the four model types will follow, focusing on EBM modeling and some selected SLM models; more in depth reviews can be found in Refs. [3, 72, 126, 128–131].

2.4.1 Analytical Thermal Models

While it is not possible to analytically solve for the temperature fields during EBM processes, Rosenthal's solution is a useful approximation [132]. It assumes constant material properties and ignores the effects of phase change and was originally developed for welding processes. For a point source moving at constant velocity in a semi-infinite domain, temperature distribution at a point (x, y, z) and time t is given by:

$$T(x, y, z, t) = T_0 + \frac{q}{2\pi kr} \exp\left\{-\frac{v(r + vt)}{2\alpha}\right\} \tag{2.65}$$

Where T_0 is the initial temperature, q is input heat flux, α is diffusivity, v is the heat source velocity, and R is the distance between the given point and the heat source position. Rosenthal's solution has been extended to account for distributed heat sources and some other factors, but remains mostly a tool of first approximation [133]. In many welding processes, it is generally only

accurate at temperatures less than 20% of the melting temperature; since almost the entire build chamber in EBM is above this point, Rosenthal's solution is not readily applicable [134].

A group from Oak Ridge National Laboratory developed a novel semi-analytical scheme that they used to analyze microstructures and cooling rates in AlSi10Mg, Fe-3Si, and several Ni superalloys [135–138]. They used this scheme to create models on the spatial scale of the entire bed and timescale of 10,000 individual spots. Similarly, a group from Arcam developed an analytical model that they used to optimize beam parameters [139]. Their model allowed for piecewise definition of scanning contours and beam parameters, which was designed to be easy to use for optimization. Al-Bermani et al. used Rosenthal's solution to predict cooling rates in EBM of Ti-6Al-4V and to understand solidification criteria [10].

2.4.2 Numerical Thermal Models

Numerical thermal models generally use the Finite Element or Finite Difference Methods (FEM/FDM) to model the thermal fields during EBM. This model allows for the definition of non-linear material properties and boundary conditions and is generally the most common type of model [3, 128]. Depending on the goal of the researchers, these models can be focused on resolving the near-beam area or more towards the part scale.

Zäh et al analyzed process parameters and process windows in EBM of SS 316L and validated it against previous experimental results [92, 140, 141]. They built a process map based on scan speed and beam power and noted that meltball formation is the main limiting defect. The Chou group has developed a thermal model in ABAQUS that they validated against in situ thermography data and used to predict process parameter effects, support structure stresses, and microstructural growth in EBM of Ti-6Al-4V [15, 43, 91, 142–147]. While the main focus of the Körner group is in discrete modeling, they have also developed a FEM continuum model that they used to analyze heat transfer effects over a larger area than was possible with their LBM solver [148]. Liu et al. simulated the thermal history of a turbine blade and grain growth in IN718 and Ti-6Al-4V using a novel type of element formulation to simplify the computational expense of modeling each additional layer [149–151]. They, among many other authors, made use of the Goldak double ellipsoidal model, which was originally developed for CWM [134]. This model emulates the teardrop-like shape of the meltpool without the added cost of solving the fluid flow equations; the power distribution can be seen in Fig. 2.26. However, the parameters that dictate the heat source shape are empirical and must be tuned for a given process and material.

Galati et al. developed and experimentally validated a novel numerical model for EBM of Ti-6Al-4V and studied the effect of single vs. multiple beams on resultant part quality [113, 152]. Ding et al. used a FEM model in ABAQUS to analyze the thermal history in EBM of IN718 for processing conditions, which they then used to predict grain growth and microstructural characteristics [153]. Neira-Arce used a simplified FEM model in Comsol to build a simulation model of EBM Ti-6Al-4V that was quick enough to simulate the build faster than it took in real life [99]. Lee et al. built a thermal model to compare the effects of 4 different hatching strategies in EBM of IN718 [95].

A group from Nanyang Technological University and the Agency for Science, Technology, and Research developed a FEM model using ABAQUS for EBM and SLM of Ti-6Al-4V [154–158]. They used their model to predict microstructural characteristics and residual stress for varying

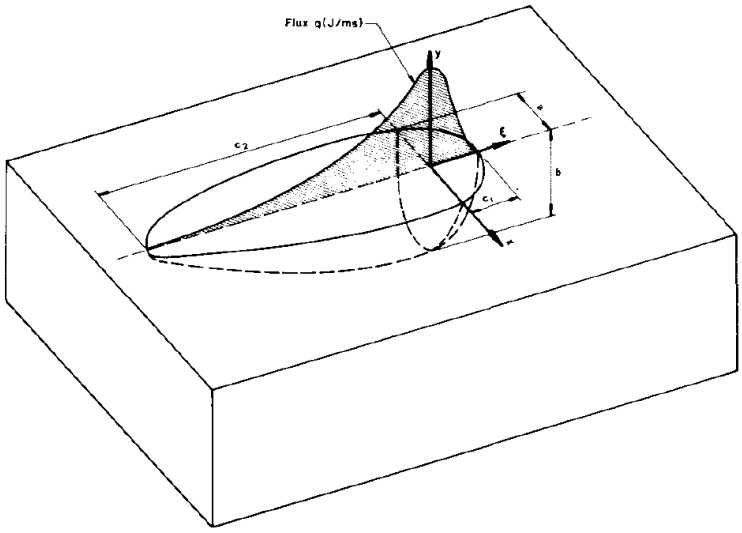

Figure 2.26: Power distribution in the Goldak double ellipsoidal heat source [134]

process parameters and build geometries and to develop optimized processing conditions. Béraud et al. also developed an ABAQUS model for EBM of Ti-6Al-4V [159, 160]. They optimized scanning parameters in order to improve the dimensional accuracy of parts and reduce thermal distortions.

2.4.3 Coupled Thermal-Fluid Dynamics Models

As noted in the dimensionless number analysis, the Péclet number in EBM is significantly greater than one, demonstrating that convective heat transfer dominates the meltpool [75]. While some pure thermal models artificially increase conductivity above the liquidus temperature to account for this effect, this is difficult to calibrate [91]. Coupled thermal-fluid models use Computational Fluid Dynamics (CFD) and the Finite Volume Method (FVM) to model both heat and mass transfer effects in the meltpool. They still assume a continuum model, which means that the inherently stochastic and non-continuous powder bed must be approximated, which introduces significant difficulty.

The Kovacevic group developed a coupled model using ANSYS Fluent for EBM of Ti-6Al-4V, which they validated by measuring meltpool sizes and used to predict dimensional variation, surface roughness, and residual stresses [74, 80, 161–163]. Unlike all other continuum models discussed in this review, Zhao et al. did not assume a flat surface, and accounted for surface tension and vapor pressure effects in shaping the meltpool surface [73, 164]. They simulated EBM of Co-Cr-Mo (CCM) and IN718 using Flow 3D and analyzed microstructural growth and meltpool dynamics; an example of their results highlighting the difference between the two chosen alloys and the effect of a non-flat surface is given in Fig. 2.27. Raghavan et al. used TRUCHAS, a multiphysics code originally developed for casting, to simulate thermal-fluid processes in EBM of IN718 in order to predict and control microstructural growth through variation in process

parameters [94, 165].The Debroy group implemented a thermal-CFD model for SLM of Ti-6Al-4V, SS 316L, IN718, and AlSi10Mg and EBM of IN718 [75, 166–169]. They analyzed residual stresses, process windows and parameter effects, and grain growth. Rahman et al. created 2D and 3D models of EBM and SLM of Ti-6Al-4V using ANSYS Fluent in order to predict the size of the meltpool for various process parameters [170–172].

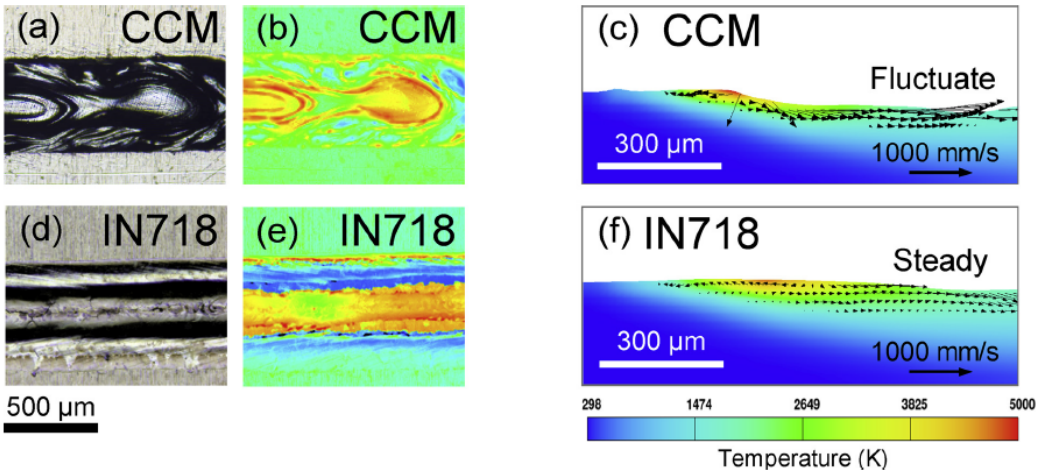

Figure 2.27: Comparison between experimental optical (left) and height (center) and simulated meltpool physics (right), highlighting different flow regimes for identical process parameters [73]

2.4.4 Discrete Particle Models

Discrete models resolve individual particles, unlike continuum models which average out the individual powder to achieve a uniform domain. Discrete models make very few assumptions about the physics of the problem and consequently are able to achieve very fine resolution of the meltpool. Discrete models generally consist of two parts: a discrete element method that solves the particle dynamics during raking and a thermal-fluid solver that solves the meltpool dynamics during melting [129]. Simulation of particle raking and distribution allows models to simulate packing density and to also capture the stochastic effects due to the inherent randomness of spreading powder [173]. Solving for the free surface of the meltpool is extremely numerically challenging, as it involves the complex interaction of a wide variety of physical processes and consequently is very numerically expensive [69]. The Körner group has developed 2D and 3D Lattice-Boltzmann method (LBM) solvers that they have used to analyze meltpool dynamics, defect formation, and microstructural growth and have extensively validated for Ti-6Al-4V and IN718 [62, 69, 79, 93, 174–184]. Examples of their LBM solver applied to EBM of Ti-6Al-4V can be seen in Fig. 2.28.

The Yan group has also developed a discrete solver using the volume-of-fluid method for EBM of Ti-6Al-4V that has been used to predict defect formation and as inputs for a microstructural model that was then used for a fatigue analysis [185–189]. While developed for SLM, the Arbitrary Lagrangian-Eulerian model of Khairallah et al. is noteworthy for its work to capture all possible boundary conditions, extensive analysis of different defect generation modes, and comparison with experimental data for Ti-6Al-4V [173]. Their methodology also highlights the power of discrete

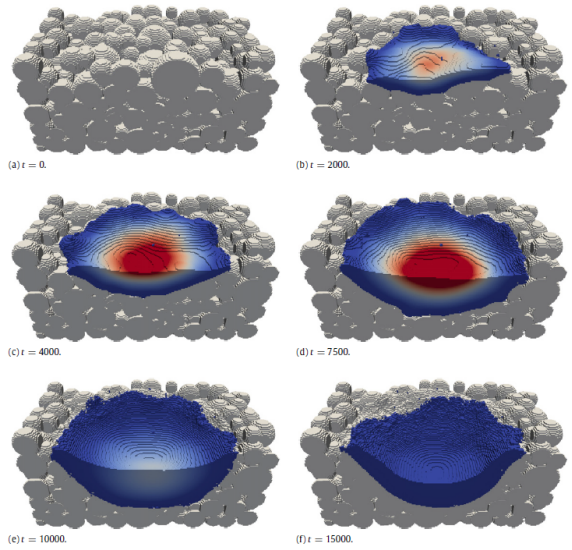

(a) 3D meltpool dynamics simulation [178]

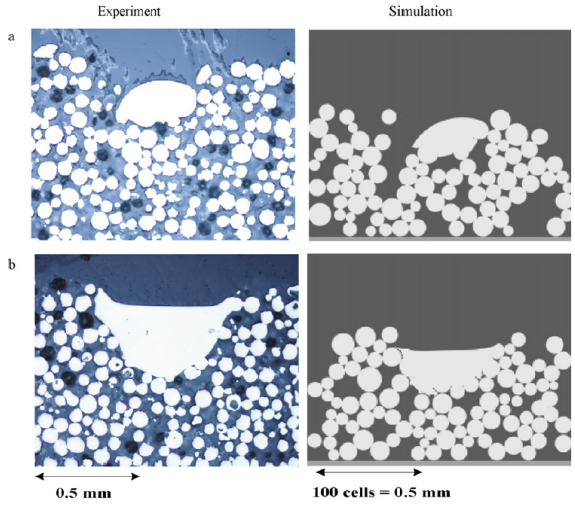

(b) Experimental (left) and 2D simulation (right) of melted bead width [69]

Figure 2.28: Discrete modeling of EBM of Ti-6Al-4V by Körner group using LBM

methods in capturing behavior at length- and time-scales not possible or practical experimentally. Panwiswas et al. and Qiu et al. also developed a discrete model for SLM of Ti-6Al-4V and IN718 which they used to predict defect generation and microstructural growth for various process parameters [190–193]. Liu and Wang implemented a novel coupled LBM-PF model that is able to simultaneously solve fluid flow, heat transfer, and dendritic growth in Ti-6Al-4V [194]. The model is currently restricted to 2D domains, but future developments include improved performance and extension to 3D domains.

The most significant downside of discrete models is their extreme computational cost. This expense limits the application of these models to very localized simulations of meltpool dynamics, even for groups with access to high-powered computing systems. For example, the 3D LBM solver developed by the Körner group takes approximately 10^5 CPU-hours to simulate a 0.6 mm^3 region for 1.5 ms [175].

2.4.5 Simulation of Defects and Microstructure

Due to the highly variable heating and repeated thermal cycling, many traditional methods for predicting microstructure cannot be easily applied to EBM. Continuous-cooling-transformation and time-temperature-transformation diagrams which are both commonly used and widely available, assume continuous cooling rates and are not applicable to EBM conditions [195]. In some cases, it is possible to extend these methods to consider the complexities present in EBM. Microstructural models can broadly be thought of as two categories: coarse models that predict the average or dominant characteristics of the microstructure and fine models that resolve individual grains. Similarly to the choice of thermal modeling technique, neither type of microstructural model is always better than the other.

Coarse microstructure models are often included as a post-processing method for an existing thermal method due to their low computational expense. Vastola et al. used a modification of the Johnson-Mehl-Avrami (JMA) method to predict formation and decomposition of α' in SLM and EBM, and were able to show that while both processes initially produce α' dominant microstructure, the high build temperature present in EBM leads to its transformation to α-β, whereas the room temperature build temperature in SLM preserves it [157]. Solidification maps are widely used as well do to their ease of implementation. The two key parameters are the thermal gradient (G) and the solidification front velocity (R) [94]:

$$G = \|\nabla T\| \tag{2.66}$$

$$R = \left|\frac{\partial T}{\partial t}\right| \frac{1}{G} \tag{2.67}$$

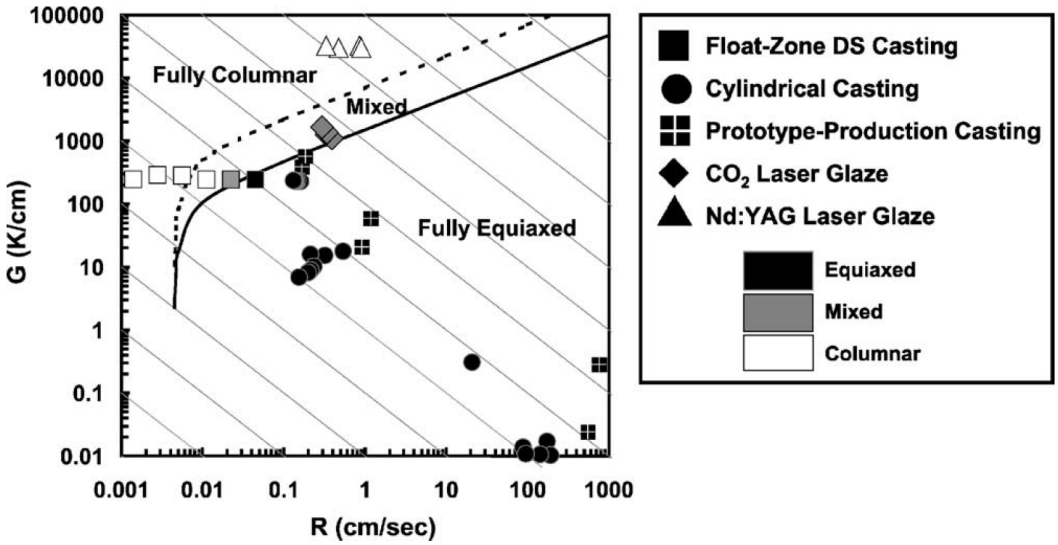

Figure 2.29: Solidification map for Ti-6Al-4V determined from experiments by Kobryn and Semiatin [196]

Based on these two parameters, the microstructure can be determined as equiaxed, columnar, or a mixed transition. These two parameters can also be plotted on a solidification map, which is typically determined experimentally. Kobryn and Semiatin developed a solidification map for Ti-6Al-4V based on experimental data for castings, which is given in Fig. 2.29. Raghavan et al. and Knapp et al. used solidification maps to analyze grain structures in Ni superalloys and Al-Bermani et al. used them to predict cooling rates based on observed microstructures [10, 75, 94, 165].

However, these coarse models inherently average out properties over a wide area and are unable to capture fine details. Furthermore, they often rely on empirical correlations [127]. Fine models, which individually simulate grain growth, are able to achieve much higher resolution at the cost of computational expense. Rodgers et al. developed a kinetic Monte Carlo (KMC) model to predict

grain growth in DED of SS 304L using a modified version of Goldak's double-ellipsoidal heat source [127]. Even though the KMC model resolves individual grains, it is relatively inexpensive and was able to simulate multiple passes. Zinovieva et al. used a cellular automata (CA) model coupled with a thermal FEM to predict grain growth in SLM of Ti-6Al-4V [197]. Koepf et al. used a CA method coupled with Rosenthal's solution to develop a model that was fast enough to simulate printing of multiple layers but still able to accurately predict microstructural growth [198]. By far the most accurate models of microstructural growth are phase field (PF) methods, though they are extremely computationally expensive. The Chou group used PF to model microstructural growth in EBM of Ti-6Al-4V [146, 199]. They analyzed the effects of process parameters on dendrite spacing and other microstructural characteristics. Kumara et al. used PF to compare the differences between EBM and casting of IN718 and to analyze compositional variations driven by solidification and the effects of build temperature [200].

In addition to predicting the microstructure, it is often desired to predict the formation of defects. Relatively few quantitative relationships have been developed to predict the formation of defects and most models rely on qualitative or empirical correlations. One commonly used metric is the meltpool length to width ratio. At meltpool length to width ratios of over 2.1, the meltpool is susceptible to the Plateau-Rayleigh instability, which leads to the formation of meltball defects [92]. This metric is particularly useful because it can easily calculated from any thermal model. Another metric is the meltpool depth, which has been found to correlate to the porosity in printed parts [51]. Discrete particle models are able to directly capture formation of LOF defects, unlike continuum based models. For example, Bauereiß et al. from the Körner group used their LBM solver to predict defects and understand how a small initial defect can propagate across multiple layers [183].

2.4.6 Comments on Different Modeling Strategies

By far the biggest discrepancies between different methods and implementations is the handling of the powder bed. Some authors assume that the powder bed has the same properties as the bulk solid, see e.g. Knapp et al [75]. However, as shown by the experimental data in Fig. 2.18 from Smith et al. and Gong et al., the conductivity of powder is less than 10% of the bulk solid. In order to properly capture the powder, many authors use the Gusarov-Tolochko model for conductivity, though this approach has the severe hurdle of requiring either measurement or assumption of the sintered neck size, see e.g. Jamshidinia et al. [74]. Many authors also use the conductivity data of Neira-Arce, even though it was measured in an atmosphere and is therefore significantly higher than during the vacuum process of EBM [99]. The powder bed presents a major numerical challenge because the particles are large enough that they have a significant effect on the meltpool physics, but small enough that individually modeling them is computationally expensive.

Capturing the fluid phenomena presents its own set of challenges. Many of the numerical thermal models artificially increase the conductivity of the liquid area in order to emulate the effects of convective heat transfer, see e.g. Shen and Chou [91]. This increase is usually on the order of 5-10x, but few authors present a justification or a study on the results of this factor. In a study and review of weld modeling, Kidess et al. noted that many of these artificial changes in material properties are generally inaccurate and do not achieve the intended effects [85]. Many authors also neglect evaporative heat loss, even though the analysis given in Fig. 2.11d shows

it to be the dominant heat mechanism at high temperatures. Experimental measurement of the properties of liquid metals is also challenging due to their high melting points and chemical reactivity [82].

Another major challenge in modeling is determination of the proper process parameters. Due to the abstraction layer implemented by Arcam, it is difficult to determine the actual values of properties like scanning speed, beam diameter, and other necessary pieces of information for implementation of a model. Furthermore, the effects of the abstraction layer are variable for the different machine architectures available [201]. This challenge is particularly frustrating because it is not rooted in any physical or numerical issue, but rather is caused by Arcam's opaqueness.

Validation of simulated results also presents a significant difficulty. Ideally, all models would be compared against in situ measurement data. Due to the expense and difficulty of measuring the temperature and velocity, this is not practical for most researchers. Even for authors that do have experimental data available, it is often of low resolution or time scale. Many authors compared measurements of a printed geometry with simulation prediction, see e.g. Jamshidinia et al [74]. Another approach is to compare the predicted and calculated microstructure, see e.g. Al-Bermani et al [10].

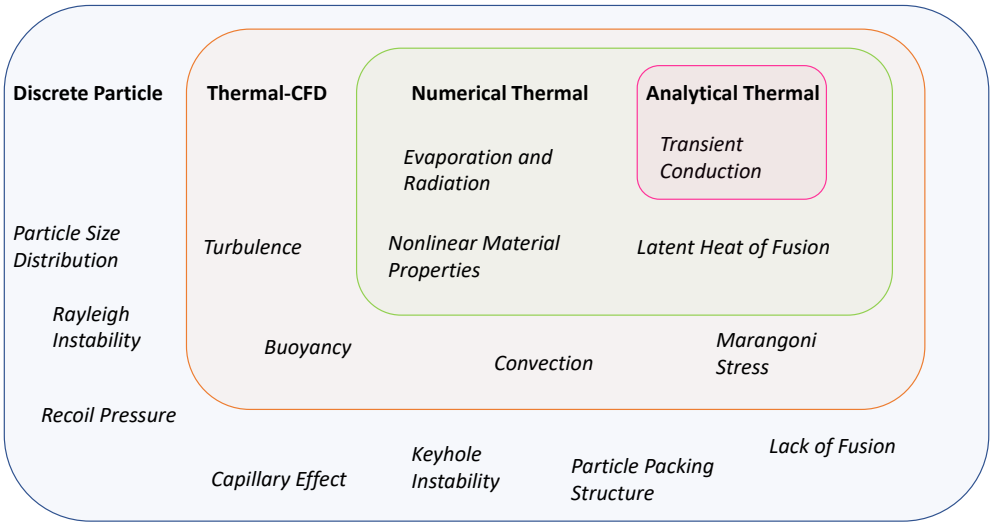

Figure 2.30: The mass and heat transfer mechanisms captured by different modeling techniques

The comparison of the different length and time scales captured by each family of models can also be considered as a categorization of the different heat and mass transfer mechanisms captured by each model and the resulting computational expense necessary to resolve these physical phenomena. This type of ordering is given in Fig. 2.30. Again, like the comparison given previously in Fig. 2.25, this is a qualitative comparison. The discrete particle models are able to capture a virtually all of the physical features of the PBF process, but have an extremely high computational cost. On the other hand, analytical thermal methods only capture one physical process,

heat conduction, but are very inexpensive to solve.

The need to develop multi-scale families of models has been repeatedly highlighted in the literature [72, 126, 129, 202]. However, due to the significant work required to develop and validate even a single model, integrated modeling across a wide spectrum of time and length scales has not been yet implemented. While the majority of the discussion has been on thermal and fluid modeling, a similar goal can also be realized for microstructural modeling, ranging from inexpensive solidification maps and empirical relationships to highly complex PF models. Rather than consider each individual model as a sole solution in itself, it should be considered as occupying its own position on the multi-scale range of models. Eventually

Chapter 3

Methods

Based on the literature review, the following goals and objectives were defined:

- Develop a multiphysics model of the EBM process
- Use the multiphysics model to predict component properties and defects
- Calibrate IR camera to measure temperatures in situ
- Compare the designed, printed, and simulated dimensions of a test piece
- Use the experimental data from the IR camera and test piece dimensions to validate the model

A coupled thermal-fluid dynamics model was chosen as it offered a balance of accuracy and computational cost between discrete and pure thermal models. In EBM, residual stress is generally of secondary importance to defects and microstructural variation, so it was decided to focus the model on accurately resolving the meltpool region, where defects are generated, than resolving temperature fields on the scale on an entire of component. It is easy to turn a coupled model into a pure model by simply disabling solution of the fluid equations in the solver, while adding in fluid flow to an existing thermal model is a much more challenging task. While discrete particle models provide unmatched accuracy in the meltpool reason, insufficient computing capacity was available to overcome the high computing costs. Ideally, several different models would be created to develop a multi-scale modeling capability, but that is out of the scope of this work.

For the test piece geometry, a line segment was chosen because it is simple to measure and simulate. The line build offers some insight into the features that would be seen with a complex, fully designed component while being much easier to measure and compare across samples. Furthermore, a larger component would result in a much higher computational expense. A front-looking camera was used rather than a top mounted camera due to the logistical difficulties of the latter approach. While the measurement quality is significantly better with the top mounted approach, it was not possible to implement the necessary vacuum mounting and Kapton film system given the limited time and resources available for this work. A FLIR A6261 camera was chosen as it has a frame rate, good resolution, and a variety of filter and lens options. Furthermore, FLIR was very willing to collaborate and work with the MSTL. A range of filter, lens, and software settings were explored in order to find the best measurement settings.

3.1 Experimental Method

Two sets of experiments were conducted at the MSTL using an Arcam A2X machine. Both sets used recycled Ti-6Al-4V powder from Arcam, with a mean diameter of 60 μm.

3.1.1 Line Topology Comparison

To assess the accuracy of the simulated meltpool size, a simple test geometry was printed and the dimensions were measured during post-processing using a Keyence 3500 VR optical microscope. This is a common test for PBF process models; the most relevant comparisons for this work are the experiments done by Galati et al., Riedlbauer et al., and Jamshidinia et al. for EBM of Ti-6Al-4V [80, 148, 152]. The advantages of this experimental design are that it is easy to measure and does not require any in situ process monitoring techniques. The disadvantages are that it only provides two measurements, meltpool width and depth, and does not capture any transient behavior, including temperatures, velocities, solidification rates, and other key process characteristics. The test geometry used in this work had five separate features, shown in Fig. 3.1. All features are 4 mm long by 0.4 mm wide and built at a layer height of 3 mm without any support material. The features consist of:

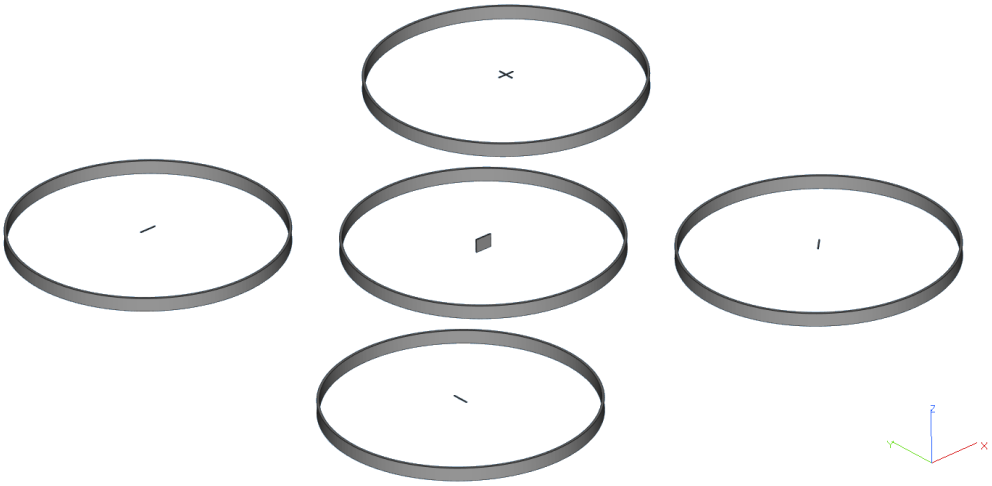

Figure 3.1: Line Build Geometry

- 1 layer tall line in the x direction
- 1 layer tall line in the y direction
- 1 layer tall line angled 45 degrees between x and y
- 1 layer tall cross
- 3 mm tall line in the x direction, built directly on the build plate

Table 3.1: Mesh sizes for convergence study

Build number	Melt theme	Settings
1	Contour	Default
2	Wafer	Default
3	Contour	Default
4	Contour	Default

These features were chosen to test the accuracy of the model and to discern the effects of different orientations on the measured size compared to the design size. In addition, a ring was printed around each feature in order to help keep the sintered powder attached to the build plate and prevent damage during post-processing. A total of four builds were completed, using the settings given in Table 3.1.

3.1.2 In situ Temperature Measurement

To assess the accuracy of the simulated meltpool temperature, an in situ temperature measurement procedure was developed using an IR camera. This experimental approach is similar to that done by the Chou group from the University of Alabama and NASA [15, 35, 37, 42, 43]. A FLIR A6261 camera was used. The resolution is 640 x 512 pixels and the maximum frame rate is 120 fps. There are three main factors that determine the temperature range of the recorded image: a neutral density (ND) filter, a lens (including optional lens extensions), and the integration time. ND filters block out a given amount of light in order to influence the range seen by the camera. The fraction of light let through is given by 10^{-n}, where n is the number of the filter, generally reported as NDn. The camera used in this work had interchangeable ND1, ND2, and ND3 filters, which correspond to 1%, 0.1%, and 0.01% transmission rates. The best results in this work were found using the ND2 filter. The camera in this work came with multiple lenses and the best images were found using a 50 mm lens, with an aperture of $F = 1.8$, and a 20 mm lens extender. The integration time is a software setting that essentially determines how long the shutter is open for. A variety of integration times were used in this work and their effects on the results will be discussed.

Camera Calibration Procedure

While the camera was provided with a factory calibration from FLIR, it was found that the leaded glass in the door of the EBM machine had an extremely low transmission rate, on the order of $5 - 10\%$. In order to compensate for this, the camera was re-calibrated at the MSTL with a piece of leaded glass in the optical path of the camera. This ensured that the transmission loss due to the leaded glass was accounted for in the measurement. The raw reading from the thermal camera is referred to as counts (C), which is a unitless measure in the range $0 \leq C \leq 16,383$. In order to calibrate the camera, a known relationship must be established between temperature and counts.

The calibration setup is pictured in Fig. 3.2. An electric furnace was used to heat a sample of EBM printed Ti-6Al-4V and the temperature was measured using a K-type thermocouple via a viewhole located on the top of the furnace. The furnace had a temperature range of approximately

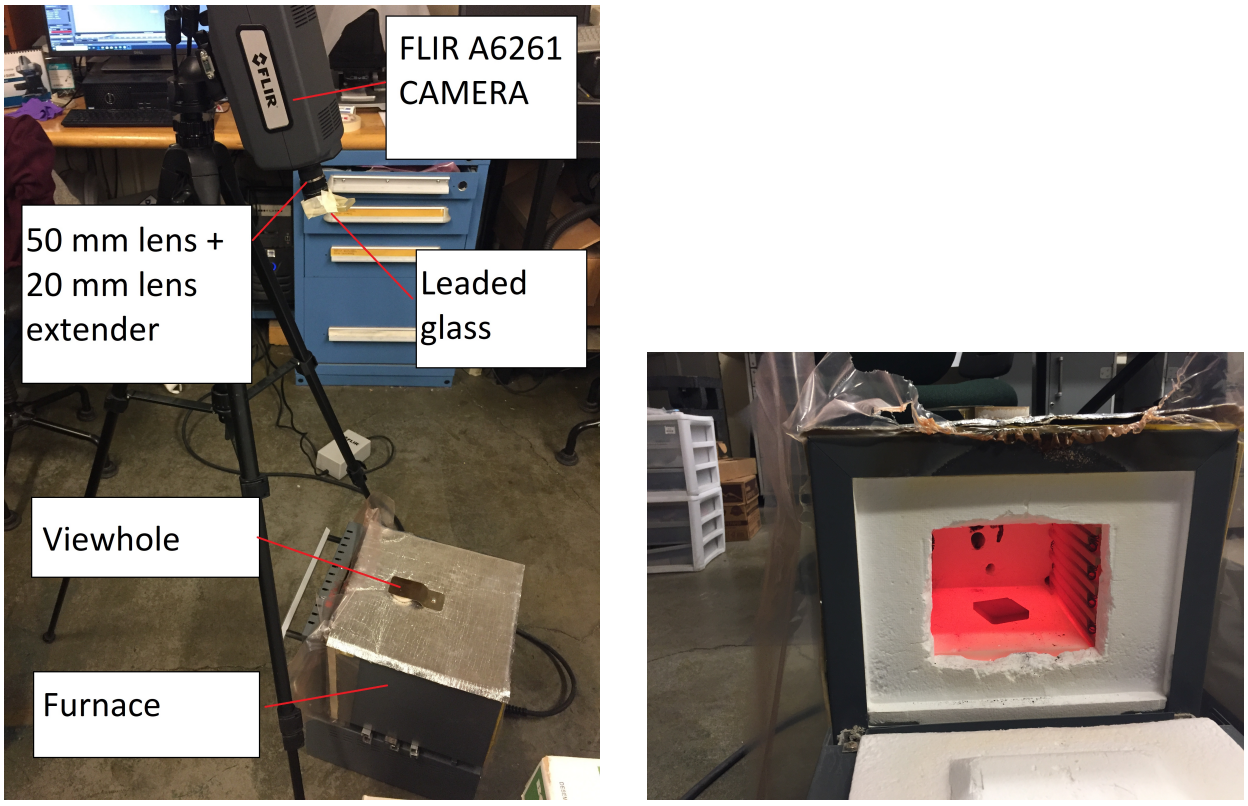

(a) Camera setup for calibration (b) Furnace interior with sample

Figure 3.2: Calibration setup for IR camera and furnace

750-1200 K. Due to equipment limitations, the calibration was conducted under a normal, sea level atmosphere, which lead to very heavy oxidation of the sample. The emissivity of the sample was assumed to be 0.45 based on the results of Li et al. for Ti-6Al-4V oxidized at 973 K, which is in good agreement with the results from Touloukian and Dewitt for oxidation at 1150 K [109, 203]. The emissivity of the furnace interior was assumed to be 0.75, based on typical values given for clay and firebrick materials [204]. Due to the small furnace size and slow rate of temperature change, the sample and furnace were assumed to be at the same temperature. Based on these assumptions and Eq. (2.9), the measured power per unit area for a given temperature can then be calculated:

$$W_{calibration} = \sigma_{SB} \left(\epsilon_{sample} + (1 - \epsilon_{sample})\epsilon_{furnace}\right) T^4_{thermocouple} \tag{3.1}$$

The temperature was increased in increments of approximately 50 K from the point at which the sample was initially visible in the thermal image until the counts were maxed out at 16,383. The results for four different integration times are given in Fig. 3.3. These measurements were taken using the ND2 filter, 50 mm lens and 20 mm lens extender, and with a piece of leaded glass in the optical path. The results for 15 ms and 0.05 ms are on the outer edges of the calibration range, and therefore the results should be used with caution. According to the manufacturer's recommendation, the ideal range for measurement is between 4,000 - 12,000 counts and this was

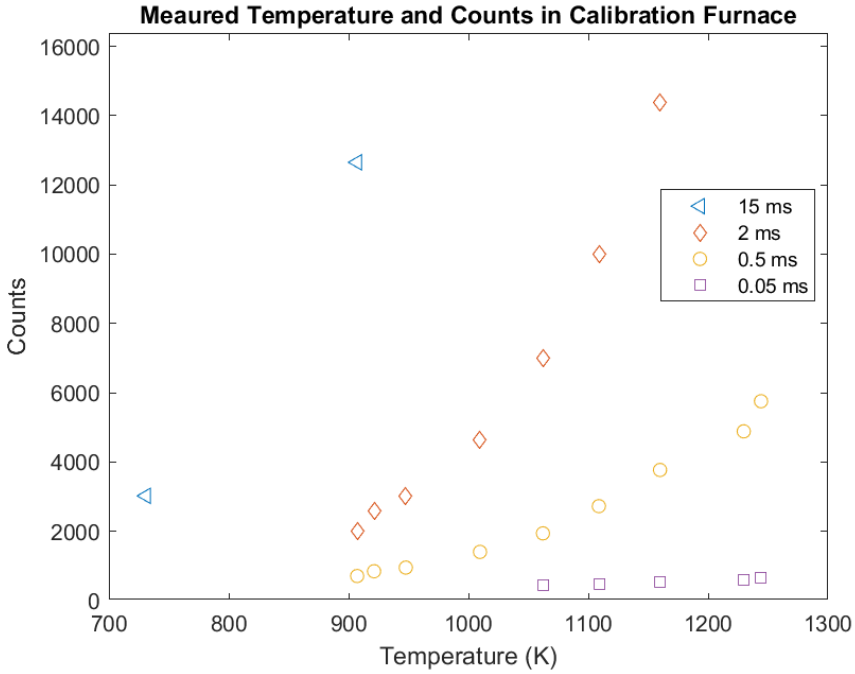

Figure 3.3: Experimentally measured temperatures and counts

also qualitatively observed to be the least noisy range of the camera. By applying Eq. (3.1), the measurements can be translated into counts versus power, which are plotted in Fig. 3.4. A best fit linear equation is plotted for each calibration setting and the power levels corresponding to 1,000 and 1,5000 K are plotted for reference; the equations are also given in Appendix A.4. The two settings with the most data, 2 ms and 0.05 ms, match the curve fit relationship very well. The relationship for 0.05 ms predicts negative work at low counts, which indicates again that inaccurate results are measured at low counts. Only two datapoints were recorded for 15 ms integration time because the temperature is significantly below the region of interest.

In order to account for effects of reflection during the EBM machine, the measurements must be compensated using essentially the opposite procedure that was used to calculate the power under calibration conditions. Under EBM conditions, the power per unit area is given by:

$$W_{EBM} = \sigma_{SB} \left(\epsilon T^4 + (1 - \epsilon) T_a^4 \right) \tag{3.2}$$

The value for ϵ from Fig. 3.5 will be used and T_a was measured by Rodriguez et al. to be 615 K [31]. In this work, the emissivity of powder will be ignored and the bulk solid emissivity will be used for the entire solid region. This provides a relationship between power and temperature $W_{EBM} = f(T_{EBM})$. The best fit lines plotted in Fig. 3.4 provide a function correlating calculated power and measured counts such that $W_{calib} = g(C)$. By setting $W_{EBM} = W_{calib}$, a relationship between counts and EBM temperature can be derived as $T_{EBM} = f^{-1}(g(C))$. The results of this relationship are plotted in Fig. 3.6. As noted above, the data for 0.05 ms and 15 ms should be used with caution and the ideal measurement range is between approximately 4,000 - 12,000 counts.

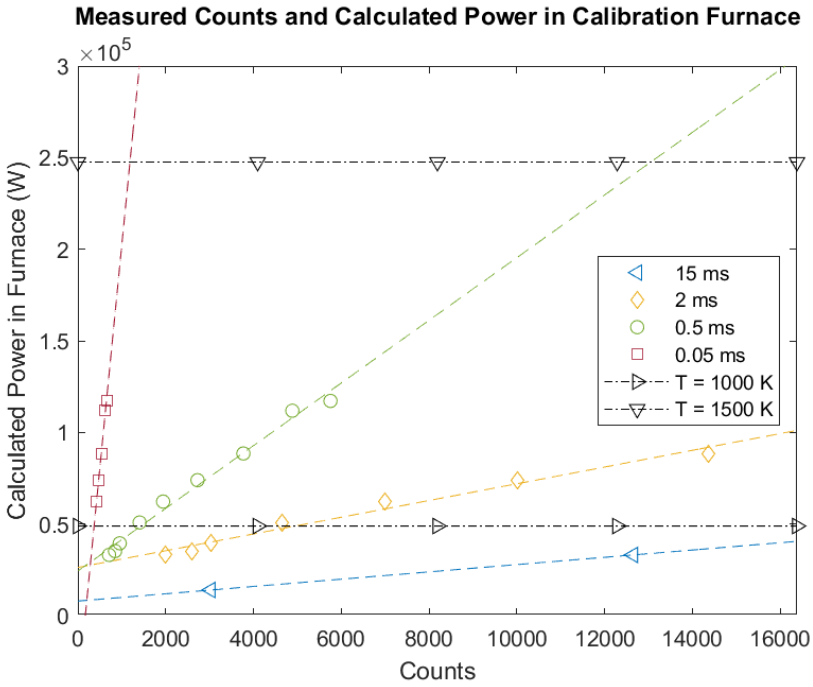

Figure 3.4: Linear fit between experimentally measured counts and calculated power

Furthermore, the emissivity data for Ti-6Al-4V has a lower limit of 780 K, so any temperatures below that level are ignored.

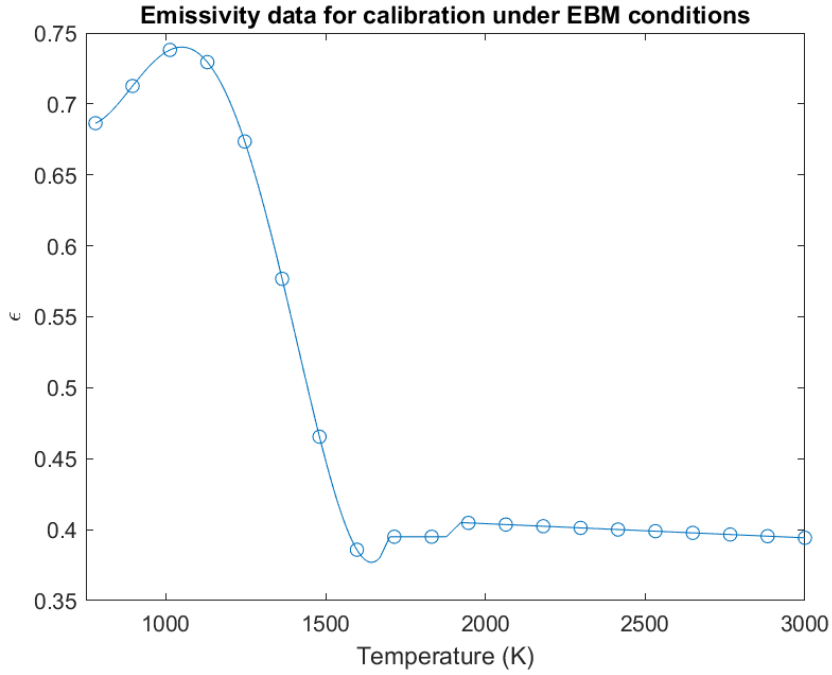

Figure 3.5: Emissivity for calibration under EBM conditions [100, 101, 107]

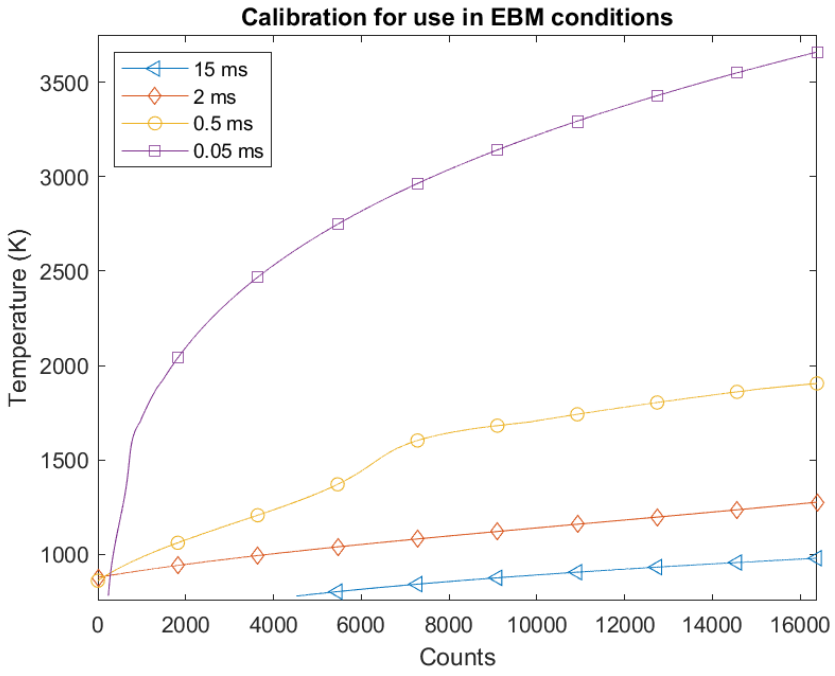

Figure 3.6: Calculated calibration curves for EBM conditions

In situ Process Measurement Procedure

The experimental setup is given in Fig. 3.7a. The camera was positioned such that it looked at approximately the center of the build plate. The distance from the build plate to the lens of the camera was measured to be 800 mm and the angle between the camera and build plate was 45 degrees. The field of view of the camera was calculated to be 110 mm x 124 mm. In order to increase the visible space of the image, the metal grating in the heat shield was removed and the hole was enlarged to a size of approximately 90 mm by 90 mm. A new piece of sacrificial glass was used to ensure a minimum of metallization. The build geometry used consisted of many large, flat pieces; this geometry was chosen in order to provide a maximum area to observe and to ensure that a melted area would be visible no matter the orientation of the camera. An overview of the build geometry is given in Fig. 3.7b.

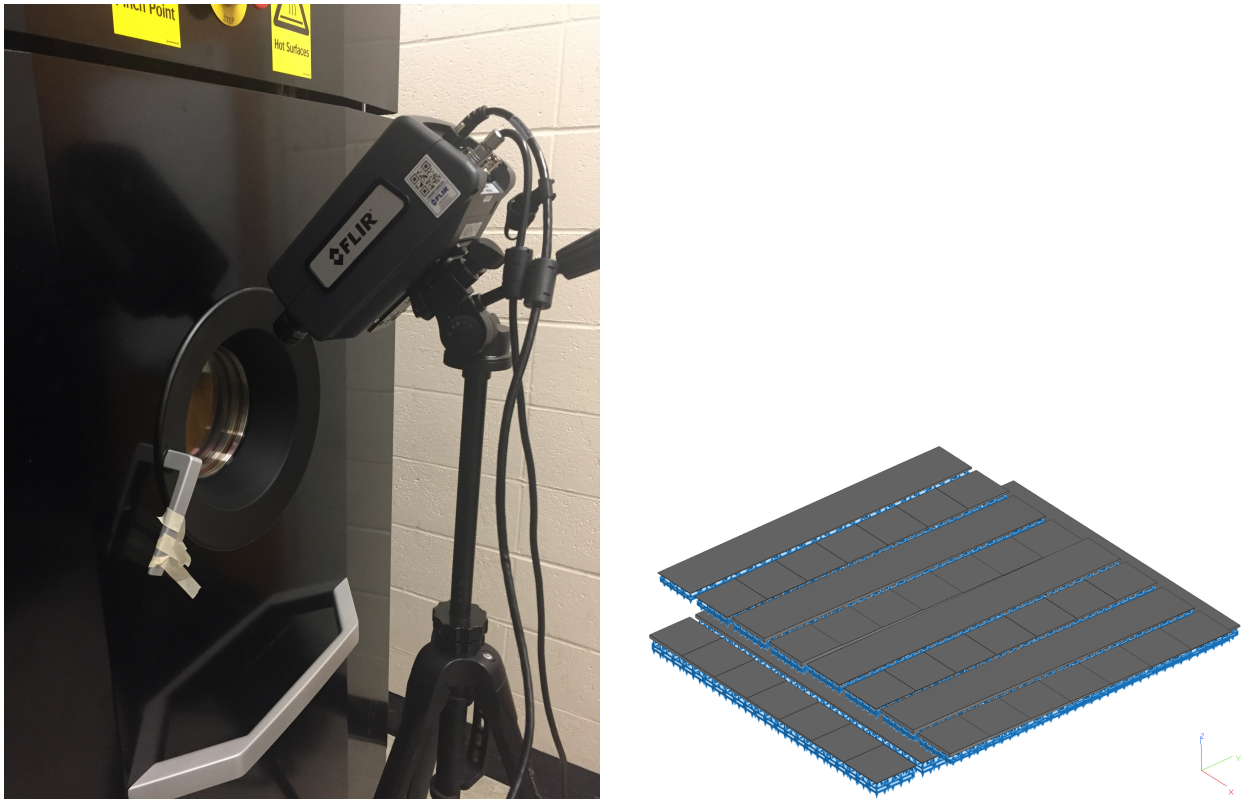

(a) Experimental setup for in situ process measurements

(b) Build geometry for IR camera test

Figure 3.7: Calibration setup for IR camera and furnace

3.2 Numerical Method

A coupled thermal-fluid model has been implemented using ANSYS Fluent. Fluent is a parallel FVM code and is widely used in AM process modeling for its high performance, multiphysics

capability, and customizability through user-defined functions (UDFs) written in C [128]. The single-precision, parallel executable was used from version 2019 R2. Fluent uses a cell-centered FVM to solve the fluid and heat transfer flows. The FVM is based on a discretization of an ordinary differential equation (ODE) using the control volume technique. Consider the transport equation of an arbitrary scalar ϕ' in a control volume with volume V and surface area A [70]:

$$\int_V \frac{\partial(\rho\phi')}{\partial t} dV + \oint \rho\phi' \vec{u} \cdot d\vec{A} = \oint \Gamma_{\phi'} \boldsymbol{\nabla}_{\phi'} \cdot d\vec{A} + \int_V S_{\phi'} dV \tag{3.3}$$

Where $\Gamma_{\phi'}$ and $S_{\phi'}$ are the diffusion coefficient and source terms for the scalar. This equation can then be discretized as [70]:

$$V\frac{\partial(\rho\phi')}{\partial t} + \sum_{f=1}^{N_{faces}} \rho_f \vec{u}_f \phi'_f \cdot \vec{A}_f = \sum_{f=1}^{N_{faces}} \Gamma_{\phi'} \boldsymbol{\nabla}_{\phi'_f} \cdot \vec{A}_f + S_{\phi'} V \tag{3.4}$$

Where N_{faces} is the number of faces in the discretized control volume. The scalar ϕ' is solved at the center of each discretized control volume, referred to as a cell or element, by approximating the scalar transport equation as [70]:

$$a_P \phi' = \sum_{i=1}^{n_{border}} a_i \phi'_i + b \tag{3.5}$$

Where n_{border} is the number of cells bordering the given cell and a_P, a_i, and b are coefficients derived by linearizing Eq. (3.4). By iterating this equation over the domain, the system can be represented as a sparse linear system and then easily solved using any number of linear algebra techniques. The challenge lies in converting the highly nonlinear discretized equations into this simple linear relationship. Another challenge is that Eq. (3.5) is defined at the cell centers, but some values, particularly the face gradient terms in Eq. (3.4), are evaluated at the cell boundaries, which means that an interpolation method is required. An in-depth discussion of the available spatial and temporal discretization methods would be out of the scope of this work; a review and background on the available methods are given in the Fluent Theory Guide from ANSYS [70].

3.2.1 Modeling Strategy and Implementation

This section discusses the FVM model that was implemented in this work and the theoretical, numerical, and experimental reasoning that was used to justify this strategy. These justifications draw heavily on the background material discussed in the literature review, particularly Sections 2.3.1, on heat and mass transfer mechanisms in EBM, and 2.3.2, on the thermal and fluid properties of Ti-6Al-4V. Wherever possible, assumptions were avoided and a physics-based reasoning was sought. The source code for the UDFs and custom material models that were used to implement many of these numerical features are given in Appendix B.

Solver Method and Settings

Fluent offers the user very in depth control of the various numerical settings used in the solver and it can often be challenging to determine which is best-suited for a given problem. Most of the settings used in this analysis were not changed from the default values, but those that were are summarized in Table. 3.2. The coupled pressure-velocity method was used because it significantly improved stability over the SIMPLE, SIMPLEC, and PISO methods. Jamshidinia et al. used SIMPLE and Rahman et al. used the coupled method, but neither give a justification for this choice [74, 171]. The bounded second order implicit timestepping method was used. Second order timestepping was found to have significantly better convergence and stability than the first order method, at a negligible cost in performance. The method is bounded by Fluent in order to damp nonphysical oscillations, though it was found that in the cases considered in this work the bounding was very rarely, if ever, invoked by the solver [70].

The timestep was chosen to be 1 μs based on stability concerns. Similar values in the literature are on the order of 50-250 μs, but a conservative value was chosen for this work due to limited experimental data and the preliminary status of the model [74, 75]. Based on the Reynolds number analysis presented in Section 2.3.1, the flow was assumed to be laminar. The Courant number, under-relaxation factors, and explicit relaxation factors are given in Table 3.2. A study was conducted to determine the effects of changes to the mushy zone constant, which is discussed in Section 3.2.3.

Table 3.2: Fluent solver settings

Solver Settings	
Pressure-Velocity Coupling	Coupled
Flow Courant Number	2000
Spatial Discretization	Second order
Timestepping Method	Bounded second order implicit
Timestep	1 μs
Model Parameters	
Turbulence model	Laminar
Mushy zone constant (A)	10^5
Explicit Relaxation Factors	
Momentum	0.5
Pressure	0.5
Under-Relaxation Factors	
Density	1
Body forces	1
Liquid fraction	0.75
Energy	0.9

Domain and Mesh

Spaceclaim was used to create the geometries and the ANSYS Meshing software was used to generate the meshes. An unstructured tetrahedral mesh was used. Initially, a structured hexahedral mesh was implemented, but it was found that the structured mesher could not consistently create high quality elements with the desired sizing. The mesh near the beam was refined significantly compared to the regions further away from the beam. Due to both the small timescale and low thermal conductivity of Ti-6Al-4V, it was found that the temperature gradients away from the beam were very low, which allowed for a very coarse beam in this areas. A convergence study was conducted to determine the optimal meshing size, which is discussed in Section 3.2.2.

The Cartesian and axisymmetric 2D versions of Fluent were investigated for usage as simple test cases, but it was found that the convergence and stability in 2D was extremely poor, even when using cases that had worked well in 3D. It is unclear if this is an inherent issue in Fluent or due to a conflict with the UDFs used in this analysis, but the 2D versions were not pursued once the lack of performance was discovered. One potential cause of the instability is the Marangoni stress implementation. It was found that in some 3D geometries, particularly ones using multiple symmetry planes, an interaction between the Marangoni stress and symmetry planes created nonphysical results. Disabling either of these boundary conditions fixed this issue, but a solution could not be found that both prevented the nonphysical behavior and maintained the desired boundary conditions.

Material Flag Algorithm

In order to correctly handle the existence of two solid states, sintered powder and fully dense bulk material, a variable called material flag (m) was defined using a UDF following the pseudocode given in Algorithm 1, based on a similar method developed by Shen and Chou using ABAQUS [91]. The first if statement is true for all cells above the liquidus temperature, which corresponds to the liquid regions. The second is true for all cells between the solidus and liquids temperature, which corresponds to the mushy region. The third if statement is true in one of two cases. In the first case, the resulting cell has just solidified from the mushy region, so $m \geq 1$ but $T < T_s$. Therefore, the first two if statements are false and the third one is true. In the second case, the cell was initialized with a value of $m = 1$ and $T < T_s$, which results in the first two if statements being false and the third being true. These two cases allow for creation of solid regions through both an initial definition of regions with $m = 1$ and the melting of cells. Lastly, the sintered region can only be reached if $T < T_s$ and $m = 0$. This means that sintered cells can only be created through an initial definition, and that a cell cooling from mushy to solid will always result in a fully dense solid.

Algorithm 1 Material flag pseudocode

```
Get element temperature T and current material flag m
if T ≥ T_liquidus then
    m = 3
else if T ≥ T_solidus then
    m = 2
else if m ≥ 1 then
    m = 1
else
    m = 0
```

Thermal and Fluid Properties

The as implemented values for k, and c_p are given in Fig. 3.8 and based on the sources provided in Table 3.3. Diffusivity is not a direct input to the model, but is given for reference. As shown by the low Bond number, which is calculated following Eq. (2.29), buoyancy is essentially negligible and Marangoni stress is the only significant source of fluid motion in EBM. Therefore, density will be assumed to be a constant value of $\rho(T_L) = 3920\,\mathrm{kg/m^3}$. In order to correctly account for the variations in density, the specific heat is normalized by the mass:

Table 3.3: Sources for thermal properties used in this analysis

State	Conductivity	Specific heat	Emissivity
Bulk solid	Neira-Arce [99]	Neira-Arce [99]	Milošević and Aleksić and Cezairliyan et al. [100, 107]
Powder bed	Neira-Arce and Smith et al. [99, 106]	Scaled by ϕ	Sih-Barlow model [112]
Liquid	Boivineau et al. [101]	Kaschnitz et al. [97]	Boivineau et al. [101]

$$c_p' = \frac{c_p \rho}{\rho(T_L)} \tag{3.6}$$

Where c_p' is the mass corrected specific heat. This assumption is allowable because in the heat equation, Eq. (2.10), c_p (or H) and ρ do not appear independently, only as a combined term. The specific heat data from Neira-Arce was chosen for the solid regime because it was measured at high heating rates and does not include microstructural effects, which better reflects the rapidly varying thermal conditions seen in EBM and the short time-scale captured by this model. For conductivity, the solid data from Neira-Arce was used for the same reason. The emissivity data of Milošević and Aleksić and Cezairliyan et al. was used because these two sources were in good agreement and provided data for the full range of temperatures considered.

Determining the correct properties to model the powder bed region was a considerable challenge due to a lack of experimental data. In particular, one major challenge is how to handle the effects of densification on the thermal properties of a cell. This problem has both physical

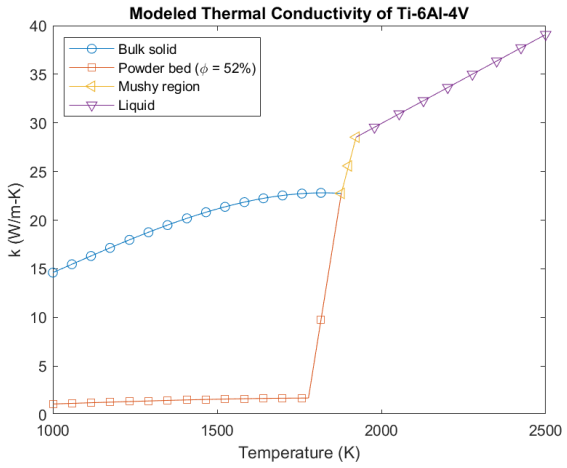

(a) Thermal conductivity

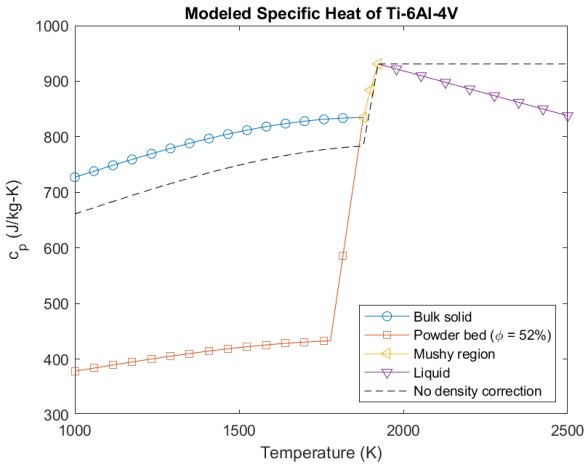

(b) Specific heat

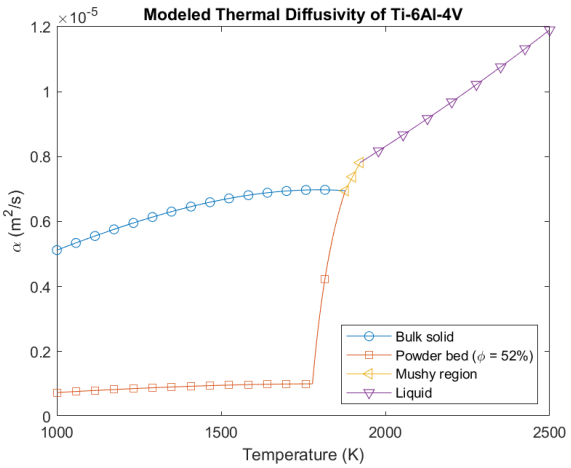

(c) Thermal diffusivity

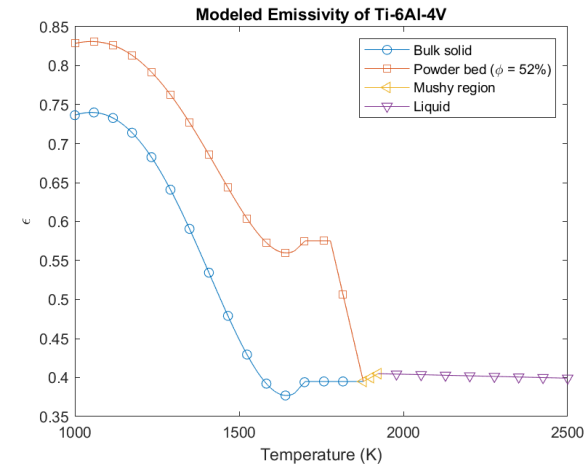

(d) Emissivity

Figure 3.8: Thermal properties of Ti-6Al-4V as modeled for all four regimes

and numerical aspects. In a physical sense, as the powder is heated, it will further sinter and eventually melt; 1 kg of melted powder is the same as 1 kg of melted bulk solid. Furthermore, for numerical purposes, it is desirable to have smoothly defined material properties, without any discontinuities. No experimental data or analytical relationship could be found in the literature to predict the resulting material properties during this densification process. Therefore, a new parameter referred to as densification temperature, $T_{dens} = 1778K$, was defined. Above this temperature, the powder properties were defined using a linear interpolation between the properties at the solidus temperature. This approach is similar to the ones adopted by Zäh and Lutzmann and Jamshidinia et al [80, 92]. Below this temperature, different methods were used for each property, which will be covered in the next two paragraphs.

The powder bed was assumed to have a porosity $\phi = 0.52$, based on the measurements of Smith et al [106]. The effective conductivity was assumed to be 7.5% of the fully dense solid, also based on the results from Smith et al [106]. The radiative term in the Gusarov-Tolochko model,

Eq. (2.54), was neglected as it is significantly less than the value of the conductivity term. Even though the Sih-Barlow model has some significant discrepancies with the available experimental data, as shown in Fig. 2.23b, it was used due to a lack of a better model. The effects of this on the overall results are likely negligible, as radiation and evaporation from the meltpool are orders of magnitude higher than the heat loss from the solid regions. Due to the assumption of constant density for both the powder bed and bulk solid, the specific heat of the powder bed is scaled by the porosity ϕ in order to achieve the correct specific heat. The effects of powder re-use on specific heat measured by Neira-Arce, shown in Fig. 2.21a, are not considered due to a lack of further experimental data to substantiate it or a theoretical understanding of what causes these effects.

One major drawback of Fluent are the limitations in defining specific heat using a UDF. For example, thermal conductivity can be defined as an arbitrary function of any solver variable desired. Specific heat, on the other hand, can only be defined as a function of temperature. Initially, in order to differentiate between the solid and powder phases, the density was manually changed. This lead to severe instabilities and convergence issues and this approach was abandoned. Instead, density was defined to be constant and specific heat instead was varied using the species transport equation capability built into Fluent, which is the recommended approach by ANSYS [205]. Three different species were defined using different material properties and their mixing ratio was controlled by a UDF to effectively control the specific heat. While this does result in the ability to control specific heat and does not increase the computation time, it is a major workaround to achieve what ideally should be a simple material behavior. One limitation of this approach and the decision to assume constant density is that the latent heat of fusion must be defined globally and cannot be locally controlled. Therefore, the as implemented latent heat of fusion was assumed to be equal to the true latent heat of fusion scaled by ϕ.

Non-linear viscosity was implemented based on experimental data from Raush [82]:

$$\eta = 2.134 \times 10^{-2}\text{Pa-s}\exp\left\{\frac{1.111 \times 10^4 K}{T}\right\} \tag{3.7}$$

Initial and Boundary Conditions

The initial temperature is defined to be 1000 K, which is the preheating temperature measured by the thermocouple on the baseplate. This neglects the effects of local preheating, which likely does result in a local temperature higher than the baseplate temperature. Knapp et al. performed simulation of the local preheating during printing of IN718 and found that depending on the process conditions, it was between 1273-1500 K [75]. They do not give details on their analysis settings, so it is not possible to recreate their results for Ti-6Al-4V.

For velocity on the free surface, Marangoni stress was implemented following Eq. (2.21) and using the experimental value of $-4.1 \times 10^{-3} N/m - K$ from Egry et al [83]. No other velocity boundary conditions were implemented.

Radiation was implemented using the emissivity values given in Fig. 3.8d and an ambient temperature of 615 K, based on experimental measurements from Rodriguez et al [31]. While Fluent does have a built in functionality for non-linear emissivity, this feature was found to be unstable, so the radiative heat flux was applied using a UDF [206].

Evaporation of Ti and Al was implemented in the liquid phase only following Eq. (2.42). As shown in Fig. 2.11d, at the liquidus temperature, evaporation only contributes 10 % of the total heat flux at the liquidus temperature. Therefore, the effects of evaporation on the solid and mushy phases are negligibly small. Furthermore, evaporation of V was ignored because it is less than 1% of the total heat flux for the range of temperatures considered in this analysis. The effects of recoil pressure were also ignored because they cannot be implemented using the chosen FVM method. The overall mass loss on the meltpool was also assumed to be negligibly small, but the compositional change due to loss of Ti and Al was calculated following Eq. (2.40) and tracked using scalar transport equations, which are discussed in the following section.

The heat flux due to the electron beam was modeled followed Eq. (2.43). Klassen's model was used to determine the vertical distribution [79]. His model, which is given in full in Section A.2, is extremely complex and would be difficult to implement in a UDF, so a polynomial model was curve-fit to his model and used instead. The horizontal distribution was calculated using the Gaussian equation from Degenhardt and with a FWHM diameter of $350\mu m$ [93]. The beam voltage and current were determined based on analysis of the log files.

Due to the low thermal conductivity of Ti-6Al-4V in the bulk solid and especially in the powder bed, the heat is highly concentrated near the electron beam and does not dissipate into the whole domain. Therefore, based on Saint-Venant's principle, an adiabatic boundary condition was used for all faces other than the top surface. A methodology to simulate the effects of the baseplate was developed using the shell-conduction feature in Fluent, which allows for the automatic creation of thin shell walls on the boundary faces of the domain. These walls can be used to very easily extend the domain and add extra thermal mass, effectively simulating the effects of a change in build height. A temperature dependent 316L stainless steel material has been created to allow for the simulations of base plate using this method. The 316L material cannot undergo phase changes and exists only to serve as a base plate. The defined properties are given in Fig. 3.9, based on data from Mills [81] and the equations are given in Section A.3.

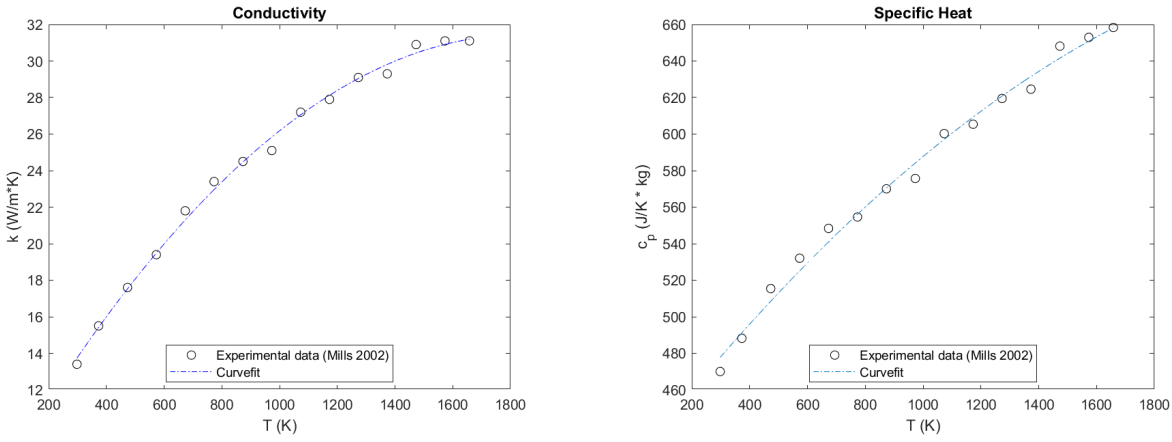

(a) k (b) c_p

Figure 3.9: Temperature dependent material properties of 316L baseplate [81]

Ti and Al Transport

In order to track the compositional change due to preferential evaporation of Ti and Al, a scalar transport model was implemented using the user-defined scalar (UDS) feature in Fluent. UDS are arbitrary scalars that are simultaneously transported with the fluid flow and can be controlled through UDFs. Note that this is not the same as the user defined species that were used to control the specific heat. For a UDS, Fluent solves the following equation [70]:

$$\frac{\partial \rho \phi'}{\partial t} + \boldsymbol{\nabla} \cdot (\rho \vec{u} \phi' - \boldsymbol{\Gamma}_{\phi'} \cdot \boldsymbol{\nabla} \phi') = S_{\phi'} \tag{3.8}$$

In this work, UDS were used to model the transport of Al and Ti driven by evaporation. As noted in Section 2.3.1, the Schmidt number is high and diffusion is therefore negligible. The only sink term is the mass evaporation flux from the meltpool surface, given by Eq. (2.40). Furthermore, density is assumed to be constant. With these assumptions and simplifications, the UDS transport equation reduces to:

$$\frac{\partial \phi'}{\partial t} + \boldsymbol{\nabla} \cdot \vec{u} \phi' = \frac{1}{\rho} W_i \tag{3.9}$$

This differential equation is then solved in conjunction with the fluid equations. Because evaporation of V is negligible, its concentration was calculated by taking the concentrations of Ti and Al and finding the balance. This simplified the transport modeling by automatically enforcing the constraint that the total concentration sum to unity. The variations in composition were assumed to have a negligible effect on the thermal and fluid properties of the alloy and were tracked only for post-processing purposes.

Post-Processing

ANSYS's CFD-Post software was used for graphical visualization and post-processing and Matlab was used to plot extracted data. It was found that it was much simpler to calculate many post-processing parameters during the analysis, than to attempt to calculate them after the analysis using the exported data. Therefore, a UDF was written that ran at the conclusion of each timestep and automatically logged several variables of interest. This code, along with all other UDFs, is given in Appendix B.

3.2.2 Mesh Convergence Study

A mesh convergence study was conducted to determine the optimal mesh sizing. Information about the analysis setup is given in Table 3.4. The domain was a 1.4 mm diameter hemisphere and a 1 mm diameter hemisphere centered on the beam was meshed with 6 different element sizes, which are given in Table 3.5. Spot melting was chosen as a test problem because it includes many of the thermal and flow features seen in larger analyses, but had a smaller computational cost than the larger analyses. After 250 μs of heating, the maximum velocity, maximum temperature, and meltpool radius were calculated. These three parameters were chosen because they capture the

ability to solve the temperature and flow fields, and are similar to the mesh convergence criteria used in the literature, e.g. Jamshidinia et al. [74].

Table 3.4: Analysis setup for mesh convergence study

Domain	
Geometry	1.4 mm diameter hemisphere
Time	250 μs
Boundary and initial conditions	
Initial temperature	1000 K
Outer face	Adiabatic
Top face	Evaporation, radiation, and Marangoni stress
Interior	1 layer (50 μm) of powder, remainder solid
Beam Parameters	
Power	660 W
Spot time	250 μs
FWHM diameter (d_B)	350 μm
Scanning speed (v_s)	0 m/s
Solver settings	
Timestep (Δt)	1 μs
Mesh size – beam region	See Table 3.5
Mesh size – outer region	100 μm
Fine region diameter	1000 μm
Element type	Unstructured tetrahedral

The results of the mesh convergence study are given in Fig. 3.10. Maximum temperature and velocity do not seem to reach a steady state value, while meltpool radius is very consistent, with the deviation being less than the size of a single element. The cause of this behavior is unclear in both cases. One possible issue is that a single, or small group of, elements near the center of the beam has a significantly higher temperature and velocity than the rest of the domain, effectively acting as a singularity. Ideally the mesh would be refined such that any such behavior is distributed over a large group of elements, but given the extremely high thermal gradients this may not be computationally practical. Furthermore, the independence of meltpool radius compared to maximum temperature and velocity suggests that further resolution of these highly

Table 3.5: Mesh sizes for convergence study

Beam region mesh size (μm)	Total elements
20	375,483
22.5	273,592
25	206,022
30	127,993
40	60,270
50	33,653

local phenomena is not necessary to capture the global behavior. Based on these inconclusive results, the 20 μm mesh size was adopted.

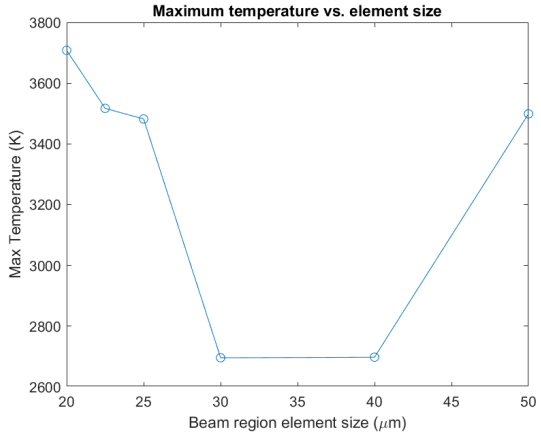

(a) Maximum temperature

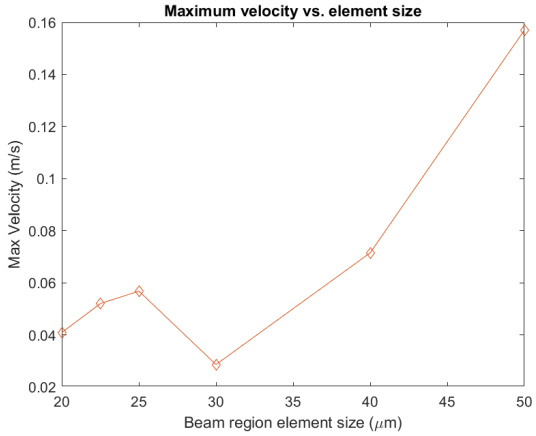

(b) Maximum velocity

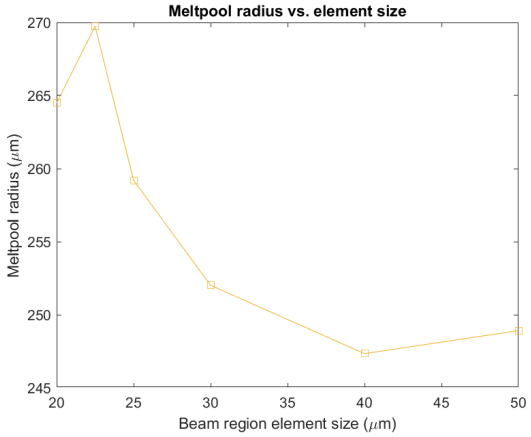

(c) Meltpool radius

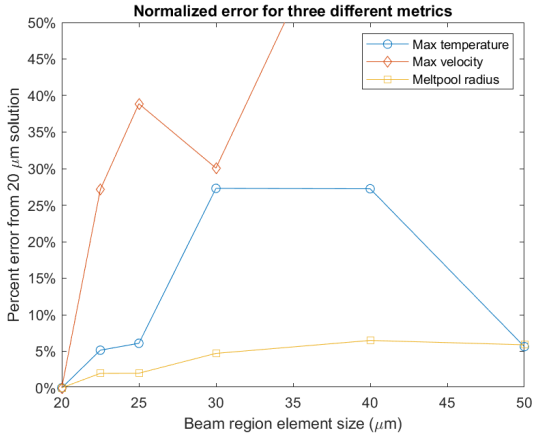

(d) Percent error compared to 20 μm mesh

Figure 3.10: Comparison of mesh convergence study results

3.2.3 Mushy Zone Constant Study

In order to assess the effects of changing the mushy zone constant (A), a study was conducted using the same spot melting problem. The setup is identical to that given in Table 3.4, except that the mushy zone constant was changed between four different values: 10^4, 10^5, 10^6, and 10^7. The same criteria were used: maximum temperature, maximum velocity, and meltpool radius. The results are given in Fig. 3.11d. There is no variation in any of the metrics for the three criteria measured. This suggests that the flow is essentially independent of the mushy zone constant. A similar study could not be found in the literature and very few authors report the value that they used. Kidess et al. used a value of 10^6 in laser welding and the default value in Fluent is 10^5. Therefore, the default value of 10^5 will be used for all other analyses, as this study does not indicate any changes due to using a non-default value.

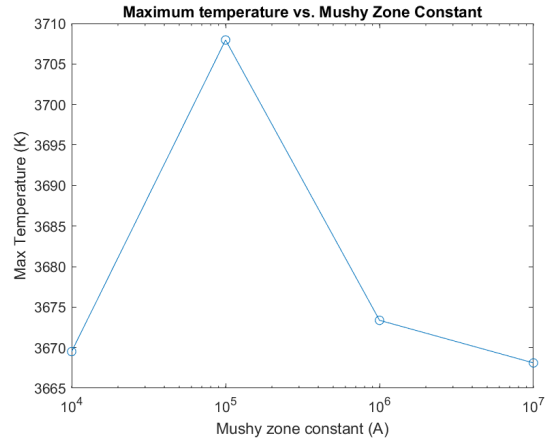

(a) Maximum temperature

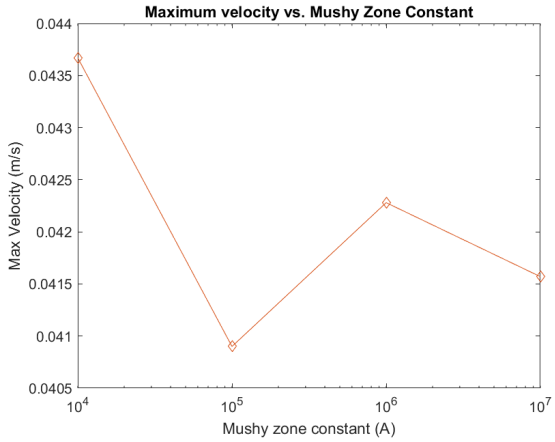

(b) Maximum velocity

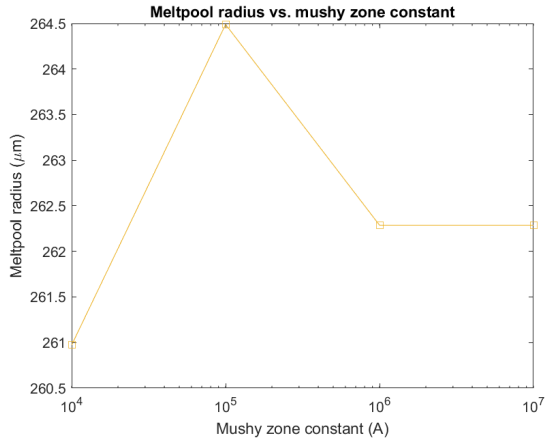

(c) Meltpool radius

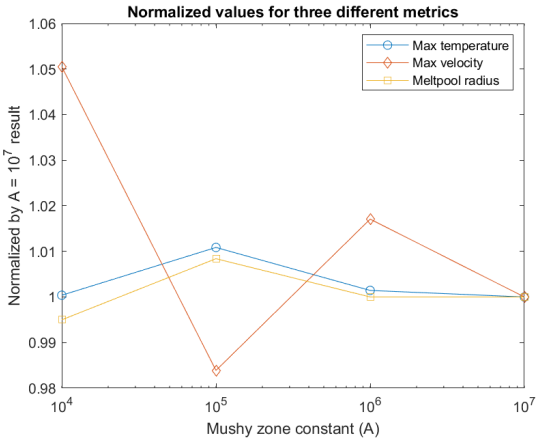

(d) Metrics normalized by $A = 10^7$ solution

Figure 3.11: Comparison of mushy zone constant study results

3.2.4 Simulated Line Build

The line build experiment described in Sec. 3.1.1 was replicated in order to assess the accuracy of the predicted meltpool size. The analysis parameters are given in Table 3.6. Sketches of the domain are given in Figs. 3.12 and 3.13. The analysis was conducted using a solid bed with 1 layer of powder on top and a fully powder bed, and with a continuous contour beam mode and a spot melting beam mode, for a total of 4 cases. In all cases, the same mesh and solver settings were used. The beam power, 660 W, and FWHM diameter, 350 μm, were also kept constant. In the contour melting case, the scanning velocity was calculated to be approximately 900 mm/s based on Eq. (2.1) from Price et al. [15]. For the spot mode, the spot spacing was assumed to be 375 μm based on experimental measurements of the samples given in Sec. 4.1.2. A relationship for the spot dwell time could not be found, so instead the dwell time was calculated such that the contour and spot builds would take the same amount of time. This resulted in a dwell time of 888 μs. A graphical comparison between the two beam modes is given in Fig. 3.14. An isometric view of the mesh is given in Fig. 3.15.

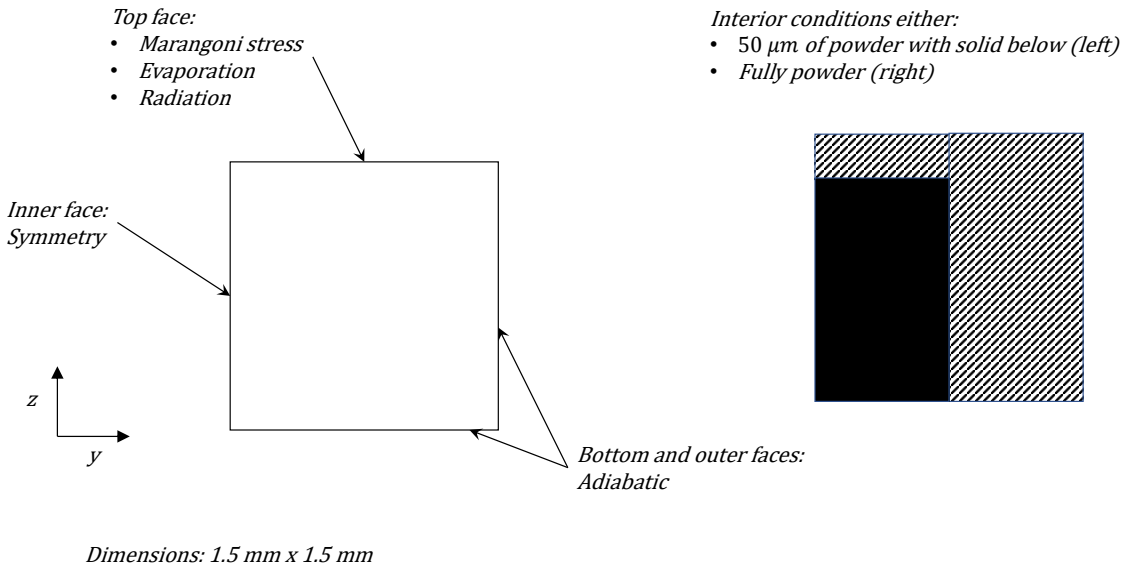

Figure 3.12: Sketch of cross-section of domain and various boundary and initial conditions (not to scale)

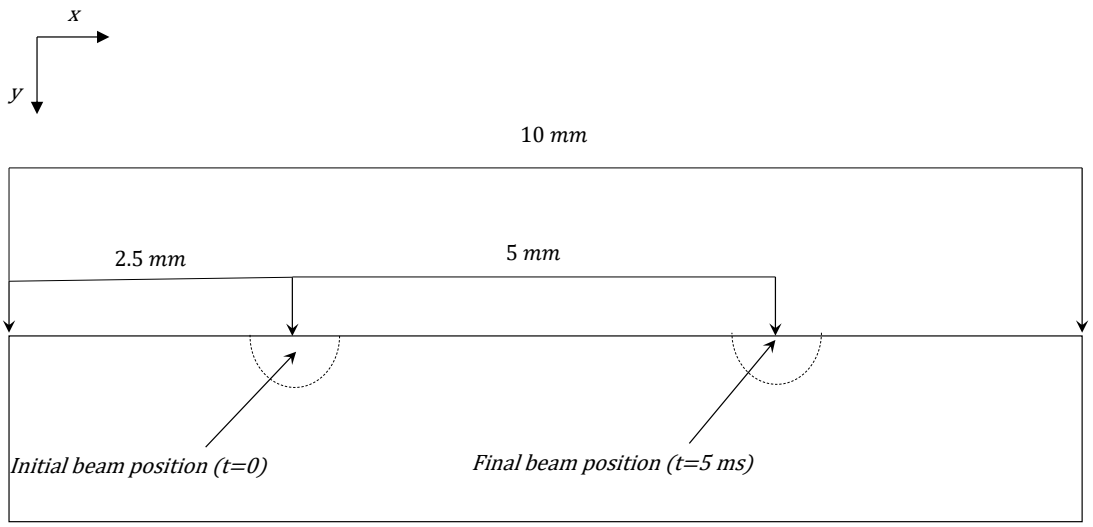

Figure 3.13: Sketch of plan view of domain and dimensions (not to scale)

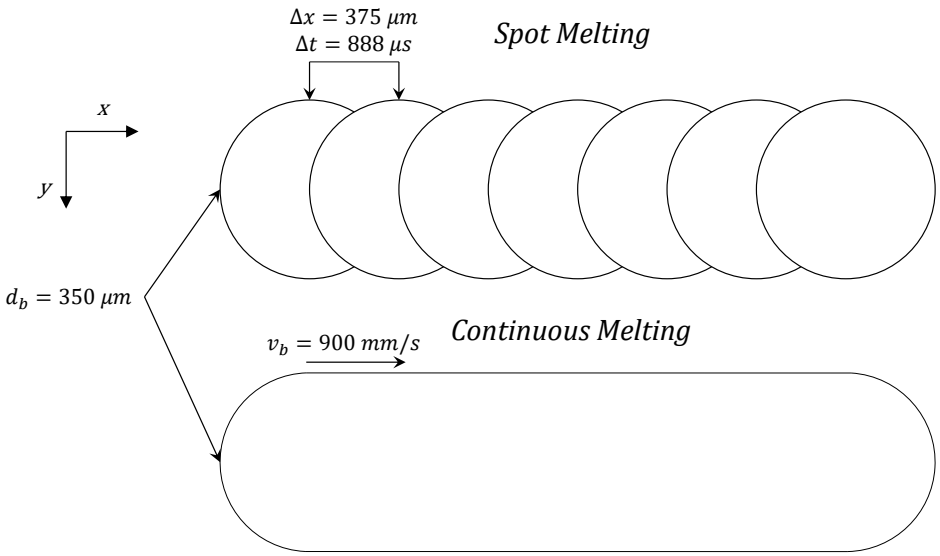

Figure 3.14: Comparison of continuous versus spot melting (not to scale)

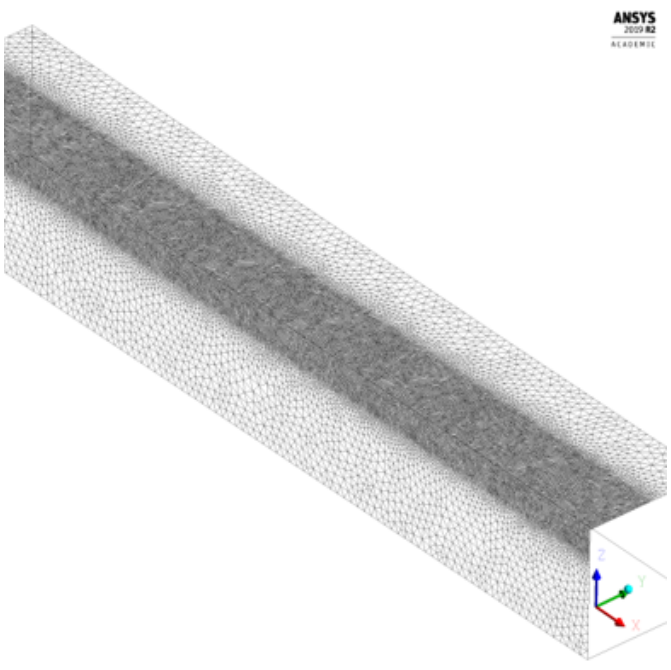

Figure 3.15: Mesh for line build simulations

Table 3.6: Analysis setup for simulated line build study

Domain	
Geometry	10 mm long x1.5 mm wide x 1.5 mm tall
Time	5000 μs
Boundary and initial conditions	
Initial temperature	1000 K
Top face	Evaporation, radiation, and Marangoni stress
Inner face	Symmetry
Other faces	Adiabatic
Interior – solid bed	1 layer (50 μm) of powder, remainder solid
Interior – powder bed	Entirely powder
Beam Parameters	
Power	660 W
FWHM diameter (d_B)	350 μm
Contour mode – velocity (v_s)	900 mm/s
Spot mode – dwell time	890 μs
Spot mode – spacing	373 μm
Solver settings	
Timestep (Δt)	1 μs
Mesh size – beam region	20 μm
Mesh size – outer region	100 μm
Fine region dimensions	500 μm in y x 250 μm in z
Element type	Unstructured tetrahedral

3.2.5 Summary of Fluent Model

As in any numerical work, many assumptions are explicitly and implicitly made in order to reduce the number of unknowns and make the problem more tractable. The key assumptions made in this work are:

- The powder bed was approximated as a homogeneous continuum
- The effects of thermal expansion and buoyancy were assumed to be negligible
- Thermal conductivity of the powder bed below T_{dens} was assumed to be 7.5% of the bulk solid
- The powder bed was assumed to densify above $T_{dens} = 1778K$
- The meltpool was assumed to be laminar
- Recoil pressure due to evaporation was assumed to be negligible
- The top of the meltpool surface was assumed to be flat

Of these assumptions, by far the most significant is the approximation of the powder bed as a homogeneous continuum. Modeling the powder bed as a continuum necessitates many more assumptions in order to properly handle all of the thermal and physical properties in a manner that is both physically accurate and numerically tractable. Particle scale modeling is currently too numerically difficult and expensive to implement and therefore the continuum approximation must be made. Wherever possible, experimental data was used to validate the continuum model, but for many properties this was not possible and assumptions had to be made. In particular, there is no experimental data or theoretical model to describe the behavior of the powder as it reaches the melting point.

A high-level flowchart of the solution procedure is given in Fig. 3.16, based on a similar flowchart given in the Fluent Theory Guide [70].

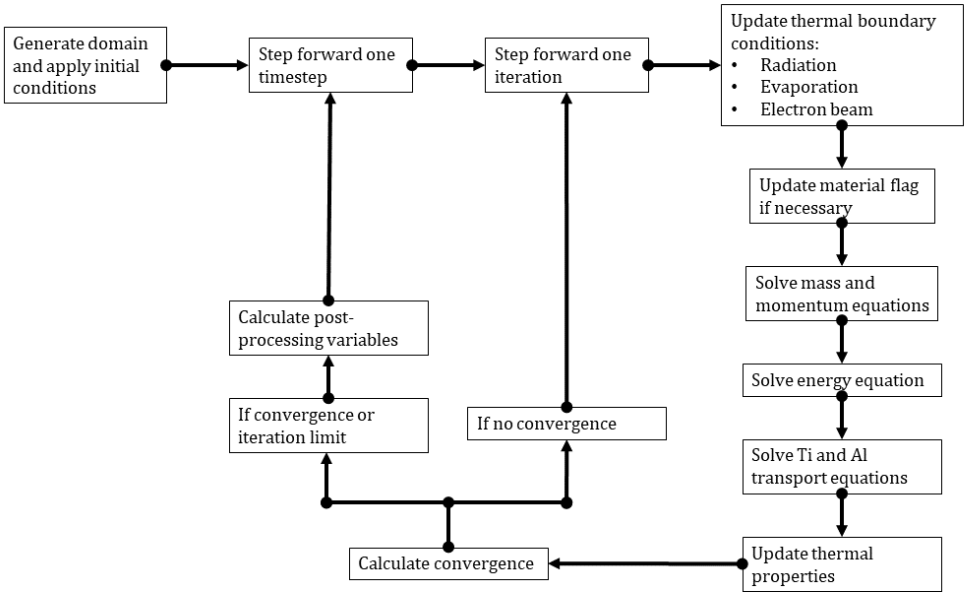

Figure 3.16: Flowchart of solution procedure

Chapter 4

Results

4.1 Experimental Results

4.1.1 Temperature Measurement Results

These results were obtained using the ND2 filter, a 50 mm lens (F = 1.8) and 20 mm lens extender, and the calibrations given in Fig. 3.6. The distance from the camera to the center of the baseplate was measured after removal of the build and was found to be 80 cm, resulting in a FOV of approximately 110 x 124 mm and a pixel size of 240 x 339 μm. Images were captured using two different integration times, 2ms and 15ms, and the results respectively are given in Figs. 4.1 and 4.2. In both cases, three images are given: the raw counts as directly measured by the camera, with no calibration applied; the work calculated based on the furnace calibration; and finally, the temperature calculated based on the vacuum emissivity and ambient temperature of the EBM process.

The full range for counts is between 0-16,383, and according to the manufacturer's recommendation the ideal range for measurements is between 4,000-12,000, which was also qualitatively observed to be the least noisy range. The 2 ms image is between 200-800 counts, which is at the lowest range possible by the equipment, and the 15 ms image is between 500-4,000 counts, which is an improvement, but still below the desired range. The 2 ms image is also visibly significantly more noisy than the 15 ms image, which is due to the higher integration time effectively smoothing out some of the variability in the image. The work was calculated using the linear fits given in Fig. 3.4 for each integration time. This was then used to back-calculate the temperature.

With the 2 ms integration time, the temperature was measured to be 886-908 K, and in the 15 ms integration time it was measured to be 640-760 K. As these temperatures are below the ambient value of 1000 K, which is measured by the thermocouple on the baseplate, the IR camera data is incorrect and should not be trusted. The most likely cause of this error is metallization of the viewing window. Even though the build was begun with a new, unused piece of sacrificial glass in place, by the end of the build it had been metallized to be completely opaque, with a mirror-like finish. These images are likely showing the effects of partial metallization, where the signal has dropped significantly enough to obsolete the calibration but not far enough to prevent any readings at all.

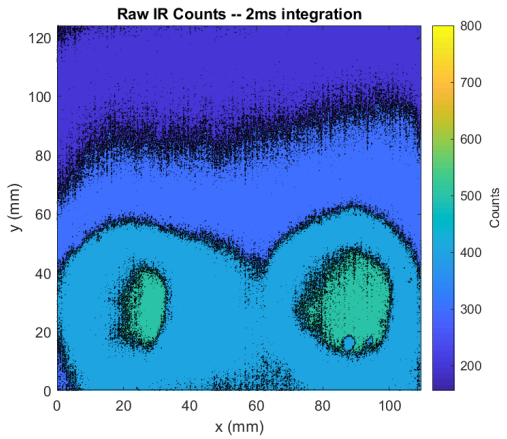

(a) Raw IR counts

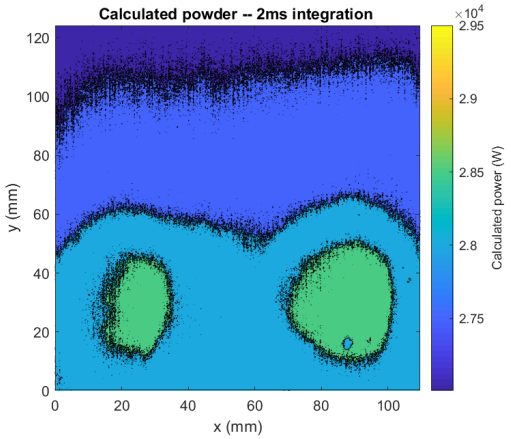

(b) Calculated work

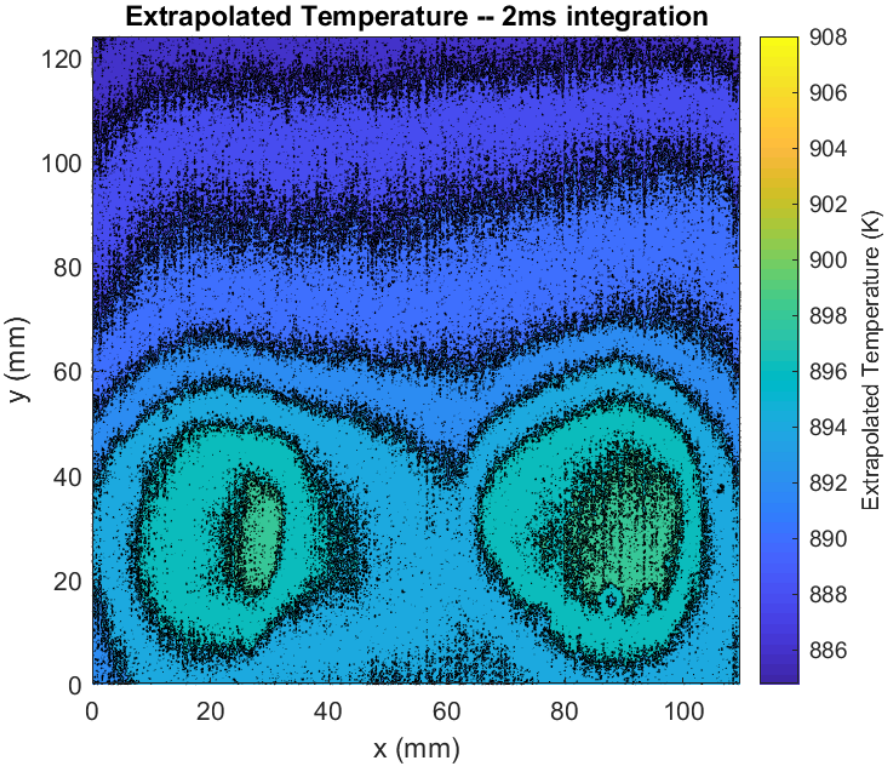

(c) Calculated temperatures under EBM conditions

Figure 4.1: Results measured using 2ms integration time

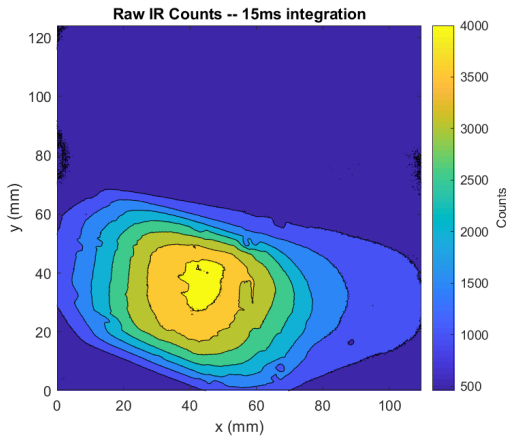

(a) Raw IR counts

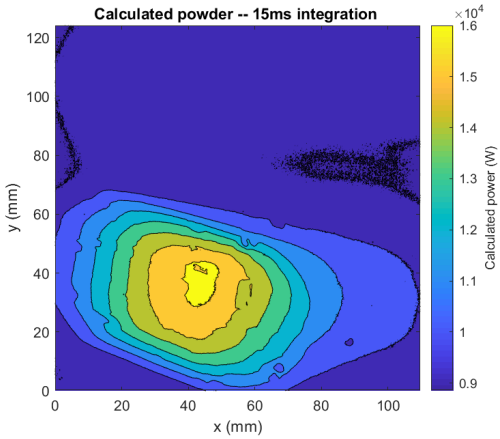

(b) Calculated work

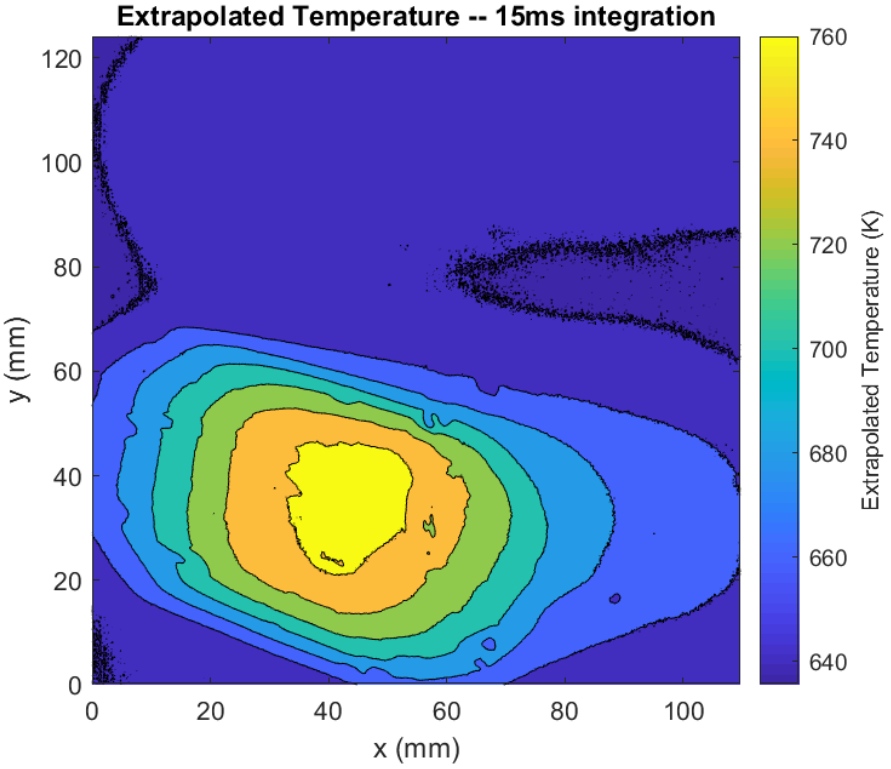

(c) Calculated temperatures under EBM conditions

Figure 4.2: Results measured using 15ms integration time

4.1.2 Line Build Results

Experimental results of the line build measurements are given in Fig. 4.3. In Fig. 4.3a, the average spot spacing is plotted for each feature in builds 1, 3, and 4. There is no clear trend in either build number or feature type, which is to be expected given that all were printed using identical process parameters. In Fig. 4.3b, the average width of each feature is plotted for each build. The cross feature from build 2 was not measured due to exceptionally poor printing quality. Build 2, which was done with continuous melting, is shorter than the spot melted builds, though both are within the standard deviation. This trend is further illustrate in Fig. 4.3c. On the x-axis, the measured length is plotted, and on the y axis the measured width is plotted. The symbol indicates which feature and the color indicates build number, and the as-designed dimensions are marked with black dashed lines. The continuously melted features are significantly longer than the as-designed dimensions while the spot melted features are significantly shorter. No clear dependency on length vs feature was observed, though there were a few outliers, in particular the line-x feature from build 3, which was almost 1 mm shorter than the average length.

Optical microscope images of builds 4 and 2 are given in Figs. 4.4 and 4.5, respectively. The difference between the continuous and spot melting is immediately obvious. In the spot melted lines, circular marks on the surface of the parts are clearly visible. The exact cause of these lines is unknown, but is hypothesized to either be the results of ripples during solidification processes or more likely caused by thermal contractions due to rapid, non-uniform heating and cooling. In some parts, areas where powder has fallen on top of the solidified features are visible, for example in the line-y (Fig. 4.4b) and line-45 (Fig. 4.4c). In the continuous melted lines, the surface is significantly more irregular and the boundaries are much less clear. No circular marks can be seen, and while a few ripples are present, they are much less clear than in the spot melted lines. In general, the quality is poorer and more variable.

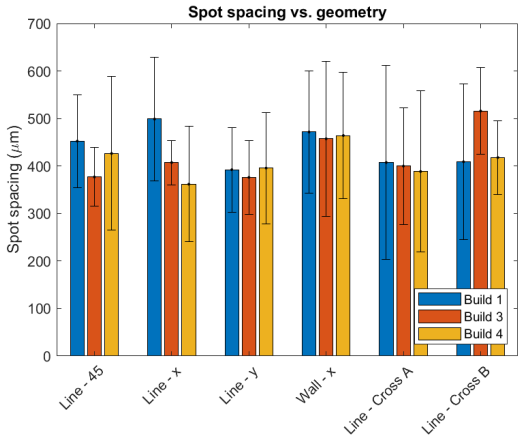

(a) Spot spacing for builds 1, 3, and 4

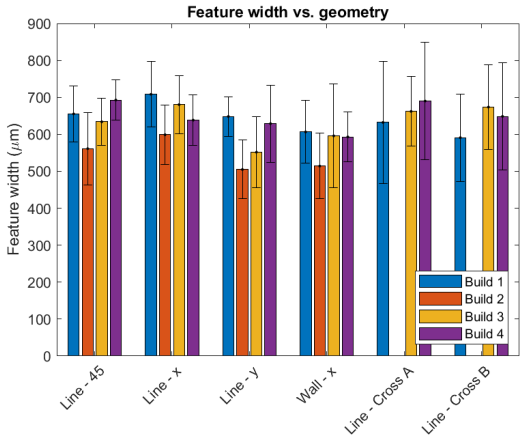

(b) Feature width compared across geometry and build

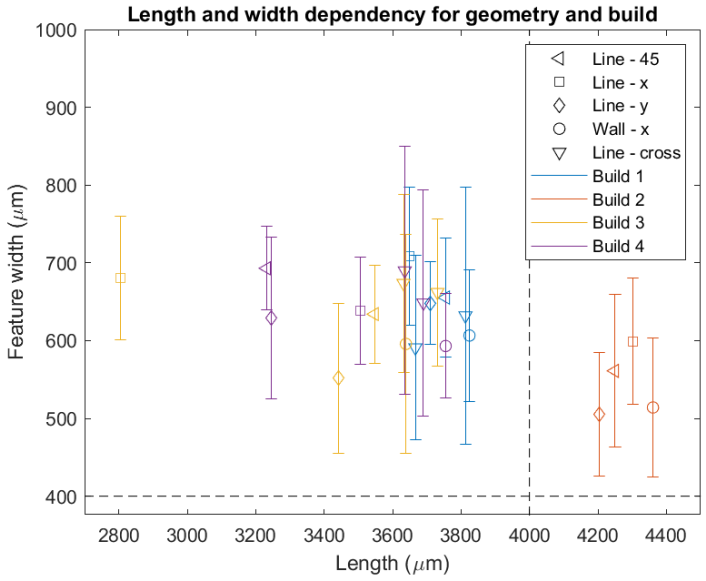

(c) Comparison between printed dimensions and as-designed dimensions (in dashed black lines)

Figure 4.3: Comparison of measured line build geometries

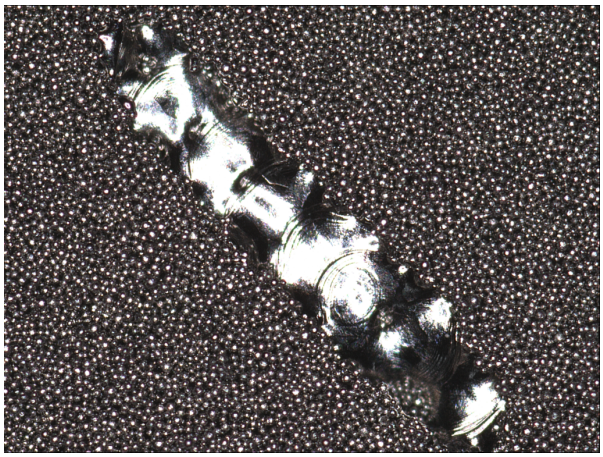

(a) Line - x direction

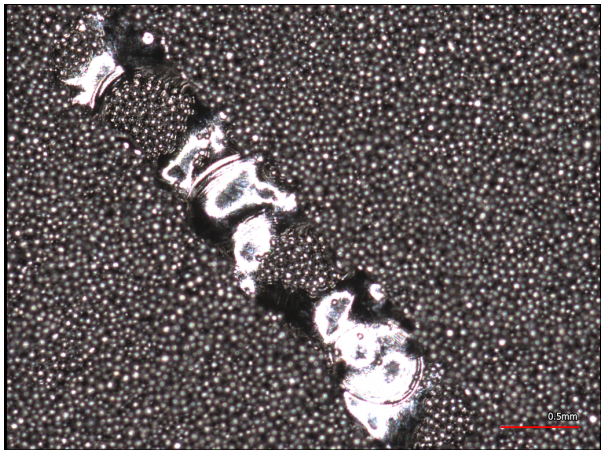

(b) Line - y direction

(c) Line - 45 degree direction

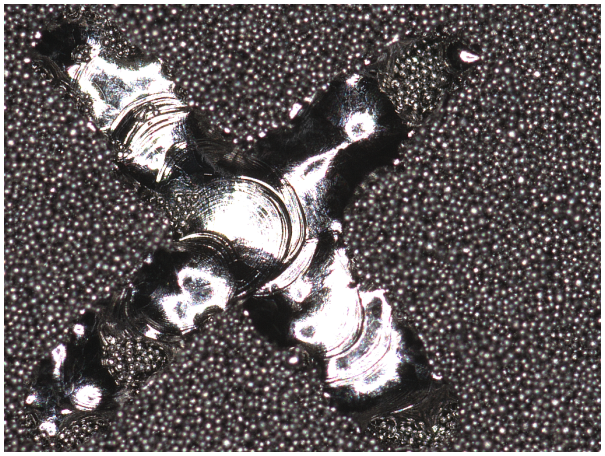

(d) Line - x-y cross

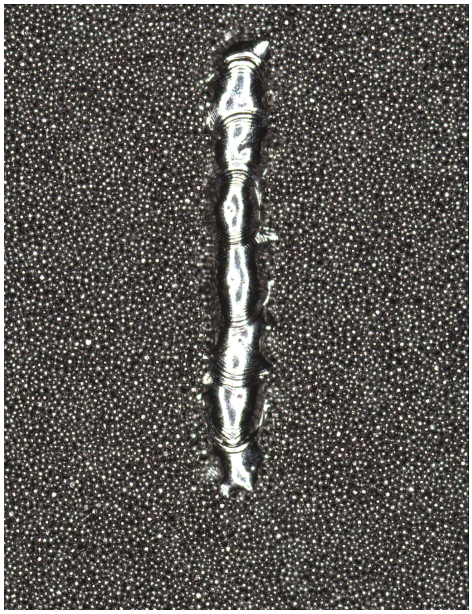

(e) Wall - x direction

Figure 4.4: 80x optical microscope photos of build 4

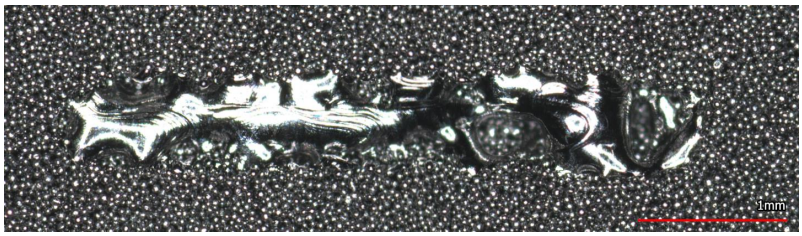

(a) Line - x direction

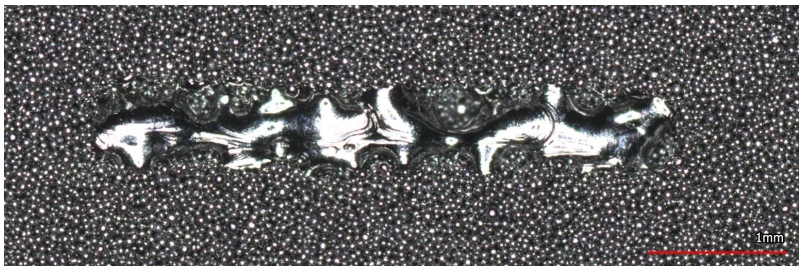

(b) Line - y direction

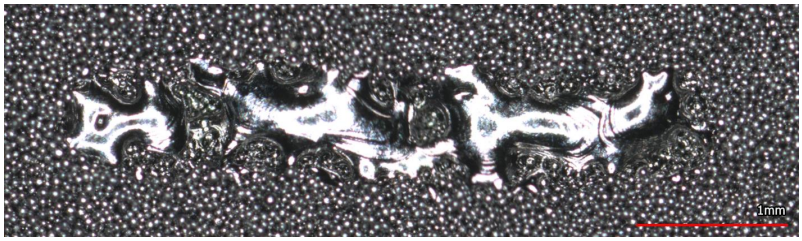

(c) Line - 45 degree direction

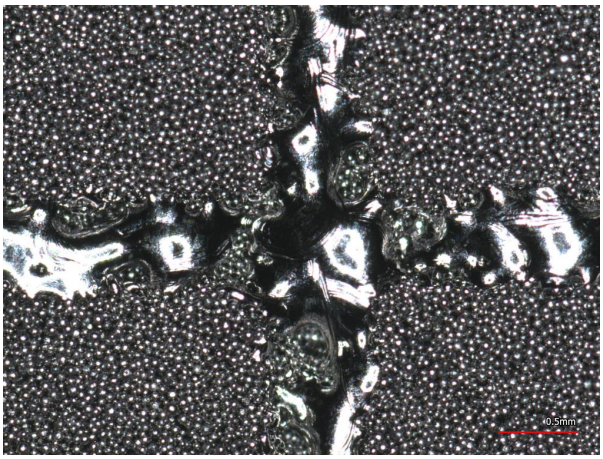

(d) Line - x-y cross

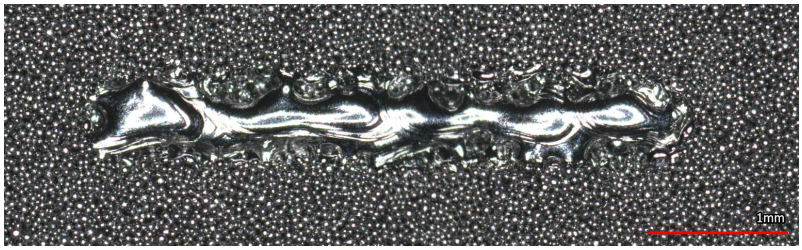

(e) Wall - x direction

Figure 4.5: 80x optical microscope photos of build 2

4.2 Numerical Results

4.2.1 Line Build Topology

The simulated and experimental line build widths are given in Fig. 4.6. In both the simulated and experimental cases, there is no significant difference between the wall and line features. This is surprising, as the higher thermal conductivity present in the wall feature is expected to greatly increase the rate at which heat is transferred out of the solidifying areas. The experimental and simulated data agrees well for the continuous melting pattern, but significantly less well for the spot melting pattern. The most likely cause of this discrepancy is process parameter differences between the spot and continuous melting patterns. Due to a lack of information about how Arcam's spot melting algorithm works, all process settings aside from beam velocity were assumed to be identical, which is likely not an accurate assumption. Unfortunately, due to a lack of direct control over process settings, it was not possible to force this behavior in the experiment.

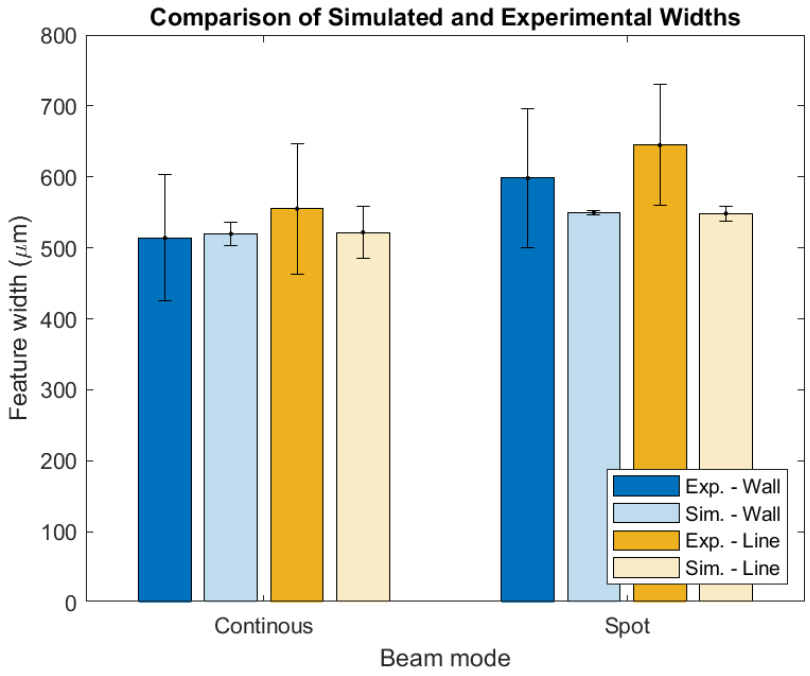

Figure 4.6: Comparison between experimental and simulated feature width

The feature width versus scanned distance is given in Fig. 4.7a. Originally, the simulation time was set to be 5 ms. However, after the continuous melting of a line feature simulation was run for 3 ms, it was found that the meltpool size very quickly reached a steady state. To save on simulation time, the resulting simulations were not run as long. Therefore, the different ending points in Figs. 4.7a and 4.7b can be ignored, as they are simply an artifact of the variable end time. In all cases, the simulation reaches a steady state width very quickly, which is in relatively good agreement with the experimental data presented above. In the spot melting patterns (blue lines), a periodic width can be seen, which is caused by the discontinuous scanning. The feature depth, which is

plotted in Fig. 4.7b, is on the order of 50-60 μm in all cases. Due to the experimental setup chosen for the linebuilds, their depth could not be measured, but based on the literature, a significantly higher depth is expected. In metal AM, due to low wetting of liquid metals, the melted depth is always higher than a single melted layer in order to reduce LOF voids [76]. Typically in EBM, the melted depth is approximately 3-4 layers thick [2].

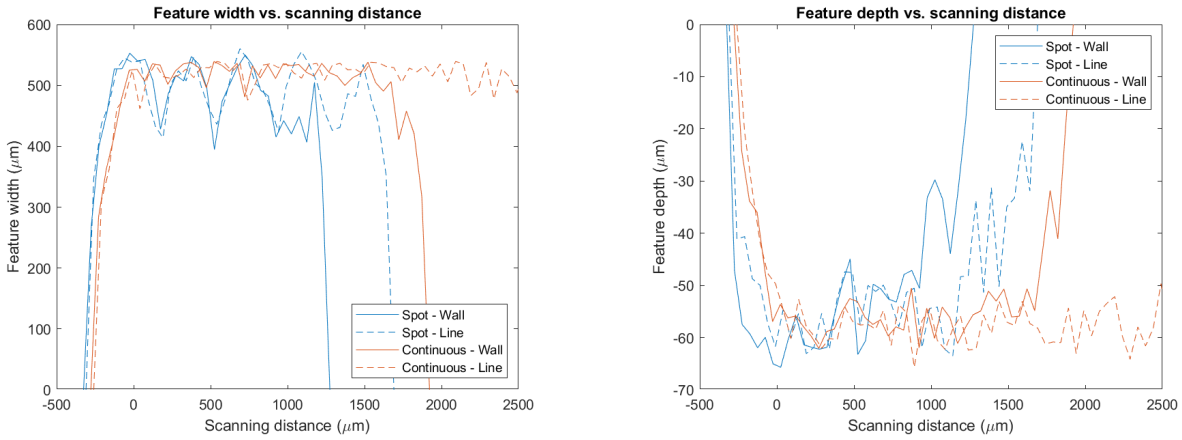

(a) Simulated feature width vs. scanning distance

(b) Simulated feature depth vs. scanning distance

Figure 4.7: Comparison of measured line build geometries

4.2.2 Meltpool Temperature and Velocity Results

The simulated difference between the powder bed and solid bed features is given in Fig. 4.8, at a time of 1.9 ms and for the continuous melting case. The powder bed case is in the upper half of each figure and the solid bed case is in the lower half. In the plan view, Fig. 4.8a, the temperature profiles agree so well that it is difficult to make out the boundary between the two simulations. There is no visible difference between the temperature in either cases, which matches the similarity in simulated and experimental line build size. In the transverse slice along the symmetry plane, Fig. 4.8b, the difference is slightly more clear, but overall both results are still highly similar.

The difference is highlighted in Fig. 4.9a, where the bounds on the contour plot have been altered such that the maximum temperature is 1100 K, a difference of only 100 K from the minimum temperature. With this difference, it is clear that the >1100 K region is significantly larger in the solid bed case than in the powder bed, due to increased thermal conductivity. The vast majority of the domain is still below a temperature of 1100 K, meaning that it has undergone essentially no thermal change from the ambient temperature of 1000 K. The thermal conductivity in both cases is plotted in Fig. 4.9b, which highlights the major difference in thermal conductivity between the bulk solid and the powder, which is assumed to have only 7.5% of the bulk conductivity. In the solid bed case, a narrow strip of powder is also visible between the existing solid bed and the newly solidified bulk material, indicating that given the extremely low melted depth, severe LOF defects would be likely.

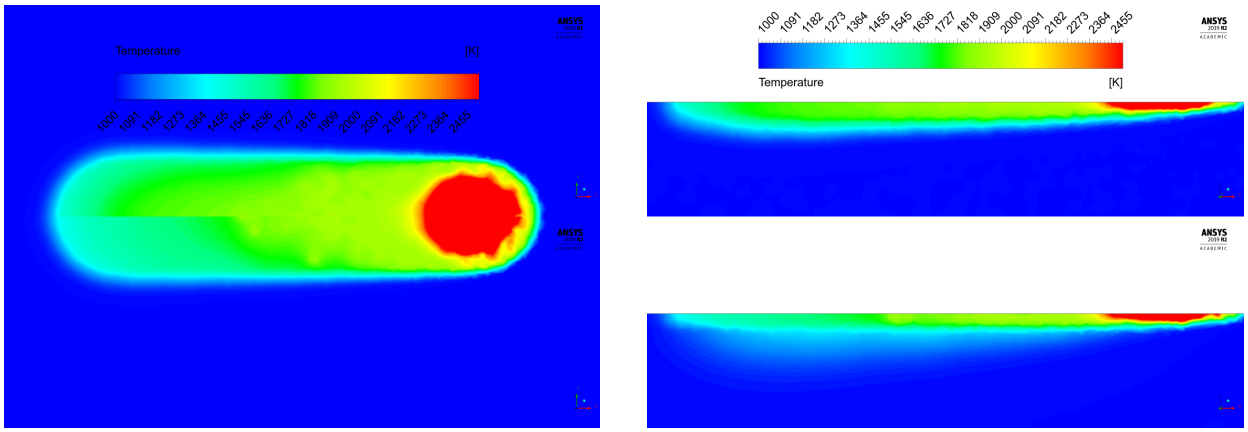

(a) Plan view of line build

(b) Transverse slice of domain

Figure 4.8: Comparison of temperature profiles between fully powder (top) and solid (bottom) domains with continuous scanning after 1.9 ms

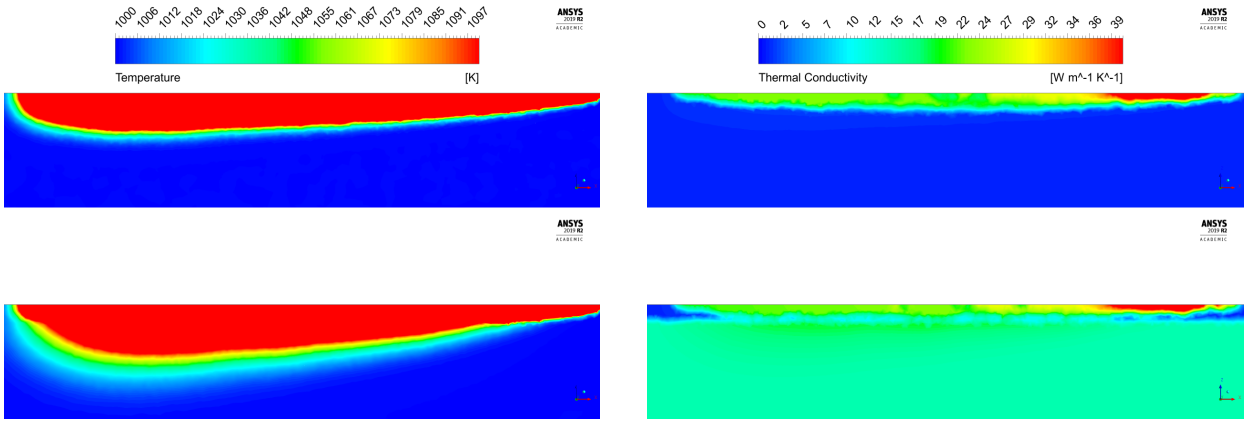

(a) Comparison of temperature distribution between 1000-1100 K

(b) Comparison of effects of bulk solid vs. powder bed thermal conductivity

Figure 4.9: Differences in low temperature regions and thermal conductivity between fully powder (top) and solid (bottom) domains with continuous scanning after 1.9 ms

The differences between the spot and continuous melting patterns are given in Fig. 4.10, at a time of 1.9 ms and in the powder bed case. The continuous melting case is located on the upper half of each figure and the spot melting case is located in the lower half of each figure. In the plan view of temperature, Fig. 4.10a, the difference between the two cases is immediately obvious. While the continuous melting case produces a smooth meltpool, the distinct outline of each spot is clearly visible in the meltpool. The beams are also not aligned in the x, which will only occur at multiples of the dwell time. In the transverse slice, there is not a significant difference between the two cases. This is because the slice is taken through the center of the domain, whereas the periodic effects of the spot melting are most apparent at the outer edge of the meltpool.

The same view and cases as Fig. 4.10a have been plotted in Fig. 4.11 but on smaller domains. In Fig. 4.11a, the temperatures in all non-powder areas have been plotted. This includes solidified

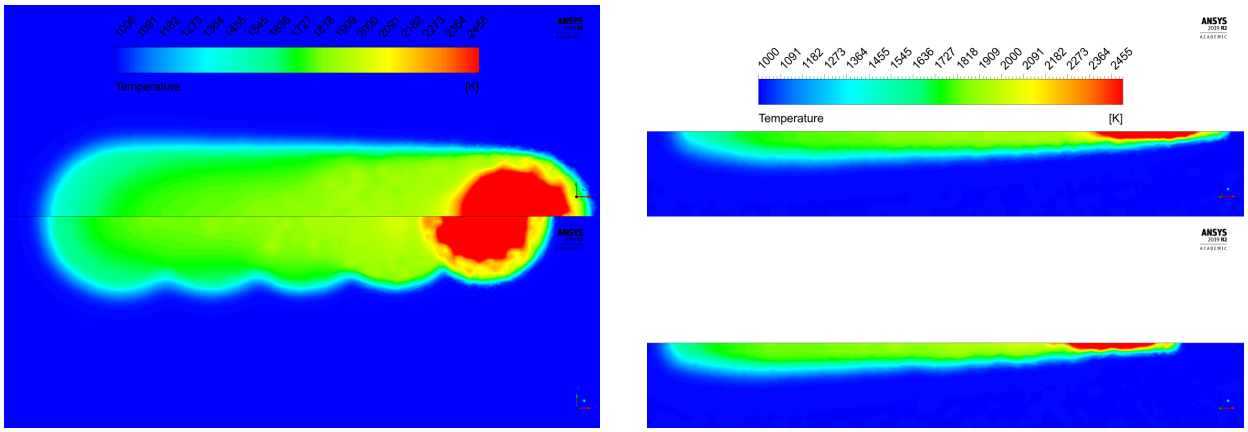

(a) Plan view of line build

(b) Transverse slice of line build

Figure 4.10: Comparison of temperature profiles between continuous (top) and spot (bottom) melting with powder domain after 1.9 ms

areas along with the mushy and liquid regions. Furthermore, the scale has been extended. In the majority of the solidified area, the temperature is still extremely high, approximately 1700-1800 K. Due to the low thermal diffusivity of the powder and the short timescale of the simulation, the heat remains in the solid and does not dissipate significantly. The mushy and liquid regions only have been plotted in Fig. 4.11b and the scale has been changed such that the minimum is the solidus temperature (1878 K). In both cases, at the center of the beam there is a region of approximately 3450 K, which very quickly drops off to approximately 2300 K around the edges of the beam.

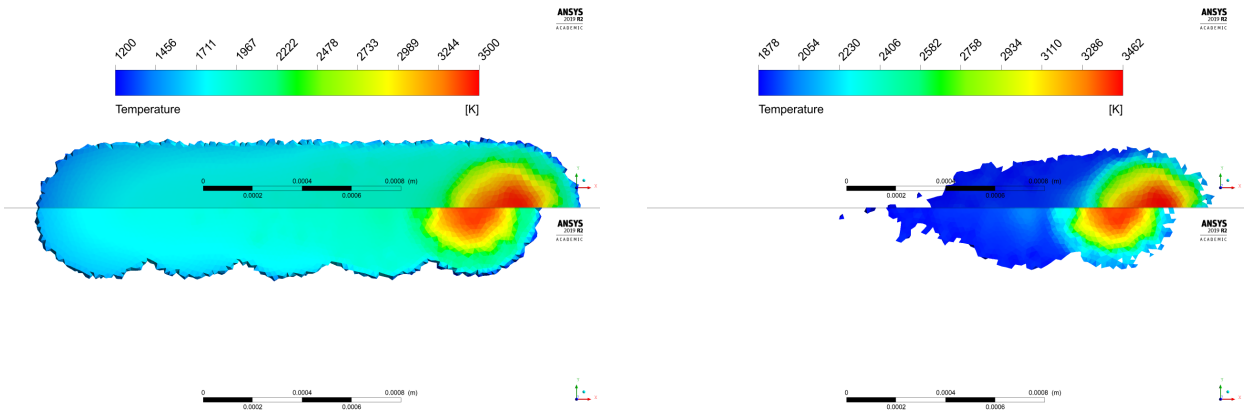

(a) Temperature contours in non-powder regions (mushy, solid, and liquid)

(b) Temperature contours in liquid and mushy regions only

Figure 4.11: Temperature profiles in solidified regions; continuous (top) and spot (bottom) melting with powder domain after 1.9 ms

A closeup of the beam region is given in Fig. 4.12, which is the same case setup and time as the above figures. In this figure, velocity vectors are overlaid on the temperature contours

from Fig. 4.11b. Due to the negative derivative of surface tension, the fluid is driven away from the center of the beam, with the velocity vectors clearly originating from the beam center. Even though the beam speed (0.9 m/s) is significantly higher than the maximum fluid velocity, there is little difference between the velocity profiles with the spot and continuous melting, with both cases having a maximum of approximately 25 mm/s. In both cases, the velocity very quickly drops outside of the beam area to values on the order of 1 mm/s. This suggests that even though convection dominates inside the beam area, outside of it, the behavior is conduction dominated.

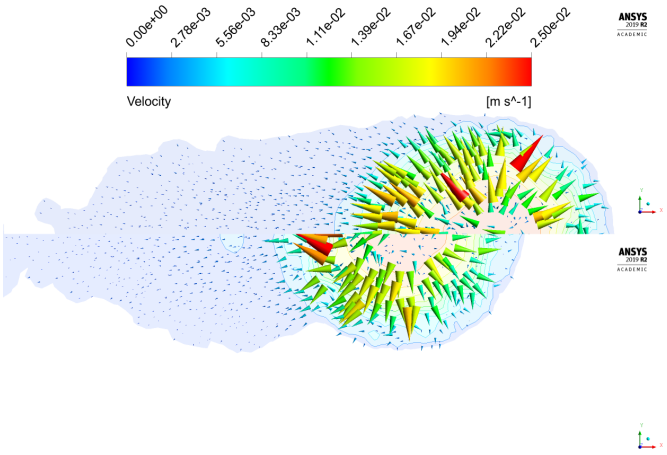

Figure 4.12: Velocity vectors overlaid onto temperature profile compared between continuous (top) and spot (bottom) melting with powder domain after 1.9 ms

4.2.3 Microstructural Results

At the time of solidification for each element, the thermal gradient and derivative were logged and used to calculate several microstructural criteria. The solidification map is from experimental work by Kobryn and Semiatin, and is plotted in Fig. 2.29. The thermal gradient ($G = \|\nabla T\|$) is given on the y axis and the solidification velocity ($R = |\partial T/\partial t| * G^{-1}$) is given on the x axis. In Fig. 4.13, the solidification data from each of the four cases is plotted onto the solidification map. The dashed line indicates the boundary between the columnar and mixed regions and the solid line indicates the boundary between the mixed and equiaxed regions. The extremely high thermal gradients, on the order of 10^6-10^7 K/m, are commonly seen in PBF and are a major reason for the complex microstructures often produced [51]. In all four cases, the mixed grain structure dominates. In particular, the vast majority of the points are clustered around a solidification velocity of 1 m/s and a thermal gradient of approximately $5e5$ K/m. The dominance of the mixed grain structure is confirmed by Fig. 4.14, which gives the volume fraction corresponding to each grain structure for all four cases. There is very little variation between case, with the average being 15% equiaxed, 74% mixed, and 10% columnar.

Based on the experimental data from Kobryn and Semiatin, the solidification map can be simplified by instead considering the ratio G^2/R. The grain structure can be calculated solely based on the value of this ratio, which simplifies the data analysis by allowing the division of the

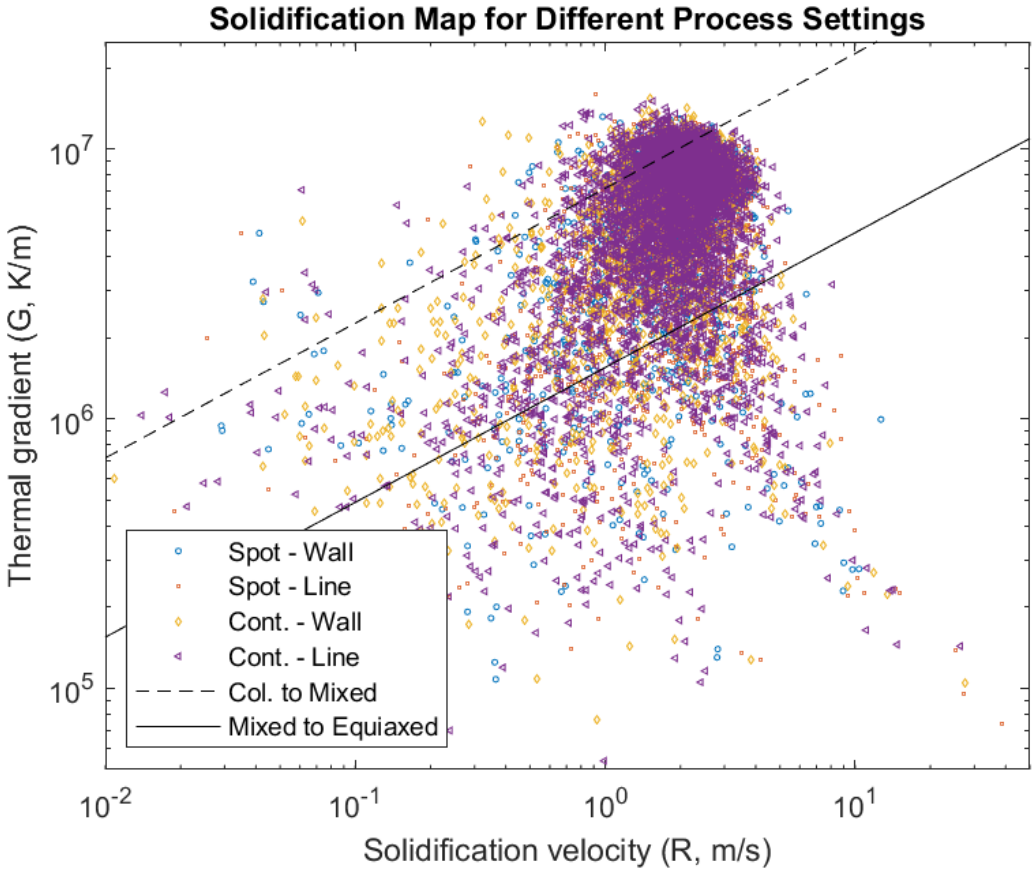

Figure 4.13: Solidification front velocity and thermal gradient compared to equiaxed-columnar data from Kobryn and Semiatin [196]

data into three categories. In Fig. 4.15, this parameter is compared versus several process and geometry characteristics in order to find any relationships that could be used to easily predict the resulting microstructure. In Fig. 4.15a, the grain structure is plotted versus solidification time. Initially, the spread of results is significantly wider, but it quickly reaches a steady state value in the mixed region. This early spread is somewhat suspect, as in theory, there should be a minimum time required for a cell to be melted and then solidified, but no minimum value is observed. This could potentially be due to a large number of elements that heated to just above the melting point and then quickly cooled or it could be indicative of a numerical issue.

In Fig. 4.15b, the structure versus distance from the scanning path is plotted. No clear trend is observed. The effects of the discretized domain are obvious here, as there is a large clustering of elements at approximately 25 μm that likely corresponds to the row of elements directly along the center of the domain. Because Fluent uses a cell-centered formulation, all post-processing data, including coordinates, is reported at the center of each element, not at the nodes. The effects of the mesh are even more apparent in Fig. 4.15c, which gives the structure versus the depth below the surface. There are three very large clusters visible that correspond to the top three layers of elements, at approximately 15, 30, and 45-50 μm. The mean of each cluster does tend to move

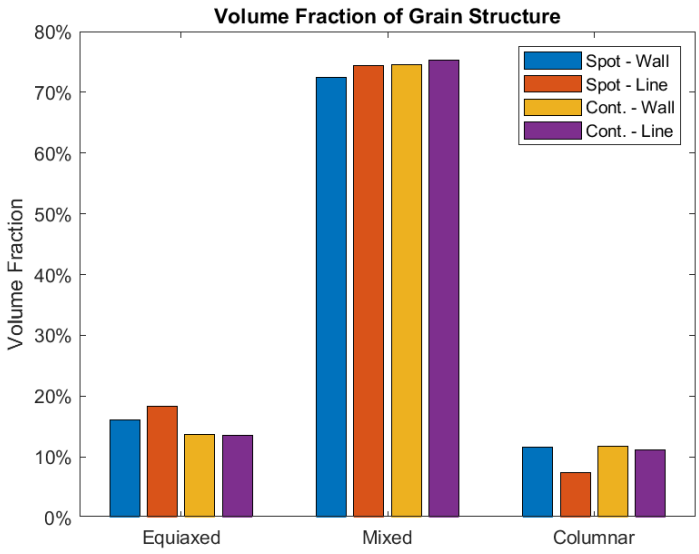

Figure 4.14: Volume fraction of each grain structure for all four cases

down over time, but due to the significant effects of mesh on this result, it is difficult to tell if it is actually indicative of a physical relationship or just a numerical artifact. For the two spot melting cases, the distance from the nearest spot melt is plotted versus structure in Fig. 4.15d. There is no significant relationship in either the powder bed or the solid case.

In order to understand the effects of meshing parameters on the predicted microstructure, the volume of each element versus its grain structure was plotted in Fig. 4.16a. There is no significant relationship between element volume and microstructure. The distribution is in line with the overall distribution of solidified elements, which is given in histogram form in Fig. 4.16b. This is only an approximate measure of the effects of the mesh on the microstructure and ideally a sensitivity test would be conducted using various mesh sizes, similarly to what was done in Section 3.2.2.

The martensitic α' phase forms when the cooling rate is greater than 410 K/s and starts above the martensitic start temperature of approximately 850-1050 K. Since the entire region of interest in this analysis meets the second criteria, the focus instead is on the first criteria, cooling rate. Cooling rate is plotted versus solidification time in Fig. 4.17. In all cases, the cooling rate is several orders of magnitude higher than the martensitic formation rate, indicating that a heavily martensite structure will be formed.

Due to the significant difference between the melting point of Al (933 K) and Ti-6Al-4V (1878 K), there is significant preferential evaporation of Al. This can lead to compositional changes, and if extreme, can result in microstructural differences. The compositional difference between the continuous and spot melting process is shown in Fig. 4.18, with both simulations being with a powder domain and at a time of 1.9 ms. The continuous melting case is in the upper half of the figure and the spot melting case is in the lower half of the figure. In the continuous melting case, there is an evenly distributed region of low Al, while in the spot melting case, the center of each spot has a significantly lower concentration of Al. It is worth noting that the overall change

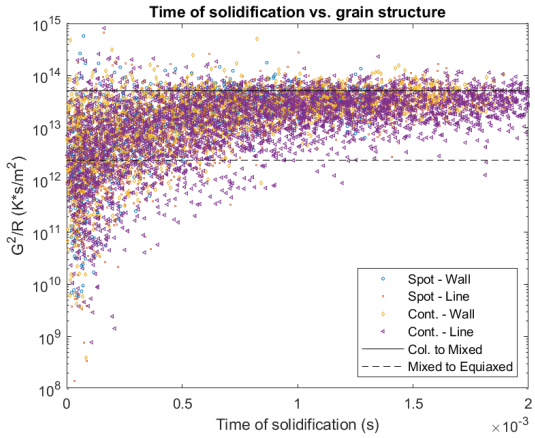

(a) Effects of time of solidification

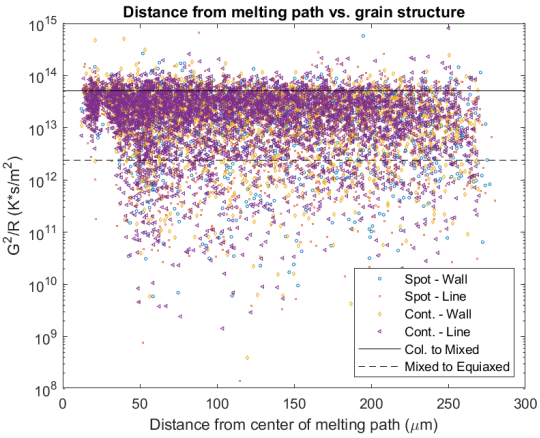

(b) Effects of distance from center line of geometry

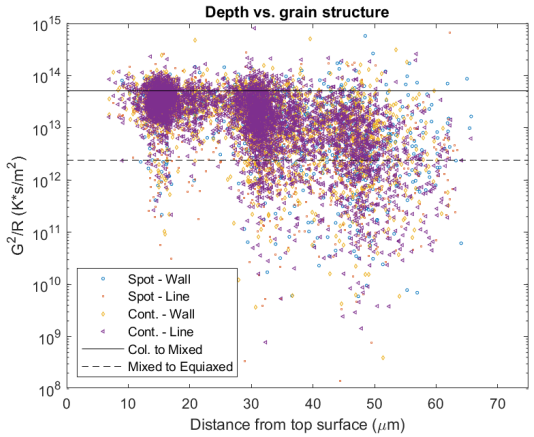

(c) Effects of depth below surface

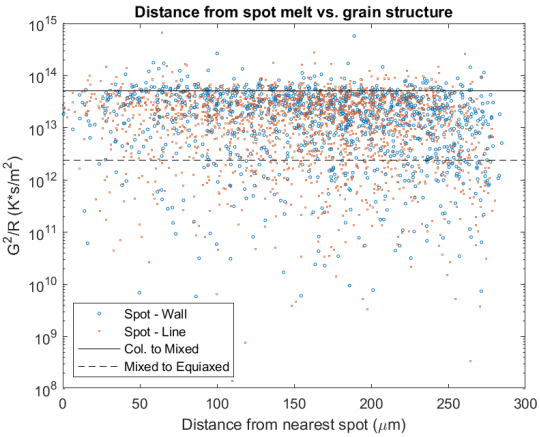

(d) Effects of distance from nearest spot melting location

Figure 4.15: Sensitivity of grain structure vs. various parameters, based on experimental data from Kobryn and Semiatin [196]

is relatively small, the minimum being a value of only 5.95%, which is a relative change of less than 1%. This is because any given area spends very little time in the liquid state, at most on the order of 1 ms.

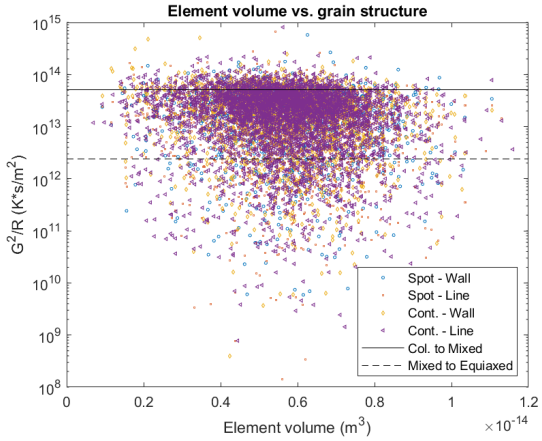

(a) Effects of element volume on predicted microstructure

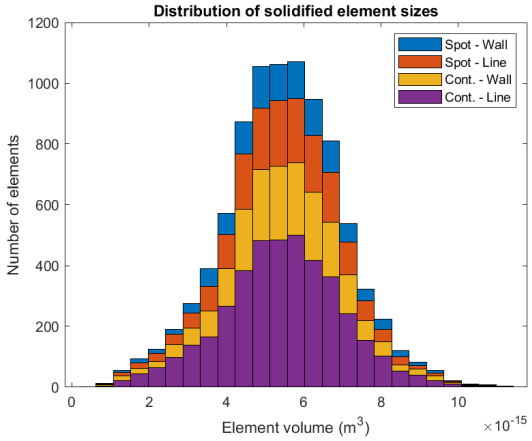

(b) Distribution of solidified element sizes

Figure 4.16: Element size dependency of solidification results

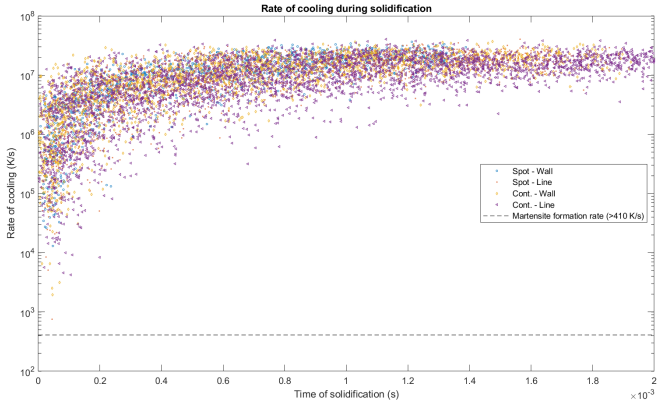

Figure 4.17: Cooling rate during solidification compared to α' formation rate (410 K/s)

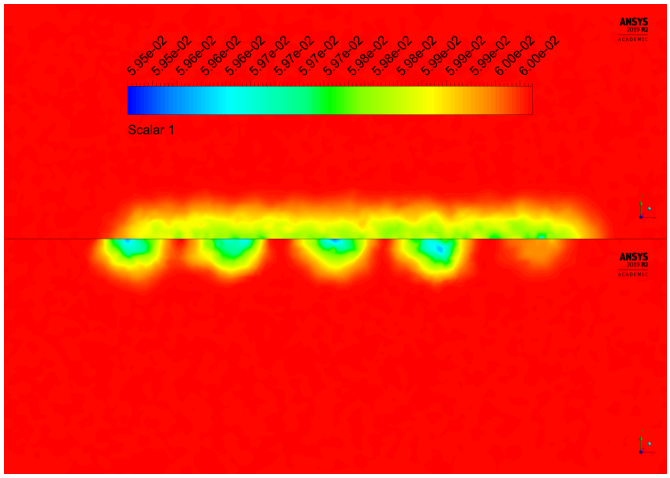

Figure 4.18: Al concentration difference between continuous (top) and spot (bottom) melting with powder domain after 1.9 ms

Chapter 5

Discussion

5.1 IR Camera Measurements

While the IR camera was successfully calibrated and an optimized optical stackup was found, metallization prevented the gathering of any useful data. Naively applying the calibration results in calculated temperatures below the ambient temperature. A new experimental method must be developed to account for the metallization. The Chou group, which uses a very similar experimental setup, based their calibration on taking measurements through glass of known metallization and then measuring the signal drop, which is shown in Fig. 5.1a [43]. They also performed a calibration based on assuming the temperature of the meltpool to be the liquidus temperature and using that as a fixed reference to calculate transmission loss. Unfortunately, they do not provide enough data on their first calibration method for it to be re-implemented and their second calibration method is of questionable accuracy. There are two possible methods to account for the effects of metallization.

The first is to develop an empirical correlation on the signal loss. A likely more accurate, but slower method, would be to deliberately expose windows to a known amount of metallization and then remove them and measure the transmission loss against the calibration source, essentially replicating the process from the Chou group that is shown in Fig. 5.1a. A less accurate but significantly quicker method would be to print a feature of consistent geometry, for example a tall, narrow cylinder, and measure the temperature over time. Based on the assumption that the melting process should be relatively constant with regards to height, the signal degradation over time could then be measured. These two methods are by no means mutually exclusive, and probably best be used as checks against each other The amount of metallization would be too difficult to calculate in closed form, but an empirical correlation between melted area and amount of metallization would likely be possible. Vapor pressure is highly non-linear with respect to temperature, and evaporation from the solid state, even for Al, is negligible.

The second method to account for metallization would be to build a device that continuously feeds Kapton film across the glass and keeps the window free of any metallization. This is the approach taken by Boone et al. and Dinwiddie et al. [22, 41]. A schematic of the design from Dinwiddie et al. is shown in Fig. 5.1b. While this type of device is mechanically simple, there are a number of design challenges. It must be able to endure the vacuums and high temperatures present during EBM. It must also be mounted on the door of the machine, unlike the previous

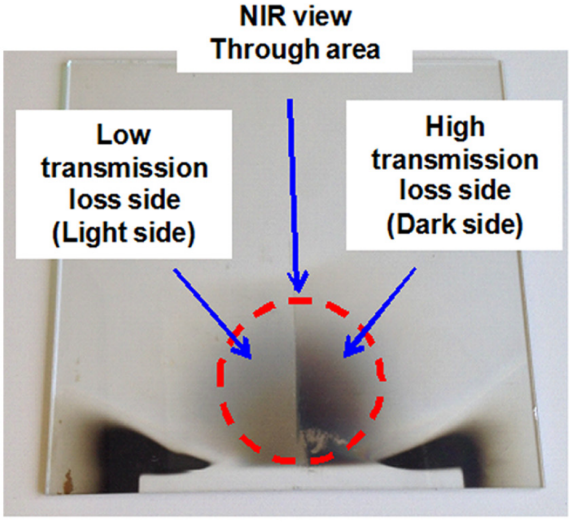

(a) Metallized glass signal loss correction [43]

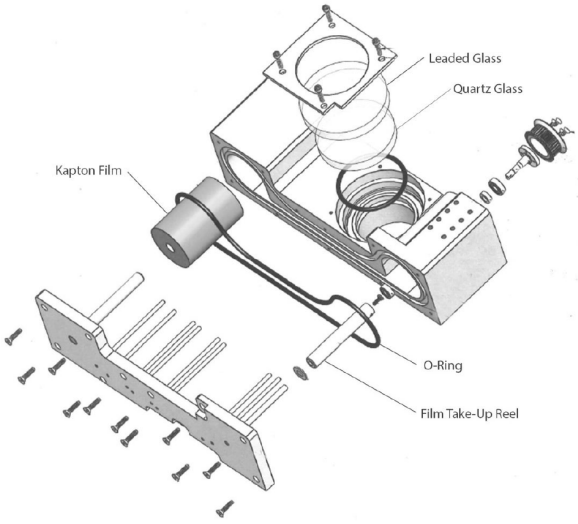

(b) Schematic of Kapton film system [22]

Figure 5.1: Potential methods to account for IR signal change due to metallization

groups, who used a top-mounted camera and therefore had a static mounting point. None of these obstacles are by any means insurmountable, but they serve to increase the cost and difficulty of implementing IR measurement.

Another issue which is of secondary importance but still could be improved is to have a more accurate calibration and to properly account for the effects of spectral dependency. In particular, using a blackbody source of known emissivity, rather than an arbitrary piece of scrap, would allow for a more accurate calibration. The maximum temperature of the furnace used for calibration was 1200 K, which is significantly below the regions of interest. Using a heat source that can reach the desired temperatures and is under an inert or vacuum atmosphere in conjunction with a better quality blackbody would be ideal. The spectral dependency of emissivity and transmission losses was also neglected during the calibration, which was necessary due to limited literature data and experimental resources but ideally should be included in the calibration as well.

In a sense, it is fortunate that the results from the IR camera were so blatantly incorrect. If the error had been smaller, say on the order of 50-100 K instead of >500 K, then the effects of metallization may have gone unnoticed. Metallization is by no means an unsolvable problem. One issue that was not covered in this work is the optimization of the temperature window. All IR cameras found in the literature review have at most a range of 500-750 K and a similar effect was found in the calibration of the FLIR A6261 camera. This is due to inherent limitations in IR sensing technology and cannot be avoided. Through clever choice of filters, lenses, and software settings, this window can be shifted, but not extended. Depending on the features of interest that are desired to be captured, the optimal window must be determined.

This work laid much of the groundwork for in situ temperature measurement, but more work must be down to get usable data. While the Kapton film system approach offers much greater accuracy, it also requires much greater resources and time to implement. Given the simplicity of developing a calibration factor, that should be purused first, as it requires very little time or

resources. In the mean time, the Kapton film system can be designed and it can be implemented, if the glass calibration factor is found to be of insufficient accuracy.

5.2 Simulated and Experimental Line Builds

A comparison between the experimental and simulated results from this work and results from the literature is given in Figs. 5.2 and 5.3. Simulated results are given using solid markers and experimental results are given using hollow markers. In order to allow for comparison across a variety of process parameters, the dimensions have been plotted as a functions of line energy, which is given by Eq. (2.2). By no means does this account for all the changes in process parameters, but it is a useful correlation. The feature width, which is given in Fig. 5.2, from this work is in good agreement with the results from the literature, particularly Riedlbauer et al. and Jamshidninia et al. The measured and simulated widths of Galati et al. are significantly less than those from this work and Riedlbauer et al. for similar line energies, but that may be because Galati et al. significantly deviated from the basic process parameters [152]. The feature depth, which is plotted in Fig. 5.3, agrees with the previous conclusion that this model significantly underpredicted depth. The only experimental results are from Jamshidinia et al., who found depths of approximately 2.8x layer height, which is in good agreement with the commonly given rule of thumb of 3-4x layer height [2]. The cause of the severe underprediction of depth in this model is unknown and will be discussed in more depth in the following section.

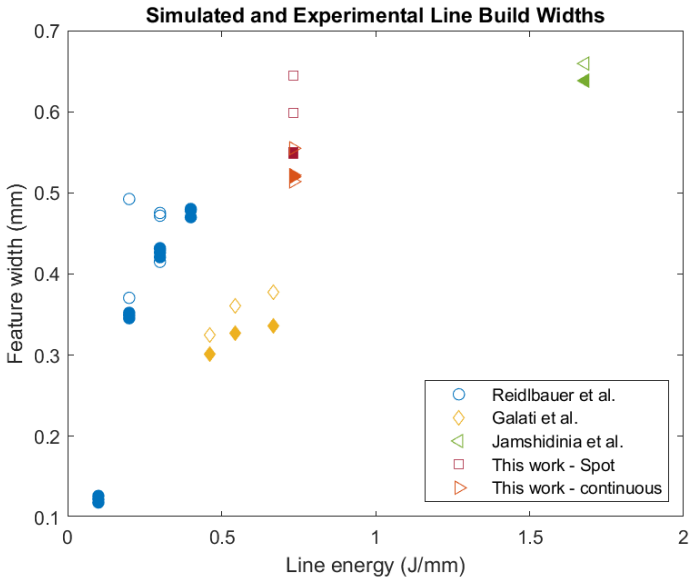

Figure 5.2: Comparison between simulated (shaded) and experimental (outline) feature width data from this work, Galati et al., Riedlbauer et al., and Jamshidinia et al. [74, 148, 152]

A visual comparison of experimental results from this work, Galati et al., and Jamshidinia et al. is given in Fig. 5.4. Note that these figures are not to scale with each other, but are only approximately sized. The continuous and spot results from this work and Galati et al. are in

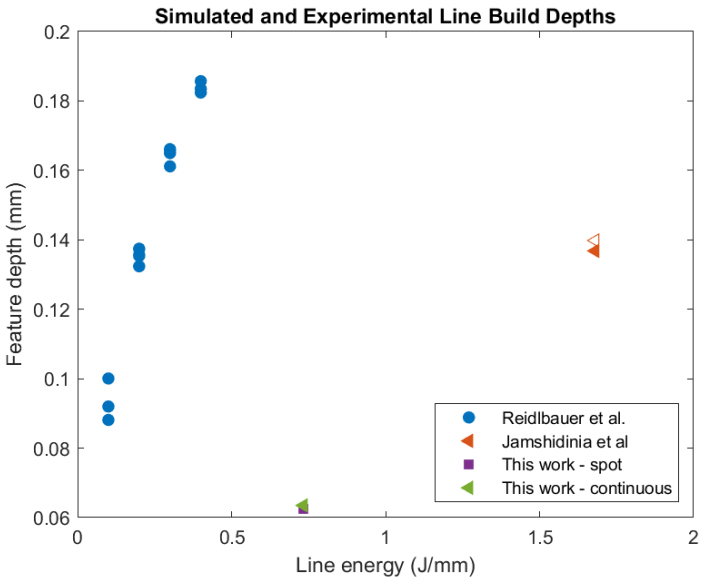

Figure 5.3: Comparison between simulated (shaded) and experimental (outline) feature depth data from this work, Galati et al., Riedlbauer et al., and Jamshidinia et al. [74, 148, 152]

good agreement. In both cases, the spot melting cases have visible circular marks, whereas the continuous melting lacks circular marks or ripples and has a wavier surface finish. Jamshidinia et al. report that their results are from continuous melting, and used a continuous beam in their model, but their experimental results have many of the characteristics of the spot melting samples from this work and Galati et al. Because spot melting is the default option unless the process parameters are deliberately modified, it is possible that they may have unknowingly used spot melting. Nevertheless, their simulated, continuous results show very good agreement with their experimental results, regardless of the scanning pattern. This suggests that the process parameters are automatically adjusted for optimal production of the given geometry.

For visual reference, the simulated and experimental results for the spot melting of a wall feature are overlaid in Fig. 5.5. As mentioned above in Fig. 4.6, the simulated spot melting was significantly below the experimental width, while the simulated and experimental continuous features were in good agreement with each other. The most likely cause of this is incorrect process parameters used for the spot melting. It was difficult to find exact details on how Arcam implemented the spot melting process, so many assumptions were made. The beam power is likely correct, as it was based on current readings from the log files, but there are a multitude of other settings that could have an effect, including dwell time, beam diameter, and preheating parameters.

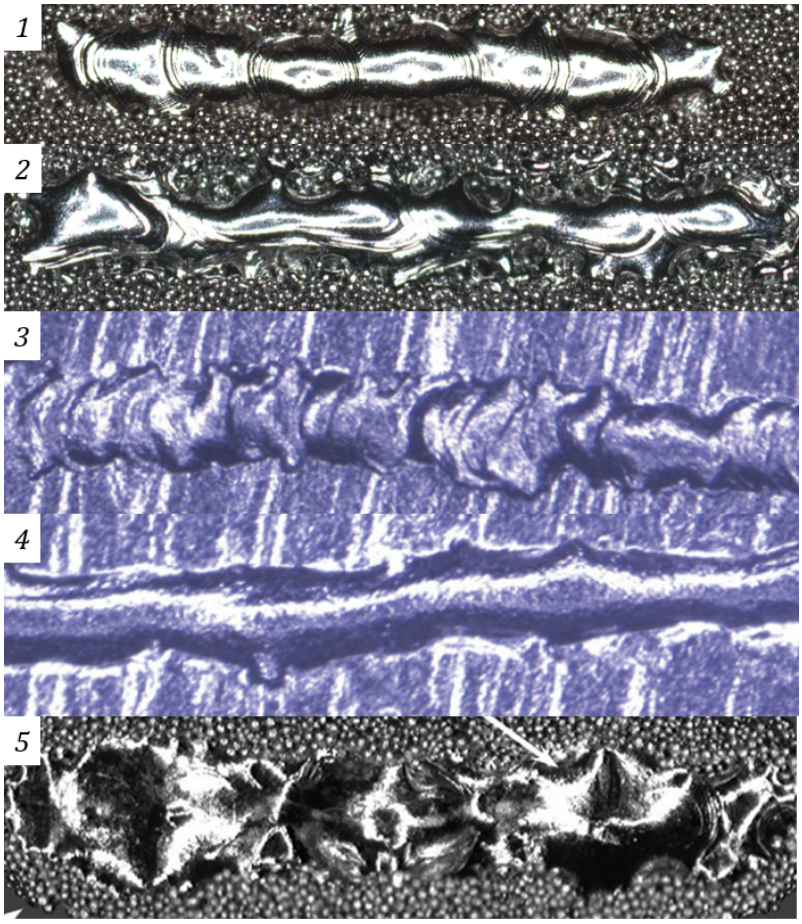

Figure 5.4: Comparison of various experimental results (not to scale); from top to bottom: (1) this work, spot melting; (2) this work, continuous melting; (3) Galati et al., spot melting at 650 /s and spot time 0.3 ms; (4) Galati et al., continuous melting at 550 m/s; (5) Jamshidinia et al. [74, 152]

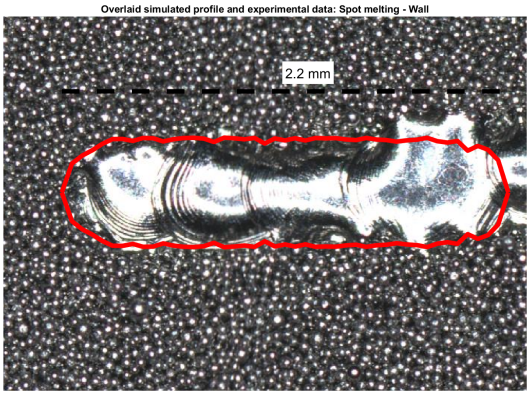

Figure 5.5: Overlaid simulated and experimental image for spot melting of a wall feature

5.3 Meltpool and Microstructure Modeling

In addition to the significant underprediction of depth, another inaccuracy noticed in this model is that the velocity field is significantly lower than what is commonly reported in the literature. The maximum velocity seen in this model was on the order of 2.5×10^{-2} m/s, in comparison with a value of 0.74 m/s from Jamshidinia et al. and 2.5 m/s with IN718 from Knapp et al [74, 75]. These two works are a particularly relevant comparison, as they essentially make all the same assumptions and use a very similar modeling technique as this work. On the face of it, there is no apparent or intended reason for this model to predict velocities over an order of magnitude lower. The most likely reason is a bug or implementation error that has the accidental effect of suppressing velocity. Meshing is unlikely to be the cause, as the mesh size used in this study was similar to the ones used in the literature. Neither author reports the value of the mushy zone constant used, but based on the convergence test conducted in this work, that has very little effect. All three models use different CFD methods, but all three models are relatively comparable. It is very likely that whatever issue is affecting velocities is also effecting the depths.

While the simulated velocities are not in good agreement with the literature, the temperature profiles are more in line with what is reported. The maximum temperature is on the order of 3460 K, which is in good agreement with the LBM results from Klassen [79]. This is also remarkably close to the point mass calculation done in Section 2.3.1, which estimated a maximum temperature of 3600 K. Given the strong effects of convection on meltpool heat transfer, it is surprising that given the low velocities the temperature profile is reasonably accurate. The small size of the region of heightened temperature, which is best illustrated in Fig. 4.9a, is expected given the low thermal conductivity of Ti-6Al-4V and the relatively short simulation timescale. There simply is not enough time for the heat to dissipate away from the electron beam. Furthermore, because the liquid has a much higher thermal diffusivity, it stores the heat much more effectively than the solid, allowing the meltpool to remain at an elevated temperature for a long time.

The predicted microstructure is a mixed columnar-equiaxed, that is dominated by martensite. Because this model only simulates the initial printing, and not the subsequent thermal cycling, it does not capture the decomposition of α' to α-β that occurs over a longer time period. This is similar to the behavior that happens at the top layers of parts, which do not undergo thermal cycling, which is shown in the experimental data from Lu et al. in Fig. 2.6b [55]. The prediction of an equiaxed microstructure also matches the experimental data, which is shown in the experimental data from Tan et al. in Fig. 2.6a [49]. Because the line build geometry is extremely small compared to any real engineering component, it does not provide insight into the microstructural formation mechanisms, particularly the thermal cycling, and is not an adequate test of that feature. Ideally, a component with much higher thermal mass would be analyzed in order to properly assess the affects of microstructural change. A comparison between the calculated average cooling rates for each process set and data from Al-Bermani et al. based on Rosenthal's solution is given in Fig. 5.6, based on the solidification map from Kobryn and Semiatin [10, 196]. This work is conducted at 660 W, which is higher than the power used by Al-Bermani et al, which may explain the significantly higher values for R and G.

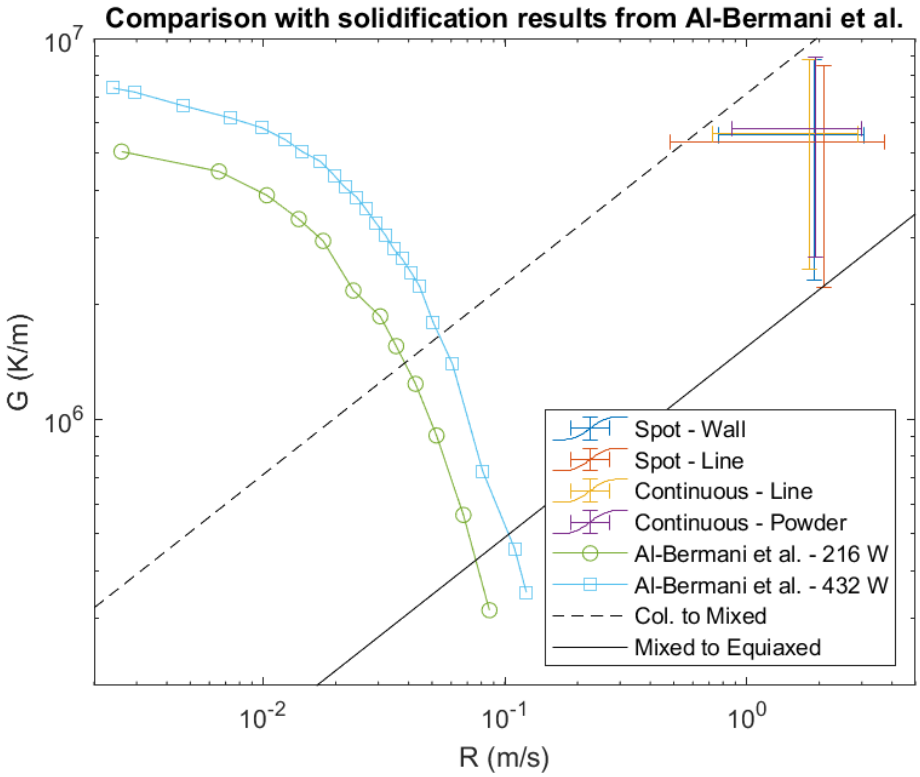

Figure 5.6: Comparison between this work and results predicted by Al-Bermani et al. [10]

Chapter 6

Conclusion

6.1 Conclusion and Summary

EBM is capable of producing components for critical structural applications, but quality and reproducibility are still major obstacles that will require significant academic and industrial research in order to resolve. EBM, like nearly all metal AM processes, has a highly homogeneous microstructure, though there is a growing amount of experimental data to understand both the causes and effects of this microstructural variability. A number of successful systems have been developed for in situ measurements and monitoring despite the many physical challenges in EBM, but there are still fundamental issues that can only be solved with simulation. Many numerical models have been developed to model the EBM process across a wide range of length and time scales and many models are able to deliver highly accurate results. No researchers as of yet have developed integrated multi-scale models that are able to capture all of the necessary length and time scales.

The IR camera data gathered in this work was unfortunately not usable due to severe degradation of the signal from metallization. This effect was not able to be captured using the calibration methods developed at the time. However, multiple solutions exist in the literature and can be applied to the problem at hand. Metallization, while a difficult problem, can be handled given the right experimental methods and using the foundation created in this work. While the designed and printed dimensions of the line build samples are not in good agreement, the discrepancy is remarkably consistent. The topology was independent of orientation and support (floating versus anchored to the build plate); the only factor that had a noticeable effect was continuous versus spot melting. The experimental dimensions are also in good agreement with the data from the literature, both qualitatively and quantitatively.

A preliminary model was developed using Fluent, designed from the ground-up to model the meltpool region in EBM. The coupled CFD-thermal approach was chosen based on both the analysis requirements and the lack of an existing model that fit the desired criteria. The widths of the simulated line builds were in relatively good agreement with the experimental data from both this work and the literature. While a comparison with experimental temperature data was unfortunately not possible, the simulated temperature profiles were in good agreement with similar results from the literature. Unfortunately, the meltpool depths and velocities were both significantly underpredicted, likely due to a bug or error in the model implementation. Despite

this, the model is reasonably accurate and comparable with much of the work and the literature, and can be significantly improved with further work.

6.2 Recommendations for Future Work

6.2.1 Experimental

Metallization IR Calibration

While the ideal option for calibration of the IR camera single to account for metallization is the development of a Kapton film system, this will require a significant resource investment to implement. Therefore, in the mean time, the more simple calibration tests on glass samples could be completed, while the Kapton film system is being investigated and developed.

Line Build for Sweep of Process Parameters

While the line build was a useful experiment, it tested two highly different sets of process parameters and made it difficult to compare across settings. It would be useful to print line builds with only one variable changed and to be able to understand the effects of a variable change in isolation.

6.2.2 Numerical

Optimization of Fluent Model

The existing model, while still in a preliminary stage, has the potential to be optimized very heavily. Once the depth and velocity issues are fixed, there are many potential avenues that can be explored. In potential, the mesh and timestep were chosen very conservatively and can likely both be increased significantly. Another major computational savings could come from the implementation of adaptive meshing and/or timestepping, both of which are natively available in Fluent.

Implementation of More Advanced Microstructure Model

Solidification maps, while simple and useful, only provide a very rough idea of the microstructure. One potential improvement is the JMA implementation from Vastola et al., which could be fully integrated with the current Fluent model without requiring any significant changes [157]. Another option would be the KMC code developed by Rodgers et al., which is open source and freely available [127]. The MSTL has also worked previously in PF of Ti-6Al-4V and while the PF implementation was not designed for AM, it could be modified to support EBM conditions [207].

Physics-Based Continuum Model of Powder

While some analytical continuum models of powder properties have been developed in the literature, for example the Sih-Barlow model for emissivity and the Gusarov-Tolochko model for

conductivity, these models have serious limitations and do not describe all the physical properties of the powder [87, 104, 112]. In particular, no useful model could be found for the densification behavior of powder near the solidus temperature. More advanced continuum models of the powder bed need to be developed, based on a combination of analytical, numerical, and experimental work. In some cases, it may be possible to borrow work from the field of pressureless sintering, but it will likely also require a novel understanding of how the powder bed behaves and how to approximate its stochastic, variable behavior as a continuum.

Extension to SLM

The current model could also be extended to support SLM as well. All of the overhead, controlling code could be left unchanged. The only parts that would need to be reimplemented are the boundary conditions (laser heat source, convection, and atmospheric evaporation effects) and powder material, which instead of a sintered powder in a vacuum would need to model a loose powder in an atmosphere. Significantly more modeling work is available in the literature for SLM and EBM, and there are many numerical models and experimental correlations that could be used as a reference.

Reimplementation in OpenFOAM

While Fluent is very customizable, the current model pushes this to and in some cases beyond its limits. Fluent was an ideal choice for a prototype model, as it allowed the focus to be on the physics of the problem while the numerical aspect of it was mostly untouched. Now that there is a preliminary understanding of how to approach the problem, OpenFOAM is an ideal choice as it is completely open to customization. While none of the AM models referenced in this work use OpenFOAM, Kidess et al. and Saldi used it for welding models that are both numerically and physically similar to this work [84, 85]. From a logistics point of view, OpenFOAM also has an advantage, as it is opensource, free, and easier to parallelize on Hyak or other clusters.

Bibliography

[1] D. L. Bourell. "Perspectives on Additive Manufacturing". *Annual Review of Materials Research* 46.1 (2016), pp. 1–18. DOI: 10.1146/annurev-matsci-070115-031606.

[2] C. Körner. "Additive manufacturing of metallic components by selective electron beam melting - a review". *International Materials Reviews* 61.5 (2016), pp. 361–377. DOI: 10.1080/09506608.2016.1176289.

[3] M. Galati and L. Iuliano. "A literature review of powder-based electron beam melting focusing on numerical simulations". *Additive Manufacturing* 19 (2018), pp. 1 –20. DOI: https://doi.org/10.1016/j.addma.2017.11.001.

[4] S. Liu and Y. C. Shin. "Additive manufacturing of Ti6Al4V alloy: A review". *Materials & Design* 164 (2019), p. 107552. DOI: https://doi.org/10.1016/j.matdes.2018.107552.

[5] D. Herzog et al. "Additive manufacturing of metals". *Acta Materialia* 117 (2016), pp. 371 –392. DOI: https://doi.org/10.1016/j.actamat.2016.07.019.

[6] M. Seifi et al. "Overview of Materials Qualification Needs for Metal Additive Manufacturing". *JOM* 68.3 (2016), pp. 747–764. DOI: 10.1007/s11837-015-1810-0.

[7] M. Ramulu et al. *Powder Bed Electron Beam Melting (EBM) Additive Manufacturing Process: Experimental Study of Ti-6Al-4V to Develop a Process-Microstructure-Property Relationship*. Tech. rep. The Boeing Company: Titanium Additive Manufacturing Group, 2019.

[8] Arcam EBM, A GE Additive Company. *Welcome to Manufacturing Unbound*. http://www.arcam.com/wp-content/uploads/arcamebm-corp-brochure-fnlv3.pdf. [Online; accessed 12/11/2019].

[9] S. Tammas-Williams et al. "XCT analysis of the influence of melt strategies on defect population in Ti-6Al-4V components manufactured by Selective Electron Beam Melting". *Materials Characterization* 102 (2015), pp. 47 –61. DOI: https://doi.org/10.1016/j.matchar.2015.02.008.

[10] S. S. Al-Bermani et al. "The Origin of Microstructural Diversity, Texture, and Mechanical Properties in Electron Beam Melted Ti-6Al-4V". *Metallurgical and Materials Transactions A* 41.13 (2010), pp. 3422–3434. DOI: 10.1007/s11661-010-0397-x.

[11] C. L. A. Leung et al. "Effect of preheating on the thermal, microstructural and mechanical properties of selective electron beam melted Ti-6Al-4V components". *Materials & Design* 174 (2019), p. 107792. DOI: https://doi.org/10.1016/j.matdes.2019.107792.

[12] X. Zhao et al. "Comparison of the microstructures and mechanical properties of Ti-6Al-4V fabricated by selective laser melting and electron beam melting". *Materials & Design* 95 (2016), pp. 21 –31. DOI: https://doi.org/10.1016/j.matdes.2015.12.135.

[13] M. Sigl, S. Lutzmann, and M. Zäh. "Transient Physical Effects in Electron Beam Sintering". In: *Proceedings of the Solid Freeform Fabrication Symposium*. 2006.

[14] W. Everhart, J. Dinardo, and C. Barr. "The Effect of Scan Length on the Structure and Mechanical Properties of Electron Beam-Melted Ti-6Al-4V". *Metallurgical and Materials Transactions A* 48.2 (2016), 697–705. DOI: 10.1007/s11661-016-3866-z.

[15] S. Price et al. "On Process Temperature in Powder-Bed Electron Beam Additive Manufacturing: Process Parameter Effects". *Journal of Manufacturing Science and Engineering* 136.6 (2014), p. 061019. DOI: 10.1115/1.4028485.

[16] J. Oliveira, T. Santos, and R. Miranda. "Revisiting fundamental welding concepts to improve additive manufacturing: From theory to practice". *Progress in Materials Science* 107 (2020), p. 100590. DOI: https://doi.org/10.1016/j.pmatsci.2019.100590.

[17] M. Mani et al. *NISTIR-8036: Measurement Science Needs for Real-time Control of Additive Manufacturing Powder Bed Fusion Processes*. Tech. rep. NIST, 2015. DOI: 10.6028/NIST.IR.8036.

[18] S. K. Everton et al. "Review of in-situ process monitoring and in-situ metrology for metal additive manufacturing". *Materials & Design* 95 (2016), pp. 431 –445. DOI: https://doi.org/10.1016/j.matdes.2016.01.099.

[19] M. Grasso and B. M. Colosimo. "Process defects and in situ monitoring methods in metal powder bed fusion: a review". *Measurement Science and Technology* 28.4 (2017), p. 044005. DOI: 10.1088/1361-6501/aa5c4f.

[20] G. Tapia and A. Elwany. "A Review on Process Monitoring and Control in Metal-Based Additive Manufacturing". *Journal of Manufacturing Science and Engineering* 136.6 (Oct. 2014). 060801. DOI: 10.1115/1.4028540.

[21] T. Scharowsky et al. "Melt pool dynamics during selective electron beam melting". *Applied Physics A* 114.4 (2014), pp. 1303–1307. DOI: 10.1007/s00339-013-7944-4.

[22] R. B. Dinwiddie et al. "Thermographic in-situ process monitoring of the electron-beam melting technology used in additive manufacturing". In: *Thermosense: Thermal Infrared Applications XXXV*. Ed. by G. R. Stockton and F. P. Colbert. Vol. 8705. International Society for Optics and Photonics. SPIE, 2013, pp. 156 –164. DOI: 10.1117/12.2018412.

[23] J. Raplee et al. "Thermographic Microstructure Monitoring in Electron Beam Additive Manufacturing". *Scientific Reports* 7.1 (2017). DOI: 10.1038/srep43554.

[24] E. Rodriguez. "Development of a Thermal Imaging Feedback Control System in Electron Beam Melting". Master's thesis. University of Texas at El Paso, 2013.

[25] FLIR AB. *The Ultimate Infrared Handbook for R&D Professionals*.

[26] J. Schwerdtfeger, R. F. Singer, and C. Körner. "In situ flaw detection by IR-imaging during electron beam melting". *Rapid Prototyping Journal* 18.4 (2012), pp. 259–263. DOI: 10.1108/13552541211231572.

[27] E. Rodriguez et al. "Integration of a Thermal Imaging Feedback Control System in Electron Beam Melting". In: *Proceedings of the Solid Freeform Fabrication Symposium*. 2012.

[28] J. Mireles et al. "Automatic Feedback Control in Electron Beam Melting Using Infrared Thermography". In: *Proceedings of the Solid Freeform Fabrication Symposium*. 2013.

[29] S. Ridwan et al. "Automatic Layerwise Acquisition of Thermal and Geometric Data of the Electron Beam Melting Process Using Infrared Thermography". In: *Proceedings of the Solid Freeform Fabrication Symposium*. 2013.

[30] J. Mireles et al. "Closed-loop automatic feedback control in electron beam melting". *The International Journal of Advanced Manufacturing Technology* 78.5 (2015), pp. 1193–1199. DOI: 10.1007/s00170-014-6708-4.

[31] E. Rodriguez et al. "Approximation of absolute surface temperature measurements of powder bed fusion additive manufacturing technology using in situ infrared thermography". *Additive Manufacturing* 5 (2015), pp. 31 –39. DOI: https://doi.org/10.1016/j.addma.2014.12.001.

[32] P. M. Cordero et al. "Evaluation of monitoring methods for electron beam melting powder bed fusion additive manufacturing technology". *Progress in Additive Manufacturing* 2.1 (2017), pp. 1–10. DOI: 10.1007/s40964-016-0015-6.

[33] B. A. Fisher et al. "Consequences of Part Temperature Variability in Electron Beam Melting of Ti-6Al-4V". *JOM* 69.12 (2017), pp. 2745–2750. DOI: 10.1007/s11837-017-2597-y.

[34] J. Mireles et al. "Analysis and correction of defects within parts fabricated using powder bed fusion technology". *Surface Topography: Metrology and Properties* 3.3 (2015), p. 034002. DOI: 10.1088/2051-672x/3/3/034002.

[35] S. Price et al. "Experimental Temperature Analysis of Powder-Nased Electron Beam Additive Manufacturing". In: *Proceedings of the Solid Freeform Fabrication Symposium*. 2013.

[36] P. Nandwana et al. "Recyclability Study on Inconel 718 and Ti-6Al-4V Powders for Use in Electron Beam Melting". *Metallurgical and Materials Transactions B* 47.1 (2016), pp. 754–762. DOI: 10.1007/s11663-015-0477-9.

[37] S. Price. "On Temperature Measurements and Analysis in Electron Beam Additive Manufacturing Using Near Infrared Thermography". Master's thesis. University of Alabama, 2014.

[38] R. B. Dinwiddie et al. "Calibrating IR cameras for in-situ temperature measurement during the electron beam melt processing of Inconel 718 and Ti-Al6-V4". In: *Thermosense: Thermal Infrared Applications XXXVIII*. Ed. by J. N. Zalameda and P. Bison. Vol. 9861. International Society for Optics and Photonics. SPIE, 2016, pp. 42 –52. DOI: 10.1117/12.2229070.

[39] P. Nandwana et al. "Correlations Between Powder Feedstock Quality, In Situ Porosity Detection, and Fatigue Behavior of Ti-6Al-4V Fabricated by Powder Bed Electron Beam Melting: A Step Towards Qualification". *JOM* 70.9 (2018), pp. 1686–1691. DOI: 10.1007/s11837-018-3034-6.

[40] J. Raplee et al. "Understanding the thermal sciences in the electron beam melting process through in-situ process monitoring". In: *Nondestructive Characterization and Monitoring of Advanced Materials, Aerospace, and Civil Infrastructure 2017*. Ed. by H. F. Wu et al. Vol. 10169. International Society for Optics and Photonics. SPIE, 2017, pp. 160 –167. DOI: 10.1117/12.2263315.

[41] N. Boone et al. "Thermal near infrared monitoring system for electron beam melting with emissivity tracking". *Additive Manufacturing* 22 (2018), pp. 601 –605. DOI: https://doi.org/10.1016/j.addma.2018.06.004.

[42] S. Price, K. Cooper, and K. Chou. "Evaluations of Temperature Measurements by near-Infrared Thermography in Powder-based Electron-beam Additive Manufacturing". In: *Proceedings of the Solid Freeform Fabrication Symposium*. 2012.

[43] B. Cheng et al. "On Process Temperature in Powder-Bed Electron Beam Additive Manufacturing: Model Development and Validation". *Journal of Manufacturing Science and Engineering* 136.6 (2014), p. 061018. DOI: 10.1115/1.4028484.

[44] H. Wong et al. "Pilot feedback electronic imaging at elevated temperatures and its potential for in-process electron beam melting monitoring". *Additive Manufacturing* 27 (2019), pp. 185 –198. DOI: https://doi.org/10.1016/j.addma.2019.02.022.

[45] H. Wong et al. "Pilot investigation of feedback electronic image generation in electron beam melting and its potential for in-process monitoring". *Journal of Materials Processing Technology* 266 (2019), pp. 502 –517. DOI: https://doi.org/10.1016/j.jmatprotec.2018.10.016.

[46] H. Wong et al. "Benchmarking spatial resolution in electronic imaging for potential in-situ Electron Beam Melting monitoring". *Additive Manufacturing* 29 (2019), p. 100829. DOI: https://doi.org/10.1016/j.addma.2019.100829.

[47] C. Arnold et al. "Layerwise monitoring of electron beam melting via backscatter electron detection". *Rapid Prototyping Journal* 24.8 (2018), pp. 1401–1406. DOI: 10.1108/rpj-02-2018-0034.

[48] C. R. Pobel et al. "Immediate development of processing windows for selective electron beam melting using layerwise monitoring via backscattered electron detection". *Materials Letters* 249 (2019), pp. 70 –72. DOI: https://doi.org/10.1016/j.matlet.2019.03.048.

[49] X. Tan et al. "Graded microstructure and mechanical properties of additive manufactured Ti–6Al–4V via electron beam melting". *Acta Materialia* 97 (2015), pp. 1 –16. DOI: https://doi.org/10.1016/j.actamat.2015.06.036.

[50] Y. Kok et al. "Anisotropy and heterogeneity of microstructure and mechanical properties in metal additive manufacturing: A critical review". *Materials & Design* 139 (2018), pp. 565 –586. DOI: https://doi.org/10.1016/j.matdes.2017.11.021.

[51] T. DebRoy et al. "Additive manufacturing of metallic components - Process, structure and properties". *Progress in Materials Science* 92 (2018), pp. 112 –224. DOI: https://doi.org/10.1016/j.pmatsci.2017.10.001.

[52] A. Antonysamy, J. Meyer, and P. Prangnell. "Effect of build geometry on the β-grain structure and texture in additive manufacture of Ti-6Al-4V by selective electron beam melting". *Materials Characterization* 84 (2013), pp. 153 –168. DOI: https://doi.org/10.1016/j.matchar.2013.07.012.

[53] P. Nandwana et al. "Post-processing to Modify the α Phase Micro-Texture and β Phase Grain Morphology in Ti-6Al-4V Fabricated by Powder Bed Electron Beam Melting". *Metallurgical and Materials Transactions A* 50.7 (2019), pp. 3429–3439. DOI: 10.1007/s11661-019-05247-4.

[54] C. Guo, W. Ge, and F. Lin. "Effects of scanning parameters on material deposition during Electron Beam Selective Melting of Ti-6Al-4V powder". *Journal of Materials Processing Technology* 217 (2015), pp. 148 –157. DOI: https://doi.org/10.1016/j.jmatprotec.2014.11.010.

[55] S. Lu et al. "Massive transformation in Ti–6Al–4V additively manufactured by selective electron beam melting". *Acta Materialia* 104 (2016), pp. 303 –311. DOI: https://doi.org/10.1016/j.actamat.2015.11.011.

[56] V. Juechter et al. "Processing window and evaporation phenomena for Ti–6Al–4V produced by selective electron beam melting". *Acta Materialia* 76 (2014), pp. 252 –258. DOI: https://doi.org/10.1016/j.actamat.2014.05.037.

[57] H. Galarraga et al. "Effects of the microstructure and porosity on properties of Ti-6Al-4V ELI alloy fabricated by electron beam melting (EBM)". *Additive Manufacturing* 10 (2016), pp. 47 –57. DOI: https://doi.org/10.1016/j.addma.2016.02.003.

[58] W. Sames et al. "Effect of Process Control and Powder Quality on Inconel 718 Produced Using Electron Beam Melting". In: *8th International Symposium on Superalloy 718 and Derivatives*. John Wiley & Sons, Ltd, 2014, pp. 409–423. DOI: 10.1002/9781119016854.ch32.

[59] H. Gong et al. "Influence of defects on mechanical properties of Ti-6Al-4V components produced by selective laser melting and electron beam melting". *Materials & Design* 86 (2015), pp. 545 –554. DOI: https://doi.org/10.1016/j.matdes.2015.07.147.

[60] N. Hrabe, T. Gnäupel-Herold, and T. Quinn. "Fatigue properties of a titanium alloy (Ti-6Al-4V) fabricated via electron beam melting (EBM): Effects of internal defects and residual stress". *International Journal of Fatigue* 94 (2017). Fatigue and Fracture Behavior of Additive Manufactured Parts, pp. 202 –210. DOI: https://doi.org/10.1016/j.ijfatigue.2016.04.022.

[61] H. Gong et al. "Analysis of defect generation in Ti-6Al-4V parts made using powder bed fusion additive manufacturing processes". *Additive Manufacturing* 1-4 (2014). Inaugural Issue, pp. 87 –98. DOI: https://doi.org/10.1016/j.addma.2014.08.002.

[62] C. Körner, A. Bauereiß, and E. Attar. "Fundamental consolidation mechanisms during selective beam melting of powders". *Modelling and Simulation in Materials Science and Engineering* 21.8 (2013), p. 085011. DOI: 10.1088/0965-0393/21/8/085011.

[63] J. L. Bartlett and X. Li. "An overview of residual stresses in metal powder bed fusion". *Additive Manufacturing* 27 (2019), pp. 131 –149. DOI: https://doi.org/10.1016/j.addma.2019.02.020.

[64] C. Li et al. "Residual Stress in Metal Additive Manufacturing". *Procedia CIRP* 71 (2018). 4th CIRP Conference on Surface Integrity (CSI 2018), pp. 348 –353. DOI: https://doi.org/10.1016/j.procir.2018.05.039.

[65] P. Edwards, A. O'Conner, and M. Ramulu. "Electron Beam Additive Manufacturing of Titanium Components: Properties and Performance". *Journal of Manufacturing Science and Engineering* 135.6 (2013), p. 061016. DOI: 10.1115/1.4025773.

[66] P. Edwards and M. Ramulu. "Fatigue performance evaluation of selective laser melted Ti-6Al-4V". *Materials Science and Engineering: A* 598 (2014), pp. 327 –337. DOI: https://doi.org/10.1016/j.msea.2014.01.041.

[67] L. M. Sochalski-Kolbus et al. "Comparison of Residual Stresses in Inconel 718 Simple Parts Made by Electron Beam Melting and Direct Laser Metal Sintering". *Metallurgical and Materials Transactions A* 46.3 (2015), pp. 1419–1432. DOI: 10.1007/s11661-014-2722-2.

[68] A. H. Chern et al. "A review on the fatigue behavior of Ti-6Al-4V fabricated by electron beam melting additive manufacturing". *International Journal of Fatigue* 119 (2019), pp. 173 –184. DOI: https://doi.org/10.1016/j.ijfatigue.2018.09.022.

[69] C. Körner, E. Attar, and P. Heinl. "Mesoscopic simulation of selective beam melting processes". *Journal of Materials Processing Technology* 211.6 (2011), pp. 978 –987. DOI: https://doi.org/10.1016/j.jmatprotec.2010.12.016.

[70] ANSYS Inc. *Fluent Theory Guide*.

[71] V. Voller and C. Prakash. "A fixed grid numerical modelling methodology for convection-diffusion mushy region phase-change problems". *International Journal of Heat and Mass Transfer* 30.8 (1987), pp. 1709 –1719. DOI: https://doi.org/10.1016/0017-9310(87)90317-6.

[72] P. S. Cook and A. B. Murphy. "Simulation of Melt Pool Behaviour during Additive Manufacturing: Underlying Physics and Progress". *Additive Manufacturing* (2019), p. 100909. DOI: https://doi.org/10.1016/j.addma.2019.100909.

[73] Y. Zhao et al. "Molten pool behavior and effect of fluid flow on solidification conditions in selective electron beam melting (SEBM) of a biomedical Co-Cr-Mo alloy". *Additive Manufacturing* 26 (2019), pp. 202–214. DOI: https://doi.org/10.1016/j.addma.2018.12.002.

[74] M. Jamshidinia, F. Kong, and R. Kovacevic. "Numerical Modeling of Heat Distribution in the Electron Beam Melting of Ti-6Al-4V". *Journal of Manufacturing Science and Engineering* 135.6 (2013), p. 061010. DOI: 10.1115/1.4025746.

[75] G. Knapp et al. "Experiments and simulations on solidification microstructure for Inconel 718 in powder bed fusion electron beam additive manufacturing". *Additive Manufacturing* 25 (2019), pp. 511 –521. DOI: https://doi.org/10.1016/j.addma.2018.12.001.

[76] J.-P. Kruth et al. "Consolidation phenomena in laser and powder-bed based layered manufacturing". *CIRP Annals* 56.2 (2007), pp. 730 –759. DOI: https://doi.org/10.1016/j.cirp.2007.10.004.

[77] T. Mukherjee et al. "Dimensionless numbers in additive manufacturing". *Journal of Applied Physics* 121.6 (2017), p. 064904. DOI: 10.1063/1.4976006.

[78] F. P. Incropera et al. *Principles of heat and mass transfer*. 7th ed. J. Wiley & Sons, 2017.

[79] A. Klassen. "Simulation of Evaporation Phenomena in Selective Electron Beam Melting". PhD thesis. Friedrich-Alexander-Universität Erlangen-Nürnberg, 2018.

[80] M. Jamshidinia, F. Kong, and R. Kovacevic. "Temperature Distribution and Fluid Flow Modeling of Electron Beam Melting (EBM)". In: *Proceedings of the ASME 2012 International Mechanical Engineering Congress & Exposition*. 2012.

[81] K. C. Mills. *Recommended values of thermophysical properties for selected commercial alloys*. Woodhead, 2002.

[82] J. R. Raush. "Thermophysical and Thermochemical Property Measurement and Prediction of Liquid Metal Titanium Alloys with Applications in Additive Manufacturing". PhD thesis. Louisiana State University, 2016.

[83] I. Egry et al. "Thermophysical Properties of Liquid AlTi-Based Alloys". *International Journal of Thermophysics* 31.4 (2010), pp. 949–965. DOI: 10.1007/s10765-010-0704-1.

[84] Z. S. Saldi. "Marangoni Driven Free Surface Flows in Liquid Weld Pools". PhD thesis. Delft University of Technology, 2012.

[85] A. Kidess et al. "Marangoni driven turbulence in high energy surface melting processes". *International Journal of Thermal Sciences* 104 (2016), pp. 412 –422. DOI: https://doi.org/10.1016/j.ijthermalsci.2016.01.015.

[86] V. G. Ivanchenko, O. M. Ivasishin, and S. L. Semiatin. "Evaluation of evaporation losses during electron-beam melting of Ti-Al-V alloys". *Metallurgical and Materials Transactions B* 34.6 (2003), pp. 911–915. DOI: 10.1007/s11663-003-0097-7.

[87] N. K. Tolochko et al. "Mechanisms of selective laser sintering and heat transfer in Ti powder". *Rapid Prototyping Journal* 9.5 (2003), pp. 314–326. DOI: 10.1108/13552540310502211.

[88] S. L. Semiatin, V. G. Ivanchenko, and O. M. Ivasishin. "Diffusion models for evaporation losses during electron-beam melting of alpha/beta-titanium alloys". *Metallurgical and Materials Transactions B* 35.2 (2004), pp. 235–245. DOI: 10.1007/s11663-004-0025-5.

[89] I. Ansara, A. T. Dinsdale, and M. H. Rand. *Thermochemical database for light metal alloys*. Tech. rep. COST 507. European Cooperation in Science & Technology, 1998.

[90] V. Morel, A. Bultel, and B. G. Chéron. "The Critical Temperature of Aluminum". *International Journal of Thermophysics* 30.6 (2009), p. 1853. DOI: 10.1007/s10765-009-0671-6.

[91] N. Shen and K. Chou. "Thermal Modeling of Electron Beam Additive Manufacturing Process: Powder Sintering Effects". *ASME 2012 International Manufacturing Science and Engineering Conference* (2012). DOI: 10.1115/msec2012-7253.

[92] M. F. Zäh and S. Lutzmann. "Modelling and simulation of electron beam melting". *Production Engineering* 4.1 (2009), pp. 15–23. DOI: 10.1007/s11740-009-0197-6.

[93] R. Degenhardt. "Advanced Lattice Boltzmann Models for the Simulation of Additive Manufacturing Processes". PhD thesis. Friedrich-Alexander-Universität Erlangen-Nürnberg, 2017.

[94] N. Raghavan et al. "Numerical modeling of heat-transfer and the influence of process parameters on tailoring the grain morphology of IN718 in electron beam additive manufacturing". *Acta Materialia* 112 (2016), pp. 303 –314. DOI: https://doi.org/10.1016/j.actamat.2016.03.063.

[95] Y. Lee et al. "Role of scan strategies on thermal gradient and solidification rate in electron beam powder bed fusion". *Additive Manufacturing* 22 (2018), pp. 516 –527. DOI: https://doi.org/10.1016/j.addma.2018.04.038.

[96] P. Homporová et al. "Dynamic phase evolution in titanium alloy Ti-6Al-4V". In: *Ti 2011 - Proceedings of the 12th World Conference on Titanium*. Vol. 1. 2012, pp. 737–740.

[97] E. Kaschnitz, P. Reiter, and J. L. McClure. "Thermophysical Properties of Solid and Liquid 90Ti–6Al–4V in the Temperature Range from 1400 to 2300 K Measured by Millisecond and Microsecond Pulse-Heating Techniques". *International Journal of Thermophysics* 23.1 (2002), pp. 267–275. DOI: 10.1023/A:1013925715428.

[98] L. González-Fernández et al. "Infrared normal spectral emissivity of Ti-6Al-4V alloy in the 500-1150K temperature range". *Journal of Alloys and Compounds* 541 (2012), pp. 144 –149. DOI: https://doi.org/10.1016/j.jallcom.2012.06.117.

[99] A. Neira-Arce. "Thermal Modeling and Simulation of Electron Beam Melting for Rapid Prototyping on Ti6Al4V Alloys". PhD thesis. North Carolina State University, 2012.

[100] N. Milošević and I. Aleksić. "Thermophysical properties of solid phase Ti-6Al-4V alloy over a wide temperature range". *International Journal of Materials Research* 103.6 (2012), pp. 707–714. DOI: 10.3139/146.110678.

[101] M. Boivineau et al. "Thermophysical Properties of Solid and Liquid Ti-6Al-4V (TA6V) Alloy". *International Journal of Thermophysics* 27.2 (2006), pp. 507–529. DOI: 10.1007/PL00021868.

[102] Y. S. Touloukian et al. *Thermophysical Properties of Matter: Volume 1. Thermal Conductivity - Metallic Elements and Alloys*. IFI/Plenum, 1970.

[103] X. Gong et al. "Powder-Bed Electron-Beam-Melting Additive Manufacturing: Powder Characterization, Process Simulation, and Metrology". In: *Proceedings of the ASME Early Career Technical Conference*. 2013.

[104] A. Gusarov et al. "Contact thermal conductivity of a powder bed in selective laser sintering". *International Journal of Heat and Mass Transfer* 46.6 (2003), pp. 1103–1109. DOI: 10.1016/s0017-9310(02)00370-8.

[105] L. C. Wei et al. "Thermal conductivity of metal powders for powder bed additive manufacturing". *Additive Manufacturing* 21 (2018), pp. 201 –208. DOI: https://doi.org/10.1016/j.addma.2018.02.002.

[106] C. J. Smith et al. "Tailoring the thermal conductivity of the powder bed in Electron Beam Melting (EBM) Additive Manufacturing". *Scientific Reports* 7.1 (2017). DOI: 10.1038/s41598-017-11243-8.

[107] A. Cezairliyan, J. L. Mcclure, and R. Taylor. "Thermophysical measurements on 90Ti-6Al-4V alloy above 1450 K using a transient (subsecond) technique". *Journal of Research of the National Bureau of Standards Section A: Physics and Chemistry* 81A.2/3 (1977), p. 251. DOI: 10.6028/jres.081a.014.

[108] D. Basak, R. A. Overfelt, and D. Wang. "Measurement of Specific Heat Capacity and Electrical Resistivity of Industrial Alloys Using Pulse Heating Techniques". *International Journal of Thermophysics* 24.6 (2003), pp. 1721–1733. DOI: 10.1023/B:IJOT.0000004101.88449.86.

[109] Y. S. Touloukian and D. Dewitt. *Thermophysical Properties of Matter: Volume 7. Thermal Radiative Properties - Metallic Elements and Alloys*. IFI/Plenum, 1970.

[110] J. Jones, P. Mason, and A. Williams. "A compilation of data on the radiant emissivity of some materials at high temperatures". *Journal of the Energy Institute* 92.3 (2019), pp. 523 –534. DOI: https://doi.org/10.1016/j.joei.2018.04.006.

[111] B. A. Shur and V. E. Peletskii. "The Effect of Alloying Additions on the Emissivity of Titanium in the Neighborhood of Polymorphous Transformation". *High Temperature* 42.3 (2004), pp. 414–420. DOI: 10.1023/B:HITE.0000033878.03086.62.

[112] S. S. Sih and J. W. Barlow. "The Prediction of the Emissivity and Thermal Conductivity of Powder Beds". *Particulate Science and Technology* 22.4 (2004), pp. 427–440. DOI: 10.1080/02726350490501682.

[113] M. Galati et al. "Modelling energy source and powder properties for the development of a thermal FE model of the EBM additive manufacturing process". *Additive Manufacturing* 14 (2017), pp. 49 –59. DOI: https://doi.org/10.1016/j.addma.2017.01.001.

[114] T. Iida and R. I. L. Guthrie. *The Physical Properties of Liquid Metals*. Clarendon Press, 1993.

[115] K. Zhou and B. Wei. "Determination of the thermophysical properties of liquid and solid Ti–6Al–4V alloy". *Applied Physics A* 122.3 (2016), p. 248. DOI: 10.1007/s00339-016-9783-6.

[116] R. K. Wunderlich. "Surface Tension and Viscosity of Industrial Ti-Alloys measured by the Oscillating Drop Method on Board Parabolic Flights". *High Temperature Materials and Processes* 27.6 (2008). DOI: 10.1515/htmp.2008.27.6.401.

[117] T. Ishikawa et al. "Spectral emissivity and constant pressure heat capacity of liquid titanium measured by an electrostatic levitator". *The Journal of Chemical Thermodynamics* 131 (2019), pp. 557 –562. DOI: https://doi.org/10.1016/j.jct.2018.12.002.

[118] J. Brillo et al. "Surface tension of liquid Ti with adsorbed oxygen and its prediction". *Journal of Molecular Liquids* 290 (2019), p. 111226. DOI: https://doi.org/10.1016/j.molliq.2019.111226.

[119] S. Schneider, I. Egry, and I. Seyhan. "Measurement of the Surface Tension of Undercooled Liquid Ti90Al6V4 by the Oscillating Drop Technique". *International Journal of Thermophysics* 23.5 (2002), pp. 1241–1248. DOI: 10.1023/A:1019896321431.

[120] T. Ishikawa et al. "Thermophysical Property Measurements of High Temperature Melts Using an Electrostatic Levitation Method". *Japanese Journal of Applied Physics* 50.11 (2011), 11RD03. DOI: 10.1143/jjap.50.11rd03.

[121] P.-F. Paradis, T. Ishikawa, and S. Yoda. "Non-Contact Measurements of Surface Tension and Viscosity of Niobium, Zirconium, and Titanium Using an Electrostatic Levitation Furnace". *International Journal of Thermophysics* 23.3 (2002), pp. 825–842. DOI: 10.1023/A:1015459222027.

[122] C. J. Smithells. *Smithells Metals Reference Book*. Ed. by W. F. Gale and T. C. Totemeier. 8th ed. Amsterdam; Boston: Elsevier Butterworth-Heinemann, 2004.

[123] K. Thurnay. *Thermal Properties of Transition Metals*. Tech. rep. FZKA 6095. Forschungszentrum Karlsruhe: Institut für Neutronenphysik und Reaktortechnik, 1998.

[124] T Zacharia et al. "Modeling of fundamental phenomena in welds". *Modelling and Simulation in Materials Science and Engineering* 3.2 (1995), pp. 265–288. DOI: 10.1088/0965-0393/3/2/009.

[125] L.-E. Lindgren and A. Lundbäck. "Approaches in computational welding mechanics applied to additive manufacturing: Review and outlook". *Comptes Rendus Mécanique* 346.11 (2018). Computational methods in welding and additive manufacturing Simulation numérique des procédés de soudage et fabrication additive, pp. 1033 –1042. DOI: https://doi.org/10.1016/j.crme.2018.08.004.

[126] M. Francois et al. "Modeling of additive manufacturing processes for metals: Challenges and opportunities". *Current Opinion in Solid State and Materials Science* 21.4 (2017), pp. 198–206. DOI: https://doi.org/10.1016/j.cossms.2016.12.001.

[127] T. M. Rodgers, J. D. Madison, and V. Tikare. "Simulation of metal additive manufacturing microstructures using kinetic Monte Carlo". *Computational Materials Science* 135 (2017), pp. 78 –89. DOI: https://doi.org/10.1016/j.commatsci.2017.03.053.

[128] B. Schoinochoritis, D. Chantzis, and K. Salonitis. "Simulation of metallic powder bed additive manufacturing processes with the finite element method: A critical review". *Proceedings of the Institution of Mechanical Engineers, Part B: Journal of Engineering Manufacture* 231.1 (2017), pp. 96–117. DOI: 10.1177/0954405414567522.

[129] M. Markl and C. Körner. "Multiscale Modeling of Powder Bed-Based Additive Manufacturing". *Annual Review of Materials Research* 46.1 (2016), pp. 93–123. DOI: 10.1146/annurev-matsci-070115-032158.

[130] W. J. Seufzer. *Additive Manufacturing Modeling and Simulation: A Literature Review for Electron Beam Free Form Fabrication*. Tech. rep. NASA Langley Research Center, 2014.

[131] J. Liu et al. "A review of computational modeling in powder-based additive manufacturing for metallic part qualification". *Rapid Prototyping Journal* 24.8 (2018), pp. 1245–1264. DOI: 10.1108/rpj-04-2017-0058.

[132] D. Rosenthal. "Mathematical Theory of Heat Distribution During Welding and Cutting". *The Welding Journal* 20.5 (1941), pp. 220–234.

[133] T. Eager and N.-S. Tsai. "Temperature Fields Produced by Traveling Distributed Heat Sources". *Welding Research Supplement* 12 (1983), pp. 346–355.

[134] J. Goldak, A. Chakravarti, and M. Bibby. "A new finite element model for welding heat sources". *Metallurgical Transactions B* 15.2 (1984), pp. 299–305. DOI: 10.1007/BF02667333.

[135] A. Plotkowski, M. Kirka, and S. Babu. "Verification and validation of a rapid heat transfer calculation methodology for transient melt pool solidification conditions in powder bed metal additive manufacturing". *Additive Manufacturing* 18 (2017), pp. 256 –268. DOI: https://doi.org/10.1016/j.addma.2017.10.017.

[136] A. Plotkowski et al. "Influence of scan pattern and geometry on the microstructure and soft-magnetic performance of additively manufactured Fe-Si". *Additive Manufacturing* 29 (2019), p. 100781. DOI: https://doi.org/10.1016/j.addma.2019.100781.

[137] B. Stump and A. Plotkowski. "An adaptive integration scheme for heat conduction in additive manufacturing". *Applied Mathematical Modelling* 75 (2019), pp. 787 –805. DOI: https://doi.org/10.1016/j.apm.2019.07.008.

[138] C. L. Frederick et al. "Geometry-Induced Spatial Variation of Microstructure Evolution During Selective Electron Beam Melting of Rene-N5". *Metallurgical and Materials Transactions A* 49.10 (2018), pp. 5080–5096. DOI: 10.1007/s11661-018-4793-y.

[139] R. Forslund, A. Snis, and S. Larsson. "Analytical solution for heat conduction due to a moving Gaussian heat flux with piecewise constant parameters". *Applied Mathematical Modelling* 66 (2019), pp. 227 –240. DOI: https://doi.org/10.1016/j.apm.2018.09.018.

[140] M. F. Zäh and M. Kahnert. "The effect of scanning strategies on electron beam sintering". *Production Engineering* 3.3 (2009), pp. 217–224. DOI: 10.1007/s11740-009-0157-1.

[141] M. F. Zäh et al. "Determination of Process Parameters for Electron Beam Sintering (EBS)". In: *Proceedings of the COMSOL Conference 2008 Hannover*. 2008.

[142] B. Cheng and K. Chou. "Meltpool Geometry Simulations for Powder-Based Electron Beam Additive Manufacturing". In: *Proceedings of the Solid Freeform Fabrication Symposium*. 2013.

[143] B. Cheng and Y. K. Chou. "Overhang Support Structure Design for Electron Beam Additive Manufacturing". *Volume 2: Additive Manufacturing; Materials* (2017). DOI: 10.1115/msec2017-3018.

[144] B. Cheng and K. Chou. "Geometric consideration of support structures in part overhang fabrications by electron beam additive manufacturing". *Computer-Aided Design* 69 (2015), pp. 102 –111. DOI: https://doi.org/10.1016/j.cad.2015.06.007.

[145] X. Gong et al. "Powder-bed electron-beam-melting additive manufacturing: Powder characterization, process simulation and metrology". In: *ASME District F - ECTC 2013: Early Career Technical Conference*. 2013.

[146] S. Sahoo and K. Chou. "Phase-field simulation of microstructure evolution of Ti-6Al-4V in electron beam additive manufacturing process". *Additive Manufacturing* 9 (2016), pp. 14 –24. DOI: https://doi.org/10.1016/j.addma.2015.12.005.

[147] X. Gong. "Microstructural Characterizations and Modelling of Ti-6Al-4V Parts Made by Electron Beam Additive Manufacturing (EBAM)". PhD thesis. University of Alabama, 2014.

[148] D. Riedlbauer et al. "Macroscopic simulation and experimental measurement of melt pool characteristics in selective electron beam melting of Ti-6Al-4V". *The International Journal of Advanced Manufacturing Technology* 88.5 (2017), pp. 1309–1317. DOI: 10.1007/s00170-016-8819-6.

[149] P. Liu et al. "Investigation of thermal responses during metallic additive manufacturing using a 'Tri-Prism' finite element method". *International Journal of Thermal Sciences* 136 (2019), pp. 217 –229. DOI: https://doi.org/10.1016/j.ijthermalsci.2018.10.022.

[150] P. Liu et al. "Investigation on evolution mechanisms of site-specific grain structures during metal additive manufacturing". *Journal of Materials Processing Technology* 257 (2018), pp. 191 –202. DOI: https://doi.org/10.1016/j.jmatprotec.2018.02.042.

[151] P. Liu et al. "Insight into the mechanisms of columnar to equiaxed grain transition during metallic additive manufacturing". *Additive Manufacturing* 26 (2019), pp. 22 –29. DOI: https://doi.org/10.1016/j.addma.2018.12.019.

[152] M. Galati, A. Snis, and L. Iuliano. "Experimental validation of a numerical thermal model of the EBM process for Ti6Al4V". *Computers & Mathematics with Applications* (2018). DOI: https://doi.org/10.1016/j.camwa.2018.07.020.

[153] X. Ding et al. "Effect of process parameters on melt pool geometry and microstructure development for electron beam melting of IN718: A systematic single bead analysis study". *Additive Manufacturing* 26 (2019), pp. 215 –226. DOI: https://doi.org/10.1016/j.addma.2018.12.018.

[154] X. Tan et al. "An experimental and simulation study on build thickness dependent microstructure for electron beam melted Ti-6Al-4V". *Journal of Alloys and Compounds* 646 (2015), pp. 303 –309. DOI: https://doi.org/10.1016/j.jallcom.2015.05.178.

[155] X. Tan et al. "Revealing competitive columnar grain growth behavior and periodic microstructural banding in additively manufactured Ti-6Al-4V parts by selective electron beam melting". *Materialia* 7 (2019), p. 100365. DOI: https://doi.org/10.1016/j.mtla.2019.100365.

[156] G. Vastola et al. "Controlling of residual stress in additive manufacturing of Ti6Al4V by finite element modeling". *Additive Manufacturing* 12 (2016). Special Issue on Modeling & Simulation for Additive Manufacturing, pp. 231 –239. DOI: https://doi.org/10.1016/j.addma.2016.05.010.

[157] G. Vastola et al. "Modeling the Microstructure Evolution During Additive Manufacturing of Ti6Al4V: A Comparison Between Electron Beam Melting and Selective Laser Melting". *JOM* 68.5 (2016), pp. 1370–1375. DOI: 10.1007/s11837-016-1890-5.

[158] G. Vastola et al. "Active Control of Microstructure in Powder-Bed Fusion Additive Manufacturing of Ti6Al4V". *Advanced Engineering Materials* 19.12 (2017), p. 1700333. DOI: 10.1002/adem.201700333.

[159] N. Béraud et al. "New Trajectories in Electron Beam Melting Manufacturing to Reduce Curling Effect". *Procedia CIRP* 17 (2014). Variety Management in Manufacturing, pp. 738 –743. DOI: https://doi.org/10.1016/j.procir.2014.02.038.

[160] N. Béraud et al. "Improving dimensional accuracy in EBM using beam characterization and trajectory optimization". *Additive Manufacturing* 14 (2017), pp. 1 –6. DOI: https://doi.org/10.1016/j.addma.2016.12.002.

[161] M. Jamshidinia, F. Kong, and R. Kovacevic. "The Coupled CFD-FEM Model of Electron Beam Melting (EBM)". In: *ASME District F - Early Career Technical Conference Proceedings*. 2013.

[162] G. Chahine. "Application of Digital Engineering in the Development of a Bio-Adaptable Dental Implant". PhD thesis. Southern Methodist University, 2011.

[163] M. Jamshidinia and R. Kovacevic. "The influence of heat accumulation on the surface roughness in powder-bed additive manufacturing". *Surface Topography: Metrology and Properties* 3.1 (2015), p. 014003. DOI: 10.1088/2051-672x/3/1/014003.

[164] Y. Zhao et al. "Comprehensive study on mechanisms for grain morphology evolution and texture development in powder bed fusion with electron beam of Co-Cr-Mo alloy". *Materialia* 6 (2019), p. 100346. DOI: https://doi.org/10.1016/j.mtla.2019.100346.

[165] N. Raghavan et al. "Localized melt-scan strategy for site specific control of grain size and primary dendrite arm spacing in electron beam additive manufacturing". *Acta Materialia* 140 (2017), pp. 375 –387. DOI: https://doi.org/10.1016/j.actamat.2017.08.038.

[166] H. L. Wei, J. Mazumder, and T. Debroy. "Evolution of solidification texture during additive manufacturing". *Scientific Reports* 5.1 (2015). DOI: 10.1038/srep16446.

[167] T. Mukherjee, W. Zhang, and T. DebRoy. "An improved prediction of residual stresses and distortion in additive manufacturing". *Computational Materials Science* 126 (2017), pp. 360 –372. DOI: https://doi.org/10.1016/j.commatsci.2016.10.003.

[168] T. Mukherjee et al. "Heat and fluid flow in additive manufacturing - Part I: Modeling of powder bed fusion". *Computational Materials Science* 150 (2018), pp. 304 –313. DOI: https://doi.org/10.1016/j.commatsci.2018.04.022.

[169] T. Mukherjee et al. "Heat and fluid flow in additive manufacturing - Part II: Powder bed fusion of stainless steel, and titanium, nickel and aluminum base alloys". *Computational Materials Science* 150 (2018), pp. 369 –380. DOI: https://doi.org/10.1016/j.commatsci.2018.04.027.

[170] M. S. Rahman et al. "Thermo-Fluid Characterizations of Ti-6Al-4V Melt Pool in Powder-Bed Electron Beam Additive Manufacturing". In: vol. Volume 1: Advances in Aerospace Technology. ASME International Mechanical Engineering Congress and Exposition. V001T03A016. Nov. 2016. DOI: 10.1115/IMECE2016-65854.

[171] M. S. Rahman et al. "Thermal Analysis of Electron Beam Additive Manufacturing Using Ti-6Al-4V Powder-Bed". In: vol. Volume 1: Advances in Aerospace Technology. ASME International Mechanical Engineering Congress and Exposition. V001T03A021. Nov. 2017. DOI: 10.1115/IMECE2017-71663.

[172] M. S. Rahman et al. "A Comparative Study Between Selective Laser Melting and Electron Beam Additive Manufacturing Based on Thermal Modeling". In: vol. Volume 1: Advances in Aerospace Technology. ASME International Mechanical Engineering Congress and Exposition. V001T03A015. Nov. 2018. DOI: 10.1115/IMECE2018-86428.

[173] S. A. Khairallah et al. "Laser powder-bed fusion additive manufacturing: Physics of complex melt flow and formation mechanisms of pores, spatter, and denudation zones". *Acta Materialia* 108 (2016), pp. 36 –45. DOI: https://doi.org/10.1016/j.actamat.2016.02.014.

[174] E. Attar. "Simulation of Selective Electron Beam Melting Processes". PhD thesis. Friedrich-Alexander-Universität Erlangen-Nürnberg, 2011.

[175] M. Markl. "Numerical Modeling and Simulation of Selective Electron Beam Melting Using a Coupled Lattice Boltzmann and Discrete Element Method". PhD thesis. Friedrich-Alexander-Universität Erlangen-Nürnberg, 2015.

[176] A. Rai, M. Markl, and C. Körner. "A coupled Cellular Automaton-Lattice Boltzmann model for grain structure simulation during additive manufacturing". *Computational Materials Science* 124 (2016), pp. 37 –48. DOI: https://doi.org/10.1016/j.commatsci.2016.07.005.

[177] M. Markl et al. "Numerical investigations on hatching process strategies for powder-bed-based additive manufacturing using an electron beam". *The International Journal of Advanced Manufacturing Technology* 78.1 (2015), pp. 239–247. DOI: 10.1007/s00170-014-6594-9.

[178] R. Ammer et al. "Simulating fast electron beam melting with a parallel thermal free surface lattice Boltzmann method". *Computers & Mathematics with Applications* 67.2 (2014). Mesoscopic Methods for Engineering and Science (Proceedings of ICMMES-2012, Taipei, Taiwan, 23-27 July 2012), pp. 318 –330. DOI: https://doi.org/10.1016/j.camwa.2013.10.001.

[179] R. Ammer et al. "Validation experiments for LBM simulations of electron beam melting". *International Journal of Modern Physics C* 25.12 (2014), p. 1441009. DOI: 10.1142/S0129183114410095.

[180] A. Rausch et al. "Predictive Simulation of Process Windows for Powder Bed Fusion Additive Manufacturing: Influence of the Powder Bulk Density". *Materials* 10.10 (2017), p. 1117. DOI: 10.3390/ma10101117.

[181] A. Klassen, A. Bauereiß, and C. Körner. "Modelling of electron beam absorption in complex geometries". *Journal of Physics D: Applied Physics* 47.6 (2014), p. 065307. DOI: 10.1088/0022-3727/47/6/065307.

[182] H. Helmer et al. "Grain structure evolution in Inconel 718 during selective electron beam melting". *Materials Science and Engineering: A* 668 (2016), pp. 180 –187. DOI: https://doi.org/10.1016/j.msea.2016.05.046.

[183] A. Bauereiß, T. Scharowsky, and C. Kørner. "Defect generation and propagation mechanism during additive manufacturing by selective beam melting". *Journal of Materials Processing Technology* 214.11 (2014), pp. 2522 –2528. DOI: https://doi.org/10.1016/j.jmatprotec.2014.05.002.

[184] A. Klassen, V. E. Forster, and C. Körner. "A multi-component evaporation model for beam melting processes". *Modelling and Simulation in Materials Science and Engineering* 25.2 (2016), p. 025003. DOI: 10.1088/1361-651x/aa5289.

[185] W. Yan et al. "Multi-physics modeling of single/multiple-track defect mechanisms in electron beam selective melting". *Acta Materialia* 134 (2017), pp. 324 –333. DOI: https://doi.org/10.1016/j.actamat.2017.05.061.

[186] W. Yan et al. "Modeling and Experimental Validation of the Electron Beam Selective Melting Process". *Engineering* 3.5 (2017), pp. 701 –707. DOI: https://doi.org/10.1016/J.ENG.2017.05.021.

[187] W. Yan et al. "An integrated process-structure-property modeling framework for additive manufacturing". *Computer Methods in Applied Mechanics and Engineering* 339 (2018), pp. 184 –204. DOI: https://doi.org/10.1016/j.cma.2018.05.004.

[188] Y. Qian, W. Yan, and F. Lin. "Parametric study and surface morphology analysis of electron beam selective melting". *Rapid Prototyping Journal* 24.9 (2018), pp. 1586–1598. DOI: 10.1108/rpj-05-2017-0088.

[189] W. Yan et al. "Multiscale modeling of electron beam and substrate interaction: a new heat source model". *Computational Mechanics* 56.2 (2015), pp. 265–276. DOI: 10.1007/s00466-015-1170-1.

[190] C. Panwisawas et al. "On the role of thermal fluid dynamics into the evolution of porosity during selective laser melting". *Scripta Materialia* 105 (2015), pp. 14 –17. DOI: https://doi.org/10.1016/j.scriptamat.2015.04.016.

[191] C. Panwisawas et al. "Mesoscale modelling of selective laser melting: Thermal fluid dynamics and microstructural evolution". *Computational Materials Science* 126 (2017), pp. 479 –490. DOI: https://doi.org/10.1016/j.commatsci.2016.10.011.

[192] C. Qiu et al. "On the role of melt flow into the surface structure and porosity development during selective laser melting". *Acta Materialia* 96 (2015), pp. 72 –79. DOI: https://doi.org/10.1016/j.actamat.2015.06.004.

[193] C. Panwisawas et al. "A Multi-Scale Multi-Physics Approach to Modelling of Additive Manufacturing in Nickel-based Superalloys". In: *Proceedings of the 13th International Symposium on Superalloys*. 2016.

[194] D. Liu and Y. Wang. "Mesoscale multi-physics simulation of rapid solidification of Ti-6Al-4V alloy". *Additive Manufacturing* 25 (2019), pp. 551 –562. DOI: https://doi.org/10.1016/j.addma.2018.12.005.

[195] W. Sha and S. Malinov. *Titanium alloys: modelling of microstructure, properties and applications*. CRC, 2009.

[196] P. Kobryn and S. Semiatin. "Microstructure and texture evolution during solidification processing of Ti–6Al–4V". *Journal of Materials Processing Technology* 135.2 (2003). Special Issue containing paper from the conference 'Research and Development in Net shape Manufacturing', pp. 330 –339. DOI: https://doi.org/10.1016/S0924-0136(02)00865-8.

[197] O. Zinovieva, A. Zinoviev, and V. Ploshikhin. "Three-dimensional modeling of the microstructure evolution during metal additive manufacturing". *Computational Materials Science* 141 (2018), pp. 207 –220. DOI: https://doi.org/10.1016/j.commatsci.2017.09.018.

[198] J. A. Koepf et al. "3D multi-layer grain structure simulation of powder bed fusion additive manufacturing". *Acta Materialia* 152 (2018), pp. 119 –126. DOI: https://doi.org/10.1016/j.actamat.2018.04.030.

[199] X. Gong and K. Chou. "Phase-Field Modeling of Microstructure Evolution in Electron Beam Additive Manufacturing". *JOM* 67.5 (2015), pp. 1176–1182. DOI: 10.1007/s11837-015-1352-5.

[200] C. Kumara et al. "Predicting the Microstructural Evolution of Electron Beam Melting of Alloy 718 with Phase-Field Modeling". *Metallurgical and Materials Transactions A* 50.5 (2019), pp. 2527–2537. DOI: 10.1007/s11661-019-05163-7.

[201] M. Seifi et al. "Defect distribution and microstructure heterogeneity effects on fracture resistance and fatigue behavior of EBM Ti–6Al–4V". *International Journal of Fatigue* 94 (2017). Fatigue and Fracture Behavior of Additive Manufactured Parts, pp. 263 –287. DOI: https://doi.org/10.1016/j.ijfatigue.2016.06.001.

[202] J. G. Michopoulos et al. "On the multiphysics modeling challenges for metal additive manufacturing processes". *Additive Manufacturing* 22 (2018), pp. 784 –799. DOI: https://doi.org/10.1016/j.addma.2018.06.019.

[203] L. Li et al. "Study of Ti–6Al–4V alloy spectral emissivity characteristics during thermal oxidation process". *International Journal of Heat and Mass Transfer* 101 (2016), pp. 699 –706. DOI: https://doi.org/10.1016/j.ijheatmasstransfer.2016.05.069.

[204] Mikron Instrument Company. *Table of Emissivity of Various Surfaces*. http://www-eng.lbl.gov/~dw/projects/DW4229_LHC_detector_analysis/calculations/emissivity2.pdf. [Online; accessed 11/19/2019].

[205] CFD Online Forums. *Problem with UDF - DEFINE_SPECIFIC_HEAT macro*. https://www.cfd-online.com/Forums/fluent-udf/189116-problem-udf-define_specific_heat-macro.html. [Online; accessed 6/15/2019]. 2017.

[206] CFD Online Forums. *Temp dependent emissivity udf*. https://www.cfd-online.com/Forums/fluent-udf/139979-temp-dependent-emissivity-udf.html. [Online; accessed 6/15/2019]. 2014.

[207] B. Ferguson. "Modeling and Experimental Analysis of Superplastic Forming and Diffusion Bonding". PhD thesis. University of Washington, 2019.

[208] ANSYS Inc. *Fluent Customization Manual*.

Appendix A

Additional Derivations and Equations

A.1 Ti and V Mixing Energies

These derivations are taken from Ivanchenko et al [86]. The excess Gibbs energy for Ti is given by:

$$\begin{aligned}\Delta\overline{G}_{Ti}^{ex} = X_{Al}(1-X_{Ti})\sum_{n=0}^{2}\left[L_{Al,Ti}^{(n)}(X_{Al}-X_{Ti})^n\right] - X_{Al}X_{Ti}(X_{Al}+2X_V)\left(L_{Al,Ti}^{(1)}+2L_{Al,Ti}^{(2)}(X_{Al}-X_{Ti})\right) \\ - X_{Al}X_V\sum_{n=0}^{1}\left[L_{Al,V}^{(n)}(X_{Al}-X_V)^n\right] + X_{Al}X_V(X_{Al}-X_V)L_{Al,V}^{(1)} \\ - X_V(1-X_{Ti})\sum_{n=0}^{1}\left[L_{Ti,V}^{(n)}(X_{Ti}-X_V)^n\right] + X_{Ti}X_V(X_{Al}+2X_V)L_{Ti,V}^{(1)} \quad \text{(A.1)}\end{aligned}$$

The excess Gibbs energy for V is given by:

$$\begin{aligned}\Delta\overline{G}_{V}^{ex} = -X_{Al}X_{Ti}\sum_{n=0}^{2}\left[L_{Al,Ti}^{(n)}(X_{Al}-X_{Ti})^n\right] - X_{Al}X_{Ti}(X_{Al}-X_{Ti})\left(L_{Al,Ti}^{(1)}+2L_{Al,Ti}^{(2)}(X_{Al}-X_{Ti})\right) \\ + X_{Al}(1-X_V)\sum_{n=0}^{1}\left[L_{Al,V}^{(n)}(X_{Al}-X_V)^n\right] - X_{Al}X_V(2X_{Al}+X_{Ti})L_{Al,V}^{(1)} \\ + X_{Ti}(1-X_V)\sum_{n=0}^{1}\left[L_{Ti,V}^{(n)}(X_{Ti}-X_V)^n\right] - X_{Ti}X_V(X_{Al}+2X_{Ti})L_{Ti,V}^{(1)} \quad \text{(A.2)}\end{aligned}$$

Where X_i is molar concentration and $L_{i,j}^{(n)}$ is the mixing energy constants for a given binary alloy, which are given in Table 2.8c based on data from Ansara et al. [89].

A.2 Klassen Electron-Beam Model

The vertical distribution for the electron beam heat source, I_Z, was based on the implementation given by Klassen in sections 3.1, A.2, and A.3 of his thesis and with additional supplementary information from Klassen et al. [79, 181]. This model is based on an in-depth theoretical analysis of the electron beam physics, with empirical factors added to match a wide range of experimental data sources. The main governing equation is:

$$\varepsilon_A = (1 - \eta_{B,\infty}\epsilon_{B,\infty})\left(1 - \frac{\eta_T \epsilon_T}{C}\right) \tag{A.3}$$

Where ε_A is the amount of energy absorbed at a given height, $\eta_{B,\infty}$ is the ratio of electrons backscattered at the surface, $\epsilon_{B,\infty}$ is the energy of backscattered electrons, η_T is the ratio of electrons that penetrate to a given distance, ϵ_T is the energy of electrons at a given penetration depth, and C is a correction term, which is assumed to be 1. Relevant physical parameters and constants are given in Table A.1. The angle of incidence, ϕ, is not relevant to this work due to the assumptions of a continuum and a flat meltpool surface and will therefore be assumed to be equal to 90 deg. τ_0 and E_0 are dependent on the voltage of the electron beam gun, which not changed from the A2X's default value of 60 kV. The atomic number (Z) is a key factor in determining how the electron beam interacts with different alloys; since this model was only developed for Ti-6Al-4V, the model was hard-coded to have a value of $Z = 21.48$, but the derivations from Klassen are valid for a wide range of Z.

Table A.1: Parameters and physical constants for Klassen model

Symbol	Name
ϕ	Angle of incidence (90 deg)
τ_0	Ratio of E_0 to rest energy of an electron, 511 keV (in A2X: 11.74%)
E_0	Initial electron energy (in A2X: 60 keV)
E_R	Rydberg unit of energy (13.606 eV)
Z	Atomic number (in Ti-6Al-4V: 21.48)
z	Depth below surface (m)
z_s	Penetration depth (in Ti-6Al-4V: 18.8×10^{-6} m)

The ratio of electrons backscattered at the surface are given by:

$$\eta_{B,\infty} = \left(\frac{a_1}{\tau_0^{a_2}\left(1 + \left(\frac{a_3}{\tau_0}\right)^{a_4}\right)\left(1 + \left(\frac{\tau_0}{a_5}\right)^{a_6 - a_2}\right)} \right)^{\cos\phi} \tag{A.4}$$

Where a_i is an empirically determined value, which is given in Table A.2. The energy of backscattered electrons, $\epsilon_{B,\infty}$, is given by:

Table A.2: Empirical factors to determine surface backscattering ratio

i	a_i
1	$9.41 \times 10^{-3} + 1.132 * \exp\left\{-\left(\frac{-57.1}{Z}\right)^{0.579}\right\}$
2	$\frac{3.47}{1+(Z/0.163)^{0.833}}$
3	$7.3 \times 10^{-4} 1 + (58.5/Z)^{5.14}$
4	0.574
5	$1.43\,(Z)^{0.447}$
6	$1.108 + \frac{0.471}{1+(13/Z)^{176}}$

$$\epsilon_{B,\infty} = 1 - \cos\phi + \frac{\cos\phi * b_1 * Z^{b_2} * \tau_0^{b_3}}{1 + (\tau_0/b_4)^{b_3} + (\tau_0/b_5)^{b_3+b_6} + (\tau_0/b_7)^{b_3+b_8}} \tag{A.5}$$

(A.6)

Table A.3: Empirical factors to determine energy lost to surface backscattering

i	b_i
1	82.6
2	0.2063
3	1.075
4	6.56×10^{-3}
5	2.54
6	2.08
7	0.082
8	0.509

Where b_i is a numerical factor, which is given in Table A.3. The fraction of electrons transmitted to a given distance, η_T, is given by:

$$\eta_T = \exp\left\{-\frac{d_1\,(z/z_s)^{d_2}}{(1 - z/z_s)^{d_3}}\right\} \tag{A.7}$$

Where d_i is an empirical factor given by:

$$d_1 = 4.17 * Z^{0.04} - 3.28\,(\sin\phi)^{0.77*Z^{0.2}} \tag{A.8}$$

$$d_2 = \frac{1.2}{Z} * \left(Z^{0.3} * \left(0.5 + (\cos\phi)^{0.5+0.75/(Z^{0.3})}\right)\right)^{3/(Z^{0.043})} \tag{A.9}$$

$$d_3 = \frac{Z^{0.92}}{72} + 0.72 * Z^{0.14} * (\sin\phi)^{1.23(Z^{0.2})} \tag{A.10}$$

The energy ratio of fractions at a given distance, ϵ_T, is given by:

$$\epsilon_T = (1 - z/z_s)^{\frac{\zeta}{\zeta+1}} \tag{A.11}$$

$$\zeta = 1 + 2\exp\{-\psi + 2 * 10^{-\psi}\} \tag{A.12}$$

$$\psi = \ln\left\{\frac{0.77}{8} * Z^{-1/6} * \frac{E_0}{E_R}\right\} \tag{A.13}$$

The backscattering parameters, $\eta_{B,\infty}$ and $\epsilon_{B,\infty}$, are given in Table A.4. The key factor is the efficiency of the beam, which is what fraction of the total energy is delivered from the beam to the substrate. In Ti-6Al-4V and with a 60 kV electron beam, the efficiency is 81.47%. The penetration parameters, η_T and ϵ_T, are plotted in Fig. A.1.

Table A.4: Backscattering parameters for Klassen electron beam model

Parameter	Value
Fraction of electrons backscattered at surface ($\eta_{B,\infty}$)	28.24%
Energy of electrons backscattered at surface ($\epsilon_{B,\infty}$)	65.61%
Beam efficiency ($1 - \epsilon_{B,\infty}\eta_{B,\infty}$)	81.47%

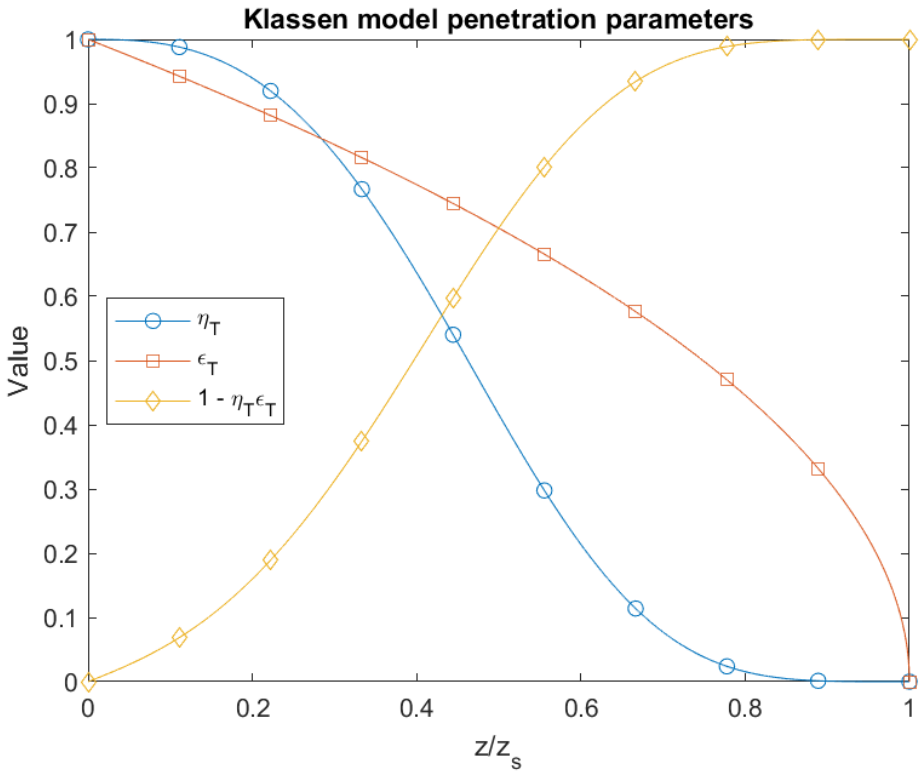

Figure A.1: Penetration parameters η_T and ϵ_T

Because the full model is highly complex but independent of material state, a simplified version was implemented by fitting an 8th order polynomial to the full model. A comparison between the full model and polynomial approximation is given in Fig. A.2. The equation for the polynomial is:

$$I_z \approx \frac{1}{z_s}\Bigg[3.668\times10^{2}\left(\frac{z}{z_s}\right)^{8} - 1.404\times10^{3}\left(\frac{z}{z_s}\right)^{7} + 2.0539\times10^{3}\left(\frac{z}{z_s}\right)^{6} - 1.424\times10^{3}\left(\frac{z}{z_s}\right)^{5} + 4.955\times10^{2}\left(\frac{z}{z_s}\right)^{4} + 1.145\times10^{2}\left(\frac{z}{z_s}\right)^{3} + 25.76\left(\frac{z}{z_s}\right)^{2} + 2.891\times10^{-2}\left(\frac{z}{z_s}\right) + 0.4328\Bigg] \quad \text{(A.14)}$$

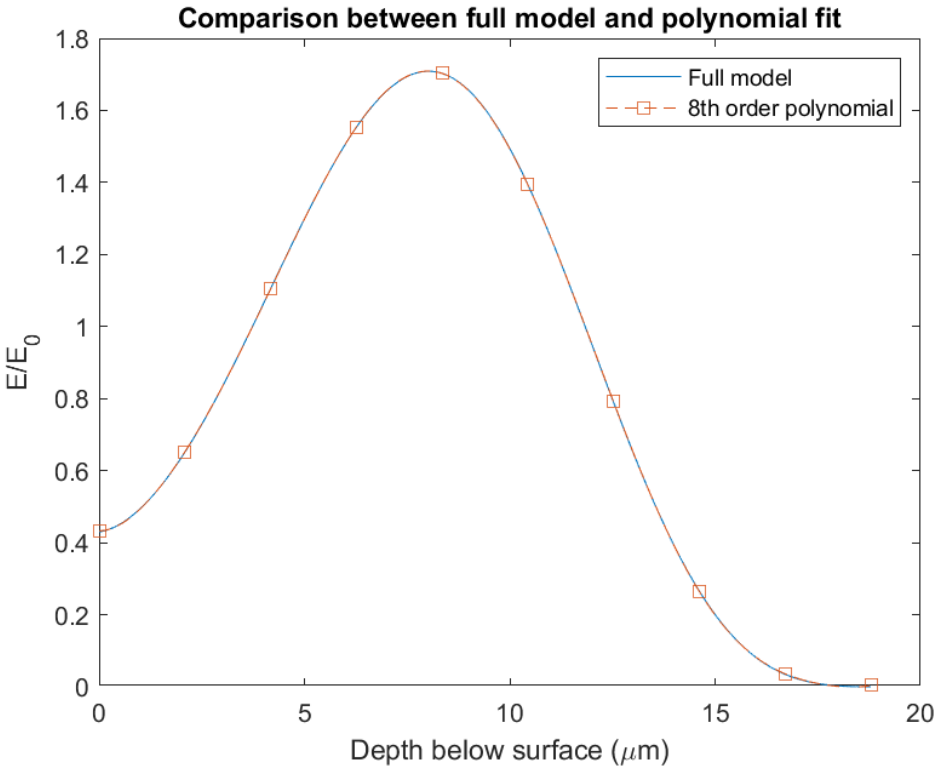

Figure A.2: Comparison between full implementation of Klassen model and best-fit 8th order polynomial

A.3 316L Material Properties

The properties for the 316L baseplate are based on the data provided by Mills [81]. Similarly to what was done for the Ti-6Al-4V material, the density was fixed at a constant value, in this

case the value at $T = 1000$ K, and the specific heat was normalized by this value. The resulting properties are:

$$\rho = 7950 \tag{A.15}$$
$$c_p = -3.6851 \times 10^{-5} T^2 + 0.2042T + 420.0936 \tag{A.16}$$
$$k = -7.4284 \times 10^{-6} T^2 + 0.0274T + 6.2402 \tag{A.17}$$

A.4 Camera Calibration Curves

The calibration equations for the four tested integration times are given in Table A.5. A further development was to develop calibration equations for arbitrary integration times. By plotting the inverse of integration time versus the slope and offset values for equations, it was found that the data for the 0.05, 0.5, and 2 ms integration times fit a linear relationship well. The 15 ms integration time does not fit this relationship as well, likely because the calibration only has 2 experimental data points. These curves are given in Figs. A.3 and A.4. For an arbitrary integration time t_{int}, the calibration equation can be expressed as:

Table A.5: Calibration equations at measured integration times

Integration time (ms)	Calibration curve
0.05	$243.335C - 4.1086 \times 10^4$
0.5	$17.1036C + 2.4342 \times 10^4$
2	$4.5663C + 2.6294 \times 10^4$
15	$1.99C + 7.9433 \times 10^3$

$$W = \left(\frac{0.124\ s}{t_{int}} - 4.5202 \right) C - \frac{3.5308\ s}{t_{int}} + 2.9665 \times 10^4 \tag{A.18}$$

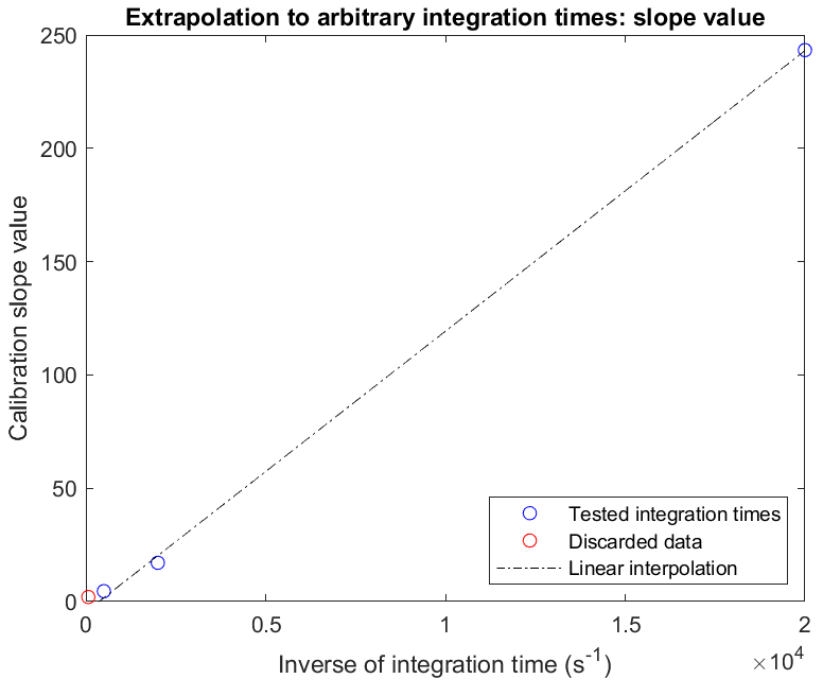

Figure A.3: Slope of calibration equation versus inverse of integration time

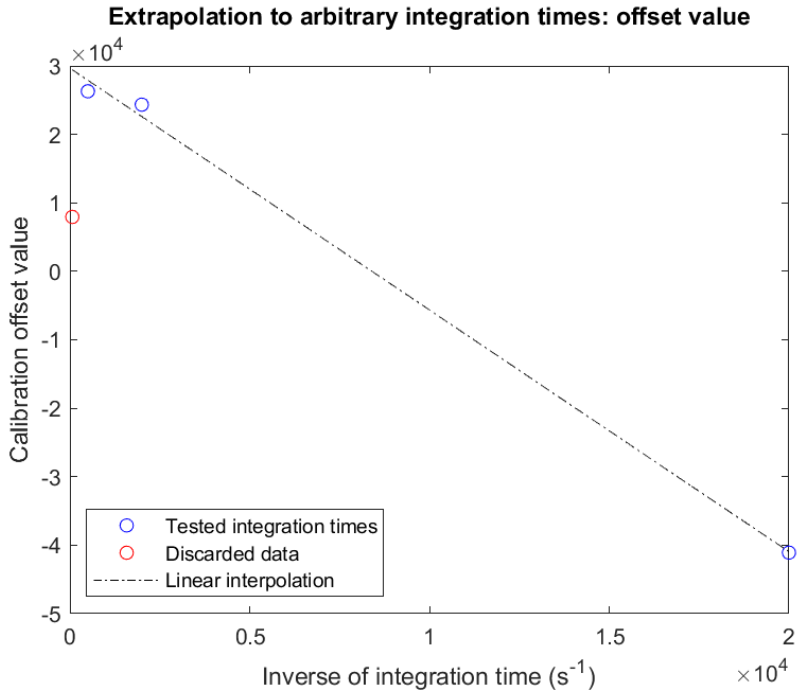

Figure A.4: Offset of calibration equation versus inverse of integration time

Appendix B

Source Code for User-Defined Functions and Material Models

B.1 User-Defined Functions

The following codes were used to implement many of the custom functionality of this model. This code is by no means error free and should be used with caution. It was used with the interpreter and its performance with Fluent's compiler has not been analyzed. 11 User-Defined Memory (UDM) variables were used, which are given in Table B.1. Two User-Defined Scalar (UDS) variables were used, which are given in Table B.2. More details on Fluent's UDF syntax and features can be found in the Fluent Customization Manual [208].

Table B.1: User-Defined Memory (UDM) Variable Names

Number	Description
0	Material flag
1	Derivative of temperature
2	Gradient of temperature in x
3	Gradient of temperature in y
4	Gradient of temperature in z
5	Gradient of temperature at solidification
6	Derivative of temperature at solidification
7	Time of solidification
8	Vanadium weight composition
9	Thermal diffusivity
10	Predicted grain structure

Table B.2: User-Defined Scalar (UDS) Variable Names

Variable number	Description
0	Ti weight composition
1	Al weight composition

Material Flag Algorithm

This code was executed every iteration and implements the pseudocode given in Algorithm 1. Many other functions use the matflag variable as a quick way to determine the state of a cell.

```
DEFINE_ADJUST(matflag_adj,d)
{
    const float t_sol = 1878;
    const float t_liq = 1923;
    float tmp;
    int matflag;
    Thread *t;
    cell_t c;
    face_t f;

    thread_loop_c(t,d)
    {
        begin_c_loop_all(c,t)
        {
            matflag = C_UDMI(c,t,0);
            tmp = C_T(c,t);

            if (tmp >= t_liq)
            {
                matflag = 3; /* liquid */
                C_UDMI(c,t,0) = matflag;
            }

            else if (tmp > t_sol)
            {
                matflag = 2; /* mushy */
                C_UDMI(c,t,0) = matflag;

            }
            else if (matflag != 0)
            {
                matflag = 1; /* solid */
                C_UDMI(c,t,0) = matflag;
            }
```

```
35              else
36              {
37                  matflag = 0;
38                  C_UDMI(c,t,0) = matflag;
39              }
40
41          end_c_loop_all(c,t)
42          }
43      }
44  }
```

Electron Beam Heat Source

This code implements the EBM heat source model, with the vertical distribution based on the implementation from Klassen and the in-plane distribution based on the Gaussian model from Degenhardt [79, 93]. In order to achieve variable beam position and/or power, lines 35-50 can be modified to be functions of time; in this case, they are left as constants.

```
1  DEFINE_PROFILE(q_ebm_zah_radial, t, position)
2  {
3      float x_b;
4      float y_b;
5      float z_b;
6      float dx;
7      float dy;
8      float dz;
9      float diam_eff;
10     float pow_eff;
11     float depth_pen;
12     float dr2;
13     float r_lim2;
14     float x[3];
15     float Iz;
16     float Ixy;
17     float speed;
18     float eta;
19     float r_init;
20     float r_cur;
21     cell_t c;
22     float cur_time;
23     float ang;
24     float r;
25
26
```

```
27
28      /* CONSTANTS*/
29      diam_eff = 4.343E-5; /* Beam diameter w/scaling factors included,
            corresponds to 0.4 mm */
30      /* pow_eff = 870; /* Power including efficencies W */
31      depth_pen = 18.8e-6; /* Penetration depth, m */
32      r_lim2 = 8e-4; /* Maximum radial distance to apply BC */
33      eta = 1; /* BACKSCATTERING FACTOR*/
34
35      /* BEAM POSITION --- */
36      speed = .5;
37      cur_time = CURRENT_TIME;
38      /*HOLD CONSTANT*/
39      x_b = 0;
40      y_b = 0;
41      z_b = 0;
42
43       if (250E-6 > cur_time) /* DISABLE BEAM AFTER 250 us */
44      {
45          pow_eff = 600;
46      }
47      else
48      {
49          pow_eff = 0;
50      }
51
52      begin_c_loop(c,t)
53      {
54          C_CENTROID(x,c,t);
55
56          dz = (z_b - x[2])/depth_pen;
57          dy = y_b - x[1];
58          dx = x_b - x[0];
59          dr2 = pow(dy,2) + pow(dx,2);
60
61          if (dz < 1 && dr2 <= r_lim2)
62          {
63
64              Ixy = 1.8323E+7 * exp(-dr2 * 5.7565E+7);
65
66              Iz = pow(depth_pen,-1) * ((0.366759463377832E+3) * pow(dz
                    ,8) + (-1.403821892842246E+3)* pow(dz,7) +
                    (2.053923371729744E+3) * pow(dz,6) +
                    (-1.424141111075024E+3) * pow(dz,5) +
```

```
                (0.495534253777850E+3) * pow(dz,4) +
                (-0.114474116881998E+3) * pow(dz,3) +
                (0.025762062707629E+3) * pow(dz,2) +
                (0.028913009773409)*dz + 0.432856523832315);

            C_PROFILE(c,t,position) = Iz*Ixy*eta * pow_eff;
        }
        else
        {
            C_PROFILE(c,t,position) = 0;
        }
    }
    end_c_loop(c,t)
}
```

Powder Layer Initialization

This code generates a 50 μm layer of powder on top of an otherwise solid domain.

```
DEFINE_INIT(cyl_sol, d)
{
    float r_thres;
    float z_thres;
    float r;
    float x[3];
    cell_t c;
    face_t f;
    Thread *t;

    r_thres = 0.75E-3;
    z_thres = 50E-6;

    thread_loop_c(t,d)
    {
        begin_c_loop_all(c,t)
        {
            C_CENTROID(x,c,t);
            r = sqrt(pow(x[0], 2) + pow(x[1],2));

            if (fabs(x[2]) > z_thres)
            {
                C_UDMI(c,t,0) = 1;
                C_YI(c,t,0) = 0;
                C_YI(c,t,1) = 0;
```

```
26              }
27              else
28              {
29                  C_UDMI(c,t,0) = 0;
30                  C_YI(c,t,0) = 0.52;
31                  C_YI(c,t,1) = 0.48;
32              }
33
34          }
35          end_c_loop_all(c,t)
36      }
37
38  }
```

Variable Specific Heat

Due to limitations in Fluent on how specific heat can be varied, this code contains two functions that effectively vary a mixture of materials in order to achieve the correct specific heat. This is based on a recommendation from the CFD online forums [205].

```
1  DEFINE_PROFILE(mixing_ti_sint_null,t,position)
2  {
3      int matflag;
4      float conc_null;
5      float poro;
6      cell_t c;
7
8
9      poro = .52;
10
11     begin_c_loop(c,t)
12     {
13         matflag = C_UDMI(c,t,0);
14
15         if (matflag == 0)
16         {
17             C_PROFILE(c,t,position) = 1 - poro;
18         }
19         else
20         {
21             C_PROFILE(c,t,position) = 0;
22         }
23     }
24     end_c_loop(c,t)
```

```
}

DEFINE_PROFILE(mixing_ti_sint_real,t,position)
{
    int matflag;
    float conc_null;
    float poro;
    cell_t c;


    poro = .52;

    begin_c_loop(c,t)
    {
        matflag = C_UDMI(c,t,0);

        if (matflag == 0)
        {
            C_PROFILE(c,t,position) = poro;
        }
        else
        {
            C_PROFILE(c,t,position) = 0;
        }
    }
    end_c_loop(c,t)
}
```

Temperature Dependent Viscosity

This code implements the Arrhenius viscosity equation, Eq. (3.7), based on experimental data from Raush [82].

```
DEFINE_PROPERTY(ti_viscosity,c,t)
{
    float temp;
    float eta;

    temp = C_T(c,t);

    eta = 0.021346470139689 * exp(1.11158E+04/temp);

    return eta;
}
```

Evaporative and Radiative Heat Loss

This code implements the evaporative and radiative heat boundary conditions. Evaporation is based on the implementations from Klassen, Ivanchenko et al, and Semiatin et al [79, 86, 88]. Radiation is based on the emissivity values given in Fig. 3.8d.

```
DEFINE_PROFILE(ti_emis_evap,t,position)
{
    float eps;
    float B;
    float temp;
    float eps1;
    float t_inf;
    float sigma_sb;
    float x_al;
    float x_ti;
    float x_v;
    float w_al;
    float w_ti;
    float w_v;
    float m_al;
    float m_ti;
    float m_v;
    float gamma_Ti;
    float gamma_al;
    float pres_Ti;
    float L_AlTi_0;
    float L_AlTi_1;
    float L_AlTi_2;
    float L_AlV_0;
    float L_AlV_1;
    float L_TiV_0;
    float L_TiV_1;
    float G_Ti;
    float A_Ti;
    float B_Ti;
    float C_Ti;
    float P_0Ti;
    float P_sTi;
    float pi;
    float R;
    float W_Ti2;
    float G_Al;
    float A_Al;
    float B_Al;
```

```
40      float C_Al;
41      float P_0Al;
42      float P_sAl;
43      float W_Al2;
44      float L_vap0_Ti;
45      float L_vapS_Ti;
46      float L_vap0_Al;
47      float L_vapS_Al;
48      float t_crit_Ti;
49      float t_crit_Al;
50      float q_evap_al;
51      float q_evap_ti;
52      float liqf;
53      float rad_temp;
54      int matflag;
55      face_t f;
56      cell_t c;
57      Thread *t0;
58
59      sigma_sb = 5.670374E-8;
60      t_inf = 615;
61      A_Al = 16379;
62      B_Al = 9.979;
63      C_Al = -0.335;
64      A_Ti = 22946;
65      B_Ti = 10.581;
66      C_Ti = -0.373;
67      m_al = 26.98E-3;
68      m_ti = 47.86E-3;
69      m_v = 50.94E-3;
70      R = 8.314;
71      pi = 3.14159;
72
73      L_vap0_Ti = 9.7e6;
74      L_vap0_Al = 11.6e6;
75
76      t_crit_Al = 6700;
77      t_crit_Ti = 7890;
78
79      begin_f_loop(f,t)
80      {
81          c = F_C0(f,t);
82          t0 = THREAD_T0(t);
83
```

```
84          matflag = C_UDMI(c,t0,0);
85          liqf = C_LIQF(c,t0);
86          temp = C_T(c,t0);
87
88          if (matflag == 3) /* LIQUID */
89          {
90              eps = 0.425 - 1.05E-5 * temp;
91
92              if (1878 < temp)
93              {
94                  L_AlTi_0 = -108250 + 38*temp;
95                  L_AlTi_1 = -6000 + 5*temp;
96                  L_AlTi_2 = 15000;
97
98                  L_AlV_0 = -50725 + 9*temp;
99                  L_AlV_1 = -15000 + 8*temp;
100
101                 L_TiV_0 = 1400;
102                 L_TiV_1 = 4100;
103
104
105
106                 w_ti = F_UDSI(f,t,0);
107                 w_al = F_UDSI(f,t,1);
108                 w_v = 1 - w_ti - w_al;
109
110                 x_ti = (w_ti/m_ti) /((w_ti/m_ti) + (w_al/m_al) + (w_v/
                        m_v));
111                 x_al = (w_al/m_al) /((w_ti/m_ti) + (w_al/m_al) + (w_v/
                        m_v));
112                 x_v = 1 - x_ti - x_al;
113
114
115                 G_Ti = (x_al * (1 - x_ti) * (L_AlTi_0 + L_AlTi_1 * (
                        x_al - x_ti) + L_AlTi_2 * pow((x_al - x_ti),2)));
116
117                 G_Ti += -x_al * x_ti * (x_v + 2*x_al) * (L_AlTi_1 + 2
                        * L_AlTi_2 * (x_al - x_ti));
118
119                 G_Ti += -x_al * x_v * (L_AlV_0 + L_AlV_1 * (x_al - x_v
                        )) - x_al*x_v * (x_al - x_v) * L_AlV_1;
120
121                 G_Ti += x_v * (1 - x_ti) * (L_TiV_0 + L_TiV_1 * (x_ti
                        - x_v));
```

```
122
123             G_Ti += x_ti * x_v * (x_al + 2 * x_v) * L_TiV_1;
124
125
126             gamma_Ti = exp((G_Ti/(R*temp)));
127
128             P_0Ti = 133 * pow(10,(-A_Ti/temp + B_Ti)) * pow(temp,
                    C_Ti);
129
130             P_sTi = P_0Ti * x_ti * gamma_Ti;
131
132             W_Ti2 =  -(0.82 * P_sTi * sqrt(m_ti/(2*pi*R*temp)));
133
134             L_vapS_Ti = L_vap0_Ti * sqrt(1 - pow((temp/t_crit_Ti)
                    ,2));
135
136             q_evap_ti = W_Ti2 * L_vapS_Ti * liqf;
137
138
139             G_Al = (x_ti * (1 - x_al) * (L_AlTi_0 + L_AlTi_1 * (
                    x_al - x_ti) + L_AlTi_2 * pow((x_al - x_ti),2)));
140
141             G_Al += (x_al * x_ti * (x_v + 2 * x_ti) * (L_AlTi_1 +
                    2 * L_AlTi_2 * (x_al - x_ti)));
142
143             G_Al += (1 - x_al) * x_v * (L_AlV_0 + L_AlV_1 * (x_al
                    - x_v));
144
145             G_Al += (x_al * x_v * (x_ti + 2 * x_v) * L_AlV_1) - (
                    x_ti * x_v * (L_TiV_0 + L_TiV_1 * (x_ti - x_v)));
146
147             G_Al += x_ti * x_v * (x_v - x_ti) * L_TiV_1;
148
149             gamma_al = exp((G_Al/(R*temp)));
150
151
152             P_0Al = 133 * pow(10,(-A_Al/temp + B_Al)) * pow(temp,
                    C_Al);
153
154
155             P_sAl = P_0Al * x_al * gamma_al;
156
157             W_Al2 = -(0.82 * P_sAl * sqrt(m_al/(2*pi*R*temp)));
158
```

```
159                 L_vapS_Al = L_vap0_Al * sqrt(1 - pow((temp/t_crit_Al)
                        ,2));
160
161                 q_evap_al = W_Al2 * L_vapS_Al * liqf;
162
163
164             }
165             else
166             {
167                 q_evap_ti = 0;
168                 q_evap_al = 0;
169             }
170
171
172         }
173         else if (matflag == 2) /* MUSHY */
174         {
175             eps = 0.7386 - (temp - 1878)*(0.7386-0.405)/(1923-1878);
176             q_evap_al = 0;
177             q_evap_ti = 0;
178         }
179         else if (matflag == 1) /* SOLID */
180         {
181             eps = 6.45343 - 0.02305 * temp + 3.32014E-5 * pow(temp,2)
                    - 2.02883E-8 * pow(temp,3) + 4.40994E-12 * pow(temp,4);
182             q_evap_al = 0;
183             q_evap_ti = 0;
184
185         }
186         else /* POWDER */
187         {
188             B = 0.6825;
189             eps1 = 6.45343 - 0.02305 * temp + 3.32014E-5 * pow(temp,2)
                        - 2.02883E-8 * pow(temp,3) + 4.40994E-12 * pow(temp,4)
                    ;
190             eps = 0.1961 * eps1 + ((eps1 * (2 + B))/(eps1*(1 + B) + 1)
                    );
191             q_evap_al = 0;
192             q_evap_ti = 0;
193         }
194
195         F_PROFILE(f,t,position) = -eps * sigma_sb * (pow(temp,4) - pow
                (t_inf,4)) + q_evap_al + q_evap_ti;
196
```

```
197     }
198     end_f_loop(f,t)
199
200
201 }
```

Ti and Al Evaporative Mass Loss

These two codes implement the evaporative mass loss boundary condition for Ti and Al, respectively. Evaporation is based on the implementations from Klassen, Ivanchenko et al, and Semiatin et al [79, 86, 88]. While this code is very similar to the evaporative and radiative heat loss boundary condition code, it is not possible for a single code to enable both a thermal and UDS scalar boundary condition due to limitations within Fluent, which meant that much of the code had to be copied.

```
1  DEFINE_PROFILE(uds_ti_evaporation,t,position)
2  {
3      float temp;
4      float x_al;
5      float x_ti;
6      float x_v;
7      float w_al;
8      float w_ti;
9      float w_v;
10     float m_al;
11     float m_ti;
12     float m_v;
13     float gamma_Ti;
14     float pres_Ti;
15     float L_AlTi_0;
16     float L_AlTi_1;
17     float L_AlTi_2;
18     float L_AlV_0;
19     float L_AlV_1;
20     float L_TiV_0;
21     float L_TiV_1;
22     float G_Ti;
23     float A_Ti;
24     float B_Ti;
25     float C_Ti;
26     float P_0Ti;
27     float P_sTi;
28     float pi;
29     float R;
```

```
30      float W_Ti;
31      face_t f;
32
33
34      pi = 3.14159;
35      m_al = 26.98e-3;
36      m_ti = 47.86e-3;
37      m_v = 50.94e-3;
38      R = 8.314;
39      A_Ti = 22946;
40      B_Ti = 10.581;
41      C_Ti = -0.373;
42
43      begin_f_loop(f,t)
44      {
45          temp = F_T(f,t);
46
47          if (1923 < temp)
48          {
49
50              L_AlTi_0 = -108250 + 38*temp;
51              L_AlTi_1 = -6000 + 5*temp;
52              L_AlTi_2 = 15000;
53
54              L_AlV_0 = -50725 + 9*temp;
55              L_AlV_1 = -15000 + 8*temp;
56
57              L_TiV_0 = 1400;
58              L_TiV_1 = 4100;
59
60
61              w_ti = F_UDSI(f,t,0);
62              w_al = F_UDSI(f,t,1);
63              w_v = 1 - w_ti - w_al;
64
65
66              x_ti = (w_ti/m_ti) /((w_ti/m_ti) + (w_al/m_al) + (w_v/m_v)
                    );
67              x_al = (w_al/m_al) /((w_ti/m_ti) + (w_al/m_al) + (w_v/m_v)
                    );
68              x_v = 1 - x_ti - x_al;
69
70              G_Ti = (x_al * (1 - x_ti) * (L_AlTi_0 + L_AlTi_1 * (x_al -
                     x_ti) + L_AlTi_2 * pow((x_al - x_ti),2)));
```

```
71
72              G_Ti += -x_al * x_ti * (x_v + 2*x_al) * (L_AlTi_1 + 2 *
                    L_AlTi_2 * (x_al - x_ti));
73
74              G_Ti += -x_al * x_v * (L_AlV_0 + L_AlV_1 * (x_al - x_v)) -
                     x_al*x_v * (x_al - x_v) * L_AlV_1;
75
76              G_Ti += x_v * (1 - x_ti) * (L_TiV_0 + L_TiV_1 * (x_ti -
                    x_v));
77
78              G_Ti += x_ti * x_v * (x_al + 2 * x_v) * L_TiV_1;


79
80
81              gamma_Ti = exp((G_Ti/(R*temp)));
82
83              P_0Ti = 133 * pow(10,(-A_Ti/temp + B_Ti)) * pow(temp,C_Ti)
                    ;
84
85              P_sTi = P_0Ti * x_ti * gamma_Ti;
86
87              W_Ti =  -(0.82 * P_sTi * sqrt(m_ti/(2*pi*R*temp)))/3920;
88
89              F_PROFILE(f,t,position) = W_Ti;
90          }
91          else
92          {
93              F_PROFILE(f,t,position) = 0;
94          }
95      }
96      end_f_loop(f,t)
97  }

1   DEFINE_PROFILE(uds_al_evaporation,t,position)
2   {
3       float temp;
4       float x_al;
5       float x_ti;
6       float x_v;
7       float w_al;
8       float w_ti;
9       float w_v;
10      float m_al;
11      float m_ti;
```

```
12      float m_v;
13      float gamma_al;
14      float pres_al;
15      float L_AlTi_0;
16      float L_AlTi_1;
17      float L_AlTi_2;
18      float L_AlV_0;
19      float L_AlV_1;
20      float L_TiV_0;
21      float L_TiV_1;
22      float G_Al;
23      float A_Al;
24      float B_Al;
25      float C_Al;
26      float P_0Al;
27      float P_sAl;
28      float pi;
29      float R;
30      float W_al;
31      face_t f;
32
33
34      pi = 3.14159;
35      m_al = 26.98e-3;
36      m_ti = 47.86e-3;
37      m_v = 50.94e-3;
38      R = 8.314;
39      A_Al = 16379;
40      B_Al = 9.979;
41      C_Al = -0.335;
42
43
44      begin_f_loop(f,t)
45      {
46          temp = F_T(f,t);
47
48          if (1923 < temp)
49          {
50
51              L_AlTi_0 = -108250 + 38*temp;
52              L_AlTi_1 = -6000 + 5*temp;
53              L_AlTi_2 = 15000;
54
55              L_AlV_0 = -50725 + 9*temp;
```

```
56              L_AlV_1 = -15000 + 8*temp;
57
58              L_TiV_0 = 1400;
59              L_TiV_1 = 4100;
60
61
62              w_ti = F_UDSI(f,t,0);
63              w_al = F_UDSI(f,t,1);
64              w_v = 1 - w_ti - w_al;
65
66              x_ti = (w_ti/m_ti) /((w_ti/m_ti) + (w_al/m_al) + (w_v/m_v)
                    );
67              x_al = (w_al/m_al) /((w_ti/m_ti) + (w_al/m_al) + (w_v/m_v)
                    );
68              x_v = 1 - x_ti - x_al;
69
70
71              G_Al = (x_ti * (1 - x_al) * (L_AlTi_0 + L_AlTi_1 * (x_al -
                     x_ti) + L_AlTi_2 * pow((x_al - x_ti),2)));
72
73              G_Al += (x_al * x_ti * (x_v + 2 * x_ti) * (L_AlTi_1 + 2 *
                    L_AlTi_2 * (x_al - x_ti)));
74
75              G_Al += (1 - x_al) * x_v * (L_AlV_0 + L_AlV_1 * (x_al -
                    x_v));
76
77              G_Al += (x_al * x_v * (x_ti + 2 * x_v) * L_AlV_1) - (x_ti
                    * x_v * (L_TiV_0 + L_TiV_1 * (x_ti - x_v)));
78
79              G_Al += x_ti * x_v * (x_v - x_ti) * L_TiV_1;
80
81              gamma_al = exp((G_Al/(R*temp)));
82
83
84              P_0Al = 133 * pow(10,(-A_Al/temp + B_Al)) * pow(temp,C_Al)
                    ;
85
86
87              P_sAl = P_0Al * x_al * gamma_al;
88
89
90              F_PROFILE(f,t,position) = -(P_sAl * 0.82 * sqrt(m_al/(2*pi
                    *R*temp)))/3920;
91          }
```

```
92          else
93          {
94              F_PROFILE(f,t,position) = 0;
95          }
96      }
97      end_f_loop(f,t)
98  }
```

Constant Solidus and Liquidus Temperatures

This code fixes an undesired side effect of the variable specific heat mixing code. It was found that that code lead to variable melting temperatures due to unforeseen behavior in Fluent, so this code was written to force constant melting temperatures.

```
1  DEFINE_PROPERTY(ti_liquidus,c,t)
2  {
3      float t_liq;
4
5      t_liq = 1923;
6
7      return t_liq;
8  }
9
10 DEFINE_PROPERTY(ti_solidus,c,t)
11 {
12     float t_sol;
13
14     t_sol = 1878;
15
16     return t_sol;
17 }
```

Post-Processing Script

This code calculates several variables for post-processing. This code is somewhat unstable and should be used with caution.

```
1  DEFINE_EXECUTE_AT_END(gradient_calc)
2  {
3      float t_space[3];
4      float t_0;
5      float t_1;
6      float t_2;
7      float tstep;
8      float tstep_1;
```

```
9       float tstep_2;
10      float g_sold;
11      float tx;
12      float ty;
13      float tz;
14      float x[3];
15      float x_plus;
16      float x_minus;
17      float y_plus;
18      float y_minus;
19      float z_plus;
20      float z_minus;
21      float xm_plus;
22      float xm_minus;
23      float ym_plus;
24      float ym_minus;
25      float zm_plus;
26      float zm_minus;
27      float l;
28      float w;
29      float h;
30      float v;
31      float lm;
32      float wm;
33      float hm;
34      float vm;
35      float tim;
36      int matflag;
37      int ID = 1;
38      FILE *fp;
39      cell_t c;
40      face_t f;
41      Domain *d;
42      Thread *t;
43      Thread *thread_name;
44      d = Get_Domain(1);
45      tstep = CURRENT_TIMESTEP;
46
47      x_plus = -100;
48      y_plus = -100;
49      z_plus = -100;
50      x_minus = 100;
51      y_minus = 100;
52      z_minus = 100;
```

```
53      v = 0;
54
55      xm_plus = -100;
56      ym_plus = -100;
57      zm_plus = -100;
58      xm_minus = 100;
59      ym_minus = 100;
60      zm_minus = 100;
61      vm = 0;
62
63      thread_loop_c(t,d)
64      {
65
66          begin_c_loop_all(c,t)
67          {
68
69
70              /* V conc calc */
71
72              C_UDMI(c,t,8) = 1 - C_UDSI(c,t,0) - C_UDSI(c,t,1);
73
74
75              /* Calc time derivative with backwards 2nd order diff*/
76
77              t_0 = C_T(c,t);
78              t_1 = C_T_M1(c,t);
79              t_2 = C_T_M2(c,t);
80
81              C_UDMI(c,t,1) = fabs((3*t_0 - 4*t_1 + t_2)/(2*tstep));
82
83               /* in order to access gradients: solve/set/expert no yes
                    yes no*/
84              tx = C_T_G(c,t)[0];
85              ty = C_T_G(c,t)[1];
86              tz = C_T_G(c,t)[2];
87
88
89              C_UDMI(c,t,2) = tx;
90              C_UDMI(c,t,3) = ty;
91              C_UDMI(c,t,4) = tz;
92
93
94              matflag = C_UDMI(c,t,0);
95              g_sold = C_UDMI(c,t,5);
```

```
96
97
98              if (matflag == 2)
99              {
100
101                 if (g_sold < 0)
102                 {
103                     C_UDMI(c,t,5) = sqrt(pow(tx,2) + pow(ty,2) + pow(
                            tz,2));
104                     C_UDMI(c,t,6) = fabs((3*t_0 - 4*t_1 + t_2)/(2*
                            tstep));
105                     C_UDMI(c,t,7) = CURRENT_TIME;
106                 }
107
108                 C_CENTROID(x,c,t);
109                 vm += C_VOLUME(c,t);
110
111                 if (x[0] > xm_plus)
112                 {
113                     xm_plus = x[0];
114                 }
115                 else if (x[0] < xm_minus)
116                 {
117                     xm_minus = x[0];
118                 }
119
120
121                 if (x[1] > ym_plus)
122                 {
123                     ym_plus = x[1];
124                 }
125                 else if (x[1] < ym_minus)
126                 {
127                     ym_minus = x[1];
128                 }
129
130
131                 if (x[2] > zm_plus)
132                 {
133                     zm_plus = x[2];
134                 }
135                 else if (x[2] < zm_minus)
136                 {
137                     zm_minus = x[2];
```

```
138             }
139
140
141         }
142         else if (matflag == 3)
143         {
144             C_UDMI(c,t,5) = -1;
145             C_UDMI(c,t,6) = -1;
146             C_UDMI(c,t,7) = -1;
147
148             C_CENTROID(x,c,t);
149             v += C_VOLUME(c,t);
150
151             if (x[0] > x_plus)
152             {
153                 x_plus = x[0];
154             }
155             else if (x[0] < x_minus)
156             {
157                 x_minus = x[0];
158             }
159
160
161             if (x[1] > y_plus)
162             {
163                 y_plus = x[1];
164             }
165             else if (x[1] < y_minus)
166             {
167                 y_minus = x[1];
168             }
169
170
171             if (x[2] > z_plus)
172             {
173                 z_plus = x[2];
174             }
175             else if (x[2] < z_minus)
176             {
177                 z_minus = x[2];
178             }
179         }
180
181         C_UDMI(c,t,9) = C_K_L(c,t)/(C_CP(c,t) * 4189);
```

```

            }
            end_c_loop_all(c,t)

        }

        if (vm > 1e-16)
        {

            l = x_plus - x_minus;
            w = y_plus - y_minus;
            h = z_plus - z_minus;
            lm = xm_plus - xm_minus;
            wm = ym_plus - ym_minus;
            hm = zm_plus - zm_minus;
            tim = CURRENT_TIME;
            fp = fopen("data_out.txt","a");

            fprintf(fp,"%e, %e, %e, %e, %e, %e ,%e, %e, %e \n",tim,l,w,h,v,lm,wm,hm,vm);

            fclose(fp);
        }
    }
```

B.2 Materials File

This file contains the custom material definitions. The first definition, `ss`, is the SS 316L baseplate material, which can only be used for the shell conduction feature and does not contain fluid properties. The second definition, `ti_mixture_10_25_19` defines the Ti-6Al-4V material as a mixture of 3 separate material models, which was a necessary feature in order to obtain variable specific heat throughout the domain. There are two sintered material models, `ti_sint_real` and `ti_sint_null`, which are identical except for the null material has no specific heat below the densification temperature, while the real material has specific heat equivalent to the bulk specific heat multiplied by the porosity ϕ. By varying the concentration of these two materials, any arbitrary specific heat can be obtained. The third material, `ti_solid`, corresponds to the bulk solid, mushy, and liquid properties. Note that the majority of the properties defined below are irrelevant to this analysis; when creating a material, Fluent automatically populates all possible fields, even if they are not used. Therefore, many of the properties not relevant to this analysis (e.g. electrical or chemical properties) have the default values from Fluent, which are not the correct values for Ti-6Al-4V.

```
;;;;;;;;;;;;;;;;;;;;;;;;;;;;;;;;;;;;;;;;;;;;;;;;;;;;;;;;;;;;;;;;;;;;
;;;                                                              ;;;
;;;             Fluent USER DEFINED MATERIAL DATABASE            ;;;
```

```
;;;                                                                    ;;;
;;; (name type[fluid/solid] (chemical-formula . formula)               ;;;
;;;              (prop1 (method1a . data1a) (method1b . data1b))       ;;;
;;;             (prop2 (method2a . data2a) (method2b . data2b)))       ;;;
;;;                                                                    ;;;
;;;;;;;;;;;;;;;;;;;;;;;;;;;;;;;;;;;;;;;;;;;;;;;;;;;;;;;;;;;;;;;;;;;;;;;

(
    (ss solid
        (chemical-formula . ss)
        (density (constant . 7950.))
        (specific-heat (polynomial 420.0936 0.2042 -3.6851e-05))
        (thermal-conductivity (polynomial 6.2402 0.0274 -7.4284e-06))
        (formation-entropy (constant . 164448.08))
        (electric-conductivity (constant . 35410000.))
        (magnetic-permeability (constant . 1.257e-06))
    )

    (ti_mixture_10_25_19 mixture
        (chemical-formula . #f)
        (species (names (ti_sint_real ti_sint_null ti_solid) () ()))
        (density (volume-weighted-mixing-law . #f))
        (specific-heat (mixing-law . #f))
        (thermal-conductivity (mass-weighted-mixing-law . #f))
        (viscosity (user-defined "ti_viscosity"))
        (mass-diffusivity (constant-dilute-appx 1.))
        (melting-heat (constant . 143000.))
        (tsolidus (user-defined "ti_solidus"))
        (tliqidus (user-defined "ti_liquidus"))
        (tmelt (constant . 2000.))
        (eutectic-temp (constant . 1923.))
        (uds-diffusivity (defined-per-uds (uds-2 (constant . 1)) (
           uds-3 (constant . 1)) (uds-4 (constant . 1)) (uds-5 (
           constant . 1)) (uds-6 (constant . 1)) (uds-7 (constant . 1)
           ) (uds-8 (constant . 1)) (uds-9 (constant . 1)) (uds-10 (
           constant . 1)) (uds-11 (constant . 1)) (uds-12 (constant .
           1)) (uds-13 (constant . 1)) (uds-14 (constant . 1)) (uds-15
            (constant . 1)) (uds-16 (constant . 1)) (uds-17 (constant
           . 1)) (uds-18 (constant . 1)) (uds-19 (constant . 1)) (
           uds-20 (constant . 1)) (uds-21 (constant . 1)) (uds-22 (
           constant . 1)) (uds-23 (constant . 1)) (uds-24 (constant .
           1)) (uds-25 (constant . 1)) (uds-26 (constant . 1)) (uds-27
            (constant . 1)) (uds-28 (constant . 1)) (uds-29 (constant
           . 1)) (uds-30 (constant . 1)) (uds-31 (constant . 1)) (
```

```
            uds-32 (constant . 1)) (uds-33 (constant . 1)) (uds-34 (
            constant . 1)) (uds-35 (constant . 1)) (uds-36 (constant .
            1)) (uds-37 (constant . 1)) (uds-38 (constant . 1)) (uds-39
             (constant . 1)) (uds-40 (constant . 1)) (uds-41 (constant
            . 1)) (uds-42 (constant . 1)) (uds-43 (constant . 1)) (
            uds-44 (constant . 1)) (uds-45 (constant . 1)) (uds-46 (
            constant . 1)) (uds-47 (constant . 1)) (uds-48 (constant .
            1)) (uds-49 (constant . 1)) (uds-0 (constant . 0.)) (uds-1
            (constant . 0.))))
36          (speed-of-sound (none . #f))
37      )
38
39      (ti_sint_real fluid
40          (chemical-formula . #f)
41          (density (constant . 3920.) (user-defined "ti_density") (
              polynomial piecewise-linear (298. . 4420.) (1878. . 4189.)
              (1938. . 3920.) (2173. . 3750.)))
42          (specific-heat (polynomial piecewise-polynomial (1. 1878.
              597.1063751400092 -0.00498192720736 0.0002139444642521371
              -8.144825918373171e-08 2.55357142858074e-12) (1878. 1923.
              -20431.58077597163 20.29007630443118 -0.004774351192911)
              (1923. 5000. 1241.6 -0.1615)))
43          (thermal-conductivity (polynomial piecewise-polynomial (1.
              1777. 0.5820839 -0.0006516842 1.733357e-06
              -5.684999999999999e-10) (1777. 1878. -127.0611559031509
              0.2140443150321 14 -0.0004587431739766537 3.378767065198651
              e-07 -7.0115e-11) (1878. 5000. 22.75)))
44          (viscosity (constant . 0.004))
45          (molecular-weight (constant . 28.966))
46          (lennard-jones-length (constant . 3.711))
47          (lennard-jones-energy (constant . 78.59999999999999))
48          (thermal-accom-coefficient (constant . 0.9137))
49          (velocity-accom-coefficient (constant . 0.9137))
50          (formation-entropy (constant . 194336))
51          (reference-temperature (constant . 298.15))
52          (critical-pressure (constant . 3758000.))
53          (critical-temperature (constant . 132.3))
54          (acentric-factor (constant . 0.033))
55          (critical-volume (constant . 0.002857))
56          (therm-exp-coeff (constant . 0))
57          (speed-of-sound (none . #f))
58          (melting-heat (constant . 286000.))
59          (tsolidus (constant . 1878.))
60          (tliqidus (constant . 1923.))
```

```
61          (uds-diffusivity (defined-per-uds (uds-1 (constant . 1)) (
                uds-2 (constant . 1)) (uds-3 (constant . 1)) (uds-4 (
                constant . 1)) (uds-5 (constant . 1)) (uds-6 (constant . 1)
                ) (uds-7 (constant . 1)) (uds-8 (constant . 1)) (uds-9 (
                constant . 1)) (uds-10 (constant . 1)) (uds-11 (constant .
                1)) (uds-12 (constant . 1)) (uds-13 (constant . 1)) (uds-14
                 (constant . 1)) (uds-15 (constant . 1)) (uds-16 (constant
                . 1)) (uds-17 (constant . 1)) (uds-18 (constant . 1)) (
                uds-19 (constant . 1)) (uds-20 (constant . 1)) (uds-21 (
                constant . 1)) (uds-22 (constant . 1)) (uds-23 (constant .
                1)) (uds-24 (constant . 1)) (uds-25 (constant . 1)) (uds-26
                 (constant . 1)) (uds-27 (constant . 1)) (uds-28 (constant
                . 1)) (uds-29 (constant . 1)) (uds-30 (constant . 1)) (
                uds-31 (constant . 1)) (uds-32 (constant . 1)) (uds-33 (
                constant . 1)) (uds-34 (constant . 1)) (uds-35 (constant .
                1)) (uds-36 (constant . 1)) (uds-37 (constant . 1)) (uds-38
                 (constant . 1)) (uds-39 (constant . 1)) (uds-40 (constant
                . 1)) (uds-41 (constant . 1)) (uds-42 (constant . 1)) (
                uds-43 (constant . 1)) (uds-44 (constant . 1)) (uds-45 (
                constant . 1)) (uds-46 (constant . 1)) (uds-47 (constant .
                1)) (uds-48 (constant . 1)) (uds-49 (constant . 1)) (uds-0
                (constant . 0.))))
62          (liquidus-slope (constant . 0.))
63          (partition-coeff (constant . 1.))
64          (eutectic-mf (constant . 1.))
65          (solid-diffusion (constant . 0.))
66      )
67
68      (ti_sint_null fluid
69          (chemical-formula . #f)
70          (density (constant . 3920.) (user-defined "ti_density") (
                polynomial piecewise-linear (298. . 4420.) (1878. . 4189.)
                (1938. . 3920.) (2173. . 3750.)) (compressible-liquid
                101325 1.225 142000. 1 1.1 0.9))
71          (specific-heat (polynomial piecewise-linear (291. . 5.) (1778.
                 . 5.) (1878. . 835.) (1923. . 931.) (2500. . 837.)) (
                constant . 1.) (polynomial piecewise-polynomial (100 1000
                1161.48214452351 -2.36881890191577 0.0148551108358867
                -5.03490927522584e-05 9.9285695564579e-08 -1.11109658897742
                e-10 6.54019600406048e-14 -1.57358768447275e-17) (1000 3000
                 -7069.81410143802 33.7060506468204 -0.0581275953375815
                5.42161532229608e-05 -2.936678858119e-08 9.237533169567681
                e-12 -1.56555339604519e-15 1.11233485020759e-19)))
```

```
72          (thermal-conductivity (polynomial piecewise-polynomial (1.
               1777. 0.582083909192637 -0.0006516841783237703
               1.733357325000014e-06 -5.685000000000037e-10) (1777. 1878.
               -127.0611559031509 0.2140443150321 14 -0.0004587431739766537
                3.378767065198651e-07 -7.011499996863311e-11) (1878. 5000.
                22.7)) (user-defined "ti_conductivity") (constant .
               0.0242))
73          (viscosity (constant . 0.004) (sutherland 1.716e-05 273.11
               110.56) (power-law 1.716e-05 273.11 0.666))
74          (molecular-weight (constant . 28.966))
75          (lennard-jones-length (constant . 3.711))
76          (lennard-jones-energy (constant . 78.59999999999999))
77          (thermal-accom-coefficient (constant . 0.9137))
78          (velocity-accom-coefficient (constant . 0.9137))
79          (formation-entropy (constant . 194336))
80          (reference-temperature (constant . 298.15))
81          (critical-pressure (constant . 3758000.))
82          (critical-temperature (constant . 132.3))
83          (acentric-factor (constant . 0.033))
84          (critical-volume (constant . 0.002857))
85          (therm-exp-coeff (constant . 0))
86          (speed-of-sound (none . #f))
87          (melting-heat (constant . 286000.))
88          (tsolidus (constant . 1878.))
89          (tliqidus (constant . 1923.))
90          (uds-diffusivity (defined-per-uds (uds-1 (constant . 1)) (
               uds-2 (constant . 1)) (uds-3 (constant . 1)) (uds-4 (
               constant . 1)) (uds-5 (constant . 1)) (uds-6 (constant . 1)
               ) (uds-7 (constant . 1)) (uds-8 (constant . 1)) (uds-9 (
               constant . 1)) (uds-10 (constant . 1)) (uds-11 (constant .
               1)) (uds-12 (constant . 1)) (uds-13 (constant . 1)) (uds-14
                (constant . 1)) (uds-15 (constant . 1)) (uds-16 (constant
               . 1)) (uds-17 (constant . 1)) (uds-18 (constant . 1)) (
               uds-19 (constant . 1)) (uds-20 (constant . 1)) (uds-21 (
               constant . 1)) (uds-22 (constant . 1)) (uds-23 (constant .
               1)) (uds-24 (constant . 1)) (uds-25 (constant . 1)) (uds-26
                (constant . 1)) (uds-27 (constant . 1)) (uds-28 (constant
               . 1)) (uds-29 (constant . 1)) (uds-30 (constant . 1)) (
               uds-31 (constant . 1)) (uds-32 (constant . 1)) (uds-33 (
               constant . 1)) (uds-34 (constant . 1)) (uds-35 (constant .
               1)) (uds-36 (constant . 1)) (uds-37 (constant . 1)) (uds-38
                (constant . 1)) (uds-39 (constant . 1)) (uds-40 (constant
               . 1)) (uds-41 (constant . 1)) (uds-42 (constant . 1)) (
               uds-43 (constant . 1)) (uds-44 (constant . 1)) (uds-45 (
```

```
            constant . 1)) (uds-46 (constant . 1)) (uds-47 (constant .
            1)) (uds-48 (constant . 1)) (uds-49 (constant . 1)) (uds-0
            (constant . 0.))))
91          (liquidus-slope (constant . 0.))
92          (partition-coeff (constant . 1.))
93          (eutectic-mf (constant . 1.))
94          (solid-diffusion (constant . 0.))
95      )
96
97      (ti_solid fluid
98          (chemical-formula . #f)
99          (density (constant . 3920.)))
100         (specific-heat (polynomial piecewise-polynomial (100. 1878.
            597.1063751400092 -0.00498192720736 0.0002139444642521371
            -8.144825918373171e-08 2.55357142858074e-12) (1878. 1923.
            -20431.58077597163 20.29007630443118 -0.004774351192911)
            (1923. 10000. 1241.588725 -0.1615)))
101         (thermal-conductivity (polynomial piecewise-polynomial (1000.
            1878. 7.761118789235163 -0.00868912237765 2.311143100000019
            e-05 -7.580000000000049e-09) (1878. 1923. -218.5437
            0.124835) (1923. 10000. -6.66 0.0183)))
102         (viscosity (constant . 0.004) (sutherland 1.716e-05 273.11
            110.56) (power-law 1.716e-05 273.11 0.666))
103         (molecular-weight (constant . 28.966))
104         (lennard-jones-length (constant . 3.711))
105         (lennard-jones-energy (constant . 78.59999999999999))
106         (thermal-accom-coefficient (constant . 0.9137))
107         (velocity-accom-coefficient (constant . 0.9137))
108         (formation-entropy (constant . 194336))
109         (reference-temperature (constant . 298.15))
110         (critical-pressure (constant . 3758000.))
111         (critical-temperature (constant . 132.3))
112         (acentric-factor (constant . 0.033))
113         (critical-volume (constant . 0.002857))
114         (therm-exp-coeff (constant . 0))
115         (speed-of-sound (none . #f))
116         (melting-heat (constant . 286000.))
117         (tsolidus (constant . 1878.))
118         (tliqidus (constant . 1923.))
119         (uds-diffusivity (defined-per-uds (uds-1 (constant . 1)) (
            uds-2 (constant . 1)) (uds-3 (constant . 1)) (uds-4 (
            constant . 1)) (uds-5 (constant . 1)) (uds-6 (constant . 1)
            ) (uds-7 (constant . 1)) (uds-8 (constant . 1)) (uds-9 (
            constant . 1)) (uds-10 (constant . 1)) (uds-11 (constant .
```

```
            1)) (uds-12 (constant . 1)) (uds-13 (constant . 1)) (uds-14
             (constant . 1)) (uds-15 (constant . 1)) (uds-16 (constant
            . 1)) (uds-17 (constant . 1)) (uds-18 (constant . 1)) (
            uds-19 (constant . 1)) (uds-20 (constant . 1)) (uds-21 (
            constant . 1)) (uds-22 (constant . 1)) (uds-23 (constant .
            1)) (uds-24 (constant . 1)) (uds-25 (constant . 1)) (uds-26
             (constant . 1)) (uds-27 (constant . 1)) (uds-28 (constant
            . 1)) (uds-29 (constant . 1)) (uds-30 (constant . 1)) (
            uds-31 (constant . 1)) (uds-32 (constant . 1)) (uds-33 (
            constant . 1)) (uds-34 (constant . 1)) (uds-35 (constant .
            1)) (uds-36 (constant . 1)) (uds-37 (constant . 1)) (uds-38
             (constant . 1)) (uds-39 (constant . 1)) (uds-40 (constant
            . 1)) (uds-41 (constant . 1)) (uds-42 (constant . 1)) (
            uds-43 (constant . 1)) (uds-44 (constant . 1)) (uds-45 (
            constant . 1)) (uds-46 (constant . 1)) (uds-47 (constant .
            1)) (uds-48 (constant . 1)) (uds-49 (constant . 1)) (uds-0
            (constant . 0.))))
120         (liquidus-slope (constant . 0.))
121         (partition-coeff (constant . 1.))
122         (eutectic-mf (constant . 1.))
123         (solid-diffusion (constant . 0.))
124     )
125
126 )
```